

AD-A238 959



2

RL-TR-91-124
In-House Report
April 1991



LINEAR PHASED ARRAY OF COAXIALLY-FED MONOPOLE ELEMENTS IN A PARALLEL PLATE WAVEGUIDE

Boris Tomasic and Alexander Hessel

APPROVED FOR PUBLIC RELEASE; DISTRIBUTION UNLIMITED.

DTIC
SELECTED
AUG 5 1991
S B D

Rome Laboratory
Air Force Systems Command
Griffiss Air Force Base, NY 13441-5700

91-06811



This report has been reviewed by the RADC Public Affairs Office (PA) and is releasable to the National Technical Information Service (NTIS). At NTIS it will be releasable to the general public, including foreign nations.

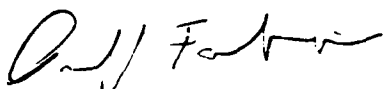
RL-TR-91-124 has been reviewed and is approved for publication.

APPROVED:



JOHN K. SCHINDLER
Chief, Antennas & Comp Division
Directorate of Electromagnetics

APPROVED:



PAUL J. FAIRBANKS, Lt Colonel, USAF
Deputy Director of Electromagnetics

FOR THE COMMANDER:



JAMES W. HYDE III
Directorate of Plans & Programs

If your address has changed or if you wish to be removed from the RADC mailing list, or if the addressee is no longer employed by your organization, please notify RADC (EEAA) Hanscom AFB MA 01731-5000. This will assist us in maintaining a current mailing list.

Do not return copies of this report unless contractual obligations or notices on a specific document require that it be returned.

REPORT DOCUMENTATION PAGE

**Form Approved
OMB No. 0704-0188**

Public reporting for this collection of information is estimated to average 1 hour per response, including the time for reviewing instructions, searching existing data sources, gathering and maintaining the data needed, and completing and reviewing the collection of information. Send comments regarding this burden estimate or any other aspect of this collection of information, including suggestions for reducing this burden, to Washington Headquarters Services, Directorate for Information Operations and Reports, 1215 Jefferson Davis Highway, Suite 1204, Arlington, VA 22202-4302, and to the Office of Management and Budget, Paperwork Reduction Project (0704-0188), Washington, DC 20503.

1. AGENCY USE ONLY (Leave blank)			2. REPORT DATE		3. REPORT TYPE AND DATES COVERED		
			April 1991		In-House 1 Jan 83 to 31 Dec 86		
4. TITLE AND SUBTITLE			5. FUNDING NUMBERS				
Linear Phased Array of Coaxially-Fed Monopole Elements in a Parallel Plate Waveguide			PE 61102F PR 2305 TA J3 WU 03				
6. AUTHOR(S)			8. PERFORMING ORGANIZATION REPORT NUMBER				
Boris Tomasic and Alexander Hessel*			RL-TR-91-124				
7. PERFORMING ORGANIZATION NAME(S) AND ADDRESS(ES)			9. SPONSORING/MONITORING AGENCY NAME(S) AND ADDRESS(ES)				
Rome Laboratory RL/EEAA Hanscom AFB Massachusetts 01731-5000			10. SPONSORING/MONITORING AGENCY REPORT NUMBER				
11. SUPPLEMENTARY NOTES			12a. DISTRIBUTION/AVAILABILITY STATEMENT				
*Weber Research Institute, Polytechnic University, Farmingdale, NY 11735			12b. DISTRIBUTION CODE				
Approved for public release; distribution unlimited			13. ABSTRACT (Maximum 200 words)				
The performance of a coaxially-fed monopole element in an infinite array environment in a parallel plate guide is analyzed. The analysis takes into account the geometry of the coaxial feed. Expressions for active admittance, coupling coefficients, and element patterns are given. Numerical data is presented for relevant parameter values, judiciously selected to illustrate the various design trade-offs. The numerical results show an excellent agreement with experiment.			14. SUBJECT TERMS				
Coaxially-Fed Monopole Parallel Plate Waveguide			Linear Array Antennas			15. NUMBER OF PAGES 290	
17. SECURITY CLASSIFICATION OF REPORT Unclassified			18. SECURITY CLASSIFICATION OF THIS PAGE Unclassified			16. PRICE CODE	
19. SECURITY CLASSIFICATION OF ABSTRACT Unclassified			20. LIMITATION OF ABSTRACT SAR			Standard Form 298 (rev. 2-89) Prescribed by ANSI Std Z39-18 298-102	



Accession For	
NTIS GRA&I	<input checked="" type="checkbox"/>
DTIC TAB	<input type="checkbox"/>
Unannounced	<input type="checkbox"/>
Justification	
By _____	
Distribution/ _____	
Availability Codes	
Dist	Avail and/or Special
A-1	

Contents

1. INTRODUCTION	1
2. MAGNETIC RING SOURCE IN AN INFINITE PARALLEL PLATE WAVEGUIDE	3
2.1 Green's Functions	5
2.2 Hertz Potential	11
2.3 Vector Potential	13
2.4 Electric Field (E_p , E_z)	17
2.5 Magnetic Field (H_ϕ)	20
3. CYLINDRICAL ELECTRIC CURRENT SOURCE IN AN INFINITE PARALLEL PLATE WAVEGUIDE	21
3.1 Green's Functions	22
3.2 Hertz Potential	23
3.3 Vector Potential	25
3.4 Electric Field (E_p , E_z)	25
3.5 Magnetic Field (H_ϕ)	26
4. ACTIVE ADMITTANCE AND REFLECTION COEFFICIENT OF AN INFINITE LINEAR PHASED ARRAY OF MONPOLE ELEMENTS IN A PARALLEL PLATE WAVEGUIDE	27
4.1 Coaxially-Fed Monopole in an Infinite Parallel Plate Waveguide	29
4.1.1 Vector Potential $\mathbf{A}_0(\rho, z)$	30
4.1.2 Electric Field $\mathbf{E}_0(\rho, z)$	31
4.1.3 Magnetic Field $\mathbf{H}_0(\rho, z)$	33
4.2 Total Axial Electric $E_z(a, z)$ on the Probe Surface	34

4.3	Probe Current, $J_z(z)$	41
4.4	Total Magnetic Field in the Aperture H_ϕ ($a \leq \rho \leq b, z=0^+$)	44
4.5	Active Admittance, $Y_a(\delta_x)$	49
4.6	Active Reflection Coefficient, $\Gamma_a(\delta_x)$	57
4.7	Coupling (Scattering) Coefficients, S^P	58
5.	FAR FIELD PATTERN OF THE SINGLE MONOPOLE IN AN INFINITE AND SEMI-INFINITE PARALLEL PLATE REGION	60
5.1	Far Field $E_{z0}(\rho, \phi)$ Represented in Terms of Radial Modes	60
5.2	Single Monopole Gain Pattern $g_{z0}^{(e)}$	65
6.	FAR-FIELD ELEMENT PATTERN OF AN INFINITE ARRAY RADIATING INTO AN INFINITE AND A SEMI-INFINITE PARALLEL PLATE REGION	68
6.1	Far-Field of the Active Array $E_z(\rho, \phi)$ Represented in Terms of Radial Modes	69
6.2	Far-Field of the Active Array $\hat{E}_z(x, y)$ Represented in Terms of Floquet Modes in a Unit Cell	71
6.3	Element Pattern $g_z^{(e)}(\hat{\phi})$	76
7.	NUMERICAL ANALYSIS	85
8.	NUMERICAL RESULTS AND DISCUSSION	91
8.1	Single Monopole in an Infinite Parallel Plate Region	91
8.2	Single Monopole in a Semi-Infinite Parallel Plate Region	107
8.3	Linear Array of Coaxially-fed Monopole Elements in an Infinite Parallel Plate Waveguide	127
8.3.1	Active Admittance, $Y_a(\delta_x)$	127
8.3.2	Probe Current, $I_z(z)$	135
8.3.3	Coupling Coefficients, S^P	143
8.4	Linear Array of Coaxially-fed Monopole Elements in a Semi-Infinite Parallel Plate Waveguide	147
8.4.1	Active Admittance, $Y_a(\delta_x)$	147
8.4.2	Probe Current, $I_z(z)$	158
8.4.3	Coupling Coefficients, S^P	166
8.4.4	Element Pattern, $g_z^{(e)}(\hat{\phi})$	169
9.	EXPERIMENTS	174
9.1	Array Description	175
9.2	Monopole Element Design	178
9.3	Waveguide Simulator	178
9.4	Coupling Coefficients	183
9.5	Element Pattern	185

10. CONCLUSIONS	189
REFERENCES	191
APPENDIX A Field Representation in Regions with Piecewise Constant Properties	193
A1 Derivation of the Time-Harmonic Field from Scalar Potentials	193
A2 Modal Representation for Unbounded Cross Sections	197
APPENDIX B Magnetic Ring Source in an Infinite Parallel Plate Waveguide - Radial Mode Representation	203
B1 Radial Transmission Line Representation	203
B2 Radial Magnetic Green's Function Representation	212
APPENDIX C Cylindrical Electric Current Source in an Infinite Parallel Plate Waveguide - Radial Mode Representation	221
C1 Radial Transmission Line Representation	221
C2 Radial Electric Green's Function Representation	225
APPENDIX D Addition Theorem for Hankel Functions	233
APPENDIX E Convergence Acceleration of Series $S_n(\delta_x)$	235
E1 Infinite Linear Array of Monopole Elements in an Infinite Parallel Plate Waveguide	235
E2 Infinite Linear Array of Monopole Elements in a Semi-Infinite Parallel Plate Waveguide	238
APPENDIX F The Fourier Integral of the Hankel Function	241
APPENDIX G The Stationary-Phase Method for Evaluation of Integrals	245
APPENDIX H Test for Power Conservation	247
H1 Evaluation of the Complex Poynting Vector Over the Coaxial Aperture Area	251
H2 Evaluation of the Complex Poynting Vector Over the Probe Surface	256
H3 Evaluation of the Complex Poynting Vector Over the Unit Cell Cross-Section Area	260
APPENDIX I Numerical Evaluation of the Integral $I(\Omega) = \int_a^b f(x) e^{-j\Omega x} dx$	269

Illustrations

2-1. Geometry of Coaxially Driven Annular Aperture in an Infinite Parallel Plate Waveguide	4
2-2. Magnetic Ring Source in an Infinite Parallel Plate Waveguide	4
2-3. Magnetic Point Source in an Infinite Parallel Plate Waveguide	6
2-4. Network Problem for the Determination of $Y_i(z, z')$	7
2-5. Magnetic Current Circular Loop in an Infinite Parallel Plate Waveguide	13
3-1. Geometry of Cylindrical Electric Current Source in an Infinite Parallel Plate Waveguide	22
3-2. Axial Electric Dipole in an Infinite Parallel Plate Waveguide	23
4-1. Linear Array of Coaxial-Monopole Elements in a Semi-Infinite Parallel Plate Waveguide	27
4-2. Coaxially-Fed Monopole in an Infinite Parallel Plate Waveguide	29
4-3. Geometry of the Linear Array and its Image for Evaluation of $E_z(a, z)$ (Top View)	35
4-4. Triangle Pertaining to the Addition Theorem for Hankel Functions $H_0^{(2)}(\kappa_n a-p_p)$	37
4-5. Geometry of Linear Array and its Image for Evaluation of $A_z(a \leq \rho \leq b, z = 0^+)$ (Top View)	45

4-6.	Triangle Pertaining to Addition Theorem for Hankel Functions $H_0^{(2)}(\kappa_n \mathbf{p}-\mathbf{p}_p)$	48
4-7.	Active Infinite Linear Array Pertaining to Uniform-Amplitude, Linear-Phase Progression Excitation	49
4-8.	Infinite Linear Array Pertaining to the Definition of Coupling (Scattering) Coefficients	59
5-1.	Coaxially-fed Monopole and Its Image in an Infinite Parallel Plate Region	62
6-1.	Infinite Linear Array Pertaining to Single Element Excitation	69
6-2.	Geometry of the Linear Array and its Image for Evaluation of $E_z(\rho, \phi)$ (Top View) ($U=1$ case shown)	71
6-3.	Unit Cell Geometry of an Infinite Linear Array of Coaxially-fed Monopoles in a Semi-Infinite Parallel Plate Waveguide	71
7-1.	Active Conductance vs Number of Probe Current Terms ($d/\lambda = 0.4$, $h/\lambda = 0.369$, $s/\lambda = 0.163$, $a/\lambda = 0.0106$, $b/\lambda = 0.034$, $Z_c = 50 \Omega$; $\hat{\phi}_0 = 0^\circ$)	87
7-2.	Active Susceptance vs Number of Probe Current Terms ($d/\lambda = 0.4$, $h/\lambda = 0.369$, $s/\lambda = 0.163$, $a/\lambda = 0.0106$, $b/\lambda = 0.034$, $Z_c = 50 \Omega$; $\hat{\phi}_0 = 0^\circ$)	88
8-1.	Input Conductance vs Probe Length; Parameter: Parallel Plate Separation $h/\lambda = 0.3, 0.35, 0.4$ ($a/\lambda = 0.016, b/\lambda = 0.037$)	92
8-2.	Input Susceptance vs Probe Length; Parameter: Parallel Plate Separation $h/\lambda = 0.3, 0.35, 0.4$ ($a/\lambda = 0.016, b/\lambda = 0.037$)	93
8-3.	Input Admittance vs Probe Length, ($h/\lambda = 0.95$, $a/\lambda = 0.016$, $b/\lambda = 0.037$)	94
8-4.	Reflection Coefficient (Contour Plot of Magnitude) vs Parallel Plate Separation and Probe Length, ($a/\lambda = 0.016, b/\lambda = 0.037$)	95
8-5.	Input Impedance vs Probe Length, ($h/\lambda = 0.35$, $a/\lambda = 0.016$, $b/\lambda = 0.037$, $Z_N = 50 \Omega$)	96
8-6.	Input Impedance vs Frequency, ($h_c/\lambda_c = 0.35$, $l_c/\lambda_c = 0.24$, $a/\lambda_c = 0.016$, $b/\lambda_c = 0.037$, $Z_N = 50 \Omega$)	97
8-7.	Input Admittance vs Probe Radius, ($h_c/\lambda = 0.35$, $l_c/\lambda = 0.24$, $b/\lambda = 2.3 a/\lambda$, $Z_c = 50 \Omega$)	98
8-8.	Current Distribution (Amplitude) Along a Coaxially-Driven Monopole in an Infinite Parallel Plate Region; Parameter: Probe Length $l/\lambda = 0.1, 0.2, 0.3$, ($h/\lambda = 0.4$, $a/\lambda = 0.016$, $b/\lambda = 0.037$)	99
8-9.	Current Distribution (Phase) Along a Coaxially-Driven Monopole in an Infinite Parallel Plate Region; Parameter: Probe Length $l/\lambda = 0.1, 0.2, 0.3$, ($h/\lambda = 0.4$, $a/\lambda = 0.016$, $b/\lambda = 0.037$)	100
8-10.	Current Distribution (Amplitude) Along a Coaxially-Driven Monopole in an Infinite Parallel Plate Waveguide; Parameter: Total Number of Current Terms $I = 1, 10$, ($l_c/\lambda = 0.24$, $h_c/\lambda = 0.35$, $a/\lambda = 0.016$, $b/\lambda = 0.037$)	103

8-11. Current Distribution (Phase) Along a Coaxially-Driven Monopole in an Infinite Parallel Plate Waveguide, Parameter: Total Number of Current Terms I = 1, 10, ($l_c/\lambda = 0.24$, $h_c/\lambda = 0.35$, $a/\lambda = 0.016$, $b/\lambda = 0.037$)	104
8-12. Current Distribution (Amplitude) Along a Coaxially-Driven Monopole in an Infinite Parallel Plate Waveguide; Parameter: Total Number of Current Terms I = 1, 10, ($l/\lambda = 0.75$, $h/\lambda = 0.95$, $a/\lambda = 0.016$, $b/\lambda = 0.037$)	105
8-13. Current Distribution (Phase) Along a Coaxially-Driven Monopole in an Infinite Parallel Plate Waveguide; Parameter: Total Number of Current Terms I = 1, 10, ($l/\lambda = 0.75$, $h/\lambda = 0.95$, $a/\lambda = 0.016$, $b/\lambda = 0.037$)	106
8-14. Input Conductance vs Probe Length; Parameter: Parallel Plate Separation $h/\lambda = 0.3, 0.35, 0.4$, ($a/\lambda = 0.016$, $b/\lambda = 0.037$, $s/\lambda = 0.25$)	108
8-15. Input Susceptance vs Probe Length; Parameter: Parallel Plate Separation $h/\lambda = 0.3, 0.35, 0.4$, ($a/\lambda = 0.016$, $b/\lambda = 0.037$, $s/\lambda = 0.25$)	109
8-16. Reflection Coefficient (Contour Plot of Magnitude) vs Probe-Ground Distance and Probe Length ($h/\lambda = 0.35$, $a/\lambda = 0.016$, $b/\lambda = 0.037$)	110
8-17. Input Impedance vs Probe-Ground Distance and Probe Length, ($h/\lambda = 0.35$, $a/\lambda = 0.016$, $b/\lambda = 0.037$, $Z_N = 50 \Omega$)	111
8-18. Input Impedance vs Probe-Ground Distance, ($l_c/\lambda = 0.2187$) and vs Probe Length ($s_c/\lambda = 0.2275$), ($h/\lambda = 0.35$, $a/\lambda = 0.016$, $b/\lambda = 0.037$, $Z_N = 50 \Omega$)	112
8-19. Input Impedance vs Frequency ($h/\lambda_c = 0.35$, $l_c/\lambda_c = 0.2187$, $s_c/\lambda_c = 0.2275$, $a/\lambda_c = 0.016$, $b/\lambda_c = 0.037$, $Z_N = 50 \Omega$)	113
8-20. Input Admittance vs Probe Radius ($h/\lambda = 0.35$, $s_c/\lambda = 0.2275$, $l_c/\lambda = 0.2187$, $b/\lambda = 2.3 a/\lambda$, $Z_N = 50 \Omega$)	114
8-21. Current Distribution Along a Coaxially-Driven Monopole in a Semi-Infinite Parallel Plate Region, ($h/\lambda = 0.35$, $l/\lambda = 0.15$, $s/\lambda = 0.15$, $a/\lambda = 0.016$, $b/\lambda = 0.037$)	115
8-22. Current Distribution Along a Coaxially-Driven Monopole in a Semi-Infinite Parallel Plate Region, ($h/\lambda = 0.35$, $l/\lambda = 0.3$, $s/\lambda = 0.15$, $a/\lambda = 0.016$, $b/\lambda = 0.037$)	116
8-23. Current Distribution Along a Coaxially-Driven Monopole in a Semi-Infinite Parallel Plate Region, ($h/\lambda = 0.35$, $l/\lambda = 0.15$, $s/\lambda = 0.3$, $a/\lambda = 0.016$, $b/\lambda = 0.037$)	117
8-24. Current Distribution Along a Coaxially-Driven Monopole in a Semi-Infinite Parallel Plate Region, ($h/\lambda = 0.35$, $l/\lambda = 0.3$, $s/\lambda = 0.3$, $a/\lambda = 0.016$, $b/\lambda = 0.037$)	118
8-25. Current Distribution Along a Coaxially-Driven Monopole in a Semi-Infinite Parallel Plate Region, ($h/\lambda = 0.35$, $l_c/\lambda = 0.2187$, $s_c/\lambda = 0.2275$, $a/\lambda = 0.016$, $b/\lambda = 0.037$)	119
8-26. Gain Pattern ($h/\lambda = 0.35$, $l/\lambda = 0.15$, $a/\lambda = 0.016$, $b/\lambda = 0.037$, $Z_c = 50 \Omega$) Parameter: $s/\lambda = 0.15, 0.3$	124
8-27. Gain Pattern ($h/\lambda = 0.35$, $l/\lambda = 0.3$, $a/\lambda = 0.016$, $b/\lambda = 0.037$, $Z_c = 50 \Omega$). Parameter: $s/\lambda = 0.15, 0.3$	125

8-28. Gain Pattern ($h/\lambda = 0.35$, $l_c/\lambda = 0.2187$, $s_c/\lambda = 0.2275$, $a/\lambda = 0.016$, $b/\lambda = 0.037$, $Z_c = 50 \Omega$)	126
8-29. Active Reflection Coefficient (Contour Plot of Magnitude) vs Parallel Plate Height and vs Probe Length ($d/\lambda = 0.4$, $a/\lambda = 0.016$, $b/\lambda = 0.0343$, $Z_c = 50 \Omega$, $\hat{\phi}_0 = 0^\circ$)	128
8-30. Active Reflection Coefficient (Contour Plot of Magnitude) vs Parallel Plate Height and vs Probe Length ($d/\lambda = 0.6$, $a/\lambda = 0.0106$, $b/\lambda = 0.0343$, $Z_c = 50 \Omega$, $\hat{\phi}_0 = 0^\circ$)	129
8-31. Active Impedance vs Parallel Plate Distance and vs Probe Length - Matched Case ($d/\lambda = 0.4$, $h_c/\lambda = 0.36$, $l_c/\lambda = 0.28$, $a/\lambda = 0.0106$, $b/\lambda = 0.0343$, $Z_c = 50 \Omega$, $\hat{\phi}_0 = 0^\circ$)	130
8-32. Active Impedance vs Parallel Plate Distance and vs Probe Length ($d/\lambda = 0.6$, $h/\lambda = 0.36$, $l/\lambda = 0.28$, $a/\lambda = 0.0106$, $b/\lambda = 0.0343$, $Z_c = 50 \Omega$, $\hat{\phi}_0 = 0^\circ$)	131
8-33. Active Impedance vs Probe Radius (Array (a): $d/\lambda = 0.4$, $h_c/\lambda = 0.36$, $l_c/\lambda = 0.28$, $b = 3.249 a$, $Z_c = 50 \Omega$, $\hat{\phi}_0 = 0^\circ$; Array (b): $d/\lambda = 0.6$, $h/\lambda = 0.36$, $l/\lambda = 0.28$, $b = 3.249 a$, $Z_c = 50 \Omega$, $\hat{\phi}_0 = 0^\circ$)	132
8-34. Active Impedance vs Frequency (Array (a): $d/\lambda_c = 0.4$, $h_c/l_c = 0.36$, $l_c/\lambda_c = 0.28$, $b/\lambda_c = 3.249 a/\lambda_c$, $Z_c = 50 \Omega$, $\hat{\phi}_0 = 0^\circ$; Array (b): $d/\lambda_c = 0.6$, $h/\lambda_c = 0.36$, $l/\lambda_c = 0.28$, $b/\lambda_c = 3.249 a/\lambda_c$, $Z_c = 50 \Omega$, $\hat{\phi}_0 = 0^\circ$)	133
8-35. Active Impedance vs Scan; Parameter: Frequency $f = 0.9 f_c$, f_c , and $1.1 f_c$ ($d/\lambda_c = 0.4$, $h_c/\lambda_c = 0.36$, $l_c/\lambda_c = 0.28$, $a/\lambda_c = 0.0106$, $b/\lambda_c = 0.0343$, $Z_c = 50 \Omega$)	134
8-36. Active Impedance vs Scan; Parameter: Frequency $f = 0.9 f_c$, f_c , and $1.1 f_c$ ($d/\lambda_c = 0.6$, $h/\lambda_c = 0.36$, $l/\lambda_c = 0.28$, $a/\lambda_c = 0.0106$, $a/\lambda_c = 0.0343$, $Z_c = 50 \Omega$)	135
8-37. Probe Current - Magnitude; Parameter: $l/\lambda = 0.15$, 0.28 , and 0.3 ($d/\lambda = 0.4$, $h/\lambda = 0.36$, $a/\lambda = 0.0106$, $b/\lambda = 0.0343$, $Z_c = 50 \Omega$, $\hat{\phi}_0 = 0^\circ$)	136
8-38. Probe Current - Phase; Parameter: $l/\lambda = 0.15$, 0.28 , and 0.3 ($d/\lambda = 0.4$, $h/\lambda = 0.36$, $a/\lambda = 0.0106$, $b/\lambda = 0.0343$, $Z_c = 50 \Omega$, $\hat{\phi}_0 = 0^\circ$)	137
8-39. Probe Current - Magnitude; Parameter: $l/\lambda = 0.15$, 0.28 , and 0.3 ($d/\lambda = 0.6$, $h/\lambda = 0.36$, $a/\lambda = 0.0106$, $b/\lambda = 0.0343$, $Z_c = 50 \Omega$, $\hat{\phi}_0 = 0^\circ$)	138
8-40. Probe Current - Phase; Parameter: $l/\lambda = 0.15$, 0.28 , and 0.3 ($d/\lambda = 0.6$, $h/\lambda = 0.36$, $a/\lambda = 0.0106$, $b/\lambda = 0.0343$, $Z_c = 50 \Omega$, $\hat{\phi}_0 = 0^\circ$)	139

8-41. Amplitude of Coupling Coefficients vs Element Serial Number; Parameter: d/λ = 0.4, 0.6 [Array (a): d/λ = 0.4, h_c/λ = 0.36, l_c/λ = 0.28, a/λ = 0.0106, b/λ = 0.0343, Z_c = 50 Ω; Array (b): d/λ = 0.6, h/λ = 0.36, l/λ = 0.28, a/λ = 0.0106, b/λ = 0.0343, Z_c = 50 Ω]	144
8-42. Phase of Coupling Coefficients vs Element Serial Number; Parameter: d/λ = 0.4, 0.6 [Array (a): d/λ = 0.4, h/λ = 0.36, l/λ = 0.28, a/λ = 0.0106, b/λ = 0.0343, Z_c = 50 Ω; Array (b): d/λ = 0.6, h/λ = 0.36, l/λ = 0.28, a/λ = 0.0106, b/λ = 0.0343, Z_c = 50 Ω]	146
8-43. Active Impedance vs Probe-Ground Distance s/λ and vs Probe Length l/λ (d/λ = 0.4, $\hat{\phi}_0 = 0^\circ$)	148
8-44. Active Impedance vs Probe-Ground Distance s/λ and vs Probe Length l/λ (d/λ = 0.6, $\hat{\phi}_0 = 0^\circ$)	149
8-45. Active Reflection Coefficient - Maginitude vs Probe-Ground Distance s/λ and vs Probe Length l/λ (d/λ = 0.4, $\hat{\phi}_0 = 0^\circ$)	150
8-46. Active Reflection Coefficient - Maginitude vs Probe-Ground Distance s/λ and vs Probe Length l/λ (d/λ = 0.6, $\hat{\phi}_0 = 0^\circ$)	151
8-47. Active Impedance vs Probe-Ground Distance s/λ and vs Probe Length l/λ for Array (a) - see Eq. (8-5) for Specifications, ($\hat{\phi}_0 = 0^\circ$)	152
8-48. Active Impedance vs Probe-Ground Distance s/λ and vs Probe Length l/λ for Array (b) - see Eq. (8-5) for Specifications, ($\hat{\phi}_0 = 0^\circ$)	153
8-49. Active Impedance vs Parallel Plate Height h/λ for Arrays (a) and (b), ($\hat{\phi}_0 = 0^\circ$)	154
8-50. Active Impedance vs Probe Radius for Arrays (a) and (b), (b = 3.249 a, $\hat{\phi}_0 = 0^\circ$)	155
8-51. Active Impedance vs Frequency for Arrays (a) and (b), ($\hat{\phi}_0 = 0^\circ$)	156
8-52. Active Impedance vs Scan for Array (a); Parameter: f = 0.9 f_c, f_c, and 1.1 f_c	157
8-53. Active Impedance vs Scan for Array (b); Parameter: f = 0.9 f_c, f_c, and 1.1 f_c	158
8-54. Probe Current - Maginitude for Array (a), ($\hat{\phi}_0 = 0^\circ$); Parameter: l/λ = 0.15, 0.233, and 0.3	159
8-55. Probe Current - Phase for Array (a), ($\hat{\phi}_0 = 0^\circ$); Parameter: l/λ = 0.15, 0.233, and 0.3	160
8-56. Probe Current - Magnitude for Array (b), ($\hat{\phi}_0 = 0^\circ$); Parameter: l/λ = 0.15, 0.25, and 0.3	161
8-57. Probe Current - Phase for Array (b), ($\hat{\phi}_0 = 0^\circ$); Parameter: l/λ = 0.15, 0.25, and 0.3	162
8-58. Coupling Coefficients - Magnitude for Arrays (a) and (b)	167

8-59. Coupling Coefficients - Phase for Arrays (a) and (b)	168
8-60. Element Pattern - Magnitude for Array (a); Parameter: $f = 0.9 f_c, f_c$, and $1.1 f_c$	170
8-61. Element Pattern - Phase for Array (a); Parameter: $f = 0.9 f_c, f_c$, and $1.1 f_c$	171
8-62. Element Pattern - Magnitude for Array (b); Parameter: $f = 0.9 f_c, f_c$, and $1.1 f_c$	172
8-63. Element Pattern - Phase for Array (b); Parameter: $f = 0.9 f_c, f_c$, and $1.1 f_c$	173
9-1. A 30-element Linear Array of Coaxially-Fed Monopoles in a Parallel Plate Region - see Eq. (8-5) for Specifications,	175
9-2. A 30-element Linear Array of Coaxially-Fed Monopoles in a Parallel Plate Region (Top Plate Removed to Display the Array Elements)	176
9-3. Top and Side View of Linear Array	177
9-4. Coaxial Monopole Element	178
9-5. A One and Two-Half Element Waveguide Simulator	179
9-6. A One and Two-Half Element Waveguide Simulator (Top Plate Removed to Display the Monopole Elements)	180
9-7. A One and Two-Half Element Waveguide Simulator with Dimensions	181
9-8. Cross Section of Waveguide Simulator Pertaining to Relation Between Frequency and Scan Angle	181
9-9. Active Reflection Coefficient Measurements Test Set-Up	182
9-10. Active Impedance vs Frequency - Theory and Simulator Measurements	183
9-11. Theoretical and Experimental Amplitude of Coupling Coefficients	184
9-12. Theoretical and Experimental Phase of Coupling Coefficients	185
9-13. Eleven-Element Linear Array on Far-Field Range	186
9-14. Test Fixture for Element Pattern Measurements	187
9-15. Theoretical and Experimental Element Pattern Amplitude	188
9-16. Theoretical and Experimental Element Pattern Phase	188
A-1. Integration Path in the Complex ξ -Plane	199
B-1. Network Representation for Voltage Point-Source Excited Radial Transmission Line	206
B-2. Coaxially Driven Annular Aperture in an Infinite Parallel Plate Waveguide	213
B-3. Annular Magnetic Current Ring Source in an Infinite Parallel Plate Waveguide	214
B-4. Unit Annular Magnetic Current Loop in an Infinite Parallel Plate Waveguide	216
C-1. Network Representation for Current Point-Source Excited Radial Transmission-Line	223

C-2.	Circular Cylindrical Axial Electric Current Source in an Infinite Parallel Plate Waveguide	226
C-3.	Unit Axial Electric Current Loop in an Infinite Parallel Plate Waveguide	227
D-1.	Triangle Pertaining to Addition Theorem for Hankel Functions $H_0^{(2)}(kR)$	234
H-1.	Top (a) and Side (b) View of the Unit Cell Pertaining to Evaluation of the Complex Poynting Vector	249

Tables

8-1.	Comparison Between Results Obtained from Eqs. (4-44) and (8-2) for Input Admittance $Y_a = G_a + jB_a$; Parameter: Probe Length $l/\lambda = 0.1, 0.2, 0.3$, $(h/\lambda = 0.4, a/\lambda = 0.016, b/\lambda = 0.037)$	101
8-2.	Probe Current Expansion Coefficients; Parameter: Total Number of Current Terms $I = 1, 10$, $(l/\lambda = 0.1, h/\lambda = 0.4, a/\lambda = 0.016, b/\lambda = 0.037)$	101
8-3.	Probe Current Expansion Coefficients; Parameter: Total Number of Current Terms $I = 1, 10$, $(l/\lambda = 0.2, h/\lambda = 0.4, a/\lambda = 0.016, b/\lambda = 0.037)$	102
8-4.	Probe Current Expansion Coefficients; Parameter: Total Number of Current Terms $I = 1, 10$, $(l/\lambda = 0.3, h/\lambda = 0.4, a/\lambda = 0.016, b/\lambda = 0.037)$	102
8-5.	Probe Current Expansion Coefficients; Parameter: Total Number of Current Terms $I = 1, 10$, $(l_c/\lambda = 0.24, h_c/\lambda = 0.35, a/\lambda = 0.016, b/\lambda = 0.037)$	104
8-6.	Probe Current Expansion Coefficients; Parameter: Total Number of Current Terms $I = 1, 10$, $(l/\lambda = 0.75, h/\lambda = 0.95, a/\lambda = 0.016, b/\lambda = 0.037)$	107
8-7.	Probe Current Expansion Coefficients; Parameter: Total Number of Current Terms $I = 1, 10$, $(h/\lambda = 0.35, l/\lambda = 0.15, s/\lambda = 0.15, a/\lambda = 0.016, b/\lambda = 0.037)$	120
8-8.	Probe Current Expansion Coefficients; Parameter: Total Number of Current Terms $I = 1, 10$, $(h/\lambda = 0.35, l/\lambda = 0.3, s/\lambda = 0.15, a/\lambda = 0.016, b/\lambda = 0.037)$	120
8-9.	Probe Current Expansion Coefficients; Parameter: Total Number of Current Terms $I = 1, 10$, $(h/\lambda = 0.35, l/\lambda = 0.15, s/\lambda = 0.3, a/\lambda = 0.016, b/\lambda = 0.037)$	121

8-10. Probe Current Expansion Coefficients; Parameter: Total Number of Current Terms I = 1, 10, (h/λ = 0.35, l/λ = 0.3, s/λ = 0.3, a/λ = 0.016, b/λ = 0.037)	121
8-11. Probe Current Expansion Coefficients; Parameter: Total Number of Current Terms I = 1, 10, (h/λ = 0.35, l _c /λ = 0.2187, s _c /λ = 0.2275, a/λ = 0.016, b/λ = 0.037)	122
8-12. Comparison Between Results Obtained from Eqs. (4-44) and (8-2) for Input Admittance Y _a = G _a + jB _a ; Parameter: Probe Length l/λ = 0.15, 0.2187, 0.3 and Probe-Ground Distance s/λ = 0.15, 0.2275, 0.3, (h/λ = 0.35, a/λ = 0.016, b/λ = 0.037)	122
8-13. Probe Current Expansion Coefficients; Parameter: Total Number of Current Terms I = 1, 10, (d/λ = 0.4, l/λ = 0.15, h/λ = 0.36, a/λ = 0.0106, b/λ = 0.0343 Z _c = 50 Ω, $\hat{\phi}_0 = 0^\circ$)	140
8-14. Probe Current Expansion Coefficients; Parameter: Total Number of Current Terms I = 1, 10, (d/λ = 0.4, l _c /λ = 0.28, h _c /λ = 0.36, a/λ = 0.0106, b/λ = 0.0343 Z _c = 50 Ω, $\hat{\phi}_0 = 0^\circ$)	140
8-15. Probe Current Expansion Coefficients; Parameter: Total Number of Current Terms I = 1, 10, (d/λ = 0.4, l/λ = 0.30, h/λ = 0.36, a/λ = 0.0106, b/λ = 0.0343 Z _c = 50 Ω, $\hat{\phi}_0 = 0^\circ$)	141
8-16. Probe Current Expansion Coefficients; Parameter: Total Number of Current Terms I = 1, 10, (d/λ = 0.6, l/λ = 0.15, h/λ = 0.36, a/λ = 0.0106, b/λ = 0.0343 Z _c = 50 Ω, $\hat{\phi}_0 = 0^\circ$)	141
8-17. Probe Current Expansion Coefficients; Parameter: Total Number of Current Terms I = 1, 10, (d/λ = 0.6, l/λ = 0.28, h/λ = 0.36, a/λ = 0.0106, b/λ = 0.0343 Z _c = 50 Ω, $\hat{\phi}_0 = 0^\circ$)	142
8-18. Probe Current Expansion Coefficients; Parameter: Total Number of Current Terms I = 1, 10, (d/λ = 0.6, l/λ = 0.30, h/λ = 0.36, a/λ = 0.0106, b/λ = 0.0343 Z _c = 50 Ω, $\hat{\phi}_0 = 0^\circ$)	142
8-19. Comparison Between Results for Active Admittance Y _a = G _a + jB _a ; Parameter: d/λ = 0.4, 0.6 [Array (a): d/λ = 0.4, l/λ = 0.15, 0.28, 0.30, h/λ = 0.36, a/λ = 0.0106, b/λ = 0.0343, Z _c = 50 Ω, $\hat{\phi}_0 = 0^\circ$; Array (b): d/λ = 0.6, l/λ = 0.15, 0.28, 0.3, h/λ = 0.36, a/λ = 0.0106, b/λ = 0.0343, Z _c = 50 Ω, $\hat{\phi}_0 = 0^\circ$)]	143
8-20. Probe Current Expansion Coefficients; Parameter: Total Number of Current Terms I = 1, 10 (d/λ = 0.4, h/λ = 0.369, l/λ = 0.15, s/λ = 0.163, a/λ = 0.0106, b/λ = 0.0343, Z _c = 50 Ω, $\hat{\phi}_0 = 0^\circ$)	163
8-21. Probe Current Expansion Coefficients; Parameter: Total Number of Current Terms I = 1, 10 (d/λ = 0.4, h/λ = 0.369, l _c /λ = 0.233, s _c /λ = 0.163, a/λ = 0.0106, b/λ = 0.0343, Z _c = 50 Ω, $\hat{\phi}_0 = 0^\circ$)	163

8-22. Probe Current Expansion Coefficients; Parameter: Total Number of Current Terms I = 1, 10 (d/λ = 0.4, h/λ = 0.369, l/λ = 0.3, s/λ = 0.163, a/λ = 0.0106, b/λ = 0.0343, Z _c = 50 Ω, $\hat{\phi}_0 = 0^\circ$)	164
8-23. Probe Current Expansion Coefficients; Parameter: Total Number of Current Terms I = 1, 10 (d/λ = 0.6, h/λ = 0.369, l/λ = 0.15, s/λ = 0.245, a/λ = 0.0106, b/λ = 0.0343, Z _c = 50 Ω, $\hat{\phi}_0 = 0^\circ$)	164
8-24. Probe Current Expansion Coefficients; Parameter: Total Number of Current Terms I = 1, 10 (d/λ = 0.6, h/λ = 0.369, l _c /λ = 0.25, s _c /λ = 0.245, a/λ = 0.0106, b/λ = 0.0343, Z _c = 50 Ω, $\hat{\phi}_0 = 0^\circ$)	165
8-25. Probe Current Expansion Coefficients; Parameter: Total Number of Current Terms I = 1, 10 (d/λ = 0.6, h/λ = 0.369, l/λ = 0.3, s/λ = 0.245, a/λ = 0.0106, b/λ = 0.0343, Z _c = 50 Ω, $\hat{\phi}_0 = 0^\circ$)	165
8-26. Comparison Between Results for Active Admittance $Y_a = G_a + jB_a$; Parameter: d/λ = 0.4, 0.6 [Array (a): d/λ = 0.4, l/λ = 0.15, 0.233, and 0.3, s/λ = 0.163, h/λ = 0.369, a/λ = 0.0106, b/λ = 0.0343, Z _c = 50 Ω, $\hat{\phi}_0 = 0^\circ$; Array (b): d/λ = 0.6, l/λ = 0.15, 0.25, 0.3, s/λ = 0.245, h/λ = 0.369, a/λ = 0.0106, b/λ = 0.0343, Z _c = 50 Ω, $\hat{\phi}_0 = 0^\circ$)]	166

Linear Phased Array of Coaxially-Fed Monopole Elements in a Parallel Plate Waveguide

1. INTRODUCTION

Linear arrays of coaxially-fed monopoles radiating into a parallel plate region are used extensively in various space-fed microwave array antenna systems. In particular, such arrays are employed in space-fed beam forming networks. In addition, the information derived from the study of these arrays is very useful in the design of a large variety of conformal arrays.

In view of its simplicity, low cost, polarization purity, reasonable bandwidth, and power handling capability, the coaxially-fed linear monopole is an attractive choice for an array element in a parallel plate waveguide. A detailed knowledge of the radiation and impedance characteristics of this element in its array environment is basic to a systematic design of such high performance arrays.

To this end we present here an analysis previously briefly reported in References 1 and 2 and in more detail in Reference 3 for the active admittance, element patterns, and coupling

(Received for Publication Oct. 14, 1987)

- ¹ Tomasic, B. and Hessel, A. (1982) Linear phased array of coaxially-fed monopole elements in a parallel plate guide, *IEEE/AP-S Symposium Digest*, 144, Albuquerque, New Mexico.
- ² Tomasic, B. and Hessel, A. (1985) Linear phased array of coaxially-fed monopole elements in a parallel plate waveguide - experiment, *IEEE/AP-S Symposium Digest*, 23, Vancouver, Canada.
- ³ Tomasic, B. and Hessel, A. (1985) Arrays of coaxially-fed monopole elements in a parallel plate waveguide, *Phased Arrays 1985 Symposium Proceedings*, RADC-TR-85-171, 223-250, ADA16931.

coefficients of an infinite linear array of coaxially-fed monopole elements in a parallel plate waveguide region. Although the theoretical analysis is carried out for arrays backed by a conducting ground, all relevant expressions can be also applied when the conducting backing is removed as well as to a single monopole radiating into an infinite or semi-infinite parallel plate region.

At the outset of analysis, a thin monopole-probe approximation is invoked in that the probe current is assumed to have only an axial component and no angular variation. This approximation is justified since the probe radius is small compared to the wavelength. Furthermore, it is assumed, for consistency, that the field distribution in each coaxial aperture is that of the coaxial feed-line TEM mode. The effect on active admittance of neglecting higher modes in the coaxial aperture is very small.^{4,5}

Numerical results, presented for representative parameter values, are selected to illustrate the various trade offs, such as the dependence of element pattern on the array and element geometry, the phase center location, and the choice of optimal geometry for element matching in the array environment.

To confirm the validity of the theory, a one and two-half element waveguide simulator, and a forty-element linear array were constructed. Excellent agreement between experiment and theory has been obtained.

The material of this report is arranged as follows:

In Chapter 2, expressions are derived for the electromagnetic field in an infinite parallel plate region due to an annular aperture driven by a coaxial transmission line.

Similarly in Chapter 3 we derive expressions for the electromagnetic field in an infinite parallel plate region due to a cylindrical electric current source.

Chapter 4 is devoted to analysis of an infinite linear array of monopole elements in a parallel plate waveguide. Expressions for active probe current, active admittance, and coupling coefficients are derived. The relevant expressions are applicable to an infinite linear array as well as to a single monopole in an infinite and semi-infinite parallel plate waveguide.

In Chapter 5 we evaluate the far-zone field due to a single monopole radiating into infinite and semi-infinite parallel plate regions.

Similarly in Chapter 6 we derive expressions for the element pattern of an infinite array radiating into infinite and semi-infinite parallel plate regions.

Numerical analysis is given in Chapter 7. Various numerical methods used in computation of probe current, active admittance, coupling coefficients, and element patterns are presented and discussed.

In Chapter 8, a detailed discussion of numerical results is presented. We discuss the following four geometrical configurations: (1) a single monopole in an infinite parallel plate region, (2) a single monopole in a semi-infinite parallel plate region, (3) an infinite linear

⁴ Williamson, A.G. and Otto, D.V. (1973) Coaxially-fed hollow cylindrical monopole in a rectangular waveguide, *Electron. Lett.*, **9**, (No.10):218-220.

⁵ Williamson, A.G. (1985) Radial line/coaxial line junctions: Analysis and equivalent circuits, *Int. J. Electronics*, **58**, (No. 1):91-104.

array of monopoles in an infinite parallel plate region, and (4) an infinite linear array of monopoles in a semi-infinite parallel plate waveguide.

Chapter 9 describes the experimental effort and presents measured data that strongly support the validity of the analysis and accuracy of the computer program.

Conclusions are found in Chapter 10.

Appendices A to I deal with various mathematical details of the derivation.

2. MAGNETIC RING SOURCE IN AN INFINITE PARALLEL PLATE WAVEGUIDE

In this chapter we derive expressions for the electromagnetic field in an infinite parallel plate region due to an annular aperture driven by a coaxial transmission line. A coaxial line of inner and outer radii a and b , respectively, is flush-mounted on the bottom plate of the perfectly conducting infinite parallel plate waveguide of height h as shown in Figure 2-1. A cylindrical coordinate system (ρ, ϕ, z) is chosen so that the z axis coincides with the axis of the annular aperture. The electric field over the aperture is assumed to be that of the TEM transmission line mode, that is,

$$E_{ap} = \rho_0 \frac{V_0}{\rho' \ln \frac{b}{a}}, \quad a \leq \rho' \leq b. \quad (2-1)$$

where V_0 is the applied voltage at the aperture of the coaxial feed transmission line. In Eq. (2-1) the prime denotes the source coordinates. Using the equivalence principle, the problem of Figure 2-1 can be reduced to that of a magnetic ring source in the infinite parallel plate waveguide shown in Figure 2-2, where the magnetic current density is given by

$$M(r', t) = \phi_0 M(\rho') \delta(z) e^{j\omega t} \quad (2-2a)$$

with

$$M(\rho') = - \frac{V_0}{\rho' \ln \frac{b}{a}}. \quad (2-2b)$$

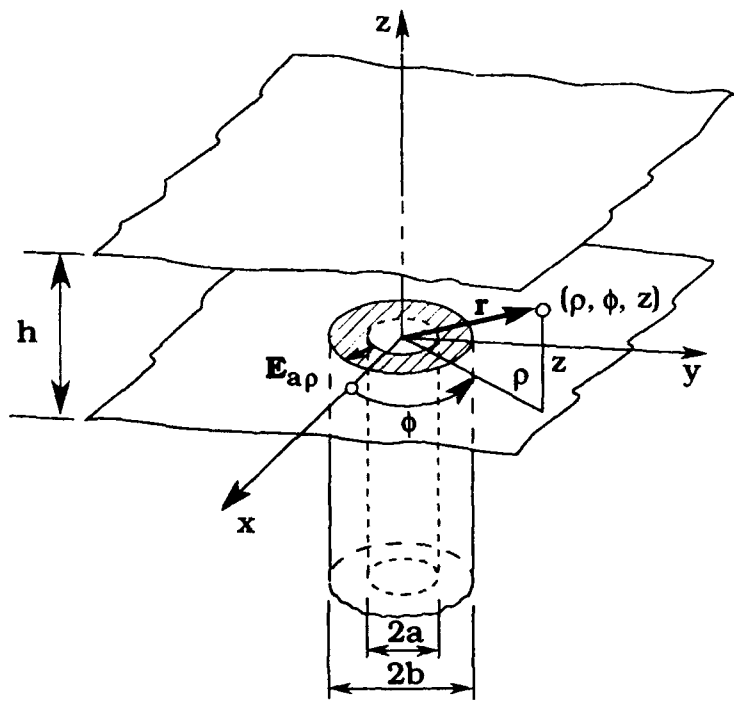


Figure 2-1. Geometry of Coaxially Driven Annular Aperture in an Infinite Parallel Plate Waveguide

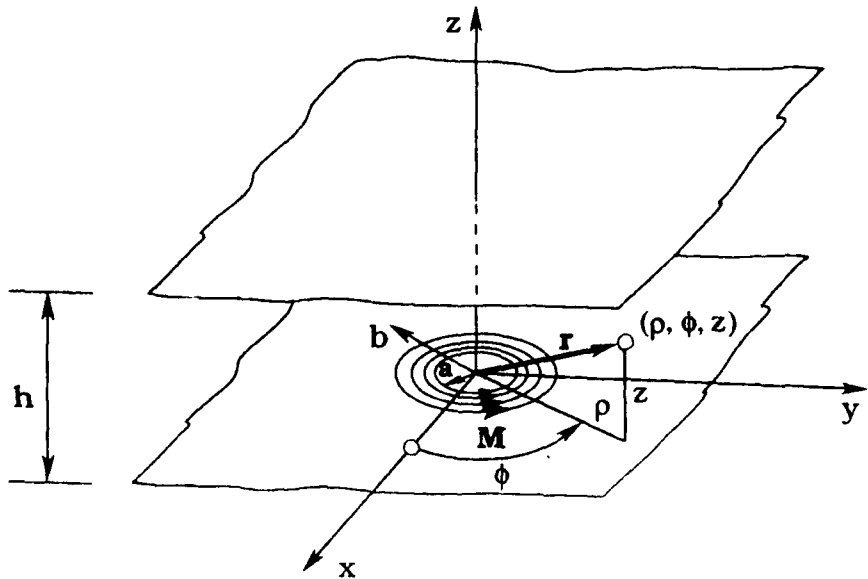


Figure 2-2. Magnetic Ring Source in an Infinite Parallel Plate Waveguide

To calculate the radiation from the magnetic ring source in Figure 2-2, one may utilize results for a transverse (to z) magnetic current element derived in Appendix A. The results are verified in Appendix B by an alternate approach where the propagation direction is assumed to be radial.

The procedure consists of several steps:

1. We begin with expression (A-16a) for the potential function S where the longitudinal Green's function g_{z1} will be determined subject to "parallel plate" boundary conditions. Since there are no transverse boundaries, the distinction between the E and H mode Green's functions resides solely in their longitudinal dependence, that is, g_{z1} . As stated in step 2, only the E mode Green's function g'_{z1} needs to be evaluated.

2. Determine the Hertz potentials using Eqs. (A-4). As shown in Appendix A, the transverse currents generally excite both E and H modes with respect to z . The lack of a source dependence on ϕ' implies that $\partial/\partial\phi' = 0$ in Eq. (A-4b) and consequently the H mode Hertz potential $\Pi''(\mathbf{r}, \mathbf{r}') = 0$. Thus for the special case of a constant ring-source distribution ($m=0$), only E-modes are excited.

3. Determine the vector potential $\mathbf{A}(\mathbf{r})$. The expression for the vector potential will be used later in the analysis of a linear array of coaxially-fed monopoles in parallel plates.

4. Determine the E-mode electric and magnetic fields (E_ϕ , H_ϕ , E_z) by means of the Hertz potential $\Pi'(\mathbf{r}, \mathbf{r}')$ and Eq. (A-1) or directly from the vector potential $\mathbf{A}(\mathbf{r})$ and Maxwell's equations.

2.1 Green's Functions

With reference to Figure 2-3, for an azimuthal vector point current element

$$\mathbf{M}^0 = \mathbf{M}_t^0 = \phi_0 M^0 \delta(\mathbf{r} - \mathbf{r}') \quad (2-3a)$$

$$M^0 = -\frac{V_0}{\rho' \ln \frac{b}{a}} \quad (2-3b)$$

one obtains for the E-mode potential function in Eq. (A-16a)

$$S'(\mathbf{r}, \mathbf{r}') = \frac{1}{4\pi} \sum_{m=-\infty}^{\infty} e^{jm(\phi-\phi')} \int_{C'_2} \frac{1}{\xi} J_m(\xi \rho_<) H_m^{(2)}(\xi \rho_>) g'_{z1}(z, z'; \kappa_1) d\xi \quad (2-3c)$$

where $\mathbf{r} = (\rho, \phi, z)$ defines the field point and $\mathbf{r}' = (\rho', \phi', z')$ specifies the source location. The $J_m(\xi \rho_<)$ and $H_m^{(2)}(\xi \rho_>)$ are Bessel and Hankel functions of order m and argument $(\xi \rho_>)$ where $\rho_<$ and $\rho_>$ denote the lesser and greater, respectively, of the quantities ρ and ρ' . The integration contour C'_2 in the complex ξ -plane is shown in Figure A-1. The E-mode Green's function g'_{z1} is given in Eq. (A-6a) where evaluation of $Y'_1(z, z')$ is based on the network representation of the equivalent axial transmission-line problem. The network procedure is illustrated in the following calculation of $Y'_1(z, z')$. Since $Y'_1(z, z')$ is defined as the current at a point z on a transmission line excited at z' (in this case $z' = 0$) by a series voltage source of amplitude $V = -1$, the pertinent network problem is shown in Figure 2-4.

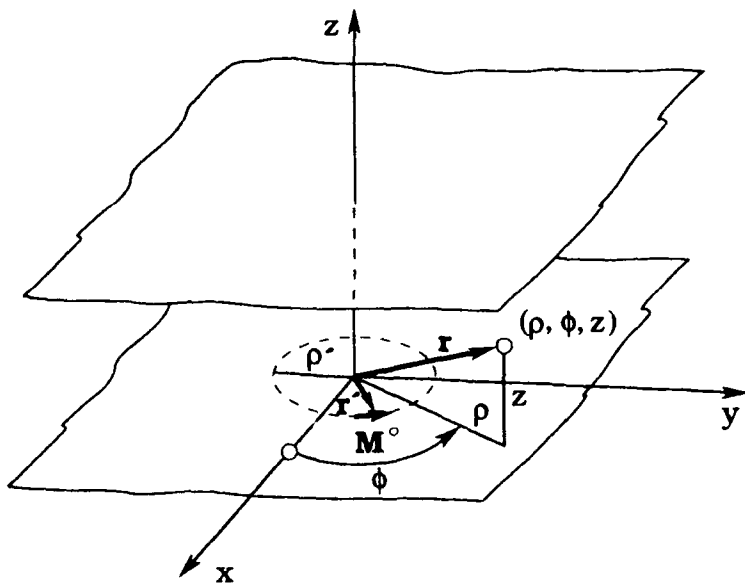


Figure 2-3. Magnetic Point Source in an Infinite Parallel Plate Waveguide

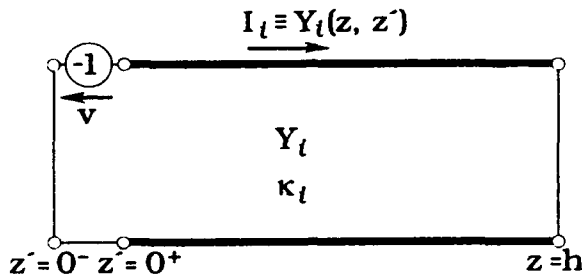


Figure 2-4. Network Problem for the Determination of $Y'_i(z, z')$

At $z = 0$ and $z = h$ the transmission line is short circuited. Thus,

$$\vec{Z}_i(z') = j Z'_i \operatorname{tg} k_i h \quad (2-4a)$$

$$\overleftarrow{Z}_i(z') = 0 \quad (2-4b)$$

where $\vec{Z}(z')$ and $\overleftarrow{Z}(z')$ are the impedances seen looking to the right and to the left, respectively, from the generator terminals. We define

$$Y'_i(z, z') = \frac{1}{\overleftarrow{Z}_i(z')} = \frac{1}{j Z'_i \operatorname{tg} k_i h} \quad (2-5)$$

The Green's function is

$$Y'_i(z, z') = Y'_i(z', z') \overleftarrow{I}(z') \vec{I}(z) \quad (2-6a)$$

where

$$\overleftarrow{I}(z) = \cos k_i z \quad z \geq z' \quad (2-6b)$$

$$\vec{I}(z_s) = \frac{\cos \kappa_1(h-z)}{\cos \kappa_1 h}. \quad (2-6c)$$

In Eq. (2-3c),

$$\begin{aligned} g'_{zi}(z, z') &= \frac{1}{j\omega \epsilon_0} \quad Y'_1(z, z') = \frac{1}{j\omega \epsilon_0} \quad \frac{1}{jZ'_1 \operatorname{tg} \kappa_1 h} \quad \frac{\cos \kappa_1 z' \cos \kappa_1(h-z)}{\cos \kappa_1 h} \\ &= -\frac{Y'_1}{\omega \epsilon_0} \frac{\cos \kappa_1 z' \cos \kappa_1(h-z)}{\sin \kappa_1 h} = -\frac{\cos \kappa_1(h-z) \cos \kappa_1 z'}{\kappa_1 \sin \kappa_1 h} \end{aligned} \quad (2-7a)$$

where the E-mode characteristic admittance is given by

$$Y'_1 = \frac{\omega \epsilon_0}{\kappa_1}. \quad (2-7b)$$

Using

$$\kappa_1 = \sqrt{k^2 - k_{ti}^2} = \sqrt{k^2 - \xi^2} \quad (2-8a)$$

upon substitution of Eq. (2-7a) into Eq. (2-3c), the function S' becomes

$$\begin{aligned} S'(\mathbf{r}, \mathbf{r}') &= -\frac{1}{4\pi} \sum_{m=-\infty}^{\infty} e^{jm(\phi-\phi')} \\ &\int_{C_2'} \frac{1}{\xi} J_m(\xi \rho_<) H_m^{(2)}(\xi \rho_>) \frac{\cos \sqrt{k^2 - \xi^2} (h-z)}{\sqrt{k^2 - \xi^2}} \frac{\cos \sqrt{k^2 - \xi^2} z'}{\sin \sqrt{k^2 - \xi^2} h} d\xi. \end{aligned} \quad (2-8b)$$

The contour integral in Eq. (2-8b) may be evaluated by Cauchy's Residue Theorem

$$\oint f(\xi) d\xi = 2\pi j \sum_n \text{Res } f(\xi)|_{\xi=\xi_n} \quad (2-9)$$

inside C'_2 . Note that C'_2 in Eq. (2-8b) is taken clockwise so that a negative sign has to be introduced in Eq. (2-9). If

$$f(\xi) = \frac{\varphi(\xi)}{\psi(\xi)} \quad (2-10a)$$

where

$$\varphi(\xi) = \frac{1}{\xi} J_m(\xi \rho_<) H_m^{(2)}(\xi \rho_>) \cos \sqrt{k^2 - \xi^2} (h - z) \cos \sqrt{k^2 - \xi^2} z' \quad (2-10b)$$

and

$$\psi(\xi) = \sqrt{k^2 - \xi^2} \sin \sqrt{k^2 - \xi^2} h \quad (2-10c)$$

then

$$\text{Res} \left[\frac{\varphi(\xi)}{\psi(\xi)} \right]_{\xi=\xi_n} = \frac{\varphi(\xi_n)}{\psi'(\xi_n)} \quad (2-10d)$$

Here, the ξ_n are simple zeros of $\psi(\xi)$. Setting

$$\sin \sqrt{k^2 - \xi_n^2} h = 0 \quad (2-11a)$$

from which

$$\sqrt{k^2 - \xi_n^2} = \frac{n\pi}{h} \equiv \kappa_1 \quad (2-11b)$$

so that one finds

$$\xi_n = \sqrt{k^2 - \left(\frac{n\pi}{h}\right)^2} = \kappa_n \quad n = 0, 1, 2, \dots \quad (2-11c)$$

Note that the pole arising from $\xi = 0$ in Eq. (2-8b) lies outside of the integration contour and therefore does not contribute to the integral in Eq. (2-9). From Eqs. (2-10b) and (2-10c),

$$\varphi(\xi_n) = \frac{1}{\xi_n} J_m(\xi_n \rho_<) H_m^{(2)}(\xi_n \rho_>) (-1)^n C_n(z) C_n(z') \quad (2-12a)$$

$$\begin{aligned} \psi'(\xi_n) &= \frac{d\psi(\xi)}{d\xi} \Big|_{\xi=\xi_n} = \left[-\frac{\xi \sin \sqrt{k^2 - \xi^2} h}{\sqrt{k^2 - \xi^2}} - \xi h \cos \sqrt{k^2 - \xi^2} h \right]_{\xi=\xi_n} \\ &= \begin{cases} -2\xi_0 h, & n = 0 \\ (-1)^n (-\xi_n h), & n \geq 1 \end{cases} \quad (2-12b) \end{aligned}$$

where the relations

$$\cos \frac{n\pi}{h} (h-z) = (-1)^n \cos \frac{n\pi}{h} z \quad (2-12c)$$

$$C_n(z) = \cos \frac{n\pi}{h} z \quad (2-12d)$$

and

$$C_n(z') = \cos \frac{n\pi}{h} z' \quad (2-12e)$$

have been used. Finally, from Eq. (2-9), using Eqs. (2-10d) and (2-12)

$$\oint_{C_2} f(\xi) d\xi = j \frac{\pi}{h} \sum_{n=0}^{\infty} \frac{\epsilon_n}{\kappa_n^2} J_m(\kappa_n \rho_<) H_m^{(2)}(\kappa_n \rho_>) C_n(z) C_n(z') \quad (2-13)$$

where $\epsilon_0 = 1$, $\epsilon_n = 2$ for $n \geq 1$.

When we substitute Eq. (2-13) into Eq. (2-8b), the E-mode potential function $S'(\mathbf{r}, \mathbf{r}')$ becomes

$$\begin{aligned} S'(\mathbf{r}, \mathbf{r}') &= -\frac{j}{4h} \sum_{m=-\infty}^{\infty} e^{j m(\phi - \phi')} \sum_{n=0}^{\infty} \frac{\epsilon_n}{\kappa_n^2} J_m(\kappa_n \rho_<) H_m^{(2)}(\kappa_n \rho_>) C_n(z) C_n(z') \\ &= -\frac{j}{4h} \sum_{m=-\infty}^{\infty} e^{j m(\phi - \phi')} \sum_{n=0}^{\infty} \frac{\epsilon_n}{\kappa_n^2} C_n(z) C_n(z') \begin{cases} J_m(\kappa_n \rho') H_m^{(2)}(\kappa_n \rho), \rho > \rho' \\ J_m(\kappa_n \rho) H_m^{(2)}(\kappa_n \rho'), \rho < \rho' \end{cases} \quad (2-14) \end{aligned}$$

2.2 Hertz Potential

When the magnetic source is transverse ($M_z^0 = 0$) the E-mode Hertz potential is given by Eq. (A-4a) as

$$\Pi'(\mathbf{r}, \mathbf{r}') = (\mathbf{M}_t^0 \times \mathbf{z}_0) \cdot \nabla'_t S'(\mathbf{r}, \mathbf{r}') \quad (2-15a)$$

where in cylindrical coordinates

$$\nabla'_t = \rho_0 \frac{\partial}{\partial \rho'} + \phi_0 \frac{1}{\rho'} \frac{\partial}{\partial \phi'} \quad (2-15b)$$

Substitution of Eq. (2-3a) for M_t^0 and Eq. (2-14) for $S'(r, r')$ into Eq. (2-15a) yields

$$\begin{aligned}\Pi'(r, r') &= M^0(\rho') \frac{\partial}{\partial \rho'} S(r, r') \\ &= -j \frac{M^0(\rho')}{4h} \sum_{m=-\infty}^{\infty} e^{-jm(\phi-\phi')} \sum_{n=0}^{\infty} \frac{\epsilon_n}{\kappa_n} C_n(z) C_n(z') \begin{cases} J'_m(\kappa_n \rho') H_m^{(2)}(\kappa_n \rho), \rho > \rho' \\ J_m(\kappa_n \rho) H_m^{(2)}(\kappa_n \rho'), \rho < \rho' \end{cases} \quad (2-16)\end{aligned}$$

where $J'_m(\kappa_n \rho')$ and $H_m^{(2)}(\kappa_n \rho')$ are derivatives of Bessel and Hankel functions, respectively, with respect to the argument.

The E-mode Hertz potential for the (constant in ϕ) magnetic current circular loop (see Figure 2-5)

$$M^0 = \phi_0 M^0 \delta(\rho - \rho') \delta(z), \quad (z' = 0) \quad (2-17)$$

can be now obtained by integrating Eq. (2-16) over ϕ' and z' . Thus,

$$\begin{aligned}\Pi'(r; \rho') &= \int_{\phi'=0}^{2\pi} \int_{z'=0}^{\infty} \Pi'(r, r') \rho' d\phi' dz' \\ &= -j KV_0 \sum_{n=0}^{\infty} \frac{\epsilon_n}{\kappa_n} C_n(z) \begin{cases} J_1(\kappa_n \rho') H_0^{(2)}(\kappa_n \rho) \\ J_0(\kappa_n \rho) H_1^{(2)}(\kappa_n \rho') \end{cases} = \begin{cases} \Pi'(r_s; \rho'), \rho > \rho' \\ \Pi'(r_s; \rho'), \rho < \rho' \end{cases} \quad (2-18a)\end{aligned}$$

where

$$K = \frac{\pi}{2h \ln \frac{b}{a}} \quad (2-18b)$$

and where the identities $J'_0(\kappa_n \rho') = -J_1(\kappa_n \rho')$ and $H_0^{(2)'}(\kappa_n \rho') = -H_1^{(2)}(\kappa_n \rho')$ have been utilized.

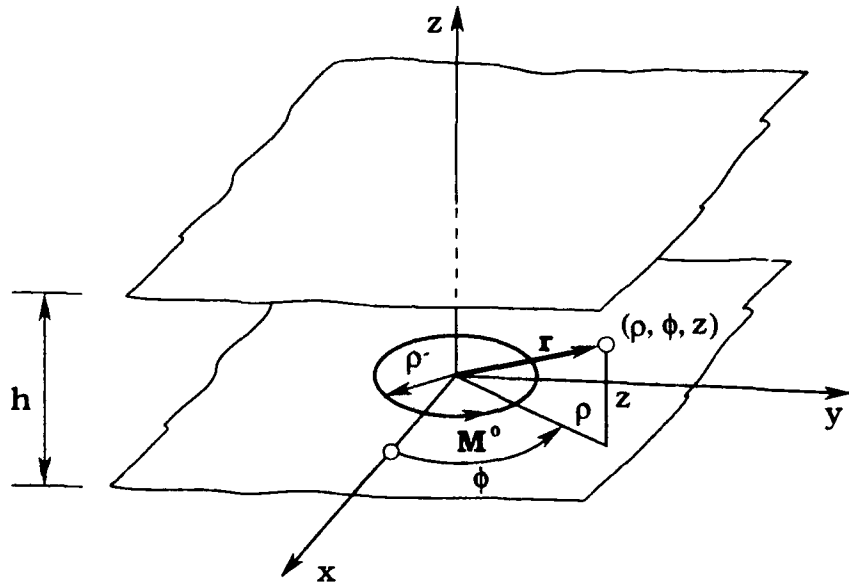


Figure 2-5. Magnetic Current Circular Loop in an Infinite Parallel Plate Waveguide

2.3 Vector Potential

The magnetic field $\mathbf{H}(\rho, z; \rho')$ due to a (constant in ϕ) magnetic current circular loop source at $\mathbf{r} \neq \mathbf{r}'$ is [see Eq. (A-1b)]

$$\mathbf{H}(\mathbf{r}; \rho') = j\omega \epsilon_0 \nabla \times \mathbf{z}_0 \Pi'(\mathbf{r}; \rho') \quad (2-19)$$

where $\Pi'(\mathbf{r}, \rho')$ is given by Eq. (2-18). For the annular magnetic ring source, with inner and outer radii a and b , respectively, the magnetic field $\mathbf{H}(\mathbf{r})$ can be obtained upon integration of Eq. (2-19) over the radial source coordinate ρ' , that is,

$$\mathbf{H}(\mathbf{r}) = j\omega\epsilon_0 \int_a^b \nabla \times \mathbf{z}_0 \Pi'(\mathbf{r};\rho') d\rho'. \quad (2-20)$$

The $\mathbf{H}(\mathbf{r})$ is related to vector magnetic potential $\mathbf{A}(\mathbf{r})$ by

$$\mathbf{H}(\mathbf{r}) = \frac{1}{\mu_0} \nabla \times \mathbf{A}(\mathbf{r}). \quad (2-21)$$

From Eqs. (2-20) and (2-21), one can now write the expression for $\mathbf{A}(\mathbf{r})$ in terms of $\Pi'(\mathbf{r},\rho')$ as follows.

When the observation point $\mathbf{r} = (\rho, \phi, z)$ is in the region $\rho \leq a$ or $\rho \geq b$, one sees by inspection that

$$\mathbf{A}(\mathbf{r}) = \mathbf{z}_0 A_z(\mathbf{r}) \quad (2-22a)$$

where

$$A_z(\mathbf{r}) = j\mu_0 k n_0 \int_a^b \Pi'(\mathbf{r},\rho') d\rho' \quad (2-22b)$$

and

$$n_0 = \sqrt{\frac{\epsilon_0}{\mu_0}}. \quad (2.22c)$$

If the observation point $\mathbf{r} = (\rho, \phi, z)$ is in the region $a \leq \rho \leq b$, $z \neq 0$, the integration limits in Eq. (2-20) become functions of the integration variable and consequently one can not simply interchange integral and curl operators; instead more careful analysis is needed.

To this end, we first rewrite Eq. (2-20) in the form

$$H(r) = -\Phi_0 j \omega \epsilon_0 \left[\int_a^{\rho'=\rho} \frac{\partial \Pi(r_>, \rho')}{\partial \rho} d\rho' + \int_{\rho'=0}^b \frac{\partial \Pi(r_<, \rho')}{\partial \rho} d\rho' \right], \quad a \leq \rho \leq b \quad (2-23a)$$

where

$$\nabla \times \mathbf{z}_0 \Pi'(r, \rho') = -\Phi_0 \frac{\partial \Pi'(r, \rho')}{\partial \rho} \quad (2-23b)$$

has been used. Equation (2-23a) can be further reformulated by introducing the identity known as Leibnitz's rule⁶, that is,

$$\int_{A(x)}^{B(x)} \frac{\partial f(x, t)}{\partial x} dt = \frac{d}{dx} \int_{A(x)}^{B(x)} f(x, t) dt - f(x, B) \frac{dB(x)}{dx} + f(x, A) \frac{dA(x)}{dx} \quad (2-24)$$

which is valid for all values of x in an interval when f and $\partial f / \partial x$ are continuous for $a \leq x \leq b$, and $A \leq t \leq B$, and when $A'(x)$ and $B'(x)$ are continuous in (a, b) . Using Eq. (2-24), the integrals in Eq. (2-23a) take the form

$$\int_a^{\rho'=\rho} \frac{\partial \Pi'(r_>, \rho')}{\partial \rho} d\rho' = \frac{d}{d\rho} \int_a^{\rho'=\rho} \Pi'(r_>, \rho') d\rho' - \Pi'(r_>, \rho) \quad (2-25a)$$

$$\int_{\rho'=0}^b \frac{\partial \Pi'(r_<, \rho')}{\partial \rho} d\rho' = \frac{d}{d\rho} \int_{\rho'=0}^b \Pi'(r_<, \rho') d\rho' + \Pi'(r_<, 0) \quad (2-25b)$$

and consequently

⁶ Hildebrand, F. (1962) *Advanced Calculus for Applications*, Prentice Hall, Inc., Englewood Cliffs, New Jersey.

$$\mathbf{H}(\mathbf{r}) = -\Phi_0 j \omega \epsilon_0 \frac{d}{dp} \int_a^b \Pi'(\mathbf{r}, p') dp' + \Pi'(\mathbf{r}_<, p) - \Pi'(\mathbf{r}_>, p), \quad a \leq (p=p') \leq b. \quad (2-25c)$$

Since,

$$\Pi'(\mathbf{r}_<, p) - \Pi'(\mathbf{r}_>, p) = -jKV_0 \sum_{n=0}^{\infty} \frac{\epsilon_n}{\kappa_n} C_n(z) \left(j \frac{2}{\pi \kappa_n p} \right) \quad (2-26a)$$

where the Wronskian relation

$$J_0(\kappa_n p) H_1^{(2)}(\kappa_n p) - J_1(\kappa_n p) H_0^{(2)}(\kappa_n p) = j \frac{2}{\pi \kappa_n p} \quad (2-26b)$$

has been utilized, Eq. (2-25c) becomes

$$\mathbf{H}(\mathbf{r}) = -\Phi_0 j \omega \epsilon_0 \frac{d}{dp} \left[\int_a^b \Pi'(\mathbf{r}, p') dp' - jKV_0 \sum_{n=0}^{\infty} \frac{\epsilon_n}{\kappa_n} C_n(z) j \frac{2}{\pi \kappa_n} \ln p \right]. \quad (2-26c)$$

In view of Eqs. (2-21) and (2-23b) from Eq. (2-26c) the vector potential for $a \leq p \leq b$ is

$$\mathbf{A}_z(\mathbf{r}) = j\mu_0 k \eta_0 \left[\int_a^b \Pi'(\mathbf{r}, p') dp' + KV_0 \sum_{n=0}^{\infty} \frac{\epsilon_n}{\kappa_n^2} C_n(z) \frac{2}{\pi} \ln p \right]. \quad (2-27)$$

Hence from Eqs. (2-22b) and (2-27) using Eq. (2-18), the vector potential $\mathbf{A}(\mathbf{r}) = \mathbf{z}_0 A_z(\mathbf{r})$ due to an annular magnetic ring source of width $(b-a)$ is

$$\mathbf{A}_z(\mathbf{r}) = -KV_0 \mu_0 k \eta_0 \sum_{n=0}^{\infty} \frac{\epsilon_n}{\kappa_n^2} C_n(z)$$

$$\begin{cases} H_0^{(2)}(\kappa_n \rho) J_n & \rho \geq b \\ -j \frac{2}{\pi} \ln \rho + J_0(\kappa_n \rho) H_0^{(2)}(\kappa_n b) - H_0^{(2)}(\kappa_n \rho) J_0(\kappa_n a), & a \leq \rho \leq b \\ J_0(\kappa_n \rho) H_n & \rho \leq a \end{cases} \quad (2-28a)$$

where

$$J_n = -\kappa_n \int_a^b J_1(\kappa_n \rho') d\rho' = J_0(\kappa_n b) - J_0(\kappa_n a) \quad (2-28b)$$

and

$$H_n = -\kappa_n \int_a^b H_1^{(2)}(\kappa_n \rho') d\rho' = H_0^{(2)}(\kappa_n b) - H_0^{(2)}(\kappa_n a). \quad (2-28c)$$

2.4 Electric Field (E_ρ, E_z)

The electric field at \mathbf{r} due to a constant magnetic current circular loop M at ρ' can be evaluated from [see Eq. (A-1a)]

$$\mathbf{E}(\mathbf{r}, \rho') = \nabla \times \nabla \times \mathbf{z}_0 \Pi'(\mathbf{r}, \rho') \quad (2-29)$$

where $\Pi'(\mathbf{r}, \rho')$ is given by Eq. (2-18). In component form, Eq. (2-29) is

$$\mathbf{E}(\mathbf{r}, \rho') = \rho_0 E_\rho + \mathbf{z}_0 E_z \quad (2-30a)$$

where

$$E_\rho(r, \rho') = \frac{\partial^2 \Pi'(r, \rho')}{\partial z \partial \rho} \quad (2-30b)$$

$$E_z(r, \rho') = -\frac{1}{\rho} \frac{\partial}{\partial \rho} \left[\rho \frac{\partial \Pi'(r, \rho)}{\partial \rho} \right] = -\left[\frac{\partial^2 \Pi'(r, \rho')}{\partial \rho^2} + \frac{1}{\rho} \frac{\partial \Pi'(r, \rho')}{\partial \rho} \right] \quad (2-30c)$$

since $\partial/\partial\phi' = 0$.

We first evaluate $E_\rho(r)$. From Eqs. (2-30b) and (2-18a),

$$E_\rho(r, \rho') = -jK \sum_{n=0}^{\infty} \epsilon_n \left(\frac{n\pi}{h} \right) \sin \frac{n\pi}{h} z \begin{cases} J_1(\kappa_n \rho') H_1^{(2)}(\kappa_n \rho), & \rho > \rho' \\ J_1(\kappa_n \rho) H_1^{(2)}(\kappa_n \rho'), & \rho < \rho' \end{cases} \quad (2-31)$$

The radial component of the electric field in the parallel plate region at $r = \rho_0 \rho + \phi_0 \rho \phi + z_0 z$ due to the annular magnetic ring source of width $(b-a)$ at $z'=0$ is obtained by integrating Eq. (2-31) over the source (prime) coordinates as follows:

$$E_\rho(r) = \int_a^b E_\rho(r, \rho') d\rho' = -jKV_0 \sum_{n=0}^{\infty} \frac{\epsilon_n}{\kappa_n} \left(\frac{n\pi}{h} \right) \sin \frac{n\pi}{h} z$$

$$\begin{cases} H_1^{(2)}(\kappa_n \rho) \int_a^b J_1(\kappa_n \rho') d\rho' & \rho \geq b \\ H_1^{(2)}(\kappa_n \rho) \int_a^\rho J_1(\kappa_n \rho') d\rho' + J_1(\kappa_n \rho) \int_\rho^b H_1^{(2)}(\kappa_n \rho') d\rho' & a \leq \rho \leq b \\ J_1(\kappa_n \rho) \int_a^b H_1^{(2)}(\kappa_n \rho') d\rho' & \rho \leq a \end{cases}$$

$$= jKV_0 \sum_{n=0}^{\infty} \frac{\epsilon_n}{\kappa_n} \left(\frac{n\pi}{h} \right) \sin \frac{n\pi}{h} z \begin{cases} H_1^{(2)}(\kappa_n \rho) J_n & , \rho \geq b \\ J_1(\kappa_n \rho) H_0^{(2)}(\kappa_n b) - H_1^{(2)}(\kappa_n \rho) J_0(\kappa_n a), & a \leq \rho \leq b \\ J_1(\kappa_n \rho) H_n & , \rho \leq a \end{cases} \quad (2-32)$$

where J_n and H_n are given in Eqs. (2-28b) and (2-28c), respectively.

The same procedure is followed to obtain the z-component of the electric field in a parallel plate region due to an annular magnetic ring source of width $(b-a)$ at $z'=0$. Utilizing Bessel's equation of zeroth order

$$\left(\frac{d^2}{d\rho^2} + \frac{1}{\rho} \frac{d}{d\rho} \right) \Pi'(\mathbf{r}, \rho') = -\kappa_n^2 \Pi'(\mathbf{r}, \rho') \quad (2-33)$$

one sees from Eq. (2-30c) that

$$E_z(\mathbf{r}, \rho') = \kappa_n^2 \Pi'(\mathbf{r}, \rho') = -jKV_0 \sum_{n=0}^{\infty} \epsilon_n \kappa_n C_n(z) \begin{cases} J_1(\kappa_n \rho') H_0^{(2)}(\kappa_n \rho), & \rho > \rho' \\ J_0(\kappa_n \rho) H_1^{(2)}(\kappa_n \rho'), & \rho < \rho' \end{cases} \quad (2-34)$$

Integration over ρ' yields

$$E_z(\mathbf{r}) = \int_a^b E_z(\mathbf{r}, \rho') d\rho' = -jKV_0 \sum_{n=0}^{\infty} \epsilon_n \kappa_n C_n(z) \begin{cases} H_0^{(2)}(\kappa_n \rho) \int_a^b J_1(\kappa_n \rho') d\rho' & , \rho \geq b \\ H_0^{(2)}(\kappa_n \rho) \int_a^{\rho} J_1(\kappa_n \rho') d\rho' + J_0(\kappa_n \rho) \int_{\rho}^b H_1^{(2)}(\kappa_n \rho') d\rho', & a \leq \rho \leq b \\ J_0(\kappa_n \rho) \int_a^b H_1^{(2)}(\kappa_n \rho') d\rho' & , \rho \leq a \end{cases}$$

$$= JK V_0 \sum_{n=0}^{\infty} \epsilon_n C_n(z) \begin{cases} H_0^{(2)}(\kappa_n \rho) J_n & , \rho \geq b \\ J_0(\kappa_n \rho) H_0^{(2)}(\kappa_n b) - H_0^{(2)}(\kappa_n \rho) J_0(\kappa_n a), & a \leq \rho \leq b \\ J_0(\kappa_n \rho) H_n & , \rho \leq a \end{cases} \quad (2-35)$$

Note that Eqs. (2-32) and (2-35) for $\mathbf{E}(\mathbf{r})$ could be alternatively derived using Eq. (2-28) for the vector potential $\mathbf{A}(\mathbf{r})$, from which, using Eq. (2-21), one determines $\mathbf{H}(\mathbf{r})$. Consequently,

$$\mathbf{E}(\mathbf{r}) = \frac{1}{j\omega \epsilon_0} \nabla \times \mathbf{H}(\mathbf{r}). \quad (2-36)$$

2.5 Magnetic Field (H_ϕ)

The magnetic field at \mathbf{r} due to the annular magnetic ring source of width $(b-a)$ at $z'=0$ can be directly obtained from

$$\mathbf{H}(\mathbf{r}) = \frac{1}{\mu_0} \nabla \times \mathbf{A}(\mathbf{r}) = -\phi_0 \frac{1}{\mu_0} \frac{\partial A_z(\mathbf{r})}{\partial \rho} = \phi_0 H_\phi(\mathbf{r}). \quad (2-37)$$

Substitution of Eq. (2-28a) into Eq. (2-37) yields

$$H_\phi(\mathbf{r}) = -K n_0 V_0 \sum_{n=0}^{\infty} \frac{\epsilon_n}{\sqrt{1 - \left(\frac{n\pi}{kh}\right)^2}} C_n(z) \begin{cases} H_1^{(2)}(\kappa_n \rho) J_n & , \rho \geq b \\ J_1(\kappa_n \rho) H_0^{(2)}(\kappa_n b) - H_1^{(2)}(\kappa_n \rho) J_0(\kappa_n a), & a \leq \rho \leq b \\ J_1(\kappa_n \rho) H_n & , \rho \leq a \end{cases} \quad (2-38)$$

Note that Eq. (2-38) can be also derived using (A-1b), that is,

$$\mathbf{H}(\mathbf{r},\rho') = j\omega\epsilon_0 \nabla \times \mathbf{z}_0 \Pi'(\mathbf{r},\rho') = -\phi_0 j\omega\epsilon_0 \frac{\partial \Pi'(\mathbf{r},\rho')}{\partial \rho} = \phi_0 \mathbf{H}_\phi(\mathbf{r},\rho') \quad (2-39a)$$

where $\Pi'(\mathbf{r},\rho')$ is given by Eq. (2-18) and

$$\mathbf{H}_\phi(\mathbf{r}) = \int_a^b \mathbf{H}_\phi(\mathbf{r},\rho') d\rho'. \quad (2-39b)$$

3. CYLINDRICAL ELECTRIC CURRENT SOURCE IN AN INFINITE PARALLEL PLATE WAVEGUIDE

In this chapter we derive expressions for the electromagnetic field in an infinite parallel plate region due to a cylindrical electric current source. The geometry under consideration is shown in Figure 3-1 where a and l are the radius and length, respectively, of the cylindrical source and h is the height of the infinite parallel plate waveguide. A cylindrical coordinate system (ρ, ϕ, z) is chosen so that the z axis coincides with the axis of the source. The source electric current density distribution is assumed to be a known function of z' given by

$$\mathbf{J}(\mathbf{r}',t) = \mathbf{z}_0 J_z(z') \delta(\rho-a) e^{j\omega t}, \quad 0 \leq z' \leq l \quad (3-1)$$

where the prime refers to source coordinates.

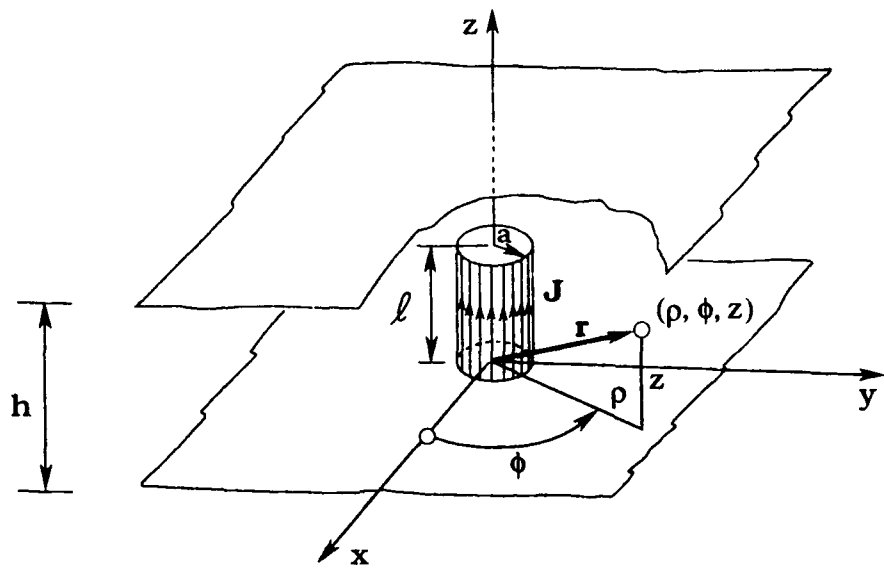


Figure 3-1. Geometry of Cylindrical Electric Current Source in an Infinite Parallel Plate Waveguide

To calculate the radiation from the cylindrical current source in Figure 3-1, one may proceed as in the previous chapter, and utilize the results in Appendix A for a longitudinal (to z) electric current element. The results are verified in Appendix C by an alternative analysis where the propagation direction is assumed to be radial.

The procedure consists of the following steps:

1. Determine the Green's function $G(\mathbf{r}, \mathbf{r}')$. Since the electric current in Eq. (3-1) is longitudinal and constant in ϕ , only E-modes with respect to z are excited.
2. Determine the E-mode Hertz potential $\Pi'(\mathbf{r}, \mathbf{r}')$ using Eq. (A-4c).
3. Determine the vector potential $\mathbf{A}(\mathbf{r})$.
4. Determine the E-mode electric and magnetic fields (E_ρ, H_ϕ, E_z) using Eq. (A-1) or step 3.

3.1 Green's Functions

The Green's function $G'(\mathbf{r}, \mathbf{r}')$ for the axial electric dipole shown in Figure 3-2 is given in (A-3a) in terms of the function $S'(\mathbf{r}, \mathbf{r}')$ defined in Eq. (2-14). Hence,

$$G'(\mathbf{r}, \mathbf{r}') = -\nabla_t^2 S'(\mathbf{r}, \mathbf{r}') = -\left[\frac{\partial^2}{\partial \rho^2} + \frac{1}{\rho} \frac{\partial}{\partial \rho} \right] S'(\mathbf{r}, \mathbf{r}') = \kappa_n^2 S'(\mathbf{r}, \mathbf{r}')$$

$$= -\frac{j}{4h} \sum_{m=-\infty}^{\infty} e^{-jm(\phi-\phi')} \sum_{n=0}^{\infty} \epsilon_n J_m(\kappa_n \rho_{<}) H_m^{(2)}(\kappa_n \rho_{>}) C_n(z) C_n(z') \quad (3-2)$$

where $C_n(z)$ and $C_n(z')$ are as given in Eqs. (2-12d) and (2-12e).

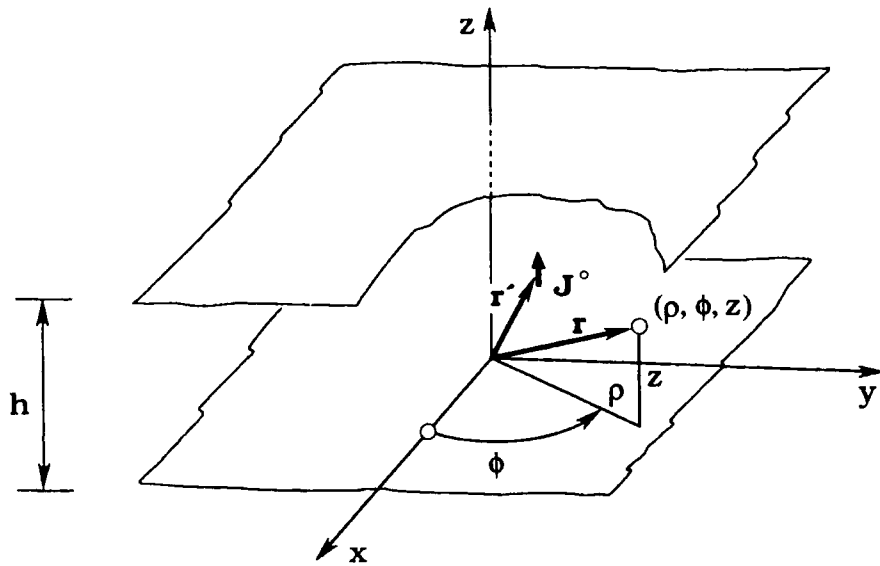


Figure 3-2. Axial Electric Dipole in an Infinite Parallel Plate Waveguide

3.2 Hertz Potential

For the longitudinal electric point current element $\mathbf{J}^0 = z_0 J_z^0 (\mathbf{M}^0 = 0)$ shown in Figure 3-2, one obtains for the Hertz potential function from Eq. (A-4), for $\exp(j\omega t)$ time dependence,

$$\Pi'(\mathbf{r}, \mathbf{r}') = \frac{J_z^0}{j\omega\epsilon_0} G'(\mathbf{r}, \mathbf{r}') \quad (3-3a)$$

$$\Pi''(\mathbf{r}, \mathbf{r}') = 0. \quad (3-3b)$$

Hence \mathbf{J}^0 contributes to $\Pi'(\mathbf{r}, \mathbf{r}')$, thereby exciting E-modes with respect to z only. Substituting Eq. (3-2) into Eq. (3-3a) we obtain for the Hertz potential:

$$\Pi'(\mathbf{r}, \mathbf{r}') = -\frac{J_z^0}{4\hbar\omega\epsilon_0} \sum_{m=-\infty}^{\infty} e^{-jm(\phi-\phi')} \sum_{n=0}^{\infty} \epsilon_n J_m(\kappa_n \rho_<) H_m^{(2)}(\kappa_n \rho_>) C_n(z) C_n(z'). \quad (3-4)$$

The E-mode Hertz potential due to the (constant in ϕ) electric cylindrical current distribution (see Figure 3-1)

$$\mathbf{J}(z') = \mathbf{z}_0 J_z(z') \delta(\rho-a), \quad 0 \leq z' \leq l \quad (3-5)$$

can be now obtained by integrating Eq. (3-4) over the source surface S' . Since the source current is constant in ϕ ($\partial/\partial\phi' = 0$) only the $m=0$ term in Eq. (3-4) contributes. Hence,

$$\begin{aligned} \Pi'(\mathbf{r}) &= \int_{\phi'=0}^{2\pi} \int_{z'=0}^l \int_{\rho'=a}^b \Pi'(\mathbf{r}, \mathbf{r}') \rho' d\rho' d\phi' dz' \\ &= Ck\eta_0 \sum_{n=0}^{\infty} \epsilon_n C_n(z) I_n \begin{cases} J_0(\kappa_n a) H_0^{(2)}(\kappa_n \rho), & \rho \geq a \\ J_0(\kappa_n \rho) H_0^{(2)}(\kappa_n a), & \rho \leq a \end{cases} \end{aligned} \quad (3-6a)$$

where

$$I_n = \int_{z'=0}^l J_z(z') C_n(z') dz' \quad (3-6b)$$

and

$$C = -\frac{\pi a}{2h}. \quad (3-6c)$$

3.3 Vector Potential

From Eq. (A-1b) the vector potential and Hertz potential are related by

$$\mathbf{A}(\mathbf{r}) = j\omega\epsilon_0\mu_0 \mathbf{z}_0 \Pi'(\mathbf{r}) = \mathbf{z}_0 A_z(\mathbf{r}). \quad (3-7)$$

Using Eq. (3-6) with the electric current distribution given by Eq. (3-5), from Eq. (3-7), the vector potential is

$$A_z(\mathbf{r}) = jC\mu_0 \sum_{n=0}^{\infty} \epsilon_n C_n(z) I_n \begin{cases} J_0(\kappa_n a) H_0^{(2)}(\kappa_n \rho), & \rho \geq a \\ J_0(\kappa_n \rho) H_0^{(2)}(\kappa_n a), & \rho \leq a \end{cases} \quad (3-8)$$

3.4 Electric Field (E_ρ , E_z)

The electric field at \mathbf{r} due to the electric current of Eq. (3-5) can be obtained from Eq. (A-1a), that is,

$$\mathbf{E}(\mathbf{r}) = \nabla \times \nabla \times \mathbf{z}_0 \Pi'(\mathbf{r}) \quad (3-9)$$

where $\Pi'(\mathbf{r})$ is given by Eq. (3-6). In component form Eq. (3-9) is

$$\mathbf{E}(\mathbf{r}) = \rho_0 E_\rho + \mathbf{z}_0 E_z \quad (3-10a)$$

where

$$E_\rho(\mathbf{r}) = \frac{\partial^2 \Pi'(\mathbf{r})}{\partial z \partial \rho} \quad (3-10b)$$

$$E_z(r) = - \left[\frac{\partial^2 \Pi'(r)}{\partial \rho^2} + \frac{1}{\rho} \frac{\partial \Pi'(r)}{\partial \rho} \right] = \kappa_n^2 \Pi'(r). \quad (3-10c)$$

Substitution of Eq. (3-6) into Eq. (3-10) yields

$$E_\rho(r) = \frac{C}{k\eta_0} \sum_{n=0}^{\infty} \epsilon_n \kappa_n \left(\frac{n\pi}{h} \right) \sin \frac{n\pi}{h} z I_n \begin{cases} J_0(\kappa_n a) H_1^{(2)}(\kappa_n \rho), & \rho \geq a \\ J_1(\kappa_n \rho) H_0^{(2)}(\kappa_n a), & \rho \leq a \end{cases} \quad (3-11a)$$

and

$$E_z(r) = \frac{C}{k\eta_0} \sum_{n=0}^{\infty} \epsilon_n \kappa_n^2 C_n(z) I_n \begin{cases} J_0(\kappa_n a) H_0^{(2)}(\kappa_n \rho), & \rho \geq a \\ J_0(\kappa_n \rho) H_0^{(2)}(\kappa_n a), & \rho \leq a \end{cases} \quad (3-11b)$$

3.5 Magnetic Field (H_ϕ)

The magnetic field at r due to the (uniform in ϕ) cylindrical electric current distribution of Eq. (3-5) can be directly obtained from

$$H(r) = \frac{1}{\mu_0} \nabla \times A(r) \quad (3-12)$$

where the vector potential $A(r)$ is given by Eq. (3-8). Hence,

$$H_\phi(r) = - \frac{1}{\mu_0} \frac{\partial A_z(r)}{\partial \rho} = jC \sum_{n=0}^{\infty} \epsilon_n \kappa_n C_n(z) I_n \begin{cases} J_0(\kappa_n a) H_1^{(2)}(\kappa_n \rho), & \rho \geq a \\ J_1(\kappa_n \rho) H_0^{(2)}(\kappa_n a), & \rho \leq a \end{cases} \quad (3-13)$$

As already mentioned in Chapter 2, $H(r)$ could be also obtained from (A-1b), i.e.,

$$H(r) = j\omega \epsilon_0 \nabla \times z_0 \Pi'(r) \quad (3-14)$$

where $\Pi'(r)$ is given by Eq. (3-6).

4. ACTIVE ADMITTANCE AND REFLECTION COEFFICIENT OF AN INFINITE LINEAR PHASED ARRAY OF MONPOLE ELEMENTS IN A PARALLEL PLATE WAVEGUIDE

In this chapter we present the analysis and expressions for the active input admittance and reflection coefficient of a coaxially-fed monopole element in an infinite linear phased array radiating into a semi-infinite parallel plate waveguide. The term "semi-infinite" in this report refers to monopole elements in a parallel plate waveguide backed by a perfectly conducting ground plane. Although all relations are written for a linear array of monopoles in a semi-infinite parallel plate waveguide, they can be applied to a single monopole in an infinite and semi-infinite parallel plate waveguide, and to a linear array of monopole elements in an infinite parallel plate waveguide after a simple modification to be described.

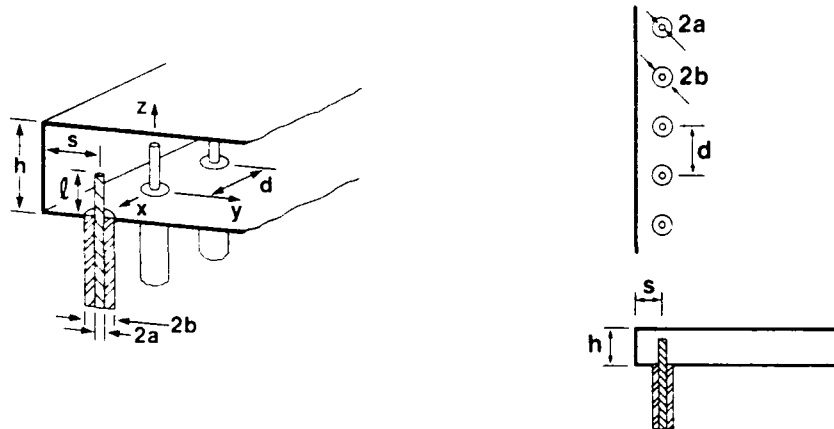


Figure 4-1. Linear Array of Coaxial-Monopole Elements in a Semi-Infinite Parallel Plate Waveguide

The model under consideration is shown in Figure 4-1. The coaxially-fed monopoles of length l are located in a parallel plate waveguide of height h (only the TEM mode propagates since $h < \lambda/2$). The uniform distance between elements is d while the distance between the probe elements and "ground plane" is s (approximately $\lambda/4$). The probe radius is $a \ll \lambda$ while the inner and outer radii of the coaxial lines are a and b . Each feed-coaxial transmission line has a characteristic impedance Z_c and a dielectric with relative permittivity ϵ_r . A cylindrical coordinate system (ρ, ϕ, z) with respective unit vectors (ρ_0, ϕ_0, z_0) is chosen so that the z axis coincides with the axis of the reference monopole radiating element ($\rho=0$).

The analysis takes into account the geometry of the feed system. The field distribution in the coaxial aperture is assumed to be that of the TEM mode of the coaxial line. The effect on the active admittance of neglecting higher modes in the aperture is very small as shown in

Reference 7. Furthermore, in the analysis we have assumed that the probe current has only an axial component and no angular variation. This approximation is justified since $a \ll l$ and $a/\lambda \ll 1$ (see Figure 4-1).

The expression for the active admittance is given in terms of array and monopole geometry, and inter-element phasing δ_x , that is, scan angle $\hat{\phi}_0$. The analysis is based on the method of images, using results from the previous two chapters for a single monopole in an infinite parallel plate waveguide. The procedure is carried out in a number of steps. Prior to presenting the details of analysis, we enumerate these steps as follows:

1. Obtain expressions for $E_{z0}(\rho, z)$ due to an isolated (single) reference annular aperture (magnetic frill) and probe current in an infinite parallel plate waveguide.
2. Define the array excitation; to evaluate the active input admittance $Y_a(\delta_x)$, all elements are initially excited with forced aperture voltages of equal amplitude $V_0(z=0^-)$ and progressive phase δ_x .
3. For an observation point located on the reference probe, $E_z(a, z)$ is obtained as a superposition of all (real and image) probe currents as well as by the assumed known equivalent magnetic ring current distributions in the coaxial apertures.
4. To apply the boundary condition on the probe, using the Addition Theorem for cylindrical functions, the field $E_z(a, z)$ is re-expanded about a cylindrical axis centered at the reference element. Because the reference probe current distribution is rotationally symmetric, only terms with no angular variation are considered.
5. The slow convergence of the infinite sum over the array elements is accelerated as described in Appendix E.
6. Steps 1 to 5, combined with the requirement that the total axial electric field $E_z(a, z)$ vanishes on the probe surface, yield a desired integral equation for the unknown probe current.
7. After expanding the probe current in a sine series, using the Galerkin procedure, we obtain a set of linear inhomogeneous equations for the determination of the unknown probe expansion coefficients.
8. Having solved for the probe current, then following the procedure indicated in steps 1 to 4, we determine the magnetic field $H_\phi(\rho, z=0^+)$ in the aperture, where $a \leq \rho \leq b$.
9. The continuity of $H_\phi(a \leq \rho \leq b, z=0^+)$ is imposed across the aperture, yielding $Y_a(\delta_x)$.

⁷ Williamson, A.G. and Otto, D.V. (1973) Coaxially-fed hollow cylindrical monopole in a rectangular waveguide, *Electron. Lett.*, 9(No. 10):218.

4.1 Coaxially-Fed Monopole in an Infinite Parallel Plate Waveguide

Expressions for the field in an infinite parallel plate region due to a single coaxially-fed monopole, shown in Figure 4-2, are presented. These expressions will be used in the subsequent sections to evaluate the active input admittance of the monopole element in a linear phased array radiating into a semi-infinite parallel plate waveguide.

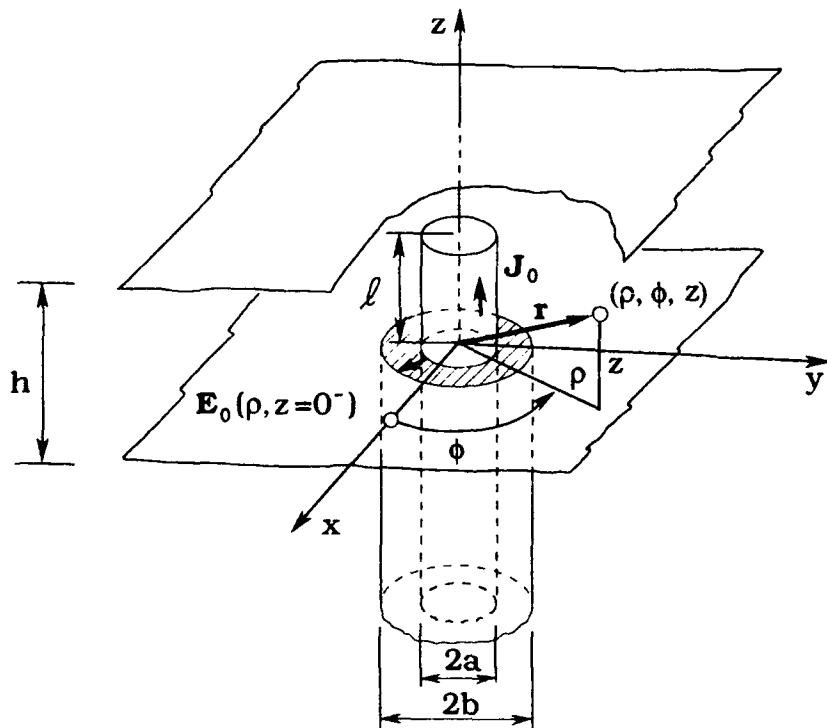


Figure 4-2. Coaxially-Fed Monopole in an Infinite Parallel Plate Waveguide

As already mentioned, the electric field over the coaxial aperture is that of the TEM transmission line mode, that is,

$$E(\rho, z=0^-) = \rho_0 \frac{V_0(z=0^-)}{\rho \ln \frac{b}{a}}, \quad a \leq \rho \leq b \quad (4-1)$$

where $V_0(z=0^-)$ is the applied voltage in the aperture between two conductors of the coaxial feed transmission line. The circular cylindrical probe current is assumed to be

$$J_0(\rho, z) = z_0 J_{z0}(z) \delta(\rho - a), \quad 0 \leq z \leq l. \quad (4-2)$$

The total field in the infinite parallel plate region may be represented as a superposition of the fields due to a single coaxially-fed annular aperture source [Eq. (4-1)] and a probe current source [Eq. (4-2)]. Relations for the fields radiated from these sources have been obtained in the previous two chapters in terms of radial waveguide modes with propagation constants κ_n . For convenience, we summarize the results below.

4.1.1 VECTOR POTENTIAL $\mathbf{A}_0(\rho, z)$

The vector potential $\mathbf{A}_0(\rho, z) = z_0 \mathbf{A}_{z0}(\rho, z)$ due to a single monopole in an infinite parallel plate waveguide is

$$\mathbf{A}_{z0}(\rho, z) = \mathbf{A}_{z0}^a(\rho, z; V_0) + \mathbf{A}_{z0}^p(\rho, z; J_{z0}) \quad (4-3a)$$

where $\mathbf{A}_{z0}^a(\rho, z; V_0)$ and $\mathbf{A}_{z0}^p(\rho, z; J_{z0})$ are defined in Eqs. (2-28) and (3-8), respectively as

$$\mathbf{A}_{z0}^a(\rho, z) = -K\mu_0 k \eta_0 V_0(z=0^-) \sum_{n=0}^{\infty} \frac{\epsilon_n}{\kappa_n^2} C_n(z)$$

$$\begin{cases} H_0^{(2)}(\kappa_n \rho) J_n & , \rho \geq b \\ -j \frac{2}{\pi} \ln \rho + J_0(\kappa_n \rho) H_0^{(2)}(\kappa_n b) - H_0^{(2)}(\kappa_n \rho) J_0(\kappa_n a), & a \leq \rho \leq b \\ J_0(\kappa_n \rho) H_n & , \rho \leq a \end{cases} \quad (4-3b)$$

$$\mathbf{A}_{z0}^p(\rho, z) = jC\mu_0 \sum_{n=0}^{\infty} \epsilon_n C_n(z) I_n \begin{cases} J_0(\kappa_n a) H_0^{(2)}(\kappa_n \rho), & \rho \geq a \\ J_0(\kappa_n \rho) H_0^{(2)}(\kappa_n a), & \rho \leq a \end{cases} \quad (4-3c)$$

4.1.2 ELECTRIC FIELD $\mathbf{E}_0(\rho, z)$

The total electric field $\mathbf{E}_0(\rho, z)$ in the parallel plate region is

$$\mathbf{E}_0(\rho, z) = \mathbf{E}_0^a(\rho, z) + \mathbf{E}_0^p(\rho, z) \quad (4-4)$$

where $\mathbf{E}_0^a(\rho, z)$ is the electric field due to the applied aperture voltage $V_0(z = 0^-)$ (or equivalent concentric magnetic current source) and $\mathbf{E}_0^p(\rho, z)$ is the electric field due to the probe electric current $J_{z0}(z)$. The $\mathbf{E}_0^a(\rho, z)$ in Eq. (4-4) is

$$\mathbf{E}_0^a(\rho, z) = \rho_0 \mathbf{E}_{\rho 0}^a(\rho, z) + z_0 \mathbf{E}_{z0}^a(\rho, z) \quad (4-5a)$$

where $\mathbf{E}_{\rho 0}^a$ and \mathbf{E}_{z0}^a are given by Eqs. (2-32) and (2-35) as

$$\mathbf{E}_{\rho 0}^a(\rho, z) = jKV_0(z=0^-) \sum_{n=0}^{\infty} \frac{\epsilon_n}{\kappa_n} \left(\frac{n\pi}{h} \right) \sin \frac{n\pi z}{h}$$

$$\begin{cases} H_1^{(2)}(\kappa_n \rho) J_n & \rho \geq b \\ J_1(\kappa_n \rho) H_0^{(2)}(\kappa_n b) - H_1^{(2)}(\kappa_n \rho) J_0(\kappa_n a), & a \leq \rho \leq b \\ J_1(\kappa_n \rho) H_n & \rho \leq a \end{cases} \quad (4-5b)$$

$$\mathbf{E}_{z0}^a(\rho, z) = jKV_0(z=0^-) \sum_{n=0}^{\infty} \epsilon_n C_n(z) \begin{cases} H_0^{(2)}(\kappa_n \rho) J_n & \rho \geq b \\ J_0(\kappa_n \rho) H_0^{(2)}(\kappa_n b) - H_0^{(2)}(\kappa_n \rho) J_0(\kappa_n a), & a \leq \rho \leq b \\ J_0(\kappa_n \rho) H_n & \rho \leq a \end{cases} \quad (4-5c)$$

with

$$K = \frac{\pi}{2h \ln \frac{b}{a}} \quad (4-5d)$$

$$\zeta_0 = \frac{1}{\eta_0} = \sqrt{\frac{\mu_0}{\epsilon_0}} = 376.6 \Omega \approx 120 \pi \Omega \quad (4-5e)$$

$$\epsilon_n = \begin{cases} 1, n=0 \\ 2, n \geq 1 \end{cases} \quad (4-5f)$$

$$C_n(z) = \cos \frac{n\pi}{h} z \quad (4-5g)$$

$$\kappa_n = \sqrt{k^2 - \left(\frac{n\pi}{h}\right)^2}, \quad \text{Im}\{\kappa_n\} \leq 0 \quad (4-5h)$$

$$J_n = J_0(\kappa_n b) - J_0(\kappa_n a) \quad (4-5i)$$

and

$$H_n = H_0^{(2)}(\kappa_n b) - H_0^{(2)}(\kappa_n a). \quad (4-5j)$$

The $E_0^P(\rho, z)$ in Eq. (4-4) is

$$E_0^P(\rho, z) = \rho_0 E_{\rho 0}^P(\rho, z) + z_0 E_{z 0}^P(\rho, z) \quad (4-6a)$$

where from Eq. (3-11), we have

$$E_{\rho 0}^P(\rho, z) = \frac{C}{k\eta_0} \sum_{n=0}^{\infty} \epsilon_n \kappa_n \left(\frac{n\pi}{h} \right) \sin \frac{n\pi z}{h} I_n \begin{cases} J_0(\kappa_n a) H_1^{(2)}(\kappa_n \rho), & \rho \geq a \\ J_1(\kappa_n \rho) H_0^{(2)}(\kappa_n a), & \rho \leq a \end{cases} \quad (4-6b)$$

$$E_{z0}^P(\rho, z) = \frac{C}{k\eta_0} \sum_{n=0}^{\infty} \epsilon_n \kappa_n^2 C_n(z) I_n \begin{cases} J_0(\kappa_n a) H_0^{(2)}(\kappa_n \rho), & \rho \geq a \\ J_0(\kappa_n \rho) H_0^{(2)}(\kappa_n a), & \rho \leq a \end{cases} \quad (4-6c)$$

with

$$C = -\frac{\pi a}{2h} \quad (4-6d)$$

and

$$I_n = \int_{z=0}^l J_{z0}(z) C_n(z) dz. \quad (4-6e)$$

4.1.3 MAGNETIC FIELD $H_0(\rho, z)$

The total magnetic field $H_0(\rho, z) = \phi_0 H_{\phi 0}(\rho, z)$ in the parallel plate region is

$$H_{\phi 0}(\rho, z) = H_{\phi 0}^a(\rho, z) + H_{\phi 0}^P(\rho, z). \quad (4-7)$$

Relations for $H_{\phi 0}^a$ and $H_{\phi 0}^P$ are given by Eqs. (2-38) and (3-13), respectively. They are:

$$H_{z0}^a(\rho, z) = -K k \eta_0 V_0(z=0^-) \sum_{n=0}^{\infty} \frac{\epsilon_n}{\kappa_n} C_n(z)$$

$$H_{z0}^a(\rho, z) = \begin{cases} H_1^{(2)}(\kappa_n \rho) J_n & \rho \geq b \\ J_1(\kappa_n \rho) H_0^{(2)}(\kappa_n b) - H_1^{(2)}(\kappa_n \rho) J_0(\kappa_n a), & a \leq \rho \leq b \\ J_1(\kappa_n \rho) H_n & \rho \leq a \end{cases} \quad (4-8a)$$

$$H_{z0}^p(\rho, z) = j C \sum_{n=0}^{\infty} \epsilon_n \kappa_n C_n(z) I_n \begin{cases} J_0(\kappa_n a) H_1^{(2)}(\kappa_n \rho), & \rho \geq a \\ J_1(\kappa_n \rho) H_0^{(2)}(\kappa_n a), & \rho \leq a \end{cases} \quad (4-8b)$$

4.2 Total Axial Electric Field $E_z(a, z)$ on the Probe Surface

Results of the previous section will be now applied to evaluate the total axial electric field on the reference probe of the infinite linear array of monopoles in the semi-infinite parallel plate waveguide. As stated in Section 4.1.2, the total axial electric field $E_{z0}(\rho, z)$ in the infinite parallel plate region due to a single coaxially-fed monopole is

$$E_{z0}(\rho, z) = E_{z0}^a(\rho, z) + E_{z0}^p(\rho, z) \quad (4-9)$$

where $E_{z0}^a(\rho, z)$ and $E_{z0}^p(\rho, z)$ are defined by Eqs. (4-5c) and (4-6c). For simplicity of presentation, we rewrite these two relations in the form

$$E_{z0}^a(a, z) = \sum_{n=0}^{\infty} F_n(V_0) H_n \quad \rho = a \quad (4-10a)$$

$$E_{z0}^p(\rho, z) = \sum_{n=0}^{\infty} f_n(V_0) H_0^{(2)}(\kappa_n \rho) \quad \rho \geq b \quad (4-10b)$$

where the functions

$$F_n(V_0) = jKV_0(z=0^-) \epsilon_n C_n(z) J_0(\kappa_n a) \quad (4-10c)$$

$$f_n(V_0) = jKV_0(z=0^-) \epsilon_n C_n(z) J_n \quad (4-10d)$$

and

$$E_{z0}^p(\rho, z) = \sum_{n=0}^{\infty} G_n(J_z) H_0^{(2)}(\kappa_n \rho) \quad (4-10e)$$

$$G_n(J_z) = \frac{C}{k\eta_0} \epsilon_n \kappa_n^2 C_n(z) I_n J_0(\kappa_n a). \quad (4-10f)$$

The relation for the total tangential electric field on the probe $E_z(\rho, z)$, where $\rho = \rho_0 a = a$ is obtained with the aid of Figure 4-3. The effect of the conducting backplane is replaced by introducing an image array. Here, the integer p denotes the element number. The location of the p -th element with respect to reference $p=0$ -th element is defined by the radial vector

$$\rho_p = x_0 p d. \quad (4-11)$$

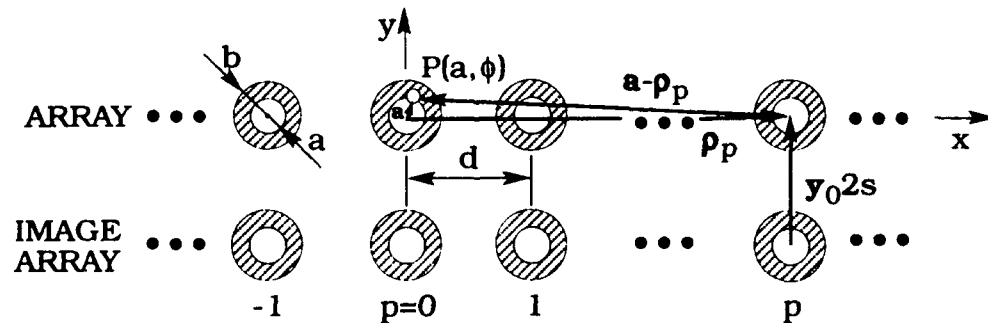


Figure 4-3. Geometry of the Linear Array and its Image for Evaluation of $E_z(a, z)$ (Top View)

All array elements are excited with aperture voltages $V_0(z=0^-)$ and progressive phase δ_x . The total field $E_z(a, z)$ is obtained as a superposition of contributions from an infinite number of probe-aperture combinations centered at ρ_p and $\rho_p - y_0 2s$ in an infinite parallel plate waveguide. This can be written in the form

$$E_z(a, \phi, z) = E_{z0}(a, z) + \sum_{p=-\infty}^{\infty}' E_{z0}(|a - \rho_p|, z) e^{-jp\delta_x} + \sum_{p=-\infty}^{\infty} E_{z0}(|a - \rho_p + y_0 2s|, z) e^{-j(p\delta_x + \pi)} \quad (4-12)$$

where the prime indicates that the $p=0$ term is excluded in the infinite sum. The first term in Eq. (4-12) represents a self contributions, i.e., the field due to the reference ($p=0$) element. The second term represents the contribution due to the rest of the elements in the array while the third term represents the contribution due to the image array. Note that a typical field contribution at $P(a, z)$ due to the p -th element is of the same form as the field due to an isolated (single) source given by Eqs. (4-9) and (4-10) except that: (1) in the argument of the Hankel functions, ρ is replaced by $|a - \rho_p|$ or $|a - \rho_p + y_0 2s|$, and (2) $J_z(z)$ in Eq. (4-6e) is not the current of the isolated (single) source but the probe current in the array environment (interaction between array elements is taken into account).

Substituting Eq. (4-9) with E_{z0}^a and E_{z0}^p given by Eqs. (4-10a), (4-10b), and (4-10e) into Eq. (4-12), we have

$$\begin{aligned} E_z(a, \phi, z) = & \sum_{n=0}^{\infty} F_n(V_0) H_n \\ & + \sum_{n=0}^{\infty} f_n(V_0) \left[\sum_{p=-\infty}^{\infty}' H_0^{(2)}(\kappa_n |a - \rho_p|) e^{-jp\delta_x} + \sum_{p=-\infty}^{\infty} H_0^{(2)}(\kappa_n |a - \rho_p + y_0 2s|) e^{-j(p\delta_x + \pi)} \right] \\ & + \sum_{n=0}^{\infty} G_n(J_z) H_0^{(2)}(\kappa_n a) \\ & + \sum_{n=0}^{\infty} G_n(J_z) \left[\sum_{p=-\infty}^{\infty}' H_0^{(2)}(\kappa_n |a - \rho_p|) e^{-jp\delta_x} + \sum_{p=-\infty}^{\infty} H_0^{(2)}(\kappa_n |a - \rho_p + y_0 2s|) e^{-j(p\delta_x + \pi)} \right]. \end{aligned} \quad (4-13)$$

To apply the boundary condition on the probe it is necessary to represent the total tangential electric field on the probe surface with respect to the reference element $p=0$. For this reason, we use the Addition Theorem for cylindrical functions to re-expand the fields $E_{z0}(|a-p_p|, z)$ and $E_{z0}(|a-p_p + y_0 2s|, z)$ in Eq.(4-12) about a cylindrical axis centered at the reference element. The Addition Theorem for Hankel functions is presented in Appendix D. Using the notation of Figure 4-4, we can write the theorem for Hankel functions in the form

$$H_0^{(2)}(\kappa_n |a-p_p|) = J_0(\kappa_n a) H_0^{(2)}(\kappa_n |p|d) + 2 \sum_{m=1}^{\infty} J_m(\kappa_n a) H_m^{(2)}(\kappa_n |p|d) \cos m\phi. \quad (4-14)$$

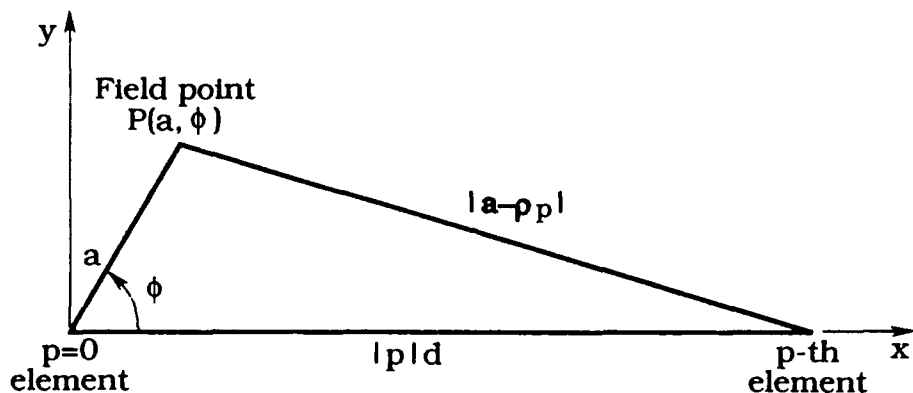


Figure 4-4. Triangle Pertaining to the Addition Theorem for Hankel Functions $H_0^{(2)}(\kappa_n |a-p_p|)$

In view of our assumption that the reference probe's current distribution is rotationally symmetric, only terms with no angular variation in Eq. (4-14), which is the $m=0$ term, need be considered. Thus,

$$H_0^{(2)}(\kappa_n |a-p_p|) \approx J_0(\kappa_n a) H_0^{(2)}(\kappa_n |p|d). \quad (4-15)$$

Similarly, one may write

$$H_0^{(2)}(\kappa_n |a-p_p + y_0 2s|) \approx J_0(\kappa_n a) H_0^{(2)}(\kappa_n \sqrt{(pd)^2 + (2s)^2}). \quad (4-16)$$

Substitution of Eqs. (4-15) and (4-16) into Eq. (4-13) yields

$$\begin{aligned}
 E_z(a, z) \simeq & \sum_{n=0}^{\infty} F_n(V_0) H_n \\
 & + \sum_{n=0}^{\infty} f_n(V_0) J_0(\kappa_n a) \left[2 \sum_{p=1}^{\infty} H_0^{(2)}(\kappa_n p d) \cos p \delta_x \right. \\
 & \left. - H_0^{(2)}(2 \kappa_n s) - 2 \sum_{p=1}^{\infty} H_0^{(2)} \left(\kappa_n d \sqrt{p^2 + \left(\frac{2s}{d} \right)^2} \right) \cos p \delta_x \right] \\
 & + \sum_{n=0}^{\infty} G_n(J_z) H_0^{(2)}(\kappa_n a) \\
 & + \sum_{n=0}^{\infty} G_n(J_z) J_0(\kappa_n a) \left[2 \sum_{p=1}^{\infty} H_0^{(2)}(\kappa_n p d) \cos p \delta_x \right. \\
 & \left. - H_0^{(2)}(2 \kappa_n s) - 2 \sum_{p=1}^{\infty} H_0^{(2)} \left(\kappa_n d \sqrt{p^2 + \left(\frac{2s}{d} \right)^2} \right) \cos p \delta_x \right] \tag{4-17a}
 \end{aligned}$$

where the identities

$$e^{-j(p\delta_x + \pi)} = -e^{-j p \delta_x} \tag{4-17b}$$

$$\sum_{p=-\infty}^{\infty} H_0^{(2)}(\kappa_n |p| d) e^{-j p \delta_x} = 2 \sum_{p=1}^{\infty} H_0^{(2)}(\kappa_n p d) \cos p \delta_x \tag{4-17c}$$

and

$$\sum_{p=-\infty}^{\infty} H_0^{(2)} \left(\kappa_n d \sqrt{p^2 + \left(\frac{2s}{d} \right)^2} \right) e^{-j p \delta_x} = 2 \sum_{p=1}^{\infty} H_0^{(2)} \left(\kappa_n d \sqrt{p^2 + \left(\frac{2s}{d} \right)^2} \right) \cos p \delta_x \quad (4-17d)$$

have been used. Finally, noting that [see Eqs. (4-10c) and 4-10d)]

$$f_n(V_0) J_0(\kappa_n a) = F_n(V_0) J_n \quad (4-18a)$$

the total axial field due to an infinite linear array of monopoles on the reference probe surface in the semi-infinite parallel plate waveguide becomes

$$\begin{aligned} E_z(a, z) \simeq & \sum_{n=0}^{\infty} F_n(V_0) [H_n + J_n S_n(\delta_x)] \\ & + \sum_{n=0}^{\infty} G_n(J_z) [H_0^{(2)}(\kappa_n a) + J_0(\kappa_n a) S_n(\delta_x)] \end{aligned} \quad (4-18b)$$

where

$$\begin{aligned} S_n(\delta_x) = & 2 \sum_{p=1}^{\infty} H_0^{(2)}(\kappa_n p d) \cos p \delta_x - H_0^{(2)}(2 \kappa_n s) \\ & - 2 \sum_{p=1}^{\infty} H_0^{(2)} \left(\kappa_n d \sqrt{p^2 + \left(\frac{2s}{d} \right)^2} \right) \cos p \delta_x. \end{aligned} \quad (4-18c)$$

The functions $F_n(V_0)$, $G_n(J_z)$, J_n , and H_n are defined by Eqs. (4-10c), (4-10f), (4-5i) and (4-5j), respectively.

Note that the first sum in Eq. (4-18b) represents the aperture field contribution while the second sum represents the probe current contribution to the total axial field on the reference

probe ($p=0$). The first term in the brackets represents the self contribution of the $p=0$ element while the second term in the brackets, which is proportional to $S_n(\delta_x)$, represents the contribution due to the rest of the array elements plus all the elements of the image array. Specifically, $S_n(\delta_x)$ as defined by Eq. (4-18c) has three basic terms. The first term represents contributions from the $|p| \geq 1$ array elements. The second term represents the contribution from the image of the $p=0$ element, while the third term represents the contribution from the rest of the image array elements. Also it is interesting to note that the function $S_n(\delta_x)$ depends only on the array lattice parameters and array phasing δ_x , while all other terms in Eq. (4-18b) depend on the geometry of the coaxial monopole element in the parallel plate waveguide.

From the above discussion, it is evident that Eq. (4-18b) for $E_z(a, z)$ can be applied to the following four geometrical configurations distinguished solely by the structure factors $S_n(\delta_x)$:

1. a single monopole in an infinite parallel plate waveguide.

$$S_n(\delta_x) = 0; \quad (4-19a)$$

2. a single monopole in a semi-infinite parallel plate waveguide.

$$S_n(\delta_x) = -H_0^{(2)}(2\kappa_n s); \quad (4-19b)$$

3. an infinite linear array of monopole elements in an infinite parallel plate waveguide.

$$S_n(\delta_x) = 2 \sum_{p=1}^{\infty} H_0^{(2)}(\kappa_n p d) \cos p \delta_x; \quad (4-19c)$$

4. an infinite linear array of monopole elements in a semi-infinite parallel plate waveguide for which S_n is given by Eq. (4-18c).

4.3 Probe Current, $J_z(z)$

The unknown probe current density $J_z(z)$ in Eq. (4-18b) will be determined in terms of $V_0(z=0^-)$ from an integral equation with the requirement that the total axial electric field $E_z(a,z)$ vanishes on the probe surface.

To do that, we expand the probe current density J_z into the series

$$J_z(z) = \sum_{j=1}^J c_j \psi_j(z), \quad 0 \leq z \leq l \quad (4-20a)$$

where c_j are the yet-undetermined expansion coefficients and

$$\psi_j(z) = \sin \left[\frac{\pi}{2l} (2j-1) (z-l) \right], \quad j=1,2,\dots,J. \quad (4-20b)$$

The coefficients c_j will be determined from the boundary condition

$$E_z(a,z) = 0, \quad 0 \leq z \leq l \quad (4-21a)$$

in the sense

$$\int_{z=0}^l E_z(a,z) \psi_i(z) dz = 0, \quad i=1,2,\dots, I=J. \quad (4-21b)$$

The $E_z(a,z)$ is given by Eq. (4-18b). For simplicity of presentation we rewrite this relation in the form

$$E_z(a,z) = jKV_0(z=0^-) \sum_{n=0}^{\infty} [R_n - P_n I'_n] C_n(z) \quad (4-22)$$

where

$$R_n = \epsilon_n J_0(\kappa_n a) [H_n + J_n S_n(\delta_x)] \quad (4-22b)$$

$$P_n = \epsilon_n \left[1 - \left(\frac{n\pi}{kh} \right)^2 \right] J_0(\kappa_n a) [H_0^{(2)}(\kappa_n a) + J_0(\kappa_n a) S_n(\delta_x)] \quad (4-22c)$$

and

$$I'_n = -j \frac{k Z_0 2\pi a}{V_0(z=0^-)} I_n \quad (4-22d)$$

with

$$Z_0 = \frac{\zeta_0}{2\pi} \ln \frac{b}{a}. \quad (4-22e)$$

As defined by Eq. (4-6e), I_n is

$$I_n = \int_{z=0}^l J_z(z) C_n(z) dz \quad (4-23a)$$

where J_z is the active probe current or, using Eq. (4-20a)

$$I_n = \sum_{j=1}^J c_j \int_{z=0}^l \psi_j C_n(z) dz. \quad (4-23b)$$

Substituting Eq. (4-23b) into Eq. (4-22d),

$$I'_n = \sum_{j=1}^J c'_j l_{jn} \quad (4-24a)$$

where

$$c'_j = -j \frac{Z_0 2\pi a}{V_0(z=0^-)} c_j \quad (4-24b)$$

and

$$l_{jn} = k \int_{z=0}^l \psi_j(z) C_n(z) dz. \quad (4-24c)$$

The integral in Eq. (4-24c) is evaluated for $\psi_j(z)$ as given by Eq. (4-20b). The result is

$$l_{jn} = \begin{cases} -2 \frac{(2j-1)\lambda}{2l} & , \frac{(2j-1)\lambda}{2l} \neq \frac{n\lambda}{h} \\ \left[\frac{(2j-1)\lambda}{2l} \right]^2 - \left(\frac{n\lambda}{h} \right)^2 & \\ -\pi \frac{l}{\lambda} (-1)^{j-1} & , \frac{(2j-1)\lambda}{2l} = \frac{n\lambda}{h} \end{cases} \quad (4-25)$$

Finally, substituting Eq. (4-24a) into Eq. (4-22a) and subsequently Eq. (4-22a) into Eq. (4-21b), having in mind (4-24c), we obtain

$$\sum_{n=0}^{\infty} \left[R_n - P_n \sum_{j=1}^J c'_j l_{jn} \right] l_{jn} = 0. \quad (4-26)$$

This relation represents the following system of linear inhomogeneous equations for determining the unknown monopole current expansion coefficients c_j :

$$\sum_{j=1}^J A_{ij} c'_j = B_i \quad (4-27a)$$

where

$$A_{ij} = \sum_{n=0}^{\infty} P_n l_{in} l_{jn} \quad (4-27b)$$

and

$$B_i = \sum_{n=0}^{\infty} R_n l_{in} \quad (4-27c)$$

4.4 Total Magnetic Field in the Aperture, $H_{\phi}(a \leq \rho \leq b, z = 0^+)$

Once the probe current $J_z(z)$ is known, the total magnetic field in the aperture $H_{\phi}(a \leq \rho \leq b, z = 0^+)$ of the reference element ($\rho = 0$) is simply found as a vector sum of the fields $H_{\phi 0}(\rho, z)$ from each individual monopole and its image. The simplest way to proceed is to first evaluate the vector potential $A_z(a \leq \rho \leq b, z = 0^+)$ which is a scalar relation and hence much simpler than the vector relation. Then, the total magnetic field is readily found from $A_z(a \leq \rho \leq b, z = 0^+)$ using

$$H(a \leq \rho \leq b, z = 0^+) = \mu_0 H_{\phi}(a \leq \rho \leq b, z = 0^+) = \frac{1}{\mu_0} \nabla \times z_0 A_z(a \leq \rho \leq b, z = 0^+). \quad (4-28)$$

The procedure follows that of Section 4.2 and is illustrated below. Using the notation of Figure 4-5, the vector potential $A_z(a \leq \rho \leq b, \phi, z)$ is

$$\begin{aligned}
 A_z(a \leq \rho \leq b, \phi, z) = & A_{z0}(\rho, z) + \sum_{p=-\infty}^{\infty} A_{z0}(|\rho - \rho_p|, z) e^{-j p \delta_x} \\
 & + \sum_{p=-\infty}^{\infty} A_{z0}(|\rho - \rho_p + y_0 2s|, z) e^{-j(p \delta_x + \pi)}. \tag{4-29}
 \end{aligned}$$

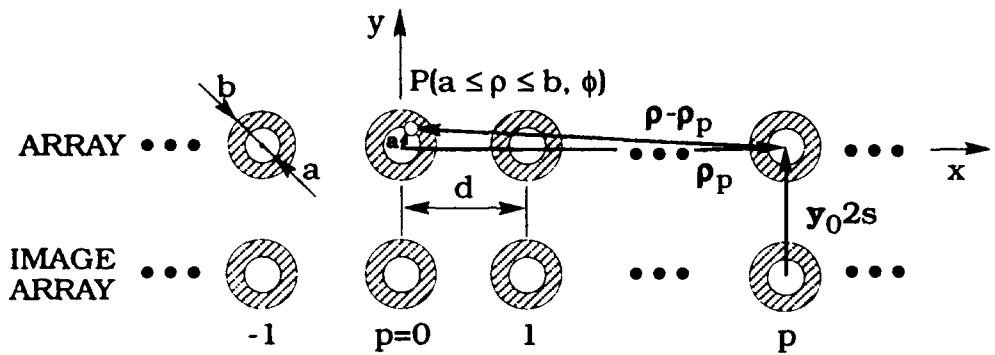


Figure 4-5. Geometry of Linear Array and its Image for Evaluation of $A_z(a \leq \rho \leq b, z = 0^+)$ (Top View)

As shown in Section 4.1.1 the vector potential $\mathbf{A}_0(\rho, z) = z_0 A_{z0}(\rho, z)$ due to a single monopole in an infinite parallel plate waveguide is

$$A_{z0}(\rho, z) = A_{z0}^a(\rho, z) + A_{z0}^p(\rho, z) \tag{4-30}$$

where $A_{z0}^a(\rho, z)$ and $A_{z0}^p(\rho, z)$ are given by Eqs. (4-3b) and (4-3c), respectively. Substituting Eqs. (4-3) into Eq. (4-29), we have

$$\begin{aligned}
A_z(a \leq \rho \leq b, \phi, z) = & -\frac{K\mu_0 V_0(z=0^-)}{k \zeta_0} \left\{ \sum_{n=0}^{\infty} \frac{\epsilon_n}{1 - \left(\frac{n\pi}{kh}\right)^2} C_n(z) \left[-j \frac{2}{\pi} \ln \rho \right. \right. \\
& \left. \left. + J_0(\kappa_n \rho) H_0^{(2)}(\kappa_n b) - H_0^{(2)}(\kappa_n \rho) J_0(\kappa_n a) \right] \right. \\
& \left. + \sum_{n=0}^{\infty} \frac{\epsilon_n}{1 - \left(\frac{n\pi}{kh}\right)^2} C_n(z) J_n \left[\sum_{p=-\infty}^{\infty} H_0^{(2)}(\kappa_n |\rho - \rho_p|) e^{jp\delta_x} + \sum_{p=-\infty}^{\infty} H_0^{(2)}(\kappa_n |\rho - \rho_p + y_0 2s|) e^{-j(p\delta_x + \pi)} \right] \right. \\
& \left. - \sum_{n=0}^{\infty} \epsilon_n C_n(z) I'_n J_0(\kappa_n a) H_0^{(2)}(\kappa_n \rho) - \sum_{n=0}^{\infty} \epsilon_n C_n(z) I'_n J_0(\kappa_n a) \right. \\
& \left. \left. \left[\sum_{p=-\infty}^{\infty} H_0^{(2)}(\kappa_n |\rho - \rho_p|) e^{jp\delta_x} + \sum_{p=-\infty}^{\infty} H_0^{(2)}(\kappa_n |\rho - \rho_p + y_0 2s|) e^{-j(p\delta_x + \pi)} \right] \right] \right\} \quad (4-31)
\end{aligned}$$

where relation (4-22d) has been used. In Eq. (4-31), I'_n is given in terms of known current expansion coefficients by Eq. (4-24a).

To impose continuity of the total magnetic field in the coaxial aperture it is essential to represent the total tangential field $H_\phi(a \leq \rho \leq b, z = 0^+)$ with respect to the reference element $p = 0$. To that end, as in Section 4.2, with the aid of the Addition Theorem for Hankel functions, we re-expand the vector potential $A_{z0}(|\rho - \rho_p|, z)$ and $A_{z0}(|\rho - \rho_p + y_0 2s|, z)$ in Eq. (4-29) about a cylindrical axis centered at the reference element. The assumption of a rotationally symmetric aperture field and use of appendix D and Figure 4-6, lets us write

$$H_0^{(2)}(\kappa_n |\rho - \rho_p|) \approx J_0(\kappa_n \rho) H_0^{(2)}(\kappa_n |p| a) \quad (4-32a)$$

$$H_0^{(2)}(\kappa_n |\rho - \rho_p + y_0 2s|) \approx J_0(\kappa_n \rho) H_0^{(2)}\left(\kappa_n \sqrt{(pd)^2 + (2s)^2}\right). \quad (4-32b)$$

Substituting Eq. (4-32a) into Eq. (4-31), one obtains

$$\begin{aligned}
 A_z(a \leq \rho \leq b, z) = & -\frac{K\mu_0 V_0(z=0^-)}{k\zeta_0} \left\{ \sum_{n=0}^{\infty} \frac{\epsilon_n}{1 - \left(\frac{n\pi}{kh}\right)^2} C_n(z) \right. \\
 & \left[-j \frac{2}{\pi} \ln \rho + J_0(\kappa_n \rho) H_0^{(2)}(\kappa_n b) - H_0^{(2)}(\kappa_n \rho) J_0(\kappa_n a) \right] + \sum_{n=0}^{\infty} \frac{\epsilon_n}{1 - \left(\frac{n\pi}{kh}\right)^2} C_n(z) J_n J_0(\kappa_n \rho) \\
 & \left[2 \sum_{p=1}^{\infty} H_0^{(2)}(\kappa_n p d) \cos p \delta_x - H_0^{(2)}(2\kappa_n s) - 2 \sum_{p=1}^{\infty} H_0^{(2)}\left(\kappa_n d \sqrt{p^2 + \left(\frac{2s}{d}\right)^2}\right) \cos p \delta_x \right] \\
 & - \sum_{n=0}^{\infty} \epsilon_n C_n(z) I'_n J_0(\kappa_n a) H_0^{(2)}(\kappa_n \rho) - \sum_{n=0}^{\infty} \epsilon_n C_n(z) I'_n J_0(\kappa_n a) J_0(\kappa_n \rho) \\
 & \left. \left[2 \sum_{p=1}^{\infty} H_0^{(2)}(\kappa_n p d) \cos p \delta_x - H_0^{(2)}(2\kappa_n s) - 2 \sum_{p=1}^{\infty} H_0^{(2)}\left(\kappa_n d \sqrt{p^2 + \left(\frac{2s}{d}\right)^2}\right) \cos p \delta_x \right] \right\} \quad (4-33)
 \end{aligned}$$

where Eqs. (4-17b) to (4-17d) have been used. This relation can be re-written in the form

$$\begin{aligned}
 A_z(a \leq \rho \leq b, z) = & -\frac{K\mu_0 V_0(z=0^-)}{k\zeta_0} \left\{ \sum_{n=0}^{\infty} \frac{\epsilon_n}{1 - \left(\frac{n\pi}{kh}\right)^2} C_n(z) \right. \\
 & \left[-j \frac{2}{\pi} \ln \rho + J_0(\kappa_n \rho) H_0^{(2)}(\kappa_n b) - H_0^{(2)}(\kappa_n \rho) J_0(\kappa_n a) + I_n J_0(\kappa_n \rho) S_n(\delta_x) \right]
 \end{aligned}$$

$$\left. - \sum_{n=0}^{\infty} \epsilon_n C_n(z) I'_n J_0(\kappa_n a) [H_0^{(2)}(\kappa_n \rho) + J_0(\kappa_n \rho) S_n(\delta_x)] \right\} \quad (4-34)$$

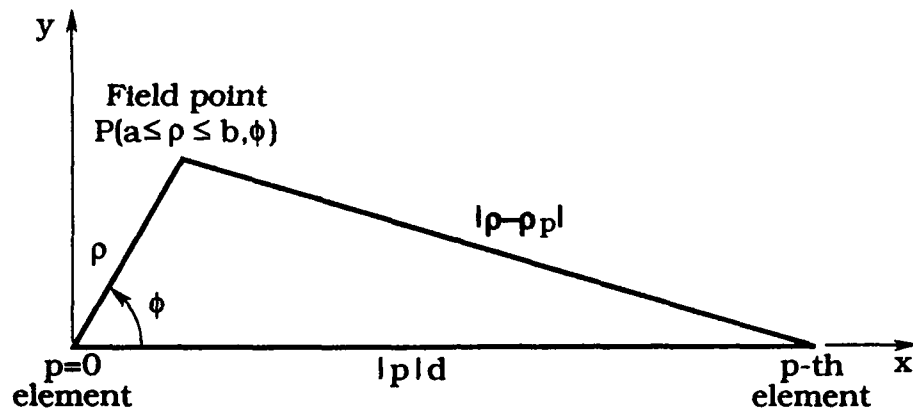


Figure 4-6. Triangle Pertaining to Addition Theorem for Hankel Functions $H_0^{(2)}(\kappa_n |\rho - \rho_p|)$

where the structure factor, $S_n(\delta_x)$ is defined in Eq. (4-18c). It should be mentioned that, as in Section 4.2, the first sum in Eq. (4-34) represents the aperture field contribution while the second sum represents the probe contribution to the total vector potential in the parallel plate region $a \leq \rho \leq b$. The first three terms in the first bracket and the first term in the second bracket represent the self-contribution due to the element ($p = 0$), while the forth term in the first bracket and the second term in the second bracket, which are proportional to $S_n(\delta_x)$, represent contributions due to the rest of the array elements ($|p| \geq 1$) and all elements of the image array. Thus, Eq. (4-34) also applies to four geometrical configurations specified by $S_n(\delta_x)$ in Eqs. (4-18c) and (4-19a) to (4-19c).

The expression for $H_\phi(a \leq \rho \leq b, z = 0^+)$ can be now obtained from Eq. (4-28), which since $\partial/\partial\phi = 0$ may be written as

$$H_\phi(a \leq \rho \leq b, z = 0^+) = -\frac{1}{\mu_0} \frac{\partial A_z(a \leq \rho \leq b, z = 0)}{\partial \rho} \quad (4-35)$$

Substitution of Eq. (4-34) into Eq. (4-35) yields the desired expression for the total magnetic field in the aperture H_ϕ ($a \leq \rho \leq b$, $z = 0^+$).

4.5 Active Admittance, $Y_a(\delta_x)$

The active input admittance $Y_a(\delta_x)$ is the admittance that each element sees when all array elements are excited with the forced aperture voltage V_0 ($z = 0^-$) and progressive phase factor $\exp(-jp\delta_x)$ as shown schematically in Figure 4-7. As already mentioned, $\delta_x = k_{x0} \sin \hat{\phi}_0$ is the inter-element phase increment, $\hat{\phi}_0$ is the scan angle off broadside, $p = 0, \pm 1, \pm 2, \dots$ is the serial element number where $p = 0$ denotes the reference element.

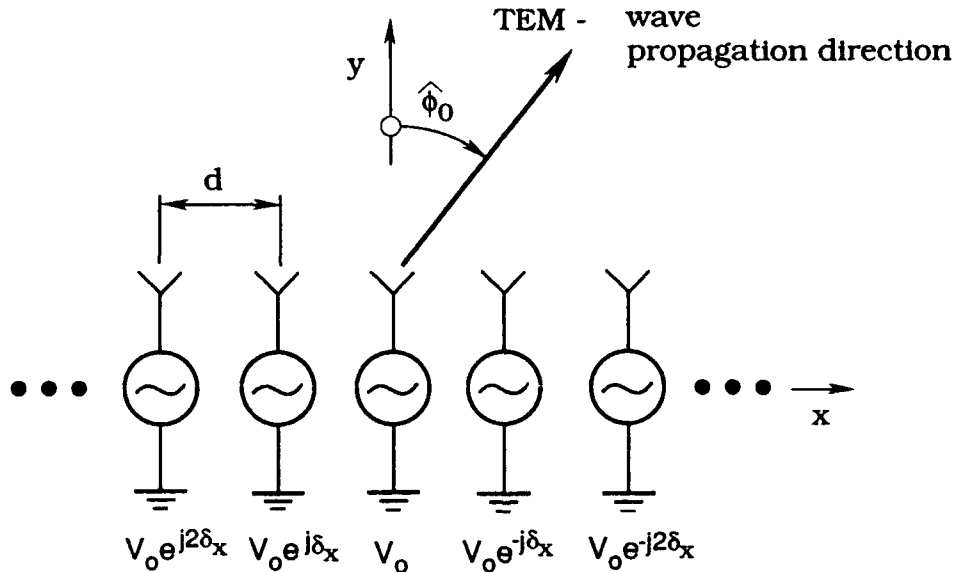


Figure 4-7. Active Infinite Linear Array Pertaining to Uniform-Amplitude, Linear-Phase Progression Excitation

The analysis is based on the continuity condition for the total magnetic field in the aperture which will lead to an expression for $Y_a(\delta_x)$ in terms of the total magnetic field in the aperture H_ϕ ($a \leq \rho \leq b$, $z = 0^+$). Utilizing results from the previous section for H_ϕ ($a \leq \rho \leq b$,

$z = 0^+$), we obtained the desired expression for the active input admittance $Y_a(\delta_x)$ as a function of array geometry and inter-element phasing δ_x , that is, scan angle $\hat{\phi}_0$. The procedure is illustrated below.

For the TEM mode approximation, the field in the aperture of the feed coaxial transmission line can be written in the form

$$\mathbf{E}(\rho, z=0^-) = V_0(z=0^-) \mathbf{e}_0(\rho) \quad (4-36a)$$

$$\mathbf{H}(\rho, z=0^-) = I_0(z=0^-) \mathbf{h}_0(\rho) \quad (4-36b)$$

where the transverse vector mode functions are

$$\mathbf{e}_0 = \rho_0 \frac{1}{\rho \ln \frac{b}{a}} \quad (4-36c)$$

$$\mathbf{h}_0 = \phi_0 \frac{1}{2\pi\rho} \quad (4-36d)$$

Modal voltage and current amplitudes V_0 and I_0 satisfy the transmission-line equations

$$\frac{dV_0(z)}{dz} = -jkZ_c I_0(z) \quad (4-37a)$$

$$\frac{dI_0(z)}{dz} = -jkY_c V_0(z) \quad (4-37b)$$

where the characteristic impedance of the coaxial transmission-line Z_c is

$$Z_c = \frac{1}{Y_c} = \frac{\zeta}{2\pi} \ln \frac{b}{a} \quad (4-37c)$$

with

$$\zeta = \sqrt{\frac{\mu_0}{\epsilon_c}} = \frac{\zeta_0}{\sqrt{\epsilon_r}}. \quad (4-37d)$$

To determine the active admittance $Y_a(\delta_x)$, defined as

$$Y_a(\delta_x) = G_a(\delta_x) + jB_a(\delta_x) = \frac{I_0(z=0^-)}{V_0(z=0^-)} \quad (4-38a)$$

continuity of the magnetic field in the aperture is imposed, that is,

$$\mathbf{H}(\rho, z=0^+) = \mathbf{H}(\rho, z=0^-), \quad a \leq \rho \leq b. \quad (4-38b)$$

Consequently, one may use Eq. (4-36b), to write

$$\mathbf{H}(a \leq \rho \leq b, z=0^+) = I_0(z=0^-) \mathbf{h}_0(\rho) \quad (4-39a)$$

or

$$\mathbf{H}(a \leq \rho \leq b, z=0^+) \cdot \mathbf{h}_0(\rho) = I_0(z=0^-) |\mathbf{h}_0(\rho)|^2 \quad (4-39b)$$

where \mathbf{h}_0 is given by Eq. (4-36d). Since \mathbf{H} above is entirely ϕ -directed [$\mathbf{H}(a \leq \rho \leq b, z = 0^+) = \Phi_0 \mathbf{H}_\phi (a \leq \rho \leq b, z = 0^+)$] [see Eqs. (4-28) and (4-35)], integration of Eq. (4-39b) over the coaxial aperture domain with $dS = \rho d\rho d\phi$, yields

$$\int_{\phi=0}^{2\pi} \int_{\rho=a}^b H_\phi(a \leq \rho \leq b, z=0^+) \frac{1}{2\pi\rho} dS = I_0(z=0^-) \int_{\phi=0}^{2\pi} \int_{\rho=a}^b \frac{1}{4\pi^2 \rho^2} dS \quad (4-40a)$$

from which,

$$\int_{\rho=a}^b H_\phi(a \leq \rho \leq b, z=0^+) d\rho = \frac{I_0(z=0^-)}{2\pi} \ln \frac{b}{a}. \quad (4-40b)$$

Thus, the input active admittance can be written as

$$Y_a(\delta_x) = \frac{I_0(z=0^-)}{V_0(z=0^-)} = \frac{2\pi}{V_0(z=0^-) \ln \frac{b}{a}} \int_{\rho=a}^b H_\phi(a \leq \rho \leq b, z=0^+) d\rho. \quad (4-41)$$

In view of Eq. (4-35), the integral in Eq. (4-41) can be expressed in terms of the total vector potential in the aperture as

$$\int_{\rho=a}^b H_\phi(a \leq \rho \leq b, z=0^+) d\rho = -\frac{1}{\mu_0} A_z(a \leq \rho \leq b, z=0^+) \Big|_{\rho=a}^b. \quad (4-42)$$

Consequently, substituting A_z in Eq. (4-34) into Eq. (4-42), we have

$$\begin{aligned} \int_{\rho=a}^b H_\phi(a \leq \rho \leq b, z=0^+) d\rho &= \frac{KV_0(z=0^-)}{k\zeta_0} \left\{ \sum_{n=0}^{\infty} \frac{\epsilon_n}{\left[1 - \left(\frac{n\pi}{kh}\right)^2\right]} \right. \\ &\quad \left[-j\frac{2}{\pi} \ln \frac{b}{a} + J_n H_0^{(2)}(\kappa_n b) - H_n J_0(\kappa_n a) + J_n^2 S_n(\delta_x) \right] \\ &\quad \left. - \sum_{n=0}^{\infty} \epsilon_n J'_n J_0(\kappa_n a) [H_n + J_n S_n(\delta_x)] \right\} \end{aligned} \quad (4-43)$$

where the functions J_n and H_n are defined in Eq. (4-5i) and (4-5j), respectively. Finally, substituting Eq. (4-43) into (4-41), the active input admittance of a coaxially-fed monopole in an infinite linear array radiating into a semi-infinite parallel plate region is

$$Y_a(\delta_x) \approx \frac{1}{4Z_0 \frac{h}{\lambda} \ln \frac{b}{a}} \left\{ \sum_{n=0}^{\infty} \frac{\epsilon_n}{\left[1 - \left(\frac{n\pi}{kh} \right)^2 \right]} \left[-j \frac{2}{\pi} \ln \frac{b}{a} + J_n H_0^{(2)}(\kappa_n b) - H_n J_0(\kappa_n a) + J_n^2 S_n(\delta_x) \right] \right. \\ \left. - \sum_{n=0}^{\infty} \epsilon_n I'_n J_0(\kappa_n a) [H_n + J_n S_n(\delta_x)] \right\}. \quad (4-44)$$

All terms in Eq. (4-44) have been already defined, but for convenience we list them below:

- k: free-space wave number, $k=2\pi/\lambda$
- λ : free-space wavelength
- a: probe radius and inner radius of coaxial transmission line; $a \ll \lambda$
- b: outer radius of coaxial transmission line; $b \ll \lambda$
- l: probe length
- d: inter-element spacing
- s: distance between probe and conducting "back-plane"; $s \approx \lambda/4$
- h: height of a parallel plate waveguide ($h < \lambda/2$ so that only TEM mode propagates)
- Z_0 : characteristic impedance of the free-space coaxial transmission line

$$Z_0 = \frac{\zeta_0}{2\pi} \ln \frac{b}{a} \approx 60 \ln \frac{b}{a} \quad (4-45b)$$

ζ_0 : free-space intrinsic impedance

$$\zeta_0 = \sqrt{\frac{\mu_0}{\epsilon_0}} = 376.7 \Omega \approx 120 \pi \Omega \quad (4-45c)$$

ϵ_n : (Newmann's number) an integer defined by

$$\epsilon_n = \begin{cases} 1, & n=0 \\ 2, & n \geq 1 \end{cases} \quad (4-45d)$$

κ_n : propagation constants of radial modes in parallel plate region

$$\kappa_n = k \sqrt{1 - \left(\frac{n\pi}{kh}\right)^2}, \quad \text{Im}\{\kappa_n\} \leq 0 \quad (4-45e)$$

$J_0(\kappa_n a)$: Bessel function of the first kind, zero-th order and argument $\kappa_n a$

$J_0(\kappa_n b)$: Bessel function of the first kind, zero-th order and argument $\kappa_n b$

$H_0^{(2)}(\kappa_n a)$: Hankel function of the second kind, order zero and of argument $\kappa_n a$

$H_0^{(2)}(\kappa_n b)$: Hankel function of the second kind, order zero and of argument $\kappa_n b$

J_n : function defined as

$$J_n = J_0(\kappa_n b) - J_0(\kappa_n a) \quad (4-45f)$$

H_n : function defined as

$$H_n = H_0^{(2)}(\kappa_n b) - H_0^{(2)}(\kappa_n a) \quad (4-45g)$$

I'_n : function defined as

$$I'_n = \sum_{j=1}^J c'_j I_{jn} \quad (4-45h)$$

$J=I$: total number of terms in probe current expansion series

I_{jn} : function defined as

$$I_{jn} = \begin{cases} -2 \frac{\frac{(2j-1)\lambda}{2l}}{\left[\frac{(2j-1)\lambda}{2l} \right]^2 - \left(\frac{n\lambda}{h} \right)^2} & , \frac{(2j-1)\lambda}{2l} \neq \frac{n\lambda}{h} \\ -\pi \frac{l}{\lambda} (-1)^{j-1} & , \frac{(2j-1)\lambda}{2l} = \frac{n\lambda}{h} \end{cases} \quad (4-45i)$$

c'_j : current expansion coefficients determined from system of equations

$$\sum_{j=1}^J A_{ij} c'_j = B_i, \quad i,j = 1, 2, \dots, I=J \quad (4-45j)$$

A_{ij} : matrix coefficient defined by

$$A_{ij} = \sum_{n=0}^{\infty} \epsilon_n \left[1 - \left(\frac{n\pi}{kh} \right)^2 \right] J_0(\kappa_n a) \left[H_0^{(2)}(\kappa_n a) + J_0(\kappa_n a) S_n(\delta_x) \right] I_{in} I_{jn} \quad (4-45k)$$

B_i : vector coefficients defined by

$$B_i = \sum_{n=0}^{\infty} \epsilon_n J_0(\kappa_n a) \left[H_n + J_n S_n(\delta_x) \right] I_{in} \quad (4-45l)$$

When high accuracy for $Y_a(\delta_x)$ is not required, it is sufficient to consider a single current term in Eq. (4-45h). In this special case, $I = J = 1$ and consequently

$$I'_n = c'_1 I_{1n} \quad (4-45m)$$

where

$$\iota_{1n} = \begin{cases} -2 \frac{\frac{\lambda}{2l}}{\left(\frac{\lambda}{2l}\right)^2 - \left(\frac{n\lambda}{h}\right)^2} & , \frac{\lambda}{2l} \neq \frac{n\lambda}{h} \\ -\pi \frac{l}{\lambda} & , \frac{\lambda}{2l} = \frac{n\lambda}{h} \end{cases} \quad (4-46b)$$

and

$$c'_1 = \frac{B_1}{A_{11}} \quad (4-46c)$$

with

$$A_{11} = \sum_{n=0}^{\infty} \epsilon_n \left[1 - \left(\frac{n\pi}{kh} \right)^2 \right] J_0(\kappa_n a) \left[H_0^{(2)}(\kappa_n a) + J_0(\kappa_n a) S_n(\delta_x) \right] \iota_{1n}^2 \quad (4-46d)$$

$$B_1 = \sum_{n=0}^{\infty} \epsilon_n J_0(\kappa_n a) \left[H_n + J_n S_n(\delta_x) \right] \iota_{1n} \quad (4-46e)$$

Based on analysis and discussions in Sections 4.2 and 4.4, it is evident that Eq. (4-44) can be directly applied to the following four geometrical configurations specified solely by structure factor $S_n(\delta_x)$:

1. a single monopole in an infinite parallel plate waveguide

$$S_n(\delta_x) = 0; \quad (4-47a)$$

2. a single monopole in a semi-infinite parallel plate waveguide

$$S_n(\delta_x) = -H_0^{(2)}(2\kappa_n s); \quad (4-47b)$$

3. an infinite linear array of monopole elements in an infinite parallel plate waveguide

$$S_n(\delta_x) = 2 \sum_{p=1}^{\infty} H_0^{(2)}(\kappa_n p d) \cos p \delta_x \quad (4-47c)$$

4. an infinite linear array of monopole elements in a semi-infinite parallel plate waveguide

$$S_n(\delta_x) = 2 \sum_{p=1}^{\infty} H_0^{(2)}(\kappa_n p d) \cos p \delta_x - H_0^{(2)}(2 \kappa_n s) - 2 \sum_{p=1}^{\infty} H_0^{(2)}\left(\kappa_n d \sqrt{p^2 + \left(\frac{2s}{d}\right)^2}\right) \cos p \delta_x \quad (4-47d)$$

p : integer, denotes element number

δ_x : phase increment between two neighboring elements.

The rate of convergence of \sum_p is predominantly determined by the behavior of $H_0^{(2)}(\kappa_n p d)$ and $H_0^{(2)}\left(\kappa_n d \sqrt{p^2 + \left(\frac{2s}{d}\right)^2}\right)$ for large p , which is proportional to $\frac{1}{\sqrt{p}}$. The slow convergence of this series with respect to the index p was accelerated as described in Appendix E.

Note that Eq. (4-44) can be also applied to above mentioned four geometries with coaxially-fed annular aperture elements simply by setting $I_n' = 0$, since in this case probe length $l = 0$.

With the probe admittance, $Y_a(\delta_x)$ defined, we can now evaluate the active reflection coefficient of the array, $\Gamma_a(\delta_x)$, as well as the scattering coefficients between array elements. The final two sections of this chapter show how those quantities are derived.

4.6 Active Reflection Coefficient, $\Gamma_a(\delta_x)$

To improve the radiation efficiency it is necessary to match the array element to the TEM coaxial feed-line. The active reflection coefficient referenced to the coaxial aperture plane is

$$\Gamma_a(\delta_x) = \frac{Y_c - Y_a(\delta_x)}{Y_c + Y_a(\delta_x)} \quad (4-48a)$$

where $Y_a(\delta_x)$ is given by Eq. (4-44) and Y_c is the characteristic admittance of the coaxial feed line

$$Y_c = \frac{\sqrt{\epsilon_r}}{Z_0} \quad (4-48b)$$

As will be shown, one can determine the probe length l_c and spacing s_c so that $\Gamma_a = 0$ at a given frequency and a particular phasing.

In the single aperture mode approximation, the aperture field is described by a single parameter - the total coaxial TEM mode voltage V_0 given by

$$V_0 = [1 + \Gamma_a(\delta_x)] V_{inc} \quad (4-49)$$

where V_{inc} is the incident TEM mode voltage in the aperture.

4.7 Coupling (Scattering) Coefficients, S^p

The coupling coefficient between two monopole elements of the infinite linear array in a parallel plate waveguide, for example, between the reference element $p = 0$ and $p - th$ element is defined as

$$S^{0p} = S^p = \frac{V_{rec}^p}{V_{inc}^0} \quad (4-50)$$

where V_{inc}^0 is the modal voltage of the incident TEM mode in the coaxial-feed line ($p = 0$) and V_{rec}^p is received TEM mode voltage in the coaxial transmission line of the receiving ($p - th$) element. All monopole elements except the excited one ($p = 0$) are match-terminated as is shown schematically in Figure 4-8.

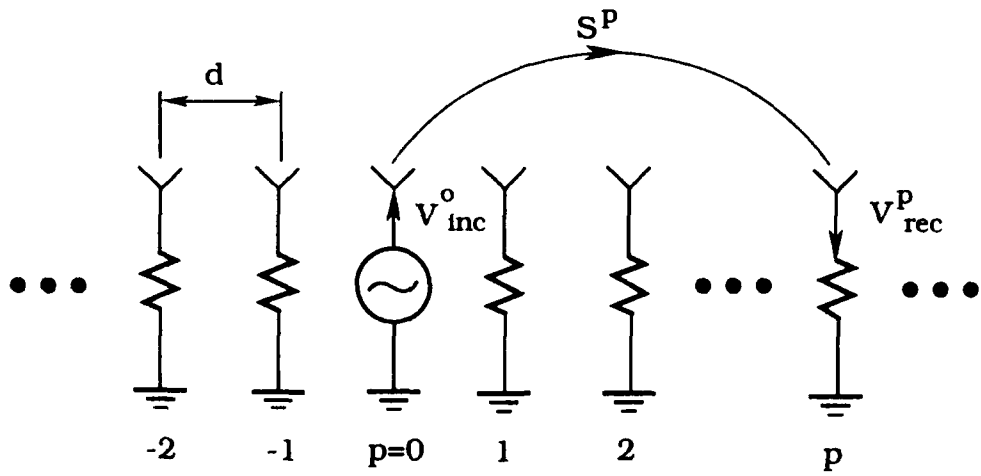


Figure 4-8. Infinite Linear Array Pertaining to the Definition of Coupling (Scattering) Coefficients

The coupling (scattering) coefficients S^p may be related to the active reflection coefficients, defined in the previous section, with the usual relation

$$\Gamma_a(k_{x0}) = \sum_{p=-\infty}^{\infty} S^p e^{jk_{x0}pd} \quad (4-51a)$$

which upon Fourier inversion yields

$$S^p = \frac{d}{2\pi} \int_{-\pi/d}^{\pi/d} \Gamma_a(k_{x0}) e^{-jk_{x0}pd} dk_{x0}. \quad (4-51b)$$

Since $\Gamma_a(k_{x0})$ is an even function of k_{x0} , we write

$$S^p = \frac{d}{\pi} \int_0^{\pi/d} \Gamma_a(k_{x0}) \cos(k_{x0}pd). \quad (4-52)$$

5. FAR FIELD PATTERN OF THE SINGLE MONPOLE IN AN INFINITE AND SEMI-INFINITE PARALLEL PLATE REGION

In this chapter we shall evaluate far-zone field $E_{z0}(\rho)$ due to a single monopole radiating into an infinite and semi-infinite parallel plate region. Throughout this and the following chapter it is assumed that $h < \lambda/2$, which is adequate for most practical applications. In this case only the TEM mode propagates in the parallel plate region.

5.1 Far Field $E_{z0}(\rho, \phi)$ Represented in Terms of Radial Modes

The simple analysis is based on expressions derived in the previous two chapters for the electric field and reflection coefficient of a single monopole in an infinite and semi-infinite parallel plate region.

We begin with the expression for electric field due to a single monopole defined in Section 4.1.2 as [see also Eq. (4-9)]

$$E_{z0}(\rho) = E_{z0}^a(\rho) + E_{z0}^p(\rho) \quad (5-1)$$

where E_{z0}^a and E_{z0}^p are defined by Eqs. (4-5c) and (4-6c), respectively. Since $h < \lambda/2$, only the $n=0$ terms in the respective sums contribute to the far field. Therefore, in this case, one has

$$E_{z0}^a(\rho) \approx jKV_0(z=0^-) J_0 H_0^{(2)}(k\rho), \quad k\rho \gg 1 \quad (5-2a)$$

$$E_{z0}^p(\rho) \approx -jKV_0(z=0^-) I'_0 J_0(k\rho) H_0^{(2)}(k\rho), \quad k\rho \gg 1 \quad (5-2b)$$

and consequently,

$$E_{z0}(\rho) \approx jKV_0(z=0^-) [J_0 - I'_0 J_0(k\rho)] H_0^{(2)}(k\rho), \quad k\rho \gg 1. \quad (5-2c)$$

In Eq. (5-2), from Eqs. (4-5d) and (4-45f) to (4-45i) we have

$$K = \frac{\pi}{2h \ln \frac{b}{a}} \quad (5-3a)$$

$$J_0 = J_0(kb) - J_0(ka) \quad (5-3b)$$

and

$$I'_0 = \sum_{j=1}^J c'_j I_{j0} \quad (5-3c)$$

where I_{j0} is given by Eq. (4-45i) with $n = 0$ and where the probe current expansion coefficients c'_j are computed from the system of equations (4-45j) with $S_n(\delta_x) = 0$ as given by Eq. (4-47a). Furthermore, $V_0(z = 0^-)$ is the total voltage in the coaxial aperture corresponding to the single TEM mode aperture field.

After the propagating TEM mode ($n = 0$), the next higher non-propagating mode in the parallel plate region is TM₁ (defined with respect to the radial direction) represented by the $n = 1$ term in Eqs. (4-5c) and (4-6c). As one can see from these two relations, the radial dependence of this mode is determined by the zero order Modified Bessel function

$K_0(k\rho \sqrt{(\lambda/2h)^2 - 1})$. The function $K_0(x)$ tends to zero as $x \rightarrow \infty$. The first order asymptotic expression for large argument is

$$K_0(x) \sim \sqrt{\frac{\pi}{2x}} e^{-x}. \quad (5-4)$$

The (fast) exponential decay of $K_0(x)$ vs x justifies the single TEM mode far-zone field approximation in Eq. (5-2).

Next we write the expression for the far field $E_{z0}(\rho, \phi)$ due to a single monopole in a semi-infinite parallel plate waveguide. This relation can be easily obtained from Eq. (5-1) by superimposing to it its image contribution, that is,

$$E_{z0}(\rho, \phi) \simeq jKV_0(z=0^-) [J_0 - I'_0 J_0(ka)] [H_0^{(2)}(k\rho) - H_0^{(2)}(k|\rho + y_0/2s|)]. \quad (5-5)$$

Here, as seen from Figure 5-1 in the far zone

$$|\rho + y_0 2s| \approx \rho + 2s \cos \hat{\phi} \quad (5-6)$$

where $\hat{\phi}$ is measured from the y-axis, that is, $\hat{\phi} = \pi/2 - \phi$. Equations (5-3) and (4-45i) apply here as well. The current expansion coefficients c_j are also computed from the system of equations (4-45j) where now $S_n(\delta_x)$ is given by Eq. (4-47b) as

$$S_n(\delta_x) = -H_0^{(2)}(2\kappa_n s). \quad (5-7)$$

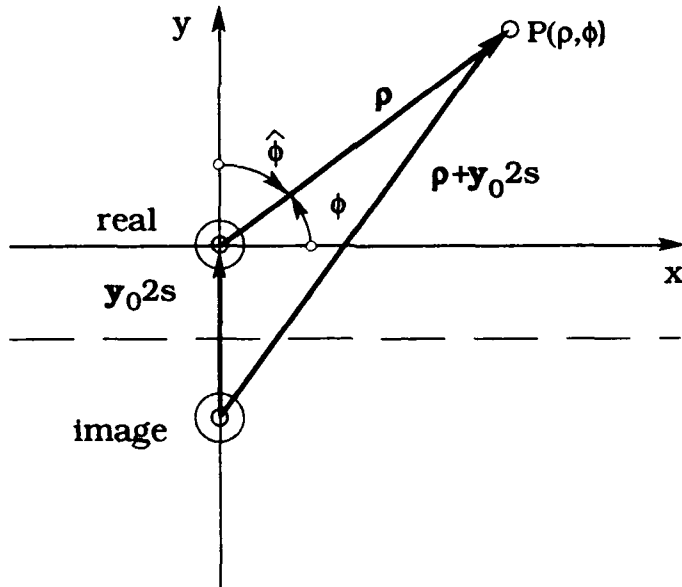


Figure 5-1. Coaxially-fed Monopole and Its Image in an Infinite Parallel Plate Region

For convenience we cast Eqs. (5-2c) and (5-5) into a uniform relation

$$E_{z0}(\rho, \phi) = jKV_0(z=0^-)[J_0 - I'_0 J_0(ka)] [H_0^{(2)}(kp) - U H_0^{(2)}(k|\rho + y_0 2s|)] \quad (5-8a)$$

where U is the unit step function defined as

$$U = \begin{cases} 0; & \text{monopole in an infinite parallel plate region} \\ 1; & \text{monopole in a semi-infinite parallel plate region} \end{cases} \quad (5-8b)$$

As already mentioned I'_0 in Eq. (5-8a) is given by Eq. (5-3c) in terms of l_{j0} and c'_j . The l_{j0} is defined by Eq. (4.45i) while the c'_j are determined from Eq. (4-45j) with S_n as given by Eq. (4-47a) for a single monopole in an infinite parallel plate region and by Eq. (4-47b) for a single monopole in a semi-infinite parallel plate region.

When x is large, the asymptotic approximation for the Hankel function of order zero $H_0^{(2)}(x)$ is

$$H_0^{(2)}(x) \approx \sqrt{\frac{2}{\pi x}} e^{-j(x - \frac{\pi}{4})}. \quad (5-9)$$

Consequently,

$$\begin{aligned} H_0^{(2)}(kp) - U H_0^{(2)}(k\rho + 2ks \cos \hat{\phi}) \\ \approx \sqrt{\frac{2}{\pi kp}} e^{-j(kp - \frac{\pi}{4})} \left[1 - U \sqrt{\frac{1}{1 + \frac{2ks}{kp} \cos \hat{\phi}}} e^{-j2ks \cos \hat{\phi}} \right]. \end{aligned} \quad (5-10)$$

For $2ks \ll kp$ we may use

$$\frac{1}{\sqrt{1+x}} \approx 1 - \frac{x}{2}, \quad x \ll 1 \quad (5-11a)$$

and then

$$\begin{aligned}
 H_0^{(2)}(k\rho) - U H_0^{(2)}(k\rho + 2ks \cos \hat{\phi}) \\
 \approx \sqrt{\frac{2}{\pi k\rho}} e^{-j(k\rho - \frac{\pi}{4})} \begin{cases} 1; & U = 0 \\ e^{-jks \cos \hat{\phi}} \left[2j \sin (ks \cos \hat{\phi}) + \frac{ks}{k\rho} \cos \hat{\phi} e^{-jks \cos \hat{\phi}} \right]; & U = 1. \end{cases} \quad (5-11b)
 \end{aligned}$$

For all practical applications $s \leq \lambda/4$ and since $k\rho \gg 1$ in Eq. (5-11b) $ks/k\rho \leq 0$.

Substituting Eq. (5-11b) into Eq. (5-8a), we get the far field due to a single monopole in an infinite ($U=0$) or semi-infinite ($U=1$) parallel plate region as

$$\begin{aligned}
 E_{z0}(\rho, \phi) = jK \sqrt{\frac{2}{\pi k\rho}} V_0(z=0^-) [J_0 - I'_0 J_0(ka)] e^{-j(k\rho - \frac{\pi}{4})} \\
 \begin{cases} 1; & U = 0 \\ 2j \sin (ks \cos \hat{\phi}) e^{-jks \cos \hat{\phi}}; & U = 1. \end{cases} \quad (5-12)
 \end{aligned}$$

The $V_0(z=0^-)$ in Eq. (5-12) can be expressed in terms of the modal voltage of the single TEM mode in the feed coaxial transmission line V_{inc} and the reflection coefficient as

$$V_0(z=0^-) = V_{\text{inc}} [1 + \Gamma_a(z=0^-)]. \quad (5-13)$$

As defined in Section 4.6, the reflection coefficient is

$$\Gamma_a = \frac{Z_a - Z_c}{Z_a + Z_c} \quad (5-14a)$$

where $Z_a = 1/Y_a$ and Z_c is the characteristic impedance of the coaxial feed line

$$Z_c = \frac{Z_0}{\sqrt{\epsilon_r}} \quad (5-14b)$$

with

$$Z_0 = \frac{\zeta_0}{2\pi} \ln \frac{b}{a}. \quad (5-14c)$$

The input impedance $Z_a(z = 0^-)$ is determined from Eq. (4-44) with S_n given by Eqs. (4-47a) and (4-47b) for a monopole in an infinite and a semi-infinite parallel plate waveguide region, respectively.

5.2 Single Monopole Gain Pattern, $g_{z0}^{(e)}$

The normalized gain pattern is

$$G_{z0}(\hat{\phi}) = \frac{P(\rho, \hat{\phi})}{P_0(\rho)} \quad (5-15a)$$

where $P(\rho, \hat{\phi})$ and $P_0(\rho)$ are the power densities at ρ due to a monopole (in an infinite or a semi-infinite parallel plate region) and an isotropic source, respectively defined as

$$P(\rho, \hat{\phi}) = E_{z0} H_{\phi 0}^* = \frac{|E_{z0}|^2}{\zeta_0} \quad (5-16a)$$

and

$$P_0(\rho) = \frac{P_{inc}}{2\pi\rho h}. \quad (5-16b)$$

In Eq. (5-16b), the incident power is

$$P_{inc} = \frac{|V_{inc}|^2}{Z_c}. \quad (5-17)$$

Consequently Eq. (5-15a) becomes

$$G_{z0}(\hat{\phi}) = \frac{|E_{z0}(\rho, \hat{\phi})|^2}{\zeta_0 \frac{P_{inc}}{2\pi\rho h}} = \frac{|E_{z0}(\rho, \hat{\phi})|^2}{|V_{inc}|^2} \frac{Z_c}{\zeta_0} \frac{2\pi\rho h}{2\pi\rho h}. \quad (5-18)$$

Substituting Eq. (5-3a) into Eq. (5-12) and then (5-12) into (5-18) we obtain an explicit relation for the gain pattern, that is,

$$G_{z0}(\hat{\phi}) = \frac{1}{4 \frac{h}{\lambda} \ln \frac{b}{a}} \frac{Z_c}{Z_0} \left| (1 + \Gamma_a) [J_0 - I'_0 J_0(ka)] \right|^2 \begin{cases} 1; & U=0 \\ 4 \sin^2 (ks \cos \hat{\phi}); & U=1 \end{cases} \quad (5-19)$$

Defining the complex field pattern by

$$g_{z0}^{(e)}(\hat{\phi}) = \frac{je^{\frac{j\pi}{4}}}{2\sqrt{2\pi}} \sqrt{\frac{\lambda}{h}} \sqrt{\frac{Z_c}{\zeta_0} \frac{\zeta_0}{Z_0} (1 + \Gamma_a) [J_0 - I'_0 J_0(ka)]} \begin{cases} 1; & U=0 \\ 2j \sin (ks \cos \hat{\phi}) e^{-jks \cos \hat{\phi}}; & U=1 \end{cases} \quad (5-20a)$$

normalized so that

$$|g_{z0}^{(e)}(\hat{\phi})|^2 = G_{z0}(\hat{\phi}). \quad (5-20b)$$

Now Eq. (5-12) can be expressed in the form

$$E_{z0}(\rho, \hat{\phi}) = \frac{1}{\sqrt{2\pi}} \sqrt{\frac{\zeta_0}{Z_c}} \frac{V_{inc}}{\sqrt{h}} \frac{e^{-jk\rho}}{\sqrt{\rho}} g_{z0}^{(e)}(\hat{\phi}). \quad (5-21)$$

Note that the field of a monopole in an infinite parallel plate region is independent of the observation angle $\hat{\phi}$. The phase center of the field is at the axis of the element ($x = 0, y = 0$). For a monopole in a semi-infinite parallel plate region however, the phase of the far field vs observation angle $\hat{\phi}$ is constant with respect to the point ($x = 0, y = -s$). Thus in this case the radiation pattern phase center is on the conducting plane behind the monopole.

In Appendix H we show that $E_{z0}(\rho, \hat{\phi})$ as given by Eq. (5-21) satisfies the conservation of power condition

$$P_{inc} \left(1 - |\Gamma_a|^2 \right) = P_t \quad (5-22a)$$

where

$$P_{\text{inc}} = \frac{|V_{\text{inc}}|^2}{Z_c} \quad (5-22b)$$

is the TEM mode incident power in the feed coaxial transmission line with characteristic impedance Z_c . The input reflection coefficient Γ_a is given by Eq. (5-14a) in terms of the input impedance, which can be computed from Eq. (4-44) with S_n given by Eq. (4-47a) for a single monopole in an infinite parallel plate waveguide and by Eq. (4-47b) for a single monopole in a semi-infinite parallel plate waveguide. Furthermore, in Eq. (5-22a) P_t represents far field radiated power defined as

$$P_t = 2\pi\phi h \operatorname{Re} P(\phi) = 2\pi\phi h \frac{|E_{z0}(\phi)|^2}{\zeta_0} \quad (5-23a)$$

for $U=0$, and

$$P_t = \operatorname{Re} \int_0^\pi \int_0^h \mathbf{E}_0(\phi, \theta) \times \mathbf{H}_0^*(\phi, \theta) \phi d\phi dz = \frac{h}{\zeta_0} \operatorname{Re} \int_0^\pi |E_{z0}(\phi)|^2 \phi d\phi \quad (5-23b)$$

for $U=1$.

6. FAR-FIELD ELEMENT PATTERN OF AN INFINITE ARRAY RADIATING INTO AN INFINITE AND A SEMI-INFINITE PARALLEL PLATE REGION

In this chapter we derive expressions for the far field $E_z^{(e)}(\rho)$ due to a singly excited monopole element in a infinite match-terminated linear array environment radiating into an infinite and a semi-infinite parallel plate region as schematically illustrated in Figure 6-1. As already mentioned in the previous chapter, the distance between the parallel plates h is less than $\lambda/2$ so that only the TEM mode propagates.

The analysis is based on the relation

$$E_z^{(e)}(\rho) = \frac{d}{2\pi} \int_{-\pi/d}^{\pi/d} \hat{E}_z(\rho) dk_{x_0} \quad (6-1)$$

where $\hat{E}_z(\rho)$ is the total far-field of the active array (all elements are excited with uniform amplitude V_0 ($z = 0^-$) and linear phase progression $\delta_x = k_{x_0}d = kd \sin \hat{\phi}_0$) at an observation point $\rho = x_0 \mathbf{x} + y_0 \mathbf{y}$.

Note that $E(\rho)$ as defined in Chapter 4 and $\hat{E}(x,y)$ in this chapter denote the same active array field in the parallel plate region. The E represents the active array field in terms of cylindrical radial modes while the \hat{E} represents the active array field in terms of Floquet modes in the unit cell. Thus, $E_z(\rho, \phi) = \hat{E}_z(x, y)$ where (ρ, ϕ) and (x, y) refer to the same observation point.

The analysis uses three basic steps:

- (1) Obtain the far-field $E_z(\rho)$ by superimposing fields $E_{z0}(\rho)$ from each individual monopole, and, in a semi-infinite parallel plate region, its image.
- (2) To facilitate integration of Eq. (6-1), using Poisson's sum formula, we re-express $E_z(\rho, \phi)$ in terms of Floquet modes in the unit cell. By this means we obtain an expression for $\hat{E}_z(x, y)$.
- (3) Evaluate the integral in Eq. (6-1) by the method of stationary phase.

We shall, of course, expand on this outline and shall analyze each of the steps in great detail.

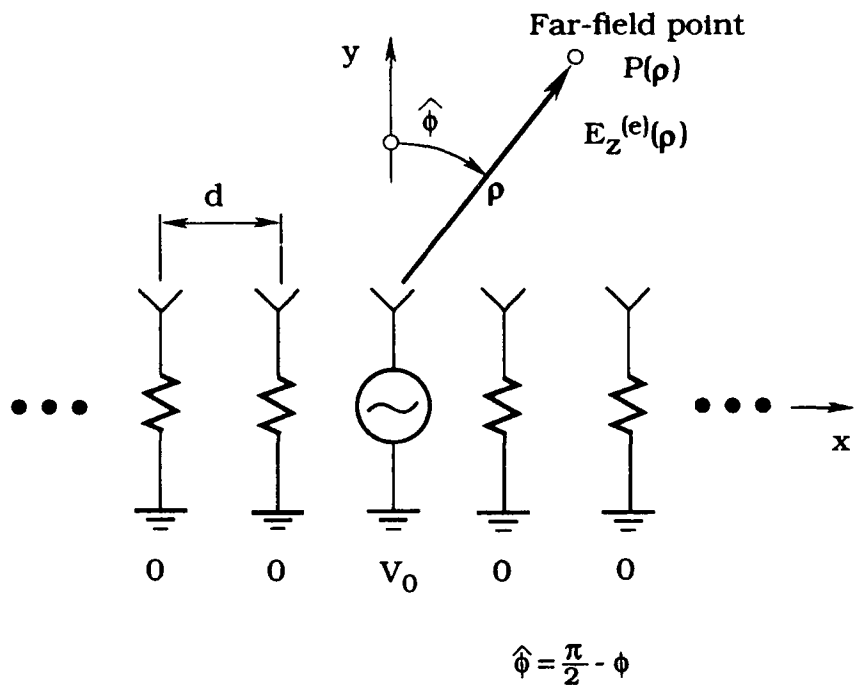


Figure 6-1. Infinite Linear Array Pertaining to Single Element Excitation

6.1 Far Field of the Active Array $E_z(\rho, \phi)$ Represented in Terms of Radial Modes

For the active array excitation, that is, when all elements are excited with uniform amplitude V_0 ($z = 0^-$) and linear phase progression δ_x the total far field $E(\rho, \phi) = z_0 E_z(\rho, \phi)$ can be expressed as a superposition of contributions from an infinite number of single monopoles located at $\rho_p = x_0 pd$ and in a semi-infinite parallel plate region their images located at $\rho_p - y_0 2s$ in a parallel plate waveguide as shown in Figure 6-2.

Thus, for $k\rho \gg 1$, one may write

$$E_z(\rho, \phi) = \sum_{p=-\infty}^{\infty} E_{z0}(|\rho - \rho_p|) e^{-j p \delta_x} + U \sum_{p=-\infty}^{\infty} E_{z0}(|\rho - \rho_p + y_0 2s|) e^{-j(p \delta_x + \pi)} \quad (6-2a)$$

where as stated in Chapter 5, U is the unit step function defined as

$$U = \begin{cases} 0; & \text{for an array in an infinite parallel plate region} \\ 1; & \text{for an array in a semi-infinite parallel plate region} \end{cases} \quad (6-2b)$$

and the electric far field due to a single monopole as defined in Section 4.1.2 is

$$E_{z0}(\rho) = E_{z0}^a(\rho) + E_{z0}^p(\rho). \quad (6-2c)$$

The E_{z0}^a and E_{z0}^p are defined by Eqs. (4-5c) and (4-6c), respectively. Since $h < \lambda/2$, only the $n=0$ terms in the respective sums contribute to the far field. Therefore, in this case

$$E_{z0}^a(\rho) \approx jKV_0(z=0^-) J_0 H_0^{(2)}(k\rho), \quad k\rho \gg 1 \quad (6-3a)$$

$$E_{z0}^p(\rho) \approx -jKV_0(z=0^-) I'_0 J_0(ka) H_0^{(2)}(k\rho), \quad k\rho \gg 1 \quad (6-3b)$$

where as indicated we used $\kappa_0 = k$. In Eq. (6-3), K , J_0 and I'_0 are given by Eq. (5-3) where the probe current expansion coefficients c'_j are computed from the system of Eqs. (4-45j) with $S_n(\delta_x)$ as given by Eq. (4-47c) for an array in an infinite parallel plate region and by Eq. (4-47d) for an array in a semi-infinite parallel plate waveguide. This implies that the probe current in Eq. (6-3b) is not that of a single monopole in an infinite or semi-infinite parallel plate waveguide as in the previous chapter but instead, the current on the probe in the active array environment.

Upon inserting Eqs. (6-3) into Eq. (6-2c), and then Eq. (6-2c) into Eq. (6-2a) using Eq. (4-17b), we obtain

$$E_z(\rho, \phi) \approx jKV_0(z=0^-) [J_0 - I'_0 J_0(ka)] \left[\sum_{p=-\infty}^{\infty} H_0^{(2)}(k|\rho - \rho_p|) e^{-jp\delta_x} - U \sum_{p=-\infty}^{\infty} H_0^{(2)}(k|\rho - \rho_p + y_0 2s|) e^{-jp\delta_x} \right]. \quad (6-4)$$

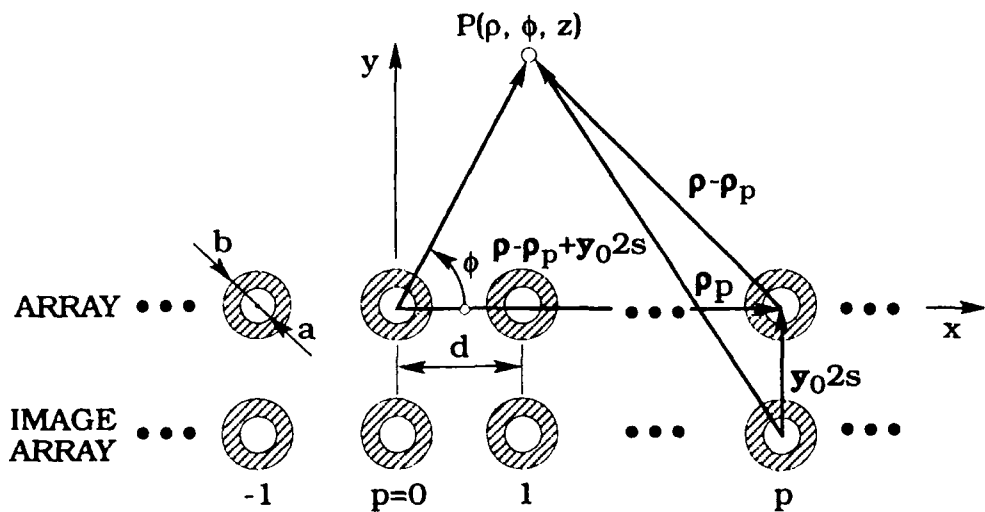


Figure 6-2. Geometry of the Linear Array and its Image for Evaluation of $E_z(p, \phi)$ (Top View) (U=1 case shown)

6.2 Far Field of the Active Array $\hat{E}_z(x, y)$ Represented in Terms of Floquet Modes in a Unit Cell

In the last section we determined the active array field in terms of an infinite sum over all (real and image) array elements. We observe, however, that Eq. (6-4) is not directly applicable in Eq. (6-1) because the relevant integral cannot be evaluated in a closed form.

To avoid this difficulty we re-express Eq. (6-4) in terms of Floquet modes of a rectangular unit cell guide with conducting top and bottom walls, and phase-shift side walls. A typical

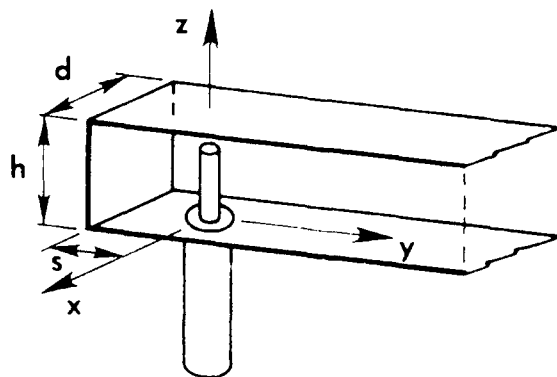


Figure 6-3. Unit Cell Geometry of an Infinite Linear Array of Coaxially-fed Monopoles in a Semi-Infinite Parallel Plate Waveguide

rectangular unit cell, of width d and height h , for an array in a semi-infinite parallel plate waveguide is illustrated in Figure 6-3. The desired representation is accomplished with the aid of the well known Poisson sum formula⁸ :

$$\sum_{p=-\infty}^{\infty} f(2\pi p) = \frac{1}{2\pi} \sum_{m=-\infty}^{\infty} F(m) \quad (6-5a)$$

where

$$F(m) = \int_{-\infty}^{\infty} f(\tau) e^{-jmt} d\tau \quad (6-5b)$$

and

$$\tau = 2\pi p. \quad (6-5c)$$

The analytical procedure is described below

Referring to Eq. (6-4), we first consider the sum

$$\sum_{p=-\infty}^{\infty} H_0^{(2)}(k|\rho - \rho_p|) e^{-jp\delta_x} \quad (6-6a)$$

where, as can be seen in Figure 6-2,

$$|\rho - \rho_p| = \sqrt{(x - pd)^2 + y^2}, \quad p = 0, \pm 1, \dots \quad (6-6b)$$

⁸ Papoulis, A. (1977) *Signal Analysis*, McGraw-Hill, New York.

In view of Eq. (6-5a) we now set

$$f(2\pi p) = H_0^{(2)} \left(k \sqrt{(x-pd)^2 + y^2} \right) e^{-jp\delta_x} \quad (6-7a)$$

in Eq. (6-5b), which, since $p = \tau/2\pi$, then becomes

$$F(m) = \int_{-\infty}^{\infty} H_0^{(2)} \left(k \sqrt{\left(x - \frac{d}{2\pi} \tau \right)^2 + y^2} \right) e^{-j \left(m + \frac{\delta_x}{2\pi} \right) \tau} d\tau. \quad (6-7b)$$

To evaluate Eq. (6-7b), we define a new integration variable

$$x - \frac{d}{2\pi} \tau = -X \quad (6-8a)$$

from which we get

$$\tau = (x + X) \frac{2\pi}{d} \quad (6-8b)$$

and

$$d\tau = \frac{2\pi}{d} dX. \quad (6-8c)$$

We now write

$$F(m) = \frac{2\pi}{d} e^{-j \left(m + \frac{\delta_x}{2\pi} \right) \frac{2\pi}{d} X} \int_{-\infty}^{\infty} H_0^{(2)} \left(k \sqrt{X^2 + y^2} \right) e^{-j \frac{2\pi}{d} \left(m + \frac{\delta_x}{2\pi} \right) X} dX. \quad (6-9)$$

Since

$$\delta_x = k_{x0}d = kd \sin \hat{\phi}_0 \quad (6-10a)$$

we find that

$$F(m) = \frac{2\pi}{d} e^{-j(k_{x0} + \frac{2\pi}{d}m)x} \int_{-\infty}^{\infty} H_0^{(2)}(k\sqrt{x^2 + y^2}) e^{-j(k_{x0} + \frac{2\pi}{d}m)x} dx. \quad (6-10b)$$

Upon using the relation

$$k_{xm} = k_{x0} + \frac{2\pi}{d}m \quad (6-11a)$$

where the k_{xm} are wavenumbers of Floquet modes in a unit cell, we finally obtain

$$F(m) = \frac{2\pi}{d} e^{-jk_{xm}x} \int_{-\infty}^{\infty} H_0^{(2)}(k\sqrt{x^2 + y^2}) e^{-jk_{xm}x} dx. \quad (6-11b)$$

The Fourier integral of the Hankel function in Eq. (6-11b) is evaluated in Appendix F. The result is

$$\int_{-\infty}^{\infty} H_0^{(2)}(k\sqrt{x^2 + y^2}) e^{-jk_{xm}x} dx = 2 \frac{e^{-jk_{m0}y}}{k_{m0}} \quad (6-12a)$$

where

$$k_{m0} = \sqrt{k^2 - k_{xm}^2}, \quad \text{Im}\{k_{m0}\} \leq 0. \quad (6-12b)$$

Thus, from Eqs. (6-11b) and (6-12a) we find that

$$F(m) = \frac{4\pi}{d} e^{-jk_{xm}x} \frac{e^{-jk_{m0}y}}{\kappa_{m0}}. \quad (6-13)$$

Finally, upon inserting Eqs. (6-7a) and (6-13) into Eq. (6-5a) we get

$$\sum_{p=-\infty}^{\infty} H_0^{(2)}(k|\rho - \rho_p|) e^{-jp\delta_x} = \frac{2}{d} \sum_{m=-\infty}^{\infty} e^{-jk_{xm}x} \frac{e^{-jk_{m0}y}}{\kappa_{m0}}. \quad (6-14)$$

The same process may be applied to obtain

$$\sum_{p=-\infty}^{\infty} H_0^{(2)}(k|\rho - \rho_p + y_0 2s|) e^{-jp\delta_x} = \frac{2}{d} \sum_{m=-\infty}^{\infty} e^{-jk_{xm}x} \frac{e^{-jk_{m0}(y+2s)}}{\kappa_{m0}}. \quad (6-15)$$

Here

$$|\rho - \rho_p + y_0 2s| = \sqrt{(x-pd)^2 + (y+2s)^2}. \quad (6-16)$$

Upon combining Eqs. (6-14) and (6-15) we may write

$$\sum_{p=-\infty}^{\infty} H_0^{(2)}(k|\rho - \rho_p|) e^{-jp\delta_x} - U \sum_{p=-\infty}^{\infty} H_0^{(2)}(k|\rho - \rho_p + y_0 2s|) e^{-jp\delta_x}$$

$$= \frac{2}{d} \sum_{m=-\infty}^{\infty} e^{-jk_{xm}x} \frac{e^{-jk_{m0}y}}{\kappa_{m0}} \begin{cases} 1: & U = 0 \\ 2j \sin \kappa_{m0}s e^{-jk_{m0}s}; & U = 1 \end{cases} \quad (6-17)$$

Substituting this identity into Eq. (6-4) we obtain the desired expression for the active electric far field

$$\hat{E}_z(x, y) = j \frac{2KV_0(z=0^-)}{d} [J_0 - I'_0 J_0(ka)]$$

$$\sum_{m=-\infty}^{\infty} e^{-jk_{xm}x} \frac{e^{-jk_{m0}y}}{\kappa_{m0}} \begin{cases} 1: & U = 0 \\ 2j \sin \kappa_{m0}s e^{-jk_{m0}s}; & U = 1 \end{cases} \quad (6-18)$$

Relation (6-18) represents the active array far field in terms of Floquet TE_{m0}^y modes propagating in the y direction in the rectangular unit cell with propagation constants κ_{m0} defined by Eq. (6-12b). From the result just obtained, it is easy to see that, as expected, the active array field is periodic in the x direction.

6.3 Element Pattern, $g_z^{(e)}(\hat{\phi})$

The identity

$$\delta_{0p} = \frac{d}{2\pi} \int_{-\pi/d}^{\pi/d} e^{-jk_{x0}dp} dk_{x0} \quad (p = 0, \pm 1, \dots) \quad (6-19a)$$

where δ_{0p} is the Kronecker delta lets us write the expression for $E_z^{(e)}$ due to the singly excited $p=0$ element in a match terminated array environment as

$$\hat{E}_z^{(e)}(\rho) = \frac{d}{2\pi} \int_{-\pi/d}^{\pi/d} \hat{E}_z(k_{x0}) dk_{x0}. \quad (6-19b)$$

The expression for the active array far field is given by Eq. (6-18), which, for convenience, we rewrite in the form

$$\hat{E}_z(\rho) = \frac{V_0(z=0)}{d} \sum_{m=-\infty}^{\infty} T_m(k_{x0}) e^{-jk_m \cdot \rho} \quad (6-20a)$$

where

$$T_m(k_{x0}) = j2K \left[J_0 - I'_0 J_0(ka) \right] \frac{1}{k_{m0}} \begin{cases} 1; & U = 0 \\ 2j \sin k_{m0} s e^{-jk_{m0}s}; & U = 1 \end{cases} \quad (6-20b)$$

$$k_m = x_0 k_{xm} + y_0 k_{m0} \quad (6-20c)$$

and, as already indicated

$$\rho = x_0 x + y_0 y. \quad (6-20d)$$

Substituting Eq. (6-20a) into (6-19b), we get

$$\hat{E}_z^{(e)}(\rho) = \frac{1}{2\pi} \sum_{m=-\infty}^{\infty} \int_{-\pi/d}^{\pi/d} V_0(k_{x0}) T_m(k_{x0}) e^{-jk_m \cdot \rho} dk_{x0}. \quad (6-21)$$

To evaluate the integral in Eq. (6-21) we introduce the transformation

$$k_{xm} = k_{x0} + \frac{2\pi}{d} m = k u \quad (6-22)$$

whereupon

$$\kappa_{m0}(k_{xm}) = \sqrt{k^2 - k_{xm}^2} = k\sqrt{1-u^2} = \kappa(u) \quad (6-22b)$$

and

$$\mathbf{k}_m \cdot \rho = [\mathbf{x}_0 u + \mathbf{y}_0 \kappa(u)] \cdot \rho = k\rho \left[\frac{x}{\rho} u + \frac{z}{\rho} \kappa(u) \right]. \quad (6-22c)$$

As a result, Eq. (6-21) transforms into

$$E_z^{(e)}(\rho) = \frac{k}{2\pi} \sum_{m=-\infty}^{\infty} \int_{-\pi/d+2\pi m/d}^{\pi/d+2\pi m/d} V_0(u) T_0(u) e^{-j\Omega\psi(u)} du \quad (6-23)$$

where the Floquet relations $V_0(k_{x0}) = V_0(k_{xm})$ [since $\Gamma_a(k_{x0}) = \Gamma_a(k_{xm})$] and $T_m(k_{x0}) = T_0(k_{xm})$ have been invoked. In Eq. (6-23) $\Omega = k\rho$ is the large parameter and

$$T_0(u) = j2K \left[J_0 - I'_0 J'_0(ka) \right] \frac{1}{\kappa(u)} \begin{cases} 1; & U = 0 \\ 2j \sin \kappa(u) s e^{-j\kappa(u)s}; & U = 1 \end{cases} \quad (6-24a)$$

$$\psi(u) = \frac{x}{\rho} u + \frac{y}{\rho} \sqrt{1-u^2}. \quad (6-24b)$$

The sum over the index m in Eq. (6-23) may be further converted into an infinite integral, so that

$$\hat{E}_z^{(e)}(\rho) = \frac{k}{2\pi} \int_{-\infty}^{\infty} V_0(u) T_0(u) e^{-j\Omega\psi(u)} du. \quad (6-25)$$

After a change of spatial variables

$$\frac{x}{\rho} = \sin \hat{\phi} \quad (6-26a)$$

$$\frac{y}{\rho} = \cos \hat{\phi} \quad (6-26b)$$

where $\hat{\phi} = \pi/2 - \phi$. Eq. (6-24b) becomes

$$\psi(u) = u \sin \hat{\phi} + \sqrt{1-u^2} \cos \hat{\phi}. \quad (6-26c)$$

The integral in Eq. (6-25) is asymptotically evaluated by the method of stationary phase (see Appendix G). The result is

$$\hat{E}_z^{(e)}(\rho) \sim \frac{k}{2\pi} V_0(u_s) \sqrt{\frac{2\pi}{k\rho |\psi''(u_s)|}} T_0(u_s) e^{-j\Omega\psi(u_s) + j\frac{\pi}{4}}. \quad \psi''(u_s) \geq 0. \quad (6-27)$$

The stationary phase point u_s defined by $\partial\psi(u)/\partial u = 0$ at $u = u_s$ is

$$u_s = \frac{k x_0}{k} = \sin \hat{\phi} \quad (6-28a)$$

and consequently

$$\psi(u_s) = 1 \quad (6-28b)$$

$$\frac{\partial^2 \Psi(u)}{\partial u^2} \bigg|_{u=u_s} = -\frac{1}{\cos^2 \hat{\phi}} < 0 \quad (6-28c)$$

$$T_0(u_s) = j2K \left[J_0 - I'_0 J_0(ka) \right] \frac{1}{k \cos \hat{\phi}} \begin{cases} 1; & U = 0 \\ 2j \sin (ks \cos \hat{\phi}) e^{-jks \cos \hat{\phi}}; & U = 1 \end{cases} \quad (6-28d)$$

Substituting Eqs. (6-28) and (4-49) into Eq. (6-27) we obtain the first-order asymptotic approximation to the far field due to a single excited monopole element in an infinite match-terminated array environment, that is

$$\hat{E}_z^{(e)}(\rho) \sim \sqrt{\frac{d}{\lambda}} \frac{1}{\sqrt{h}} \frac{e^{-jk\rho}}{\sqrt{\rho}} \sqrt{\frac{\zeta_0}{Z_c}} F(\hat{\phi}) V_{inc} \quad (6-29a)$$

where

$$F(\hat{\phi}) = j \frac{e^{j\frac{\pi}{4}}}{4\pi} \sqrt{\frac{\lambda^2}{dh}} \sqrt{\frac{Z_c}{\zeta_0}} \frac{\zeta_0}{Z_0} [J_0 - I'_0 J_0(ka)] [1 + \Gamma_a(kd \sin \hat{\phi})] \begin{cases} 1 & ; U=0 \\ j2 \sin (ks \cos \hat{\phi}) e^{-jks \cos \hat{\phi}} & ; U=1 \end{cases} \quad (6-29b)$$

The realized element gain pattern

$$G_z^{(e)}(\hat{\phi}) = \frac{|\hat{E}_z^{(e)}(\rho, \hat{\phi})|^2}{\zeta_0 \frac{P_{inc}}{2\pi\rho h}} \quad (6-30a)$$

which, normalized to the available power $P_{\text{inc}} = |V_{\text{inc}}|^2/Z_c$, may now be written as

$$G_z^{(e)}(\hat{\phi}) = 2\pi \frac{d}{\lambda} |F(\hat{\phi})|^2. \quad (6-30b)$$

Note that the factor $2\pi d/\lambda$ represents the uniformly illuminated unit cell power gain since it is the maximum gain (directivity) of an antenna with an area d . This implies that $|F(\hat{\phi})| \leq 1$.

We denote the complex field element pattern by

$$g_z^{(e)}(\hat{\phi}) = \sqrt{\frac{2\pi d}{\lambda}} F(\hat{\phi}). \quad (6-31)$$

Consequently, Eq. (6-29) can be expressed in the form

$$\hat{E}_z^{(e)}(\rho) \equiv \frac{1}{\sqrt{2\pi}} \sqrt{\frac{\zeta_0}{Z_c}} \frac{V_{\text{inc}}}{\sqrt{h}} \frac{e^{-jk\rho}}{\sqrt{\rho}} g_z^{(e)}(\hat{\phi}). \quad (6-32)$$

Note that Eqs. (6-31) with (6-29b) for the element pattern $g_z^{(e)}(\hat{\phi})$ in an infinite array environment are exactly of the same form as the equation for the radiation pattern of the single (isolated) element $g_{z0}^{(e)}(\hat{\phi})$ given by Eq. (5-20a). However it is important to mention that $\Gamma_a(kd \sin \hat{\phi})$ in Eq. (6-29b) is the active reflection coefficient, while Γ_a in Eq. (5-20a) is the input reflection coefficient of a single element. In addition the c_j' in the expression for I_0' in Eq. (6-29b) are probe current expansion coefficients of the active infinite array while the c_j' in the expression for I_0' in Eq. (5-20a) are probe current expansion coefficients of the single monopole in the parallel plate region.

It is known that within a "single mode approximation" the array element pattern $g_z^{(e)}(\hat{\phi})$ can be expressed simply in terms of a single (isolated) monopole radiation pattern $g_{z0}^{(e)}(\hat{\phi})$ and infinite array coupling (scattering) coefficients as

$$g_z^{(e)}(\hat{\phi}) \approx g_{z0}^{(e)} \left[1 + \frac{1}{1+S^0} \sum_{p=1}^{\infty} S^p \cos(kdp \sin \hat{\phi}) \right] \quad (6-33)$$

where S^p as discussed in Section 4.7 are mutual coupling coefficients. We obtained this relation by comparing Eq. (5-20a) with Eq. (6-31) having in mind Eq. (6-29b). We see that

$$g_z^{(e)}(\hat{\phi}) = g_{z0}^{(e)}(\hat{\phi}) \frac{1 + \Gamma_a(\hat{\phi})}{1 + S^0} \quad (6-34)$$

where $\Gamma_a(\hat{\phi})$ is the active coefficient and S^0 represents self reflection of the excited reference element ($p=0$) in the match-terminated array environment. In Eq. (6-34) we assumed that S^0 is equal to the input reflection coefficient of the single monopole [$\Gamma_a = S^0$ in Eq. (5-20)], thus we neglected second order backscattering contributions to S^0 from neighboring elements. Also we assumed that the single-term probe current of the active array is the same as the one on a single (isolated) monopole. From Eq. (4-51a)

$$1 + \Gamma_a(\hat{\phi}) = 1 + S^0 + \sum_{p=1}^{\infty} S^p \cos(kdp \sin \hat{\phi}). \quad (6-35)$$

Substitution of Eq. (6-35) into Eq. (6-34) yields (6-33).

When there are no grating lobes in real space $|g_z^{(e)}(\hat{\phi})|$ can be also obtained from

$$|g_z^{(e)}(\hat{\phi})| = \sqrt{\frac{2\pi d}{\lambda}} \sqrt{1 - |\Gamma_a(\hat{\phi})|^2} \cos \hat{\phi} \quad (6-36)$$

where $\Gamma_a(\hat{\phi})$ may be computed from Eq. (4-48a). Equation (6-36), which is based on the conservation of power principle, is well known. It has also been derived below for an infinite linear array of coaxially-fed monopoles in the parallel plate waveguide.

We start from Eq. (6-29) which after using Eq. (H-54) can be rewritten in the form

$$E_z^{(e)}(\rho, \hat{\phi}) = -\frac{ke^{j\frac{\pi}{4}}}{\sqrt{2\pi}} \sqrt{\frac{d}{h}} \frac{k_{x0}}{|k_{x0}|} \frac{e^{-jk\rho}}{\sqrt{kp}} T_{00}'' V_{inc} \cos \hat{\phi} \quad (6-37a)$$

since the transmission coefficient

$$T_{00}'' = \frac{\hat{V}_{00}''}{V_{inc}}. \quad (6-37b)$$

In Eq. (6-37b), V_{inc} is the modal voltage of the incident TEM mode in the coaxial feed line ($p=0$), and \hat{V}_{00}'' is the modal voltage of the single-propagating ($m=0, n=0$) TE Floquet mode in the unit cell [see Eqs. (H-49a) and (H-54)].

Substituting Eq. (6-37a) into Eq. (6-30a) gives the element gain pattern as

$$G_z^{(e)}(\hat{\phi}) = \frac{Z_c}{\zeta_0} kd \cos^2 \hat{\phi} |T_{00}''|^2. \quad (6-38)$$

On the other hand when only a single Floquet mode propagates in the unit cell the power conservation principle states

$$|V_{inc}|^2 Y_c - |\Gamma_a(\hat{\phi})|^2 Y_c = |\hat{V}_{00}''|^2 \hat{Y}_{00}'' \quad (6-39a)$$

where \hat{Y}_{00}'' is the modal admittance of the ($m=0, n=0$) Floquet mode in the unit cell given by Eq. (H-50c) as

$$\hat{Y}_{00}'' = \frac{\cos \hat{\phi}}{\zeta_0}. \quad (6-39b)$$

Thus $|\hat{V}_{00}''|^2 \hat{Y}_{00}'' = P_t$ in Eq. (6-39a) represents transmitted power in the unit cell. From Eq. (6-39a)

$$Y_c \left(1 - |\Gamma_a(\hat{\phi})|^2 \right) = |T_{00}''|^2 \hat{Y}_{00}'' \quad (6-40a)$$

or

$$|T_{00}''|^2 = \frac{Y_c}{\hat{Y}_{00}''} \left(1 - |\Gamma_a(\hat{\phi})|^2 \right). \quad (6-40b)$$

Substituting Eq. (6-39b) into Eq. (6-40b) and then Eq. (6-40b) into Eq. (6-38) we obtain

$$G_z^{(e)}(\hat{\phi}) = kd \left(1 - |\Gamma_a(\hat{\phi})|^2 \right) \cos \hat{\phi} \quad (6-41)$$

from which, the relation for the element voltage gain pattern [Eq. (6-36)] readily follows.

In Appendix H we show that the expressions for the active array field due to an infinite array of monopoles radiating into a semi-infinite parallel plate region satisfy the conservation of power condition which may be stated as

$$P_{inc} \left(1 - |\Gamma_a(\delta_x)|^2 \right) = P_t. \quad (6-42)$$

Here

$$P_{inc} = |V_{inc}|^2 Y_c \quad (6-43)$$

is the TEM mode incident power in the feed coaxial transmission line with characteristic admittance Y_c . As indicated in Chapter 4, Γ_a represents the active reflection coefficient defined by Eq. (4-48a). The P_t in Eq. (6-42) represents the far field radiated power within a unit cell of cross section area $d \times h$. It is given by

$$P_t = \operatorname{Re} \int_{-d/2}^{d/2} \int_0^h \hat{\mathbf{E}} \times \hat{\mathbf{H}}^* \cdot \mathbf{y}_0 \, dx \, dy. \quad (6-44)$$

7. NUMERICAL ANALYSIS

Based on the preceding analysis, a Fortran IV computer program was generated to evaluate the probe current distribution, active impedance, coupling coefficients, and the far-field element patterns. A comprehensive description of the computer program including a complete listing and printout for the typical test case will be given in a subsequent RADC Technical Report. The program was run on a CDC Cyber 860 computer at the GL Computer Center, Hanscom AFB, MA. All calculations were performed in single precision (15 significant digits on a Cyber 860) complex arithmetic. The execution time to compute the active admittance and reflection coefficient for one scan angle, and the far-field element pattern value for one observation angle, is 2.5 seconds. The time required to compute the coupling coefficient between two elements of the infinite linear array is approximately 1.5 seconds. This program requires 150 kbytes of memory.

The active admittance is computed from Eq. (4-44) using the relevant relations [Eqs. (4-45)]. The $(I \times I)$ matrix with the elements A_{ij} as given by Eq. (4-45k), is Hermitian and therefore only $I(I+1)/2$ matrix coefficients need to be evaluated. The series over index n in Eq. (4-45k) converges as $1/n^3$. Forty terms ($n_{\max} = 40$) were used throughout, unless otherwise stated. The $S_n(\delta_x)$ in Eq. (4-45k) is computed for the desired geometry from Eqs. (4-47a) to (4-47d). The series \sum_p in Eqs. (4-47c) and (4-47d) converge as $1/\sqrt{p}$ for $p \rightarrow \infty$. The slow convergence of these series was accelerated as described in Appendix E, based on the relation:⁹

$$2 \sum_{p=1}^{\infty} H_0^{(2)}(2\pi y p) \cos(2\pi x p) = -1 + \frac{2}{\pi} \left(\ln \frac{y}{2} + \gamma \right) + \frac{j}{\pi} \frac{1}{\sqrt{x^2 - y^2}} + \frac{j}{\pi} \sum_{m=1}^{\infty} \left[\frac{1}{\sqrt{(m+x)^2 - y^2}} + \frac{1}{\sqrt{(m-x)^2 - y^2}} - \frac{2}{m} \right] \quad (7-1)$$

⁹ Infeld, L. et al (1974) On some series of Bessel functions, *J. Math. and Phys.*, **26**, 22.

valid for $0 \leq x \leq 1$. In Eq. (7-1) $\operatorname{Im} \left\{ \left[(m \pm x)^2 - y^2 \right]^{1/2} \right\} \geq 0$, and $\gamma = 0.577\dots$ is the Euler constant.

The new series \sum_m converges as $1/m^3$.

The inner products I_{in} in Eq. (4-45 k) were computed from Eq. (4-45i).

The zero-order Bessel and Hankel functions in the expression for A_{ij} were evaluated by the usual numerical methods.¹⁰ The computational accuracy of these functions was better than 10 significant digits.

The coefficients B_i are computed using Eq. (4-45l).

The monopole current density expansion coefficients were solved from Eq. (4-45j) using Gauss's elimination method. Ten current terms ($I=10$) were used in numerical evaluation unless otherwise indicated.

The relative convergence phenomenon¹¹ was observed by monitoring the current expansion coefficients and the active admittance value as a function of the number of parallel plate radial modes n_{max} and of the number of current terms I . It was found that for a stable solution it is necessary to impose the condition

$$I < \frac{1}{h} n_{max} . \quad (7-2)$$

For example if $n_{max} = 20$ and $h = 0.369\lambda$ one requires $I < 5$ for $l = 0.1\lambda$, $I < 10$ if $l = 0.2\lambda$ and $I < 16$ if $l = 0.3\lambda$. If I increases beyond these values, the numerical values for Y_a tend to become progressively less accurate. This can be seen from Figures 7-1 and 7-2 which show the active input conductance and susceptance at broadside scan for an infinite array radiating into a semi-infinite parallel plate region ($U = 1$) vs the number of monopole current terms for four probe lengths: $l = 0.1\lambda$, $l = 0.2\lambda$, $l = 0.3\lambda$, and $l = 0.233\lambda$ (matched case). One also observes that for short monopoles a single current term yields a good approximation to the active admittance. It was found that for all four possible array geometries [Eqs. (4-47a) to (4-47d)], the plots Y_a vs I exhibit a similar behavior.

¹⁰ Abramowitz, M. and Stegun, I.A. (1964) *Handbook of Mathematical Functions*, United States Department of Commerce, National Bureau of Standards, Applied Mathematics, 55.

¹¹ Lee, S.W., Jones, W.R. and Campbell, J.J. (1970) Convergence of numerical solution of iris type discontinuity problems, *Antennas and Propagation Symposium Digest*, Columbus, Ohio.

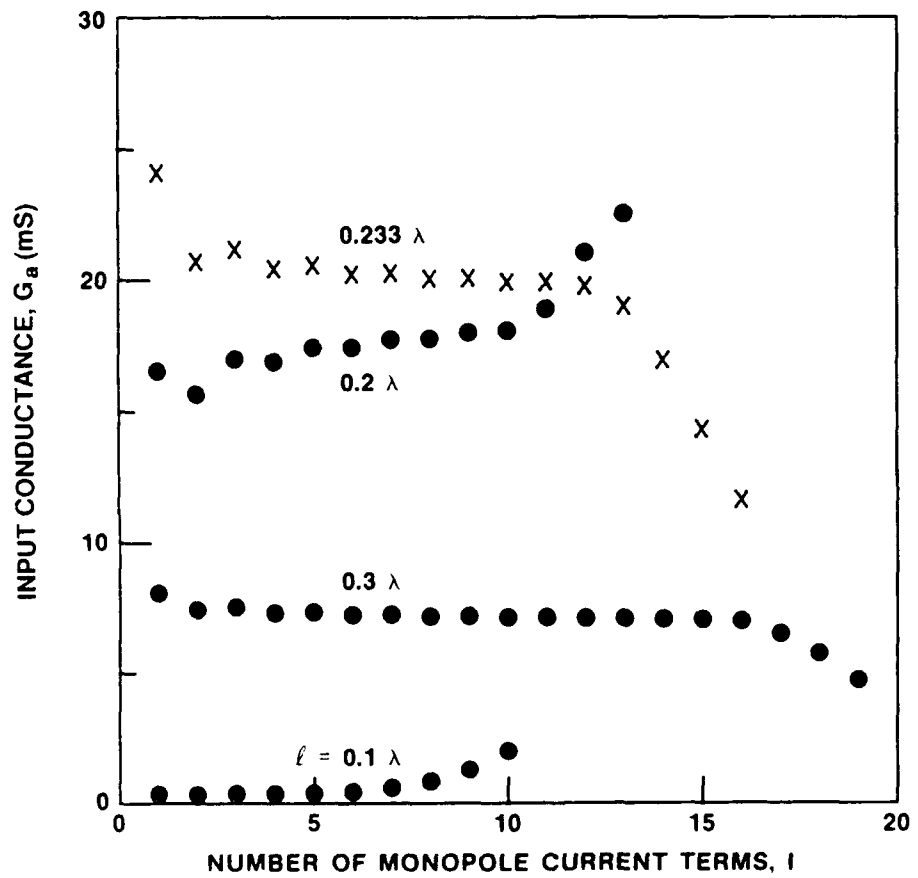


Figure 7-1. Active Conductance vs Number of Probe Current Terms

($d/\lambda = 0.4$, $h/\lambda = 0.369$, $s/\lambda = 0.163$, $a/\lambda = 0.0106$, $b/\lambda = 0.034$, $Z_c = 50 \Omega$; $\hat{\phi}_0 = 0^\circ$)

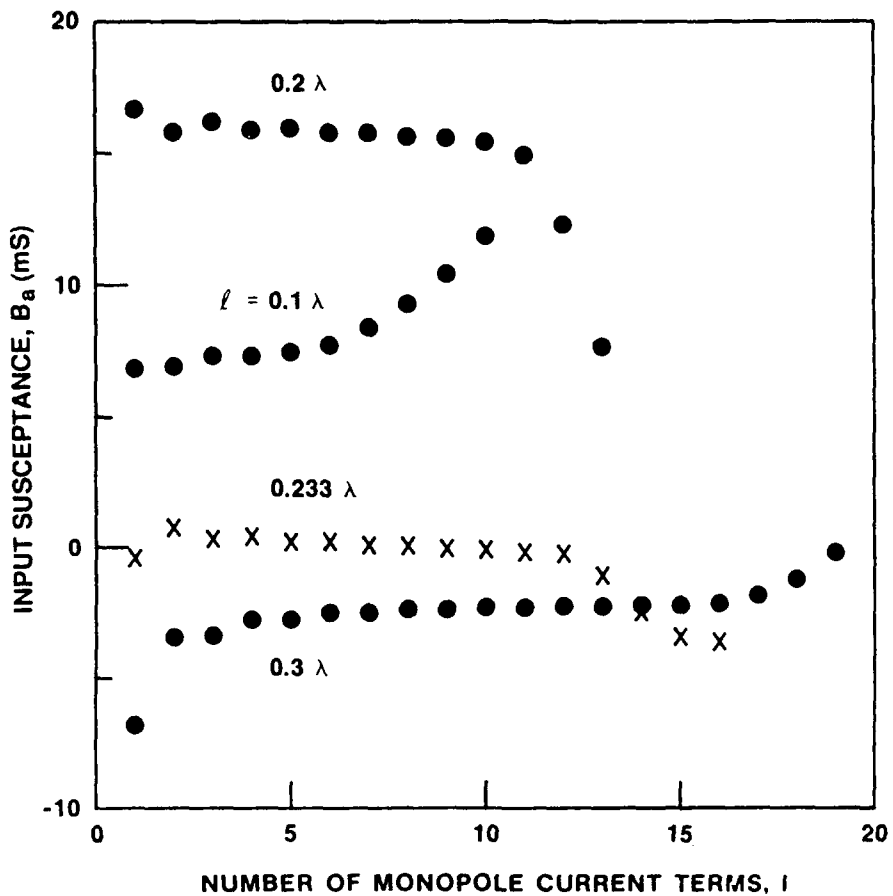


Figure 7-2. Active Susceptance vs Number of Probe Current Terms

($d/\lambda = 0.4$, $h/\lambda = 0.369$, $s/\lambda = 0.163$, $a/\lambda = 0.0106$, $b/\lambda = 0.034$, $Z_c = 50 \Omega$; $\hat{\phi}_0 = 0^\circ$)

With $n_{\max} = 40$ and ten current terms ($I = 10$) in the probe current expansion the active admittance was computed with an accuracy of better than four significant digits. If a high degree of accuracy of Y_a is desired, more current terms are needed and n_{\max} must be increased according to Eq. (7-2).

The active reflection coefficients $\Gamma_a(k_{x0})$ are computed from Eq. (4-48a).

The probe current distribution has been computed based on Eq. (4-20a). From Eqs. (4-20a) and (4-24b), the probe current is

$$I_z(z) = 2\pi a J_z(z) = \sum_{i=1}^l c_i'' \sin \left[\frac{\pi}{2l} (2i-1)(z-l) \right] \quad (7-3a)$$

where the probe current expansion coefficients c_i'' are

$$c_i'' = j \frac{V_0}{Z_0} c_i' = |c_i''| e^{j\phi_i''}; \quad i = 1, 2, \dots, l. \quad (7-3b)$$

In Eq. (7-3b) Z_0 is given by Eq. (4-45b) and the c_i' are the solutions of Eq. (4-45j). In our numerical evaluation of c_i'' we set V_0 to unity.

Coupling coefficients were computed using Eq. (4-51b). A numerical integration method based on cubic spline interpolation is described in Appendix I and is outlined below.

For this purpose we cast Eq. (4-51b) into the form

$$I(\Omega) = \int_a^b f(x) e^{-j\Omega x} dx \quad (7-4)$$

where the function $f(x) = \Gamma_a(k_x)$ is given at a finite number of equally spaced sample points, and $\Omega = pd$ is the large parameter when p is large. If we use the standard numerical integration techniques to evaluate Eq. (7-4), it is important to notice that as p , that is Ω , increases, the numerical integration error increases if the number of integration intervals is constant. On the other hand, the values for coupling coefficients in a linear array in a semi-infinite parallel plate waveguide decay monotonically as $p^{-3/2}$ which suggests that the numerical integration error should decrease with p to attain the desired accuracy. Thus, the usual numerical integration methods cannot be applied in this case because of the large number of integration steps needed to achieve a desired computational accuracy.

To evaluate Eq. (7-4) we assume that $f(x)$ is given by a set of values $\{f(x_i)\}$, $i=1, 2, \dots, N+1$ on the interval $[a, b]$ where

$$x_i = a + (i-1) \frac{b-a}{N} \quad (7-5)$$

and N is the number of subintervals. We approximate $f(x)$ in each subinterval by a cubic polynomial

$$P_i(x) = \sum_{n=0}^3 A_{ni} x^n \quad (7-6)$$

where coefficients A_{ni} are determined in Appendix I by the method known as cubic spline interpolation. Based on that one may write

$$\int_a^b f(x) e^{-j\Omega x} dx \approx \sum_{i=1}^N \sum_{n=0}^3 A_{ni} \int_{x_i}^{x_{i+1}} x^n e^{-j\Omega x} dx \quad (7-7)$$

where the integrals can be evaluated in a closed form. Thus the integration error is due only to the approximation of $f(x)$ in each subinterval by a piecewise-cubic polynomial $P_i(x)$. The small interpolation error is estimated in Reference 12. In evaluating the coupling coefficients by using Eq. (4-51b) we set $N=300$, which enabled us to compute efficiently values for coupling coefficients below - 65 dB without noticeable error.

The integration routine was tested using Eq. (4-51b) with $k_{x0}=0$, that is,

$$\Gamma_a(0) = \sum_{p=-\infty}^{\infty} S^p. \quad (7-8)$$

Truncating the series at $|p| = 50$, it was found that this identity holds within approximately three significant digits.

The field (voltage) element patterns of the excited element ($p=0$) were calculated according to Eqs. (6-31) using Eq. (6-29b), and were normalized to the unit cell gain $(2 \pi d/\lambda)^{1/2}$.

¹² Conte, S.D. and de Boor, Carl (1972) *Elementary Numerical Analysis*, McGraw-Hill, New York.

8. NUMERICAL RESULTS AND DISCUSSION

The active impedance, active reflection coefficient, coupling (scattering) coefficients, probe current distribution, and element patterns were computed for representative values of array parameters to show the significant trends. Most of the numerical results refer to monopole elements with a 50 ohm characteristic impedance of the corresponding feed-transmission line. As already mentioned, field amplitude (voltage) element patterns were normalized to the unit cell gain $(2\pi d/\lambda)^{1/2}$. Unless otherwise stated, in numerical computations we used 40 waveguide modes ($n_{\max} = 40$) and 10 monopole current terms ($I = 10$) in Galerkin's procedure.

The results are grouped according to array structure factor $S_n(\delta_x)$ as defined by Eq. (4-47). We discuss: (1) a single monopole in an infinite parallel plate region; (2) a single monopole in a semi-infinite parallel plate region; (3) an infinite linear array of monopole elements in an infinite parallel plate region; and (4) an infinite linear array of monopole elements in a semi-infinite parallel plate region.

8.1 Single Monopole in an Infinite Parallel Plate Region

Figures 8-1 and 8-2 show input conductance and susceptance, respectively, of a single monopole in an infinite parallel plate region vs probe length l for three heights of parallel plates, $h/\lambda = 0.3$, $h/\lambda = 0.35$ and $h/\lambda = 0.4$. The feed-coaxial line has an air dielectric and a characteristic impedance of 50 ohms. The coaxial conductor dimensions are $a/\lambda = 0.016$, $b/\lambda = 0.037$.

It is observed, from Figure 8-1, that the input conductance is very sensitive to the probe length l and almost insensitive to the separation between the two parallel plates h . In fact, for values $l/\lambda \leq 0.2$, the conductance is practically independent of h . The same observation also applies to the susceptance shown in Figure 8-2. From these two figures one also sees that for short probes, $l/\lambda \leq 0.1$, the admittance is a linear function of the probe length. This is because $Y_a \approx I_z(z=0)$ and, as will be discussed, for short probes, the current distribution is proportional to the probe length. Both curves, G_a and B_a exhibit resonant behavior at $l/\lambda \approx 0.25$. From Figure 8-2 it is seen that for $l/\lambda < 0.25$ the input admittance is capacitive, for $l/\lambda > 0.25$ it is inductive, and, for $l/\lambda \approx 0.25$, passes through resonance.

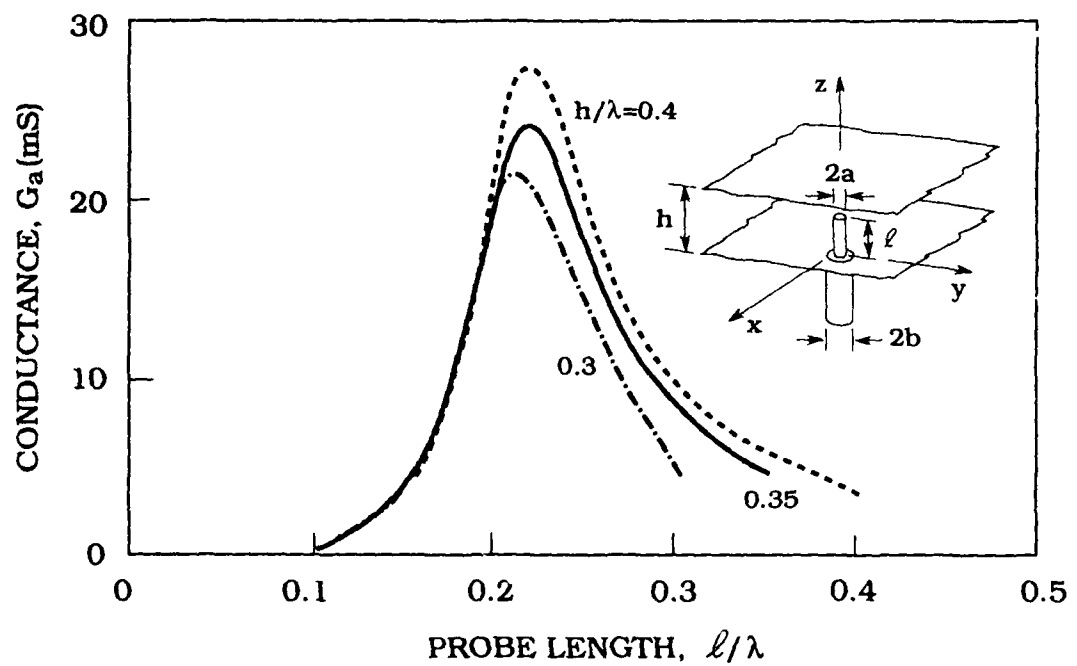


Figure 8-1. Input Conductance vs Probe Length; Parameter: Parallel Plate Separation $h/\lambda = 0.3, 0.35, 0.4$, ($a/\lambda = 0.016, b/\lambda = 0.037$)

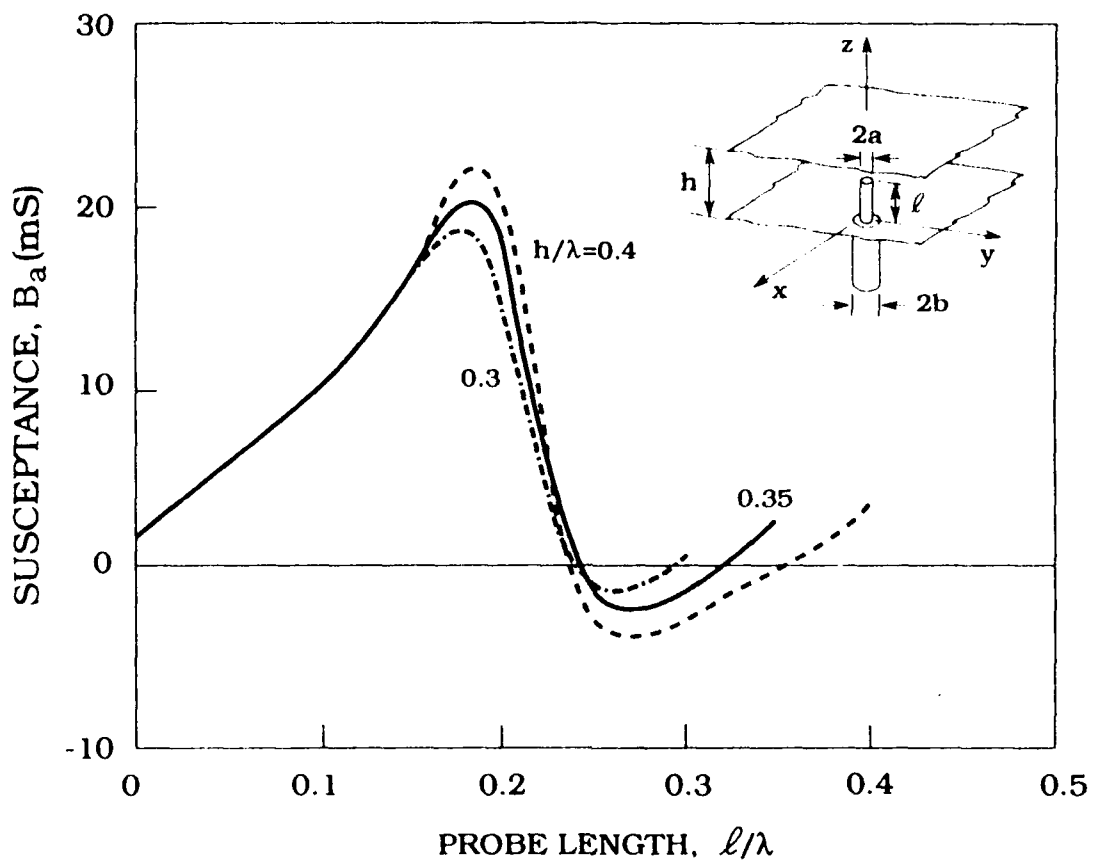


Figure 8-2. Input Susceptance vs Probe Length; Parameter: Parallel Plate Separation $h/\lambda = 0.3, 0.35, 0.4$, ($a/\lambda = 0.016, b/\lambda = 0.037$)

It should be mentioned that the analysis presented breaks down when the probe extends very close to the top plate, that is, when $l \approx h$. This is because in the analysis we assumed a sine expansion for the probe current; hence we forced the current to be zero at the tip of the probe. However, this is not true when $l \approx h$ because of the displacement current flowing through the capacitance between the tip of the probe and top plate of the guide. By monitoring the behavior of the input impedance vs l/h , we found that the analysis is valid for $0 \leq l/h \leq 0.99$.

When the parallel plate separation is greater than a half-wavelength, higher radial modes propagate in the guide. Figure 8-3 shows input admittance vs probe length for $h/\lambda = 0.95$. In this case two radial modes, $n=0$ (TEM) and $n=1$ (TM^2) propagate.

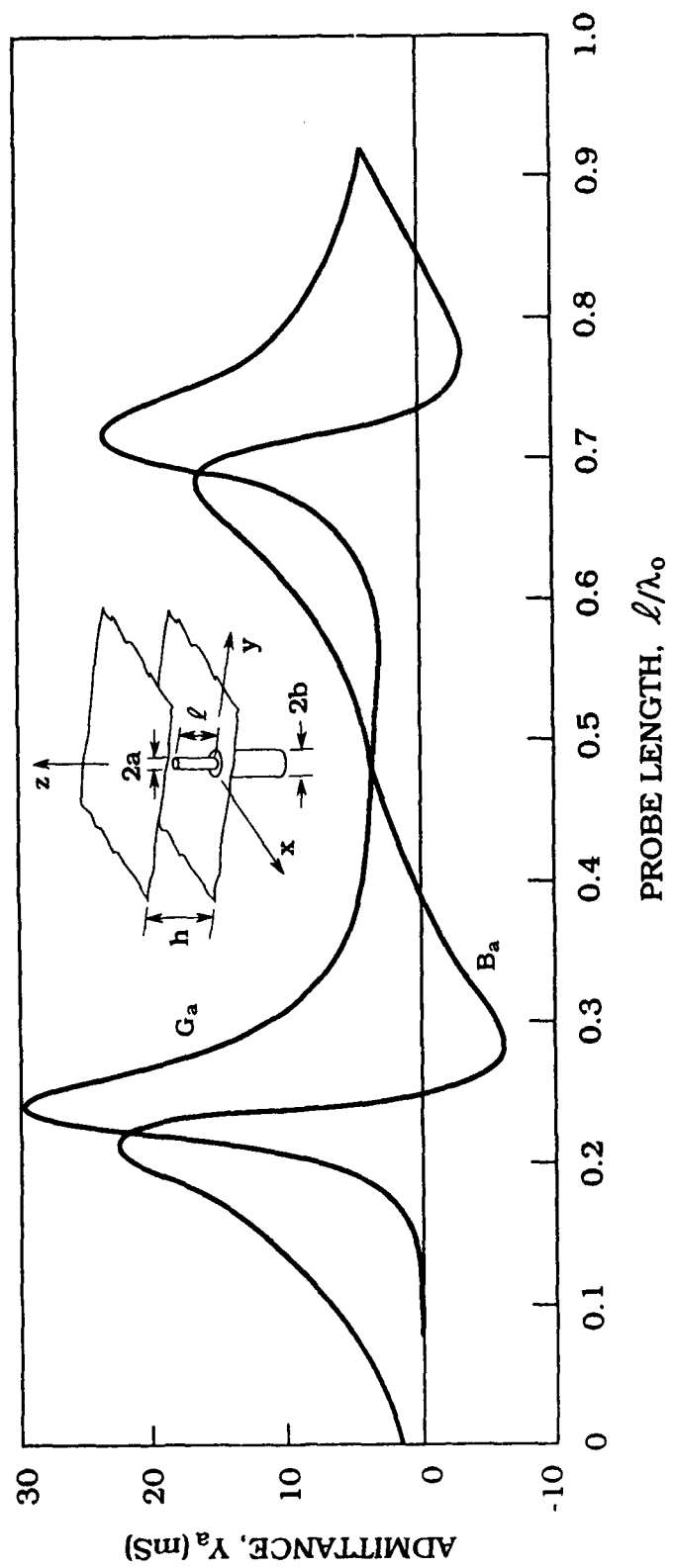


Figure 8-3. Input Admittance vs. Probe Length. ($h/\lambda = 0.95$, $a/\lambda = 0.016$, $b/\lambda = 0.037$)

Curves G_a and B_a vs l exhibit double resonance behavior. The first resonance occurs at $l/\lambda \approx 0.25$, and the second, as expected, at $l/\lambda \approx 0.25 + 1/2 = 3/4$. We choose to present the admittance curve for $h/\lambda = 0.95$ because at this particular plate separation and $l/\lambda = 0.75$ the reflection coefficient is zero ($|\Gamma_a| = 0$). To avoid the relative convergence phenomenon, we stay within the range allowed by Eq. (7-2), and use $I=1$ for $0 \leq l/\lambda < 0.05$, $I=3$ for $0.05 \leq l/\lambda < 0.1$, $I=5$ for $0.1 \leq l/\lambda < 0.2$ and $I=10$ for $0.2 \leq l/\lambda < 0.3$ with $n_{\max}=60$. In the region $0.3 \leq l/\lambda \leq 0.95$ we used $I=10$ and $n_{\max}=40$.

In most practical applications it is useful to know the optimal separation of the parallel plates and probe length so that the monopole is matched to the coaxial feed line at a particular center frequency f_c . For this reason Figure 8-4 displays the contour plot of the magnitude of the reflection coefficient vs h and l . One sees that for $h/\lambda = h_c/\lambda = 0.35$ and $l/\lambda = l_c/\lambda = 0.24$,

the reflection coefficient is zero, that is, a monopole element in an infinite parallel plate region is matched to the coaxial-feed transmission line.

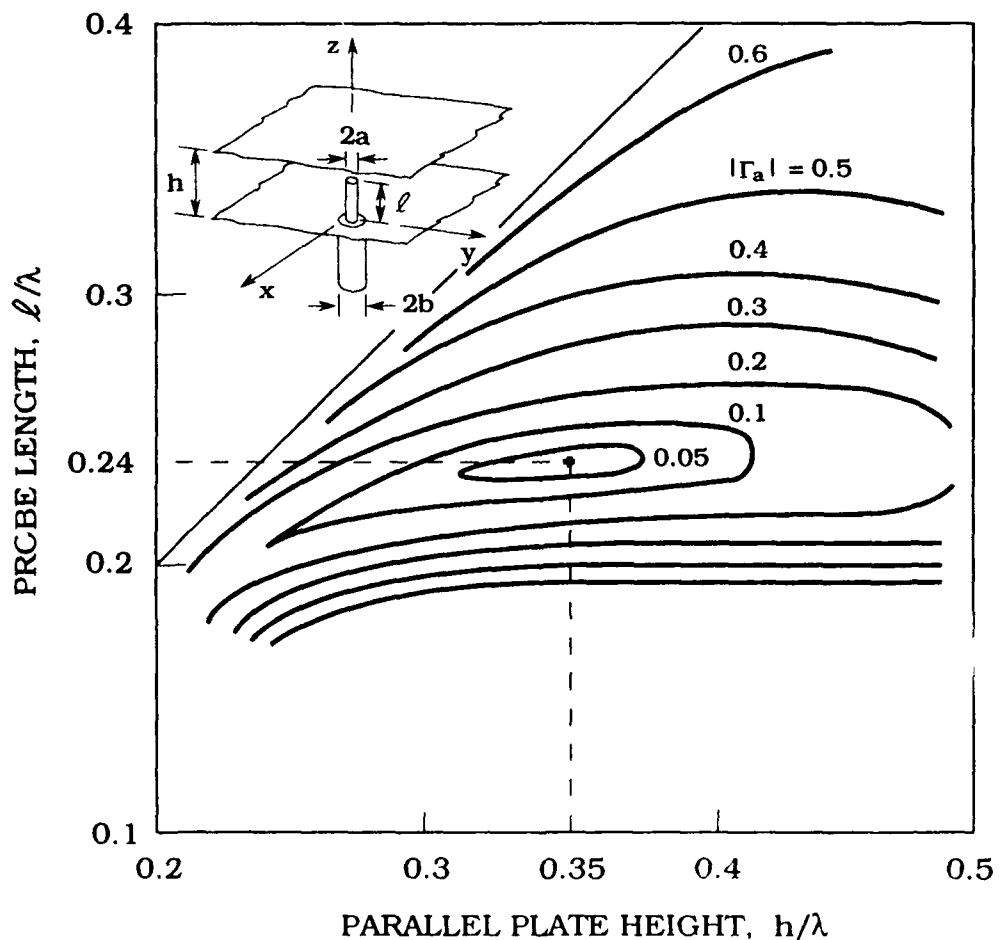


Figure 8-4. Reflection Coefficient (Contour Plot of Magnitude) vs Parallel Plate Separation and Probe Length, ($a/\lambda = 0.016$, $b/\lambda = 0.037$)

For this case ($h_c/\lambda = 0.35$), Figure 8-5 shows input impedance vs probe length. The Smith chart normalization is $Z_N = 50$ ohms. Note that for $l/\lambda = 0.24$, VSWR = 1 (reflection coefficient $\Gamma_a = 0$) and for $0.2 < l/\lambda < 0.3$, the VSWR < 2.

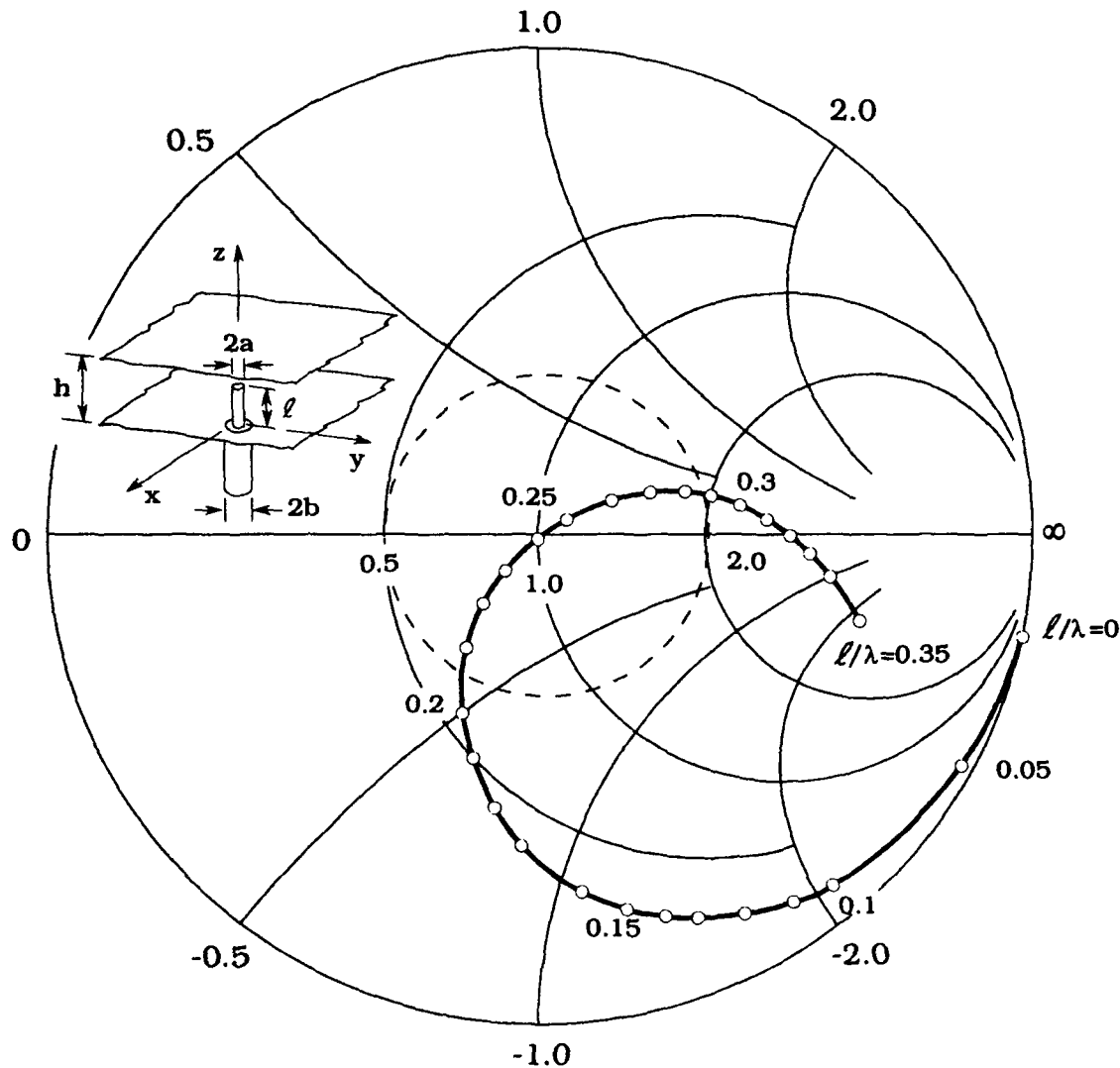


Figure 8-5. Input Impedance vs Probe Length.
($h/\lambda = 0.35$, $a/\lambda = 0.016$, $b/\lambda = 0.037$, $Z_N = 50 \Omega$)

The input impedance vs frequency plot in Figure 8-6 allows us to assess the frequency bandwidth of the single coaxially-fed monopole element. As one may note, the frequency bandwidth corresponding to a VSWR of 2:1 is approximately 40 percent.

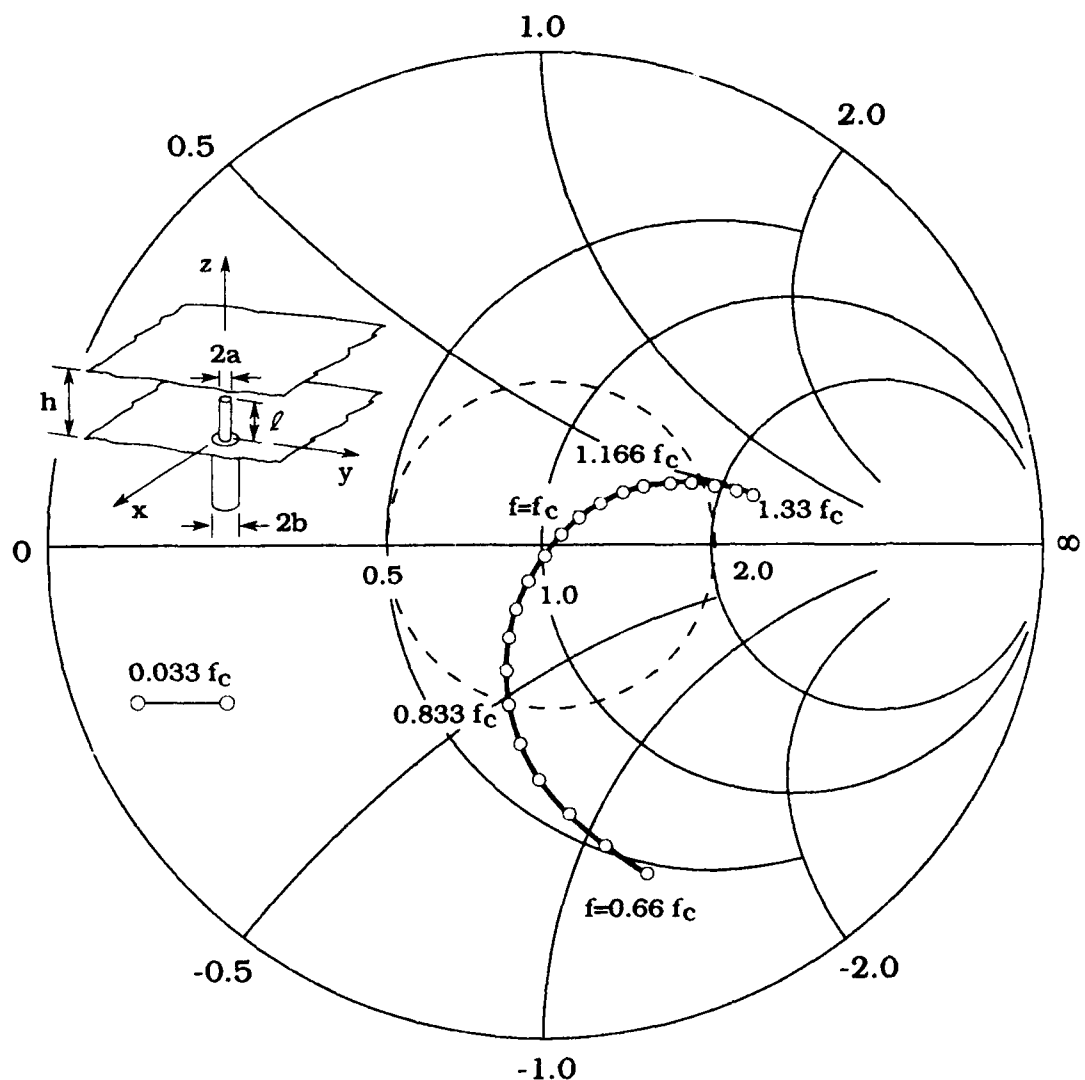


Figure 8-6. Input Impedance vs Frequency. ($h_c/\lambda_c = 0.35$, $l_c/\lambda_c = 0.24$, $a/\lambda_c = 0.016$, $b/\lambda_c = 0.037$, $Z_N = 50 \Omega$)

Figure 8-7 shows the dependence of input impedance on probe radius, a . The radius of the outer coaxial conductor is $b = 2.3 a$, so that in all cases the characteristic impedance of the coaxial feed lines $Z_c = 50$ ohms. It is seen that the influence of these parameters on input admittance is practically insignificant.

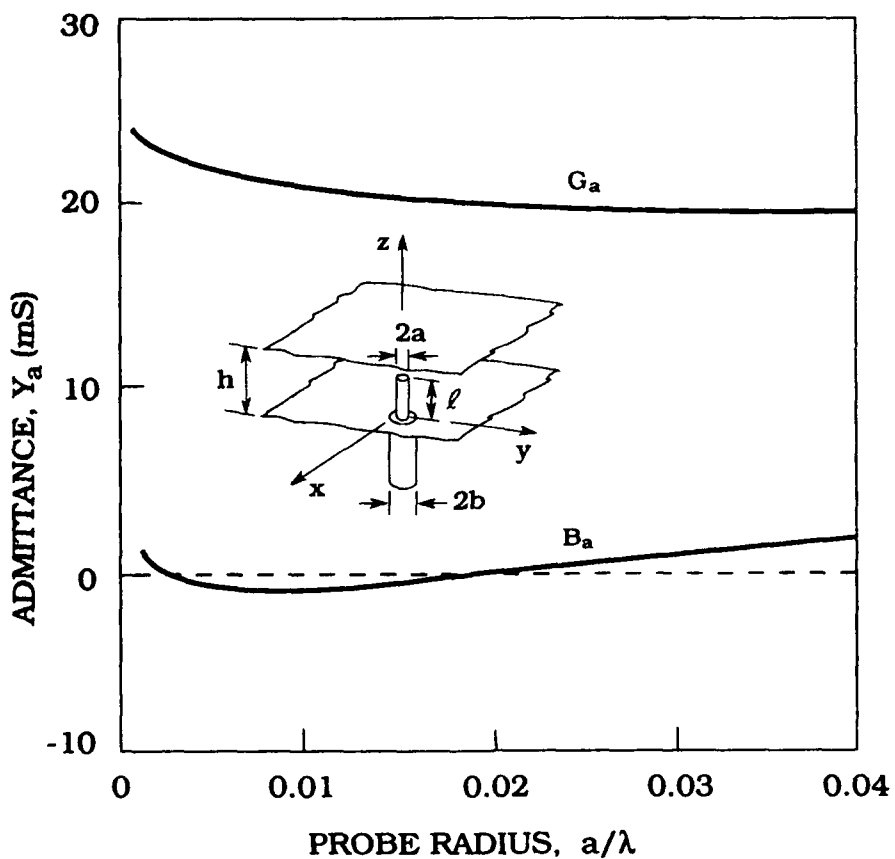


Figure 8-7. Input Admittance vs Probe Radius,
 $(h_c/\lambda = 0.35, L_c/\lambda = 0.24, b/\lambda = 2.3 a/\lambda, Z_c = 50 \Omega)$

The numerical computation of the probe current distribution based on Eq. (7.3) has also been carried out. In our numerical evaluation of c_1'' we set $V_0(z=0) = 1$ V for the aperture voltage in the coaxial feed line.

Figure 8-8 shows the magnitude of the current vs z/λ for three probe lengths $l/\lambda = 0.1, 0.2$, and 0.3 . For each case two curves are plotted: the dashed line represents the probe current distribution for a single current term [$I = 1$ in Eq. (7-3a)] and the solid line represents the probe current distribution with ten current terms [$I = 10$ in Eq. (7-3a)]. It is seen that the current along the probe has a basic $\sin k(z - l)$ variation. For short probes ($l/\lambda \leq 0.1$) the magnitude of the probe current is almost a linear function of z . This is expected since $\sin k(z - l) \approx k(z - l)$ when $l/\lambda \leq 0.1$.

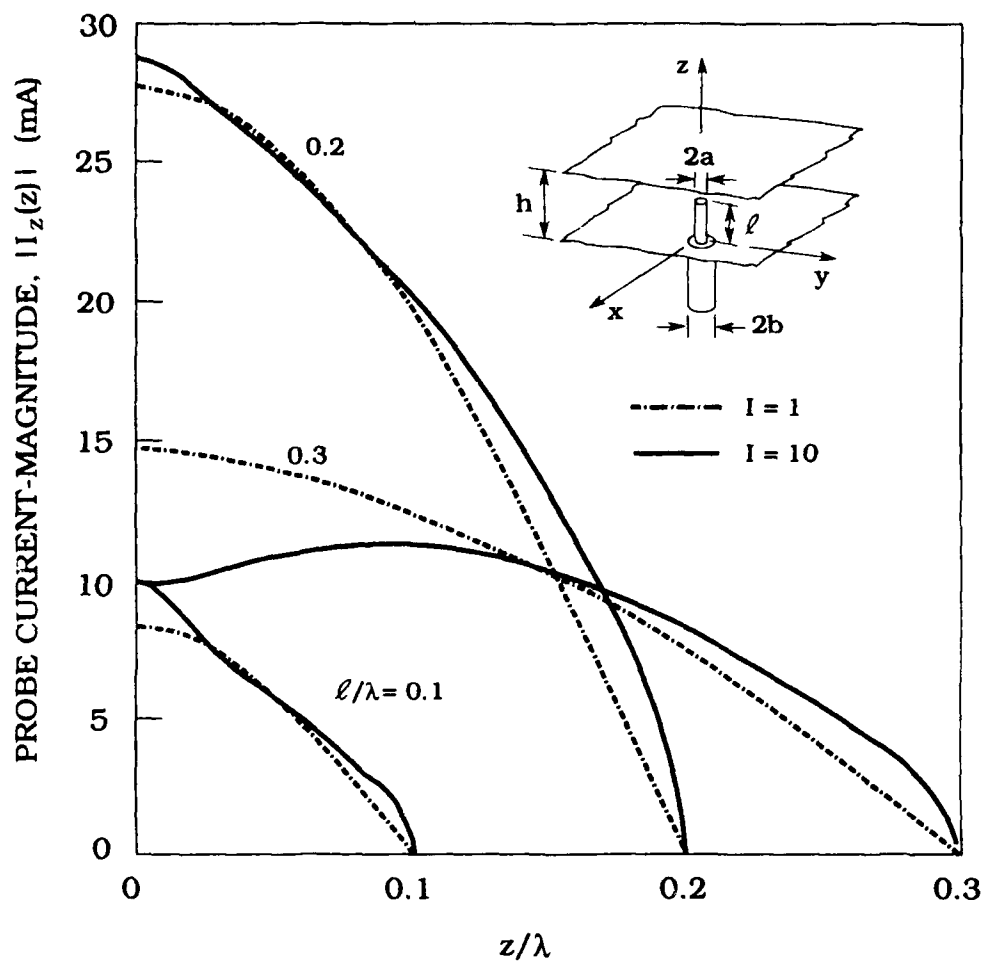


Figure 8-8. Current Distribution (Amplitude) Along a Coaxially-Driven Monopole in an Infinite Parallel Plate Region; Parameter: Probe Length $\ell/\lambda = 0.1, 0.2, 0.3$, ($h/\lambda = 0.4, a/\lambda = 0.016, b/\lambda = 0.037$)

Figure 8-9 exhibits corresponding phases of the current along the probe for the same geometry.

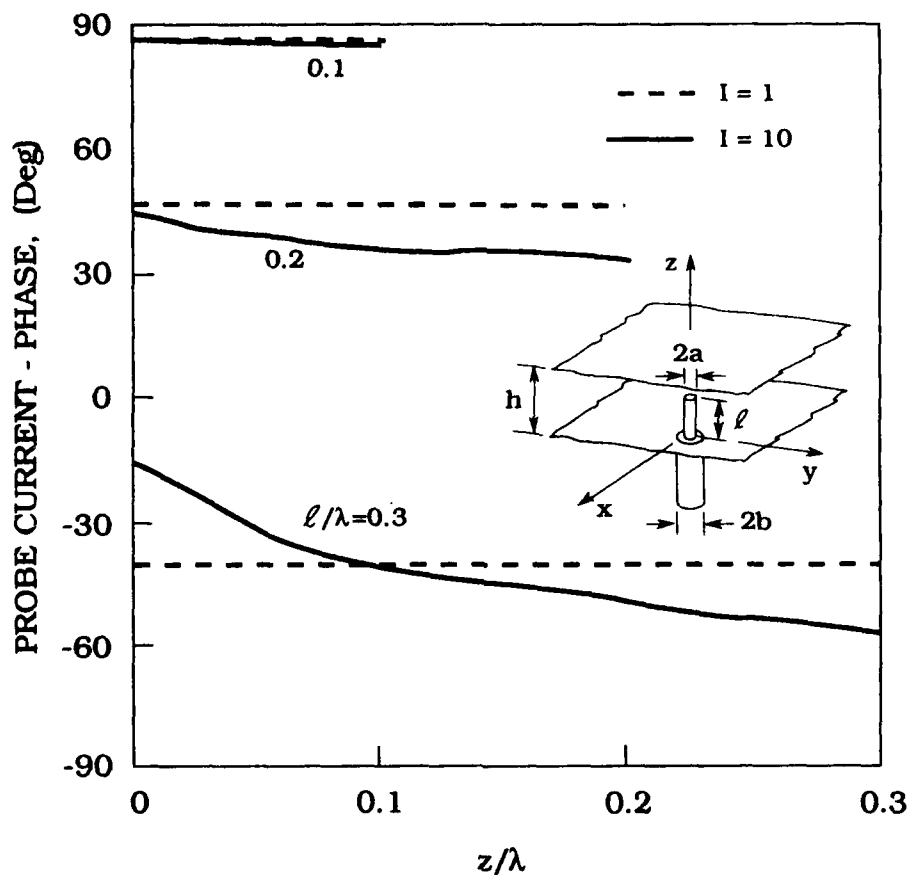


Figure 8-9. Current Distribution (Phase) Along a Coaxially-Driven Monopole in an Infinite Parallel Plate Region; Parameter: Probe Length $\ell/\lambda = 0.1, 0.2, 0.3$, ($h/\lambda = 0.4, a/\lambda = 0.016, b/\lambda = 0.037$)

It is interesting to note that since the probe current across the aperture ($z = 0$) is continuous, one can approximately determine the input admittance simply from

$$Y_a = \frac{I_z(z=0^+)}{V_0(z=0^-)} \quad (8-1)$$

where we assumed that the probe current at $z = 0$ is the same as that of the TEM mode in the coaxial feed-line. Setting $V_0(z=0^-) = 1V$ in Eq. (8-1) we obtain

$$Y_a = \frac{I_z(z=0^+)}{IV}$$

(8-2)

In Table 8-1, for the geometry of Figures 8-8 and 8-9, we compare results for the input admittance obtained from Eqs. (4-44) and (8-2). In both cases, $I = 10$ and $n_{max} = 40$. As one may see, the difference between these two results is less than 1 percent, which substantiates the single mode approximation for the field in the aperture.

Table 8-1. Comparison Between Results Obtained from Eqs. (4-44) and (8-2) for Input Admittance $Y_a = G_a + jB_a$:
Parameter: Probe Length $l/\lambda = 0.1, 0.2, 0.3$,
($h/\lambda = 0.4, a/\lambda = 0.016, b/\lambda = 0.037$)

l/λ	Y_a from Eq. (4-44)		Y_a from Eq. (8-2)	
	G_a mS	B_a mS	G_a mS	B_a mS
0.1	0.511	9.642	0.502	9.801
0.2	20.710	20.034	20.654	20.041
0.3	9.473	-2.732	9.471	-2.856

The probe current expansion coefficients c_i'' as given by Eq. (7-3b) are tabulated in Tables 8-2, 8-3 and 8-4 for probe lengths $l/\lambda = 0.1, 0.2$, and 0.3 , respectively. In each case coefficients are given for the single ($I = 1$) and ten ($I = 10$) current terms in Eq. (7-3a).

Table 8-2. Probe Current Expansion Coefficients:
Parameter: Total Number of Current Terms $I = 1, 10$,
($l/\lambda = 0.1, h/\lambda = 0.4, a/\lambda = 0.016, b/\lambda = 0.037$)

I	I=1		I=10	
	$ c_i'' $ mA	ϕ_i'' Deg.	$ c_i'' $ mA	ϕ_i'' Deg.
1	8.222	-93.26	8.566	-93.76
2			0.201	112.75
3			0.697	-93.02
4			0.033	-133.46
5			0.279	-93.33
6			0.041	-107.54
7			0.161	-93.64
8			0.044	-101.62
9			0.120	-94.04
10			0.074	-97.74

Table 8-3. Probe Current Expansion Coefficients:
 Parameter: Total Number of Current Terms $I = 1, 10$,
 $(l/\lambda = 0.2, h/\lambda = 0.4, a/\lambda = 0.016, b/\lambda = 0.037)$

i	I=1		I=10	
	$ c_i'' $ mA	ϕ_i'' Deg.	$ c_i'' $ mA	ϕ_i'' Deg.
1	27.623	-132.37	28.369	-141.27
2			2.050	167.40
3			1.406	-131.42
4			0.575	178.17
5			0.592	-132.76
6			0.303	-176.53
7			0.341	-134.16
8			0.195	-172.99
9			0.227	-135.36
10			0.139	-170.34

Table 8-4. Probe Current Expansion Coefficients:
 Parameter: Total Number of Current Terms $I = 1, 10$,
 $(l/\lambda = 0.3, h/\lambda = 0.4, a/\lambda = 0.016, b/\lambda = 0.037)$

i	I=1		I=10	
	$ c_i'' $ mA	ϕ_i'' Deg.	$ c_i'' $ mA	ϕ_i'' Deg.
1	14.341	139.43	12.479	141.35
2			3.155	97.28
3			0.329	-135.17
4			0.752	101.78
5			0.133	-146.52
6			0.368	103.33
7			0.074	-156.17
8			0.224	104.34
9			0.048	-164.80
10			0.153	105.12

Figures 8-10 and 8-11 show the magnitude and phase, respectively, of the probe current, for the geometry of Figure 8-6, that is, $h_c/\lambda = 0.35$, and $l_c/\lambda = 0.24$. In this case, as indicated, the monopole is matched to a 50Ω coaxial feed line. One may see from these two figures that, as expected, the magnitude of the probe current at $z = 0$ is 20 mA and the phase is zero, that is

$$I_z(z = 0^+) = 0.020 \text{ A.}$$

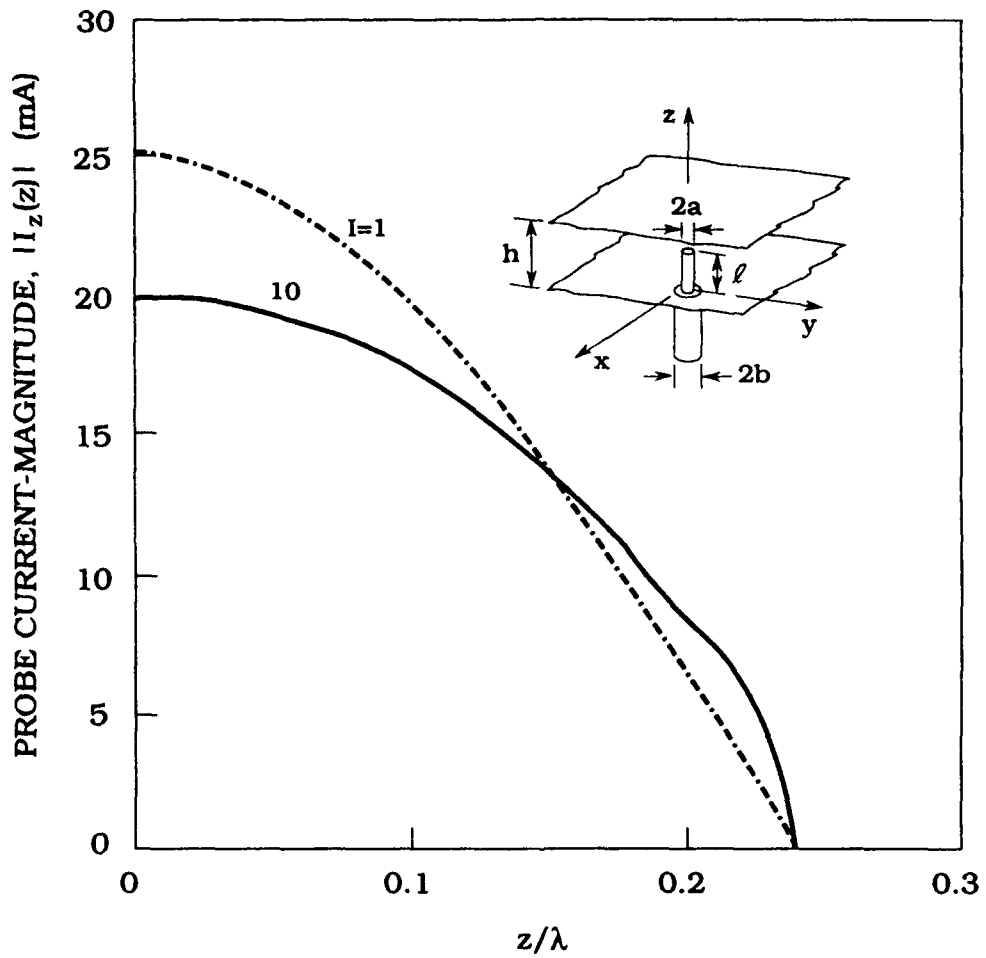


Figure 8-10. Current Distribution (Amplitude) Along a Coaxially-Driven Monopole in an Infinite Parallel Plate Waveguide; Parameter: Total Number of Current Terms $I = 1, 10$. ($l_c/\lambda = 0.24, h_c/\lambda = 0.35, a/\lambda = 0.016, b/\lambda = 0.037$)

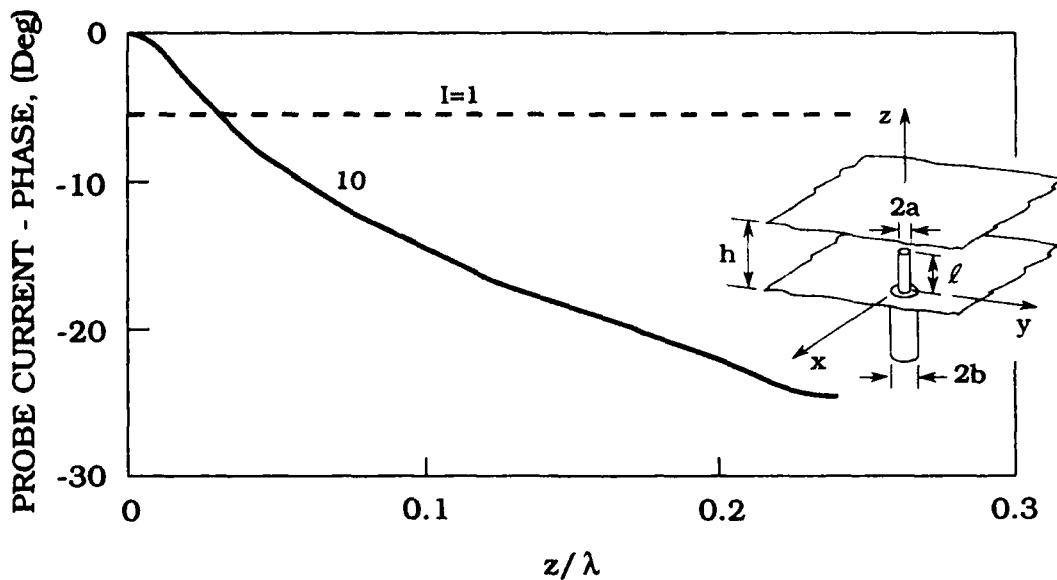


Figure 8-11. Current Distribution (Phase) Along a Coaxially-Driven Monopole in an Infinite Parallel Plate Waveguide; Parameter: Total Number of Current Terms $I = 1, 10, (l_c/\lambda = 0.24, h_c/\lambda = 0.35, a/\lambda = 0.016, b/\lambda = 0.037)$

The respective coefficients in the expansion for the probe current are tabulated in Table 8-5.

Table 8-5. Probe Current Expansion Coefficients;
Parameter: Total Number of Current Terms $I = 1, 10, (l_c/\lambda = 0.24, h_c/\lambda = 0.35, a/\lambda = 0.016, b/\lambda = 0.037)$

I	I=1		I=10	
	$ c_1'' $ mA	ϕ_1'' Deg.	$ c_1'' $ mA	ϕ_1'' Deg.
1	25.254	174.56	21.671	169.09
2			3.075	120.91
3			0.785	-164.33
4			0.782	127.02
5			0.339	-167.85
6			0.390	129.82
7			0.190	-171.34
8			0.240	131.79
9			0.134	-174.24
10			0.165	133.32

Figures 8-12 and 8-13 show the amplitude and phase of the probe current for $h/\lambda = 0.95$, $l/\lambda = 0.75$. From Figure 8-3 one sees that for this geometry $Y_a = 20 \text{ mS}$, that is, in this case, the monopole is also matched to a 50Ω coaxial feed-line. The curve $|I_z(z)|$ exhibits a typical double maximum variation vs z since $1/2 < l/\lambda < 1$. Note that the second maximum ($z \approx \lambda/2$) is lower than the first maximum ($z = 0$) which is also typical for a long dipole antenna driven from a coaxial line. The respective coefficients in the probe current expansion are tabulated in Table 8-6.

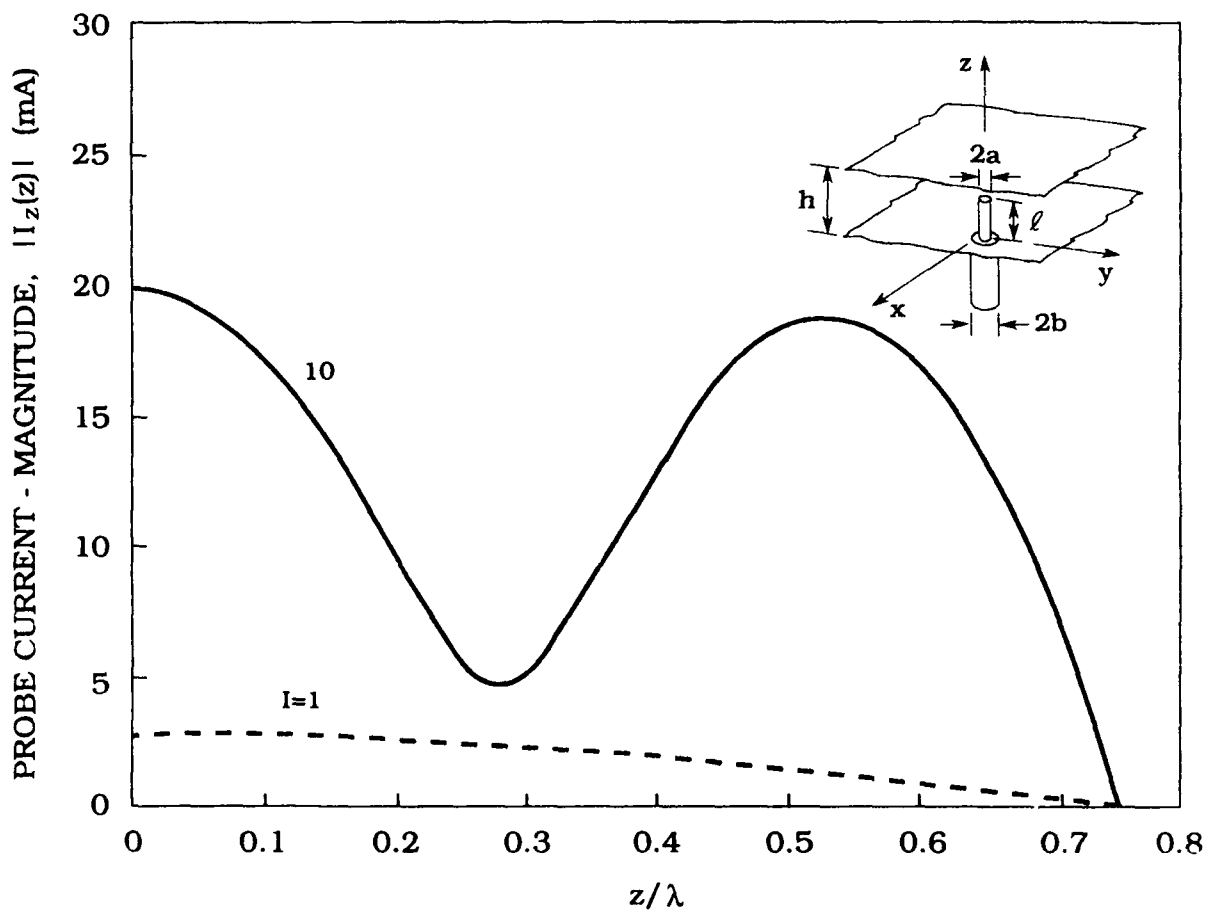


Figure 8-12. Current Distribution (Amplitude) Along a Coaxially-Driven Monopole in an Infinite Parallel Plate Waveguide; Parameter: Total Number of Current Terms $I = 1, 10$. ($l/\lambda = 0.75$, $h/\lambda = 0.95$, $a/\lambda = 0.016$, $b/\lambda = 0.037$)

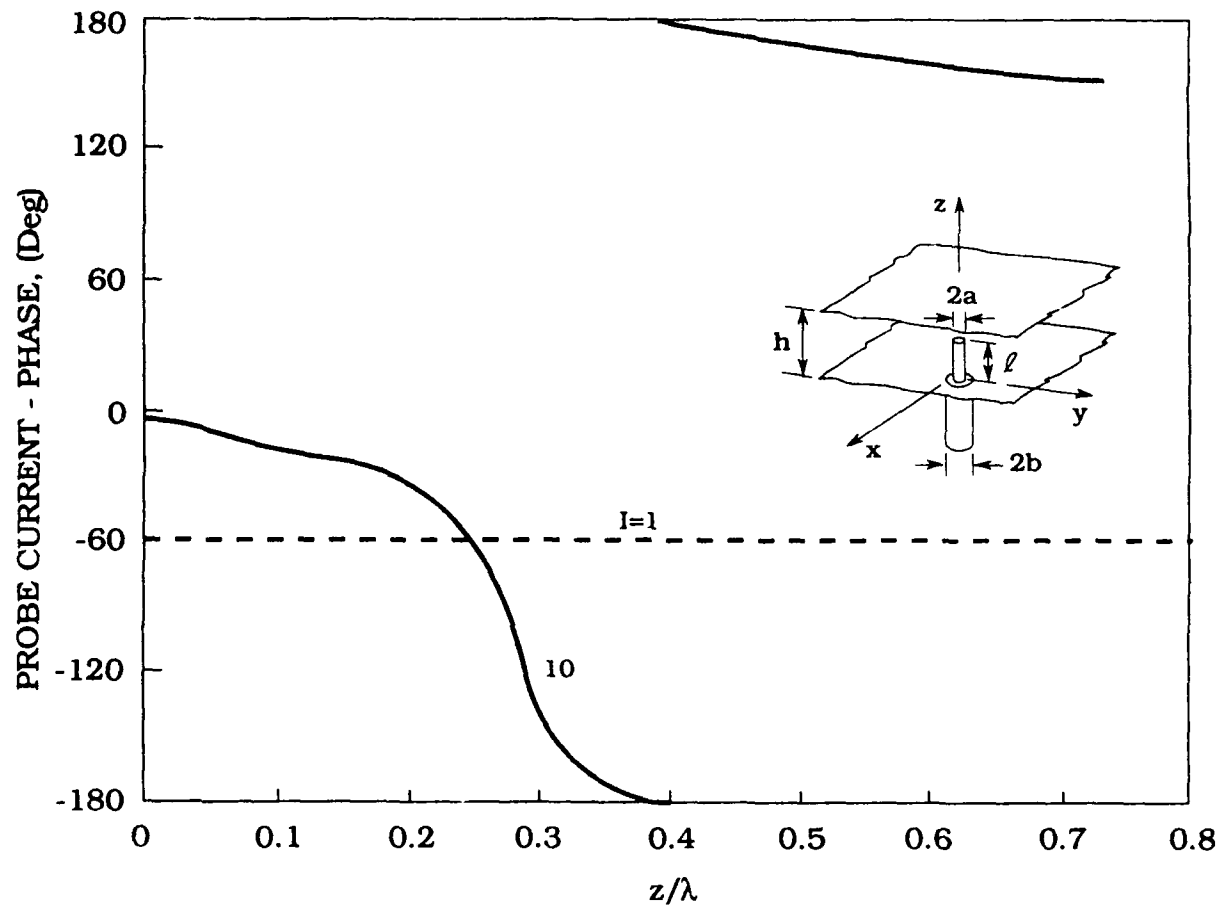


Figure 8-13. Current Distribution (Phase) Along a Coaxially-Driven Monopole in an Infinite Parallel Plate Waveguide; Parameter: Total Number of Current Terms $I = 1, 10$, ($l/\lambda = 0.75$, $h/\lambda = 0.95$, $a/\lambda = 0.016$, $b/\lambda = 0.037$)

Table 8-6. Probe Current Expansion Coefficients;
 Parameter: Total Number of Current Terms $I = 1, 10$,
 $(l/\lambda = 0.75, h/\lambda = 0.95, a/\lambda = 0.016, b/\lambda = 0.037)$

I	I=1		I=10	
	$ c_1'' $ mA	ϕ_1'' Deg.	$ c_1'' $ mA	ϕ_1'' Deg.
1	2.795	121.73	3.350	120.55
2			19.257	-11.75
3			3.316	-68.78
4			0.734	23.99
5			0.962	-61.00
6			0.360	25.37
7			0.512	-59.38
8			0.234	24.84
9			0.332	-57.74
10			0.165	23.73

8.2 Single Monopole in a Semi-Infinite Parallel Plate Region

Figures 8-14 and 8-15 show input conductance and susceptance, respectively, of a single monopole in a semi-infinite parallel plate region vs probe length l for parallel plate separations $h/\lambda = 0.3, 0.35$ and 0.4 . The distance between the probe and "back-plane", $s/\lambda = 0.25$. The feed-coaxial line with dimensions $a/\lambda = 0.016, b/\lambda = 0.037$ has an air dielectric and characteristic impedance of 50 ohms.

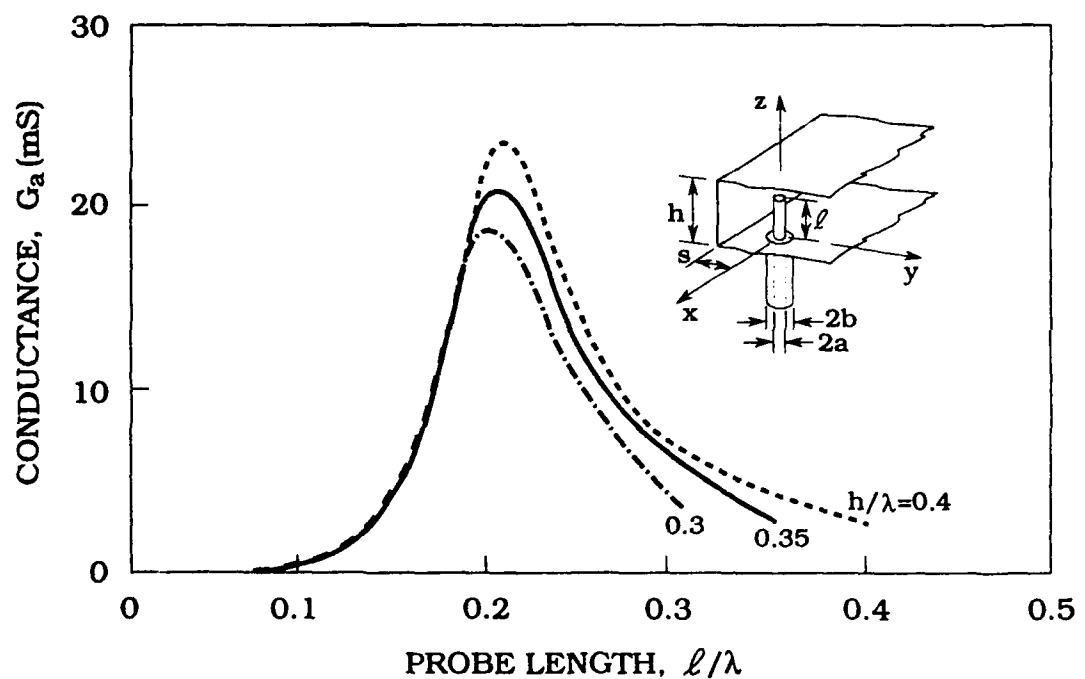


Figure 8-14. Input Conductance vs Probe Length;
 Parameter: Parallel Plate Separation $h/\lambda = 0.3, 0.35,$
 $0.4, (a/\lambda = 0.016, b/\lambda = 0.037, s/\lambda = 0.25)$

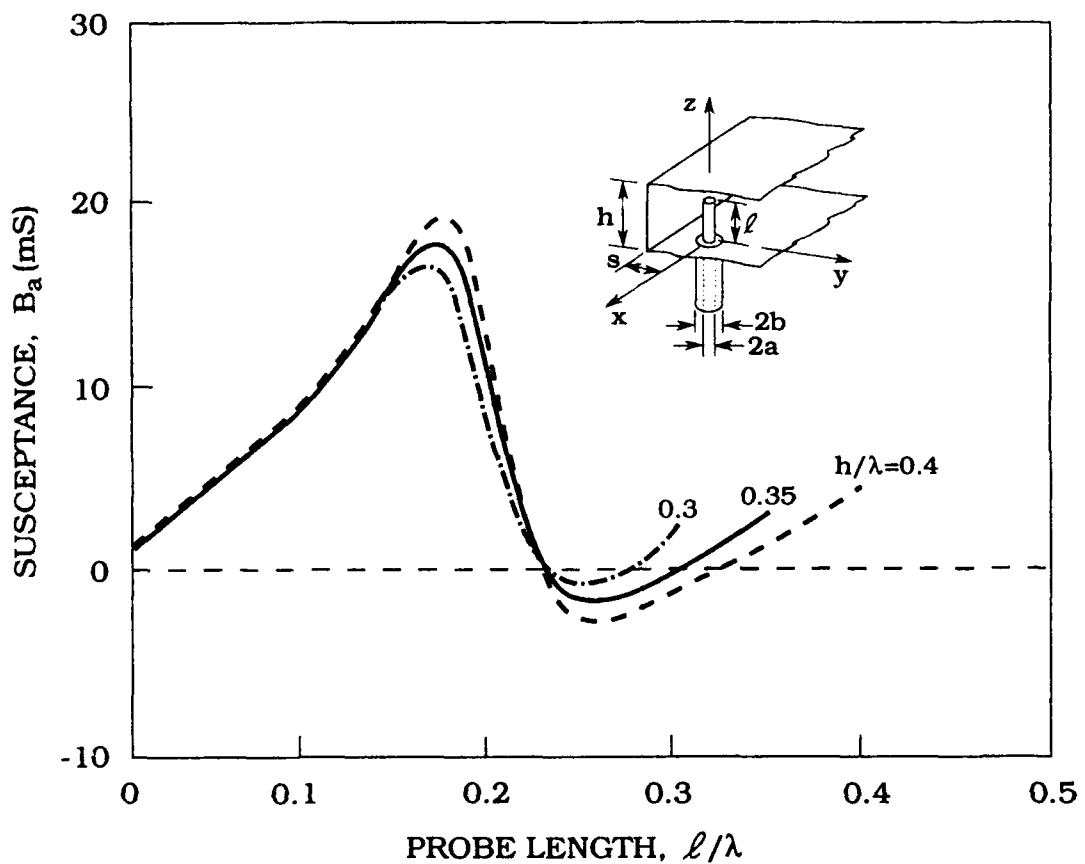


Figure 8-15. Input Susceptance vs Probe Length;
 Parameter: Parallel Plate Separation $h/\lambda = 0.3, 0.35, 0.4$, $(a/\lambda = 0.016, b/\lambda = 0.037, s/\lambda = 0.25)$

It is observed, from Figures 8-1, 8-2, 8-14, and 8-15 that for the short probes ($l/\lambda < 0.1$) the input conductance and susceptance of the single monopole in a semi-infinite parallel plate waveguide is practically the same as that of a single monopole in an infinite parallel plate region. This is expected because a short probe radiates very little power into the parallel plate region. Consequently, for a monopole in a semi-infinite parallel plate waveguide, coupling or mutual interaction between the probe and its image is small. As probe length increases, the curves for conductance and susceptance in Figures 8-14 and 8-15 slowly depart from those in Figures 8-1 and 8-2. The difference is due to mutual coupling between the probe and its image.

As for a single monopole in an infinite parallel plate region, one sees from Figures 8-14 and 8-15 that the input admittance of a single monopole in a semi-infinite parallel plate region is very sensitive to probe length (l) and almost independent of the distance between the two parallel plates (h). Here also, curves G_a and B_a exhibit resonance at approximately $l/\lambda = 0.25$. It is seen from Figure 8-15 that for $l/\lambda < 0.25$ the input admittance is capacitive for $l/\lambda <$

0.25 it is inductive, and for $l/\lambda \approx 0.25$, it passes through resonance.

For practical design applications, Figure 8-16 displays the contour plot of the magnitude of the input reflection coefficient vs the probe-ground distance (s/λ) and probe length (l/λ) for $h/\lambda = 0.35$. It is seen that for $s/\lambda = s_c/\lambda = 0.227$ and $l/\lambda = l_c/\lambda = 0.219$, the reflection coefficient is zero. Thus a single monopole radiating into a semi-infinite parallel plate region is matched to the 50 ohm coaxial-feed line. It was found that for any h/λ one can find a corresponding s_c/λ and l_c/λ so that the input reflection coefficient $\Gamma_a = 0$.

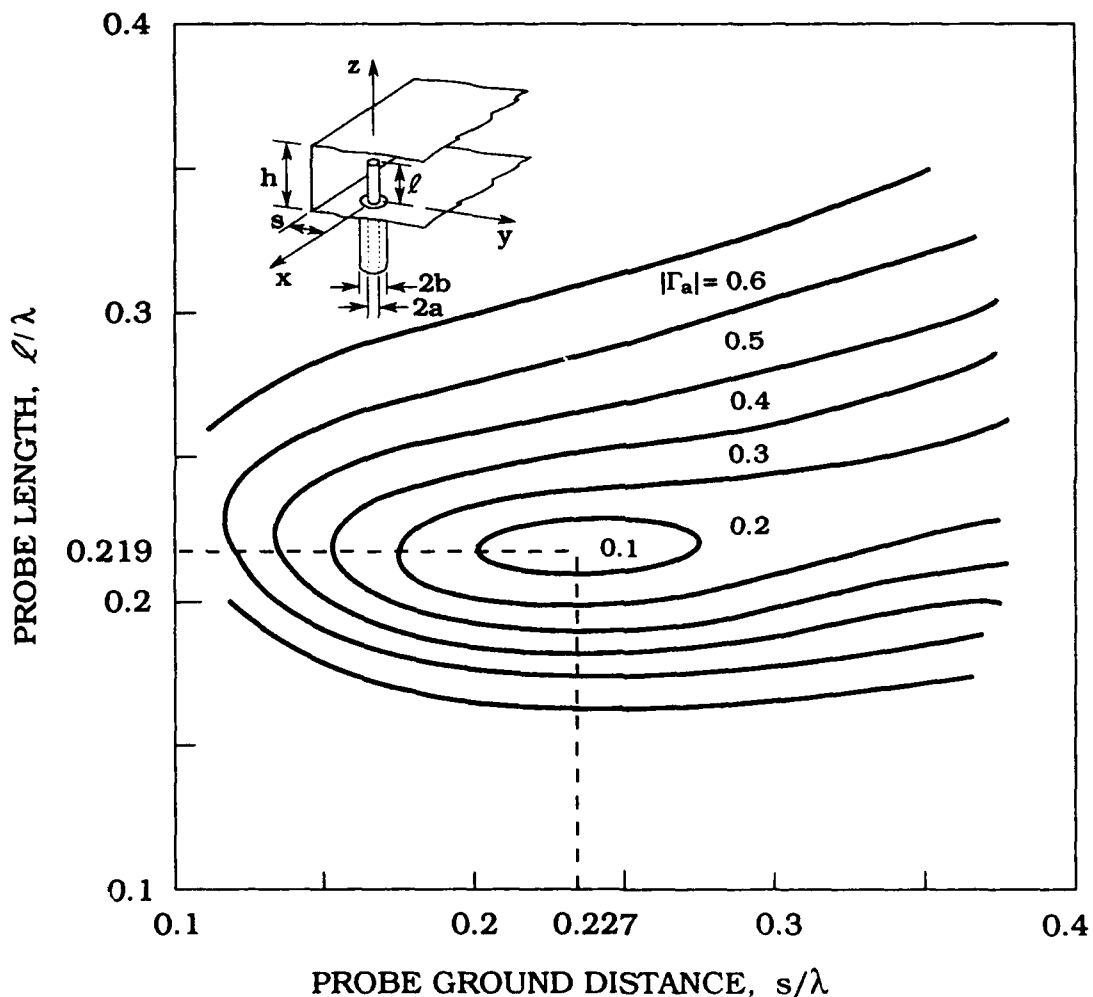


Figure 8-16. Reflection Coefficient (Contour Plot of Magnitude) vs Probe-Ground Distance and Probe Length ($h/\lambda = 0.35$, $a/\lambda = 0.016$, $b/\lambda = 0.037$)

Input impedance vs probe-ground distance (dashed curve) for $l/\lambda = 0.15, 0.2, 0.25$, and 0.3 and vs probe length (solid curve) for $s/\lambda = 0.15, 0.2, 0.25$, and 0.3 is shown in Figure 8-17. The Smith chart normalization $Z_N = 50$ ohms. Note that although impedance is more sensitive to l/λ than s/λ , the curves $l/\lambda = \text{const}$ and $s/\lambda = \text{const}$ are approximately orthogonal. This property is useful in determination of l_c/λ and s_c/λ which correspond to a point $\Gamma_a = 0$.

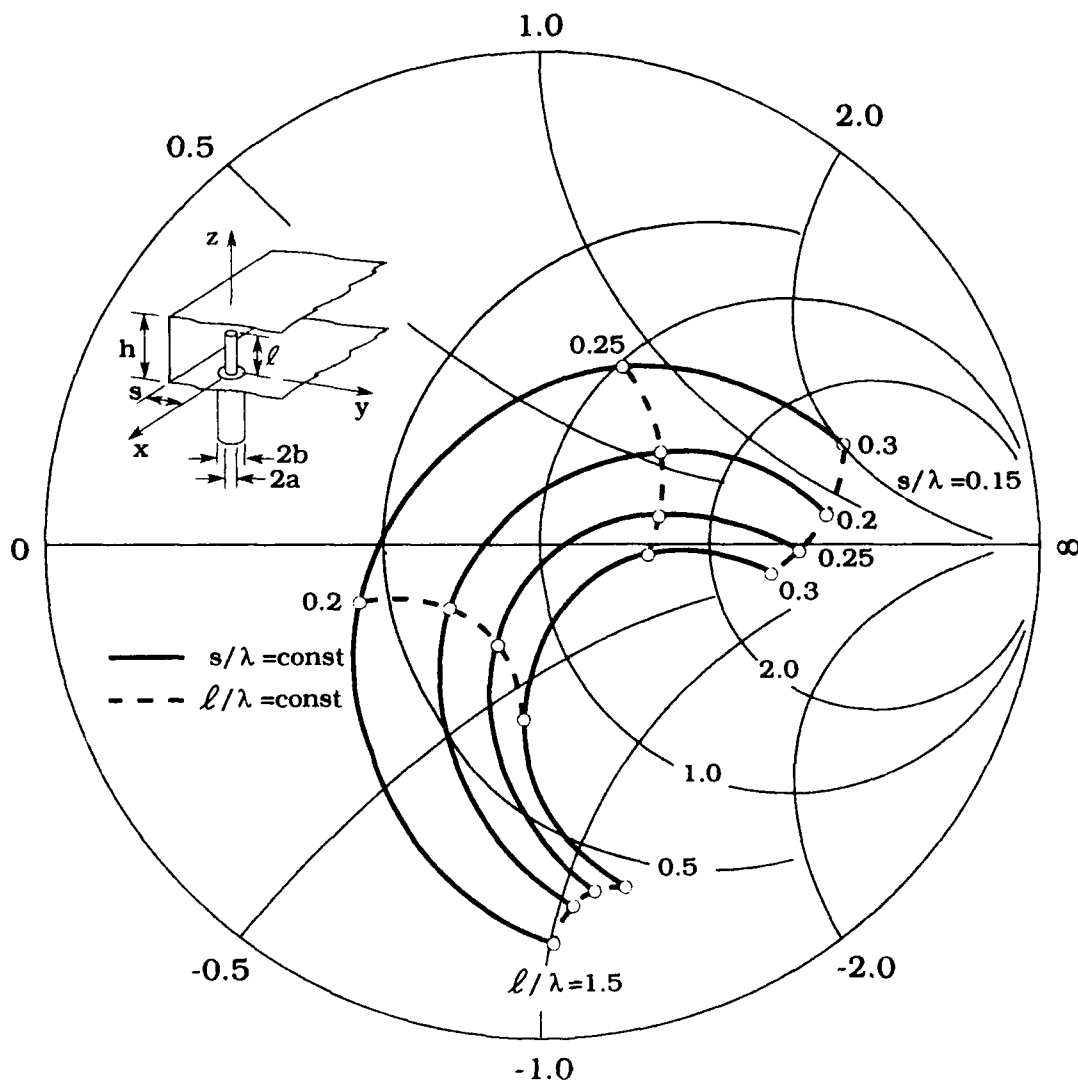


Figure 8-17. Input Impedance vs Probe-Ground Distance and Probe Length. ($h/\lambda = 0.35$, $a/\lambda = 0.016$, $b/\lambda = 0.037$, $Z_N = 50 \Omega$)

Figure 8-18 shows input impedance vs probe length for $s_c/\lambda = 0.2275$ (solid curve) and input impedance vs probe-ground distance for $l_c/\lambda = 0.2187$ (dashed curves). The two curves intersect at the point $\Gamma_a = 0$ since as already mentioned for $s_c/\lambda = 0.2275$, $l_c/\lambda = 0.2187$ the monopole input impedance is 50 ohms.

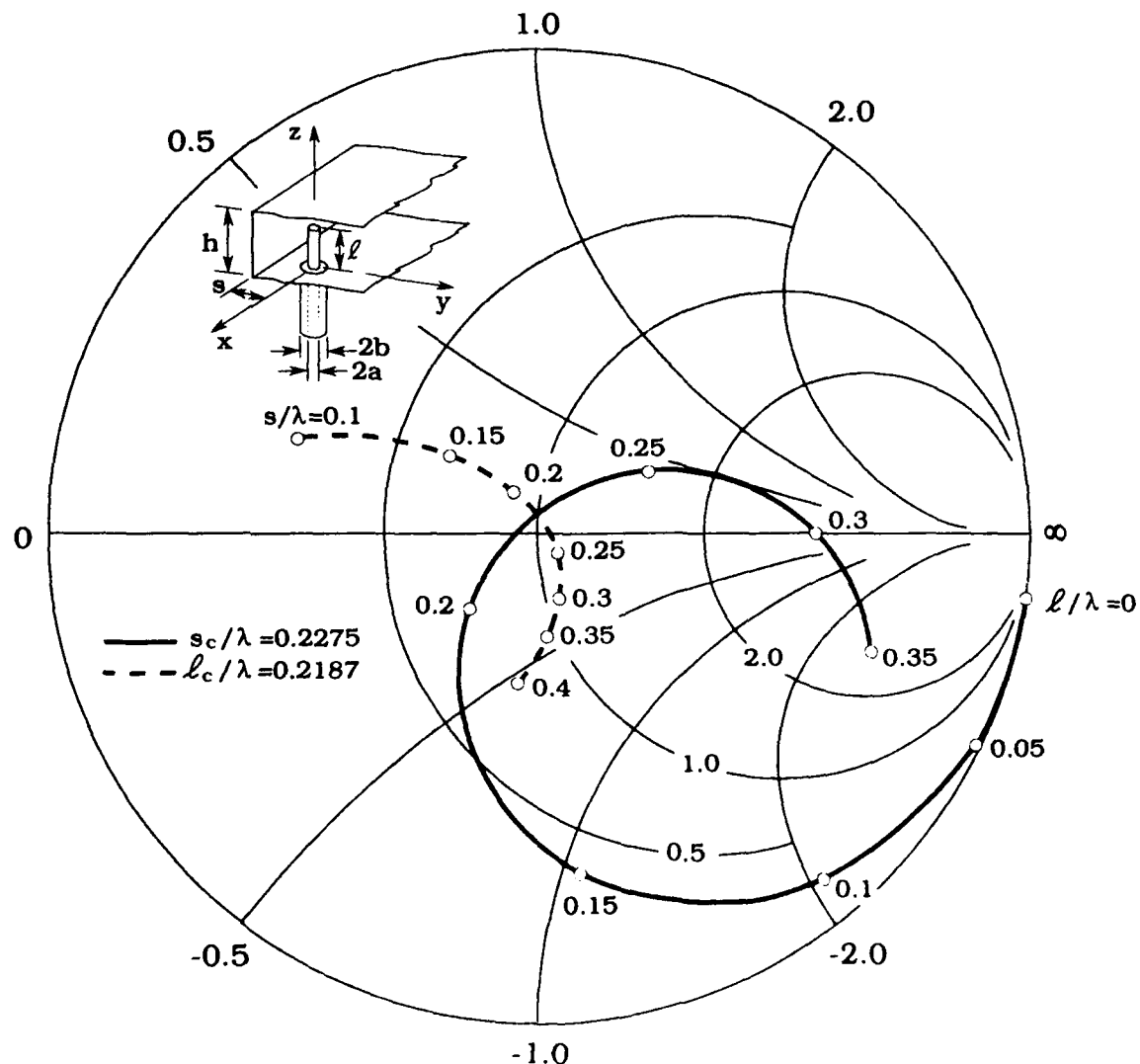


Figure 8-18. Input Impedance vs Probe-Ground Distance ($l_c/\lambda = 0.2187$) and vs Probe Length ($s_c/\lambda = 0.2275$).
($h/\lambda = 0.35$, $a/\lambda = 0.016$, $b/\lambda = 0.037$, $Z_N = 50 \Omega$)

For the same case ($l_c/\lambda = 0.2187$, $s_c/\lambda = 0.2275$), Figure 8-19 shows input impedance vs frequency. It is seen that the frequency bandwidth corresponding to a VSWR of 2:1 is approximately 40 percent.

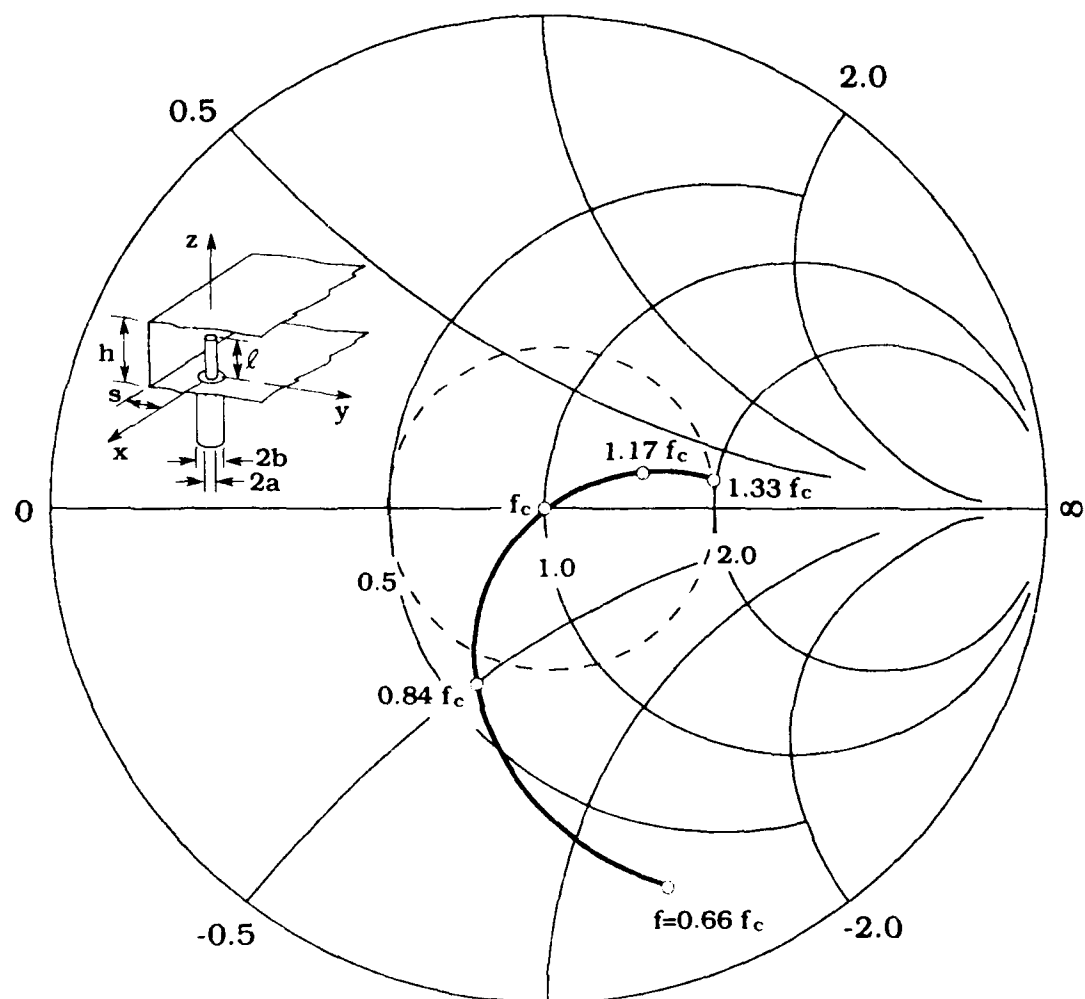


Figure 8-19. Input Impedance vs Frequency ($h/\lambda_c = 0.35$, $l_c/\lambda_c = 0.2187$, $s_c/\lambda_c = 0.2275$, $a/\lambda_c = 0.016$, $b/\lambda_c = 0.037$, $Z_N = 50 \Omega$)

Figure 8-20 shows the dependence of input impedance on probe radius (a). As in Section 8.1, the radius of the outer coaxial conductor is $b = 2.3 a$, so that in all cases the characteristic impedance of the coaxial feed lines $Z_c = 50$ ohms. From this figure it is seen that input admittance is almost independent of probe radius for $a/\lambda > 0.01$.

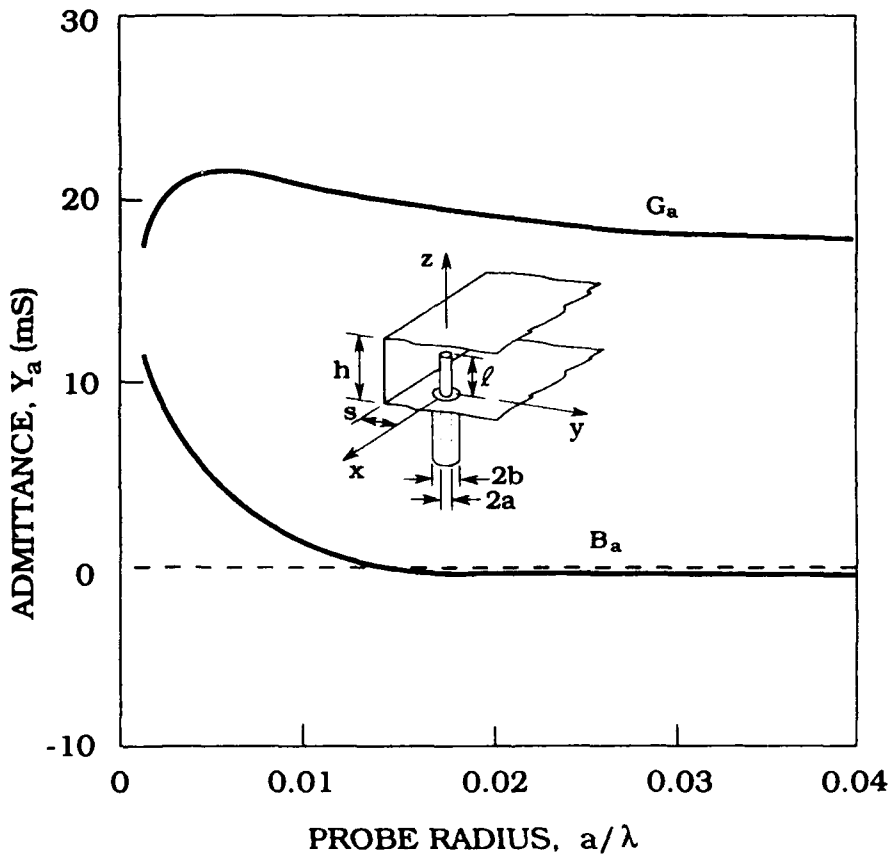


Figure 8-20. Input Admittance vs Probe Radius ($h/\lambda = 0.35$, $s_c/\lambda = 0.2275$, $l_c/\lambda = 0.2187$, $b/\lambda = 2.3 a/\lambda$, $Z_N = 50 \Omega$)

Based on Eq. (7-3), Figures 8-21 to 8-25 show the amplitude and phase of the probe current. The dashed curve represents the probe current distribution for a single current term [$I = 1$ in Eq. (7-3a)] and the solid curve represents the probe current distribution with ten current terms [$I = 10$ in Eq. (7-3a)]. The aperture voltage in the coaxial feed-line [see Eq. (7-3b)] is $V_0(z = 0^-) = 1$ V.

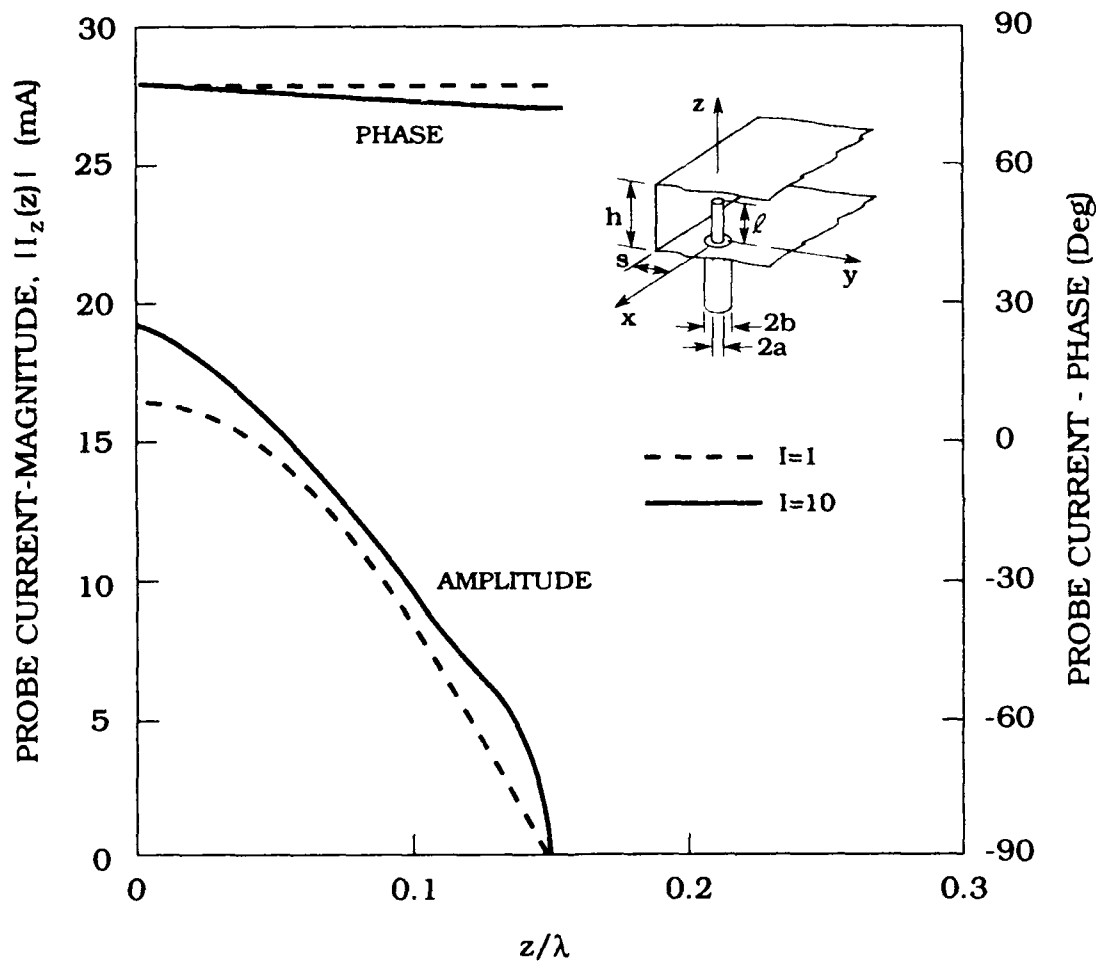


Figure 8-21. Current Distribution Along a Coaxially-Driven Monopole in a Semi-Infinite Parallel Plate Region.
 $(h/\lambda = 0.35, l/\lambda = 0.15, s/\lambda = 0.15, a/\lambda = 0.016, b/\lambda = 0.037)$

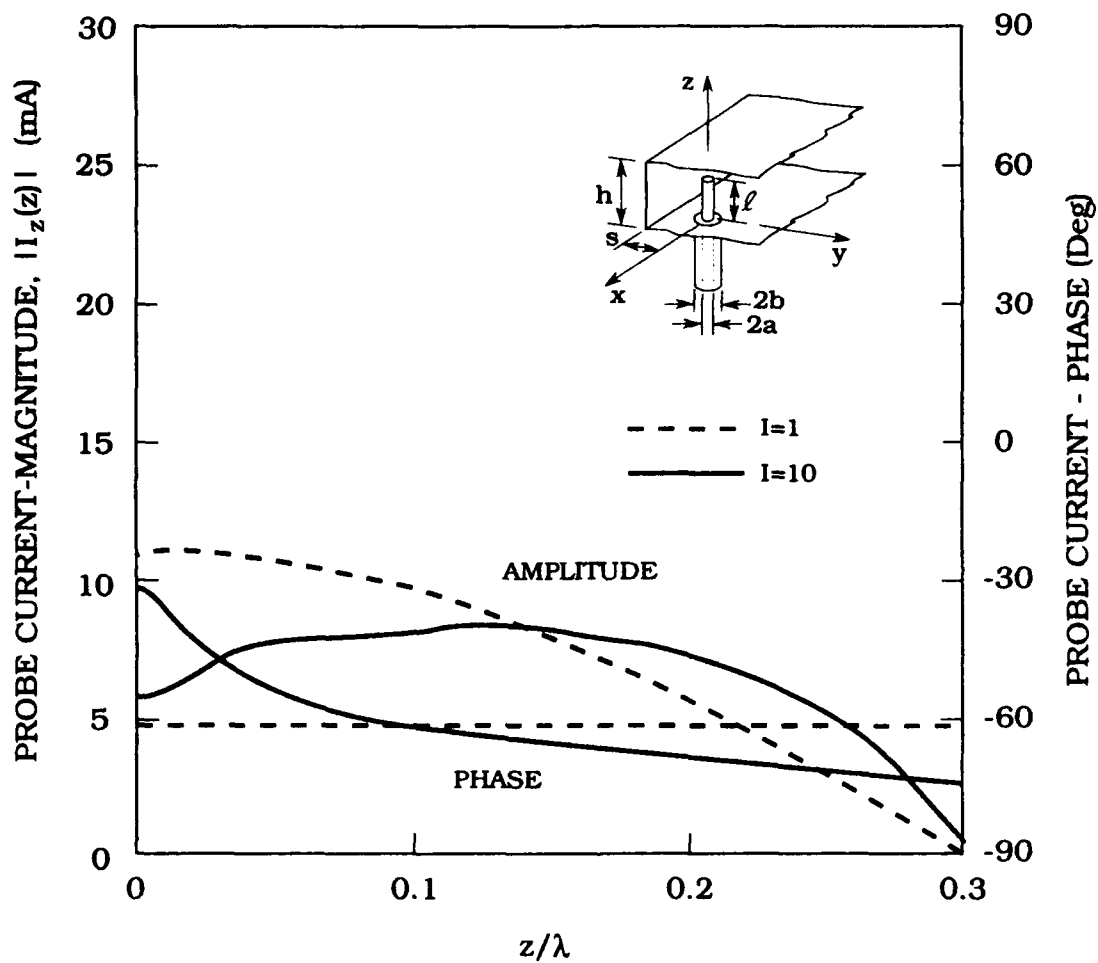


Figure 8-22. Current Distribution Along a Coaxially-Driven Monopole in a Semi-Infinite Parallel Plate Region.
 $(h/\lambda = 0.35, l/\lambda = 0.3, s/\lambda = 0.15, a/\lambda = 0.016, b/\lambda = 0.037)$

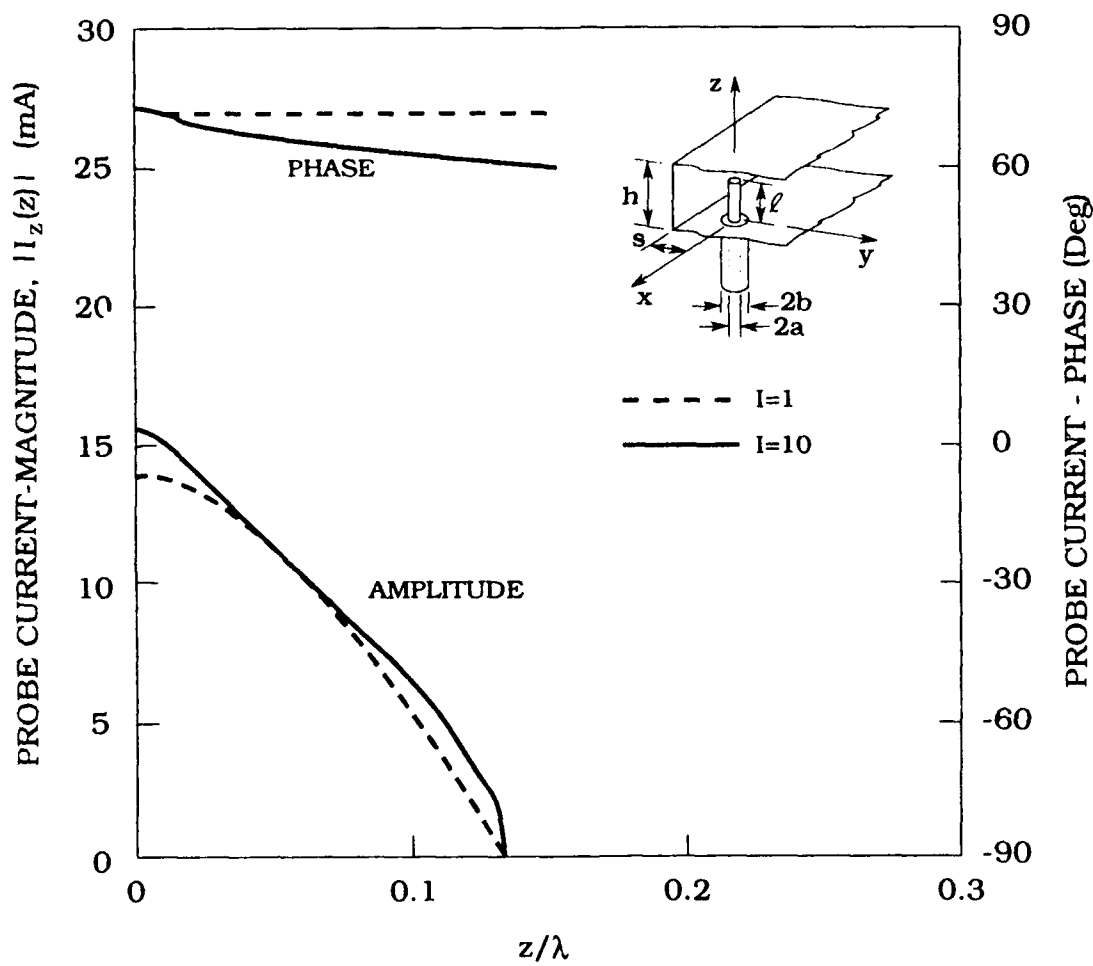


Figure 8-23. Current Distribution Along a Coaxially-Driven Monopole in a Semi-Infinite Parallel Plate Region.
 $(h/\lambda = 0.35, l/\lambda = 0.15, s/\lambda = 0.3, a/\lambda = 0.016, b/\lambda = 0.037)$

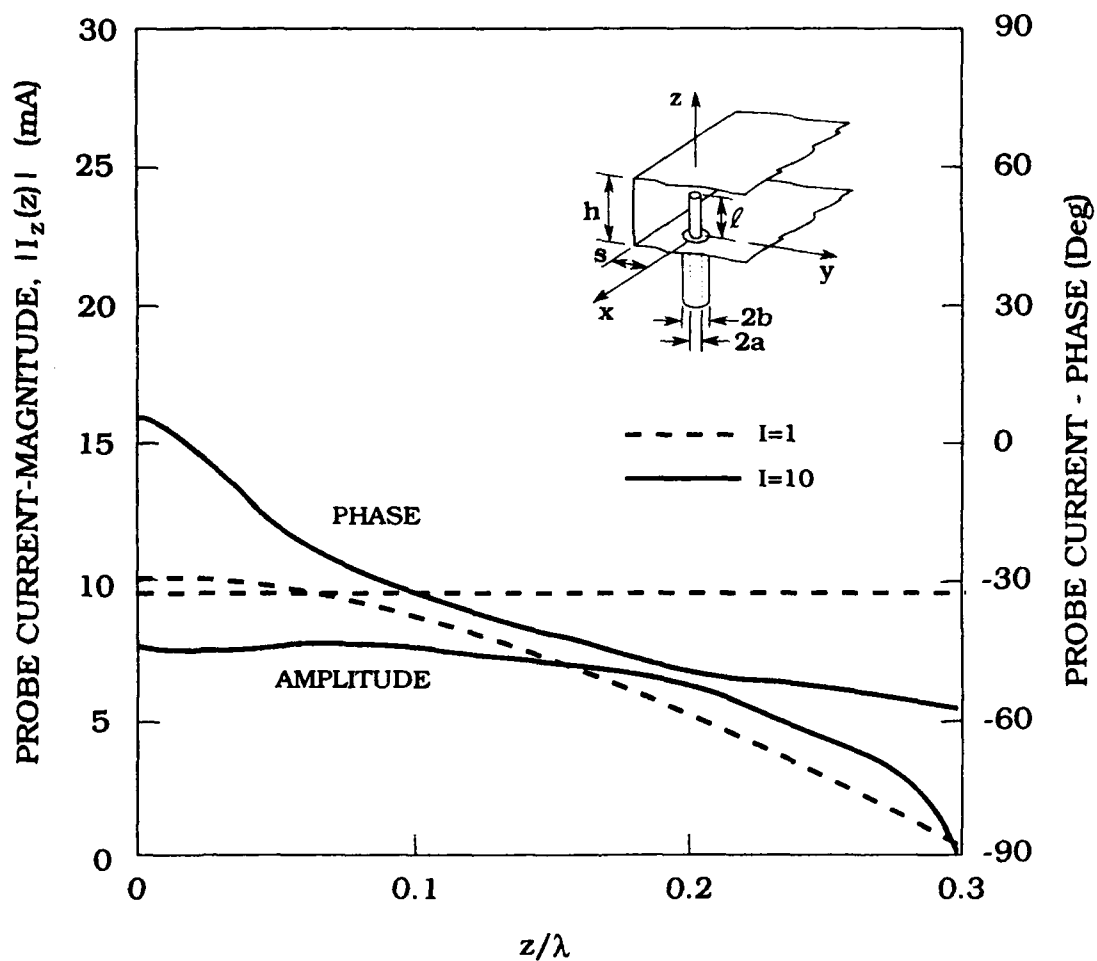


Figure 8-24. Current Distribution Along a Coaxially-Driven Monopole in a Semi-Infinite Parallel Plate Region.
 $(h/\lambda = 0.35, l/\lambda = 0.3, s/\lambda = 0.3, a/\lambda = 0.016, b/\lambda = 0.037)$

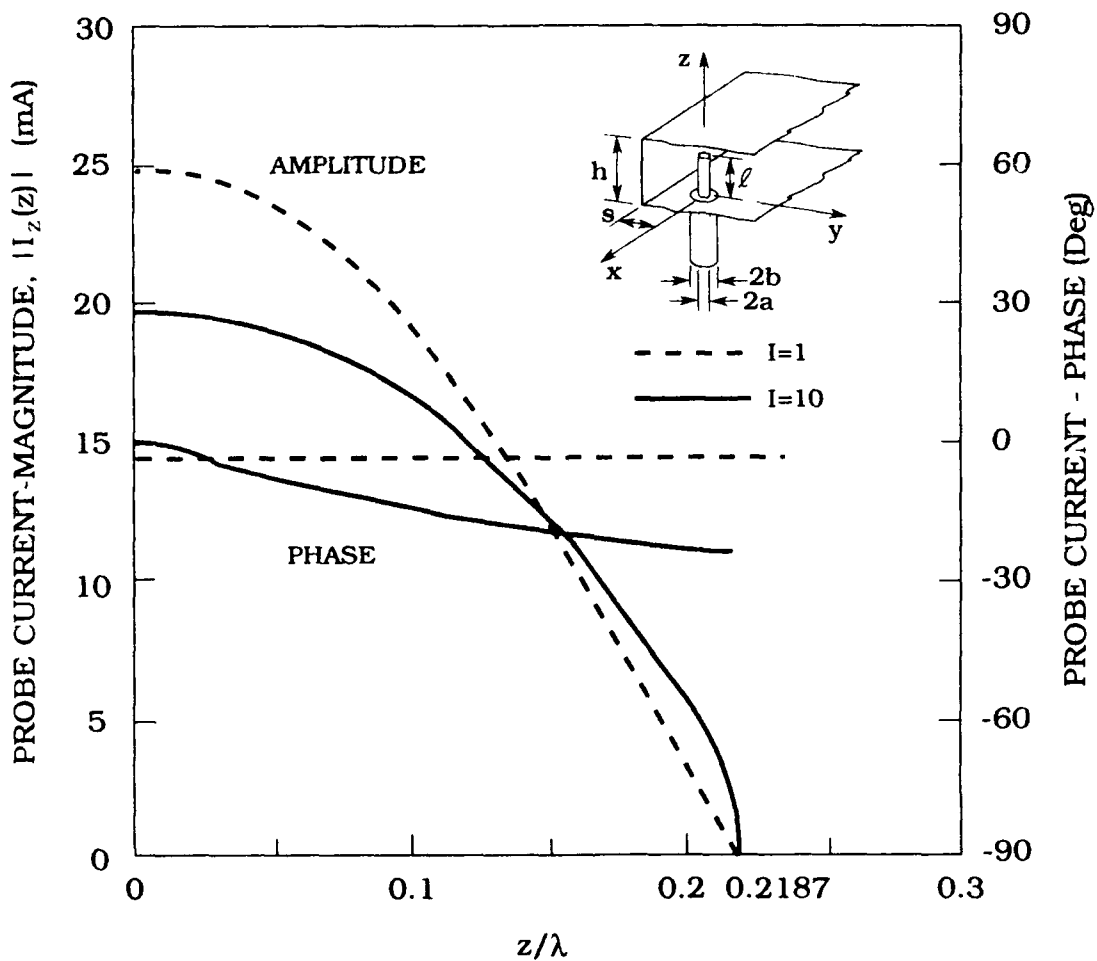


Figure 8-25. Current Distribution Along a Coaxially-Driven Monopole in a Semi-Infinite Parallel Plate Region, $(h/\lambda = 0.35, l_c/\lambda = 0.2187, s_c/\lambda = 0.2275, a/\lambda = 0.016, b/\lambda = 0.037)$

Figures 8-21 to 8-24 present current distribution along the probe for $s/\lambda = 0.15, 0.3$ and $l/\lambda = 0.15, 0.3$. Notice that as in Section 8.6 for the short probes ($l/\lambda \leq 0.15$) a single current term in (7-3a) approximates the total probe current fairly well while for $l/\lambda > 0.15$ more terms are needed.

Figure 8-25 exhibits probe current variation vs z/λ for the monopole matched ($s_c/\lambda = 0.2275, l_c/\lambda = 0.2187$) to a 50 ohm coaxial feed-line. Notice that, as expected, at $z = 0^+$ $|I_z(z = 0^+)| \approx 20$ mA and the probe current phase is zero.

For the same geometries the probe current expansion coefficients c_i'' as given by Eq. (7-3b) are given in Tables 8-7 to 8-11. In each case coefficients are given for the single ($I = 1$) and ten ($I = 10$) current terms in Eq. (7-3a).

Table 8-7. Probe Current Expansion Coefficients:

Parameter: Total Number of Current Terms $I = 1, 10$,

($h/\lambda = 0.35$, $l/\lambda = 0.15$, $s/\lambda = 0.15$, $a/\lambda = 0.016$, $b/\lambda = 0.037$)

i	I=1		I=10	
	$ c_i'' $ mA	ϕ_i'' Deg.	$ c_i'' $ mA	ϕ_i'' Deg.
1	16.498	-100.93	17.940	-103.39
2			0.523	-152.86
3			1.155	-100.69
4			0.197	-131.88
5			0.471	-101.17
6			0.121	-124.41
7			0.264	-101.64
8			0.085	-120.54
9			0.172	-102.05
10			0.065	-118.08

Table 8-8. Probe Current Expansion Coefficients:

Parameter: Total Number of Current Terms $I = 1, 10$,

($h/\lambda = 0.35$, $l/\lambda = 0.3$, $s/\lambda = 0.15$, $a/\lambda = 0.016$, $b/\lambda = 0.037$)

i	I=1		I=10	
	$ c_i'' $ mA	ϕ_i'' Deg.	$ c_i'' $ mA	ϕ_i'' Deg.
1	11.085	118.03	9.139	120.05
2			3.240	93.75
3			0.225	-123.03
4			0.766	95.98
5			0.080	-135.45
6			0.373	96.69
7			0.040	-149.19
8			0.226	97.16
9			0.025	-164.04
10			0.154	97.52

Table 8-9. Probe Current Expansion Coefficients;
 Parameter: Total Number of Current Terms $I = 1, 10$,
 $(h/\lambda = 0.35, l/\lambda = 0.15, s/\lambda = 0.3, a/\lambda = 0.016, b/\lambda = 0.037)$

I	I=1		I=10	
	$ c''_I $ mA	ϕ''_I Deg.	$ c''_I $ mA	ϕ''_I Deg.
1	13.939	-108.58	14.546	-111.73
2			0.637	162.64
3			0.977	-106.63
4			0.173	-171.87
5			0.395	-107.50
6			0.096	-157.90
7			0.220	-108.37
8			0.065	-149.64
9			0.143	-109.14
10			0.049	-144.11

Table 8-10. Probe Current Expansion Coefficients;
 Parameter: Total Number of Current Terms $I = 1, 10$,
 $(h/\lambda = 0.35, l/\lambda = 0.3, s/\lambda = 0.3, a/\lambda = 0.016, b/\lambda = 0.037)$

I	I=1		I=10	
	$ c''_I $ mA	ϕ''_I Deg.	$ c''_I $ mA	ϕ''_I Deg.
1	9.979	147.65	8.489	151.57
2			3.075	97.24
3			0.360	-126.16
4			0.709	101.09
5			0.142	-132.99
6			0.342	102.45
7			0.077	-139.67
8			0.207	103.36
9			0.048	-146.28
10			0.140	104.08

As discussed in Section 8.1 the input admittance can also be calculated using Eq. (8-2). For the geometries of Figures 8-21 to 8-25, Table 8-11 compares results for input admittance obtained from Eqs. (4-44) and (8-2). In all cases $I = 10$. Like the results for a single monopole in an infinite parallel plate region, the difference between these two results is very small (less than 1 percent).

Table 8-11. Probe Current Expansion Coefficients;
 Parameter: Total Number of Current Terms $i = 1, 10$,
 $(h/\lambda = 0.35, l_c/\lambda = 0.2187, s_c/\lambda = 0.2275, a/\lambda = 0.016, b/\lambda = 0.037)$

i	I=1		I=10	
	$ c_i'' $ mA	ϕ_i'' Deg.	$ c_i'' $ mA	ϕ_i'' Deg.
1	25.182	176.54	21.321	169.18
2			3.049	124.51
3			0.831	-167.70
4			0.784	129.92
5			0.357	-170.96
6			0.391	132.66
7			0.210	-174.25
8			0.241	134.61
9			0.141	-176.96
10			0.166	136.14

Table 8-12. Comparison Between Results Obtained from
 Eqs. (4-44) and (8-2) for Input Admittance $Y_a = G_a + jB_a$;
 Parameter: Probe Length $l/\lambda = 0.15, 0.2187, 0.3$ and Probe-
 Ground Distance $s/\lambda = 0.15, 0.2275, 0.3$, $(h/\lambda = 0.35, a/\lambda = 0.016,$
 $b/\lambda = 0.037)$

l/λ	Y_a from Eq. (4-44)					
	$s/\lambda = 0.15$		$s/\lambda = 0.2275$		$s/\lambda = 0.3$	
	G_a mS	B_a mS	G_a mS	B_a mS	G_a mS	B_a mS
0.15	3.830	18.811			4.961	15.169
0.2187			19.709	-0.046		
0.3	4.431	-2.745			7.196	0.997

l/λ	Y_a from Eq. (8-2)					
	$s/\lambda = 0.15$		$s/\lambda = 0.2275$		$s/\lambda = 0.3$	
	G_a mS	B_a mS	G_a mS	B_a mS	G_a mS	B_a mS
0.15	3.811	18.861			4.936	15.237
0.2187			19.672	-0.051		
0.3	4.430	-2.896			7.194	0.845

Figures 8-26 to 8-28 show far-field patterns of the single monopole in a semi-infinite parallel plate waveguide region. The patterns were computed from Eq. (5-20a). As described in Section 5.2, gain patterns are normalized with respect to the power density of an isotropic source.

Figure 8-26 exhibits far-field patterns for two different spacings between probe and conducting back-plane, $s/\lambda = 0.15, 0.3$, and for the following geometry: $h/\lambda = 0.35$, $l/\lambda = 0.15$, $a/\lambda = 0.016$, $b/\lambda = 0.037$. As one may see from the Smith chart in Figure 8-17, for this geometry the monopole is "poorly" matched ($|\Gamma_a| \approx 0.75$). Consequently, the gain in the $\hat{\phi} = 0^\circ$ direction is low (about 0.45 dB). The gain patterns for $s/\lambda = 0.15$ and 0.3 differ as one may see from Figure 8-26. For $s/\lambda = 0.15$, the peak of the pattern is at $\hat{\phi} = 0^\circ$ while for $s/\lambda = 0.3$ the maximum is at $\hat{\phi} \approx 35^\circ$. The half power points are approximately at 50° off broadside for $s/\lambda = 0.15$ and 65° off broadside for $s/\lambda = 0.3$.

Figure 8-27 presents the gain pattern for the same geometry as in Figure 8-26 while the probe length is now $l/\lambda = 0.3$. Except for the higher gain ($\Gamma_a \approx 0.55$) the same pattern shape may be observed.

The gain pattern of the single monopole in an semi-infinite parallel plate waveguide region for the matched case ($l_c/\lambda = 0.2187$, $s_c/\lambda = 0.2275$) is shown by the solid curve in Figure 8-28. At $\hat{\phi} = 0^\circ$ the gain is 2.55 dB. If monopole were matched at $s_c/\lambda = 0.25$ then at $\hat{\phi} = 0^\circ$ the gain would be exactly 3.0 dB (in field). The dashed curve on the same figure represents the gain pattern also for the case $l/\lambda = 0.2187$ and $s/\lambda = 0.25$. The 3 dB points are at 57° off broadside for $s/\lambda = 0.2275$ and 60° off broadside for $s/\lambda = 0.25$.

The pattern shapes in Figures 8-26 to 8-28 are consistent with $\sin(ks \cos \hat{\phi})$ dependence on observation angle $\hat{\phi}$ as stated in Eq. (5-20a), which is typical for the two-element array with spacing $2s$ and 180° inter-element phase difference. Thus for $s/\lambda < 0.25$, the pattern is narrower than the one corresponding to $s/\lambda = 0.25$. On the other hand when $s/\lambda > 0.25$, the pattern is wider than that for $s/\lambda = 0.25$ and it will exhibit a dip in region $\hat{\phi} \approx 0^\circ$ as borne out in Figures 8-26 and 8-27.

As already discussed, the input reflection coefficient primarily depends on probe length. Thus we may conclude that the maximum gain level primarily depends on probe length (l) while the pattern shape vs observation angle $\hat{\phi}$ is primarily a function of the probe-ground spacing (s).

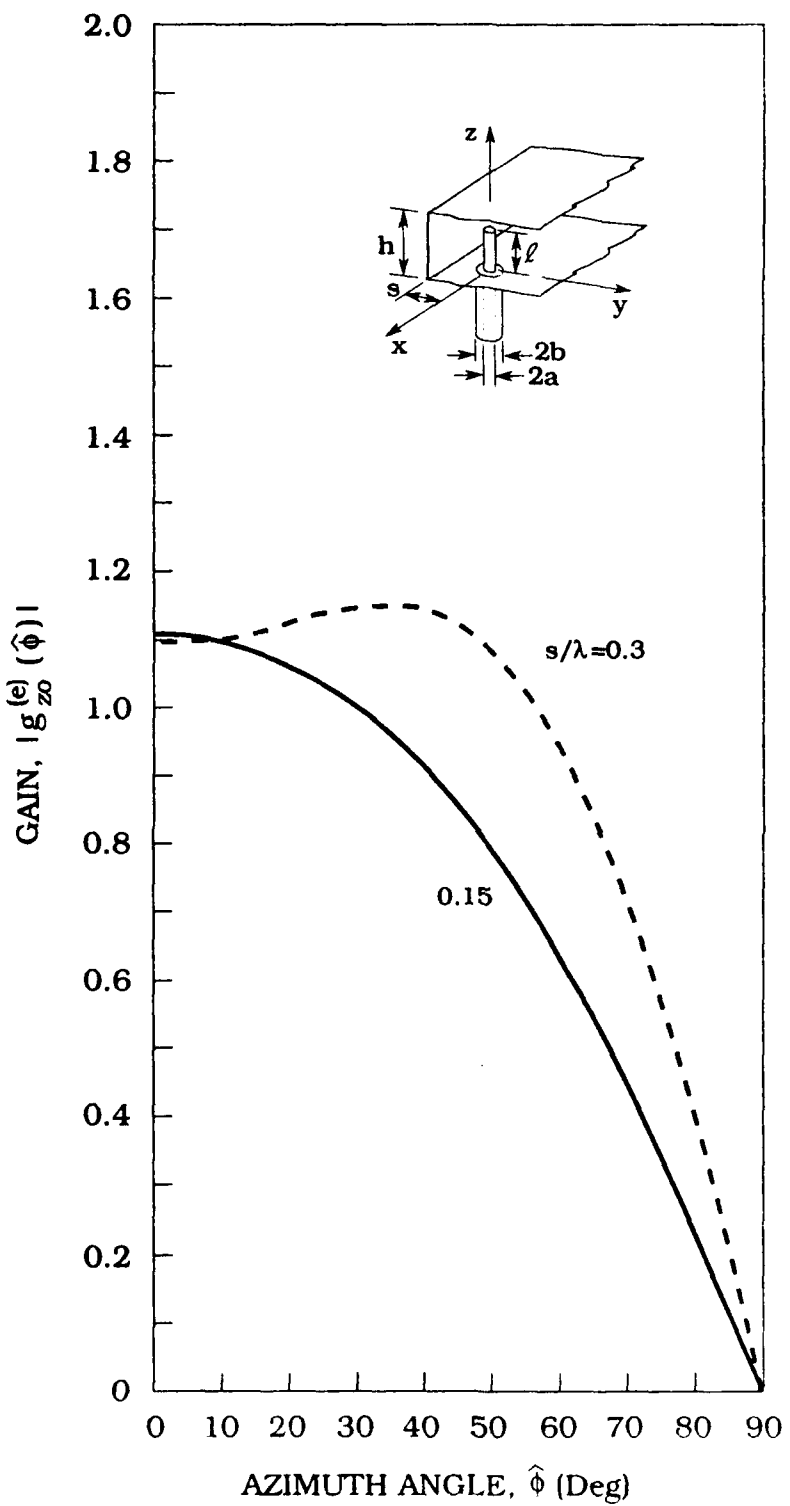


Figure 8-26. Gain Pattern ($h/\lambda = 0.35$, $l/\lambda = 0.15$, $a/\lambda = 0.016$, $b/\lambda = 0.037$, $Z_c = 50 \Omega$). Parameter: $s/\lambda = 0.15, 0.3$

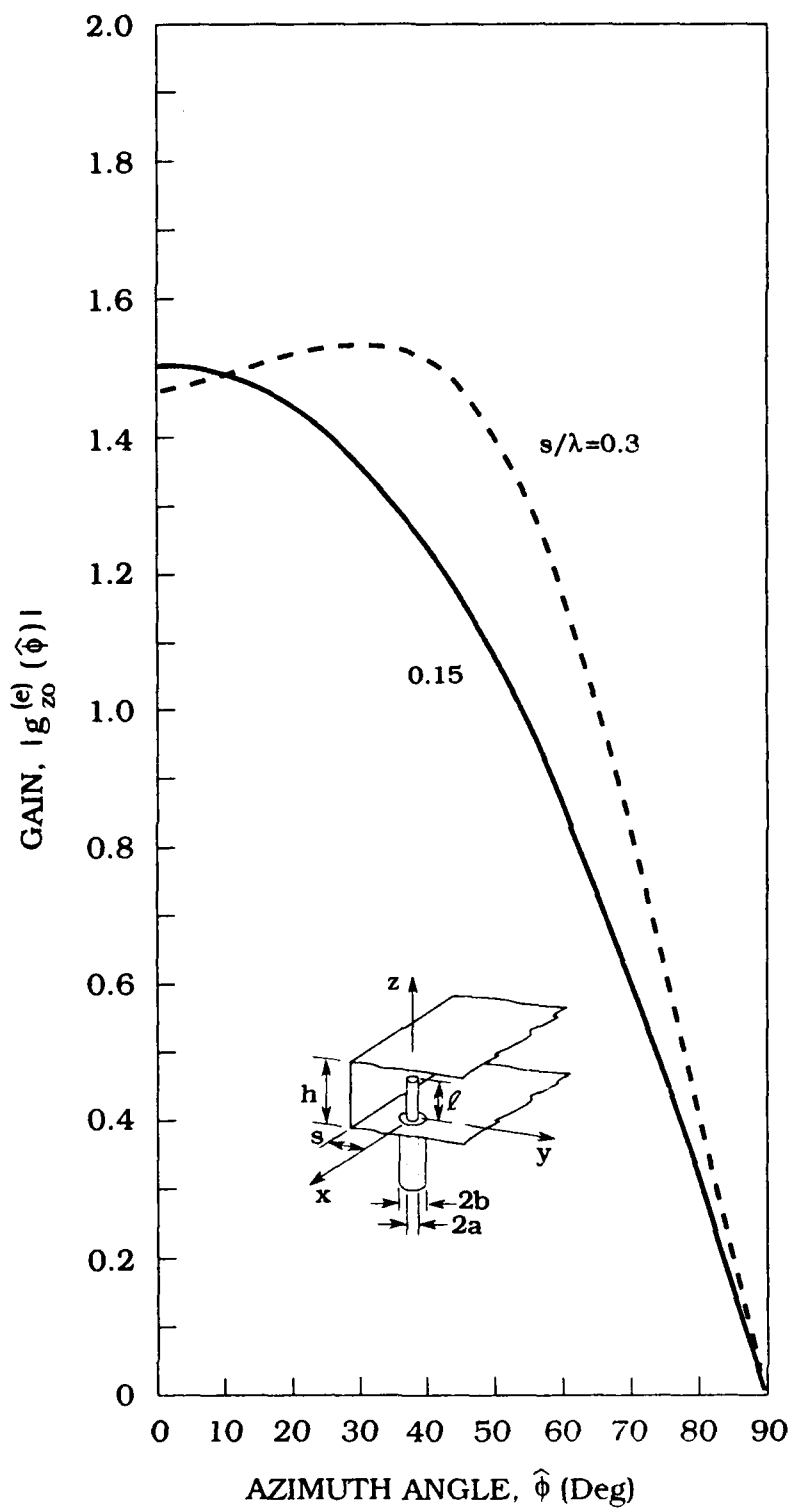


Figure 8-27. Gain Pattern ($h/\lambda = 0.35$, $l/\lambda = 0.3$, $a/\lambda = 0.016$, $b/\lambda = 0.037$, $Z_c = 50 \Omega$). Parameter: $s/\lambda = 0.15, 0.3$

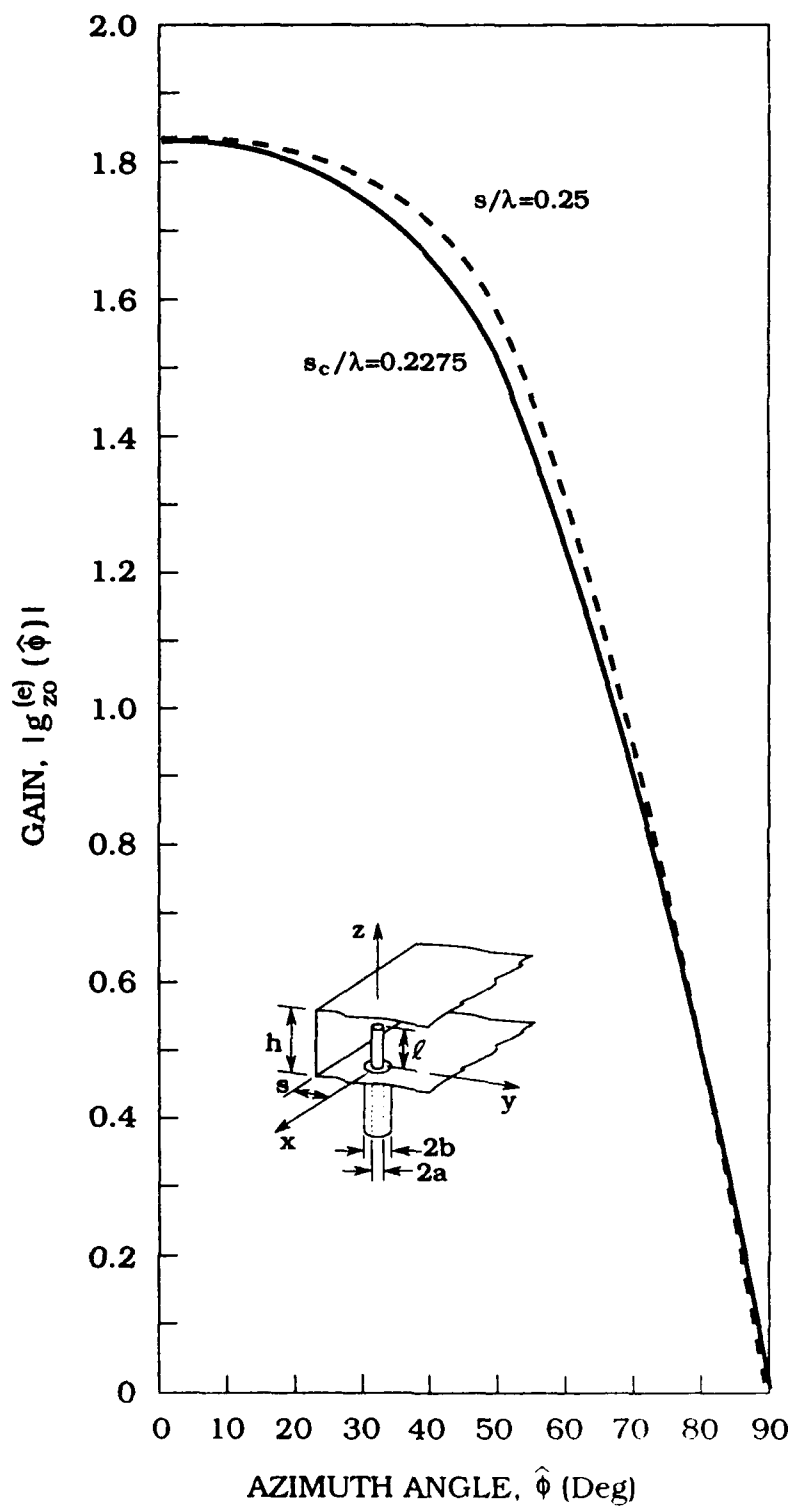


Figure 8-28. Gain Pattern ($h/\lambda = 0.35$, $l_c/\lambda = 0.2187$, $s_c/\lambda = 0.2275$, $a/\lambda = 0.016$, $b/\lambda = 0.037$, $Z_c = 50 \Omega$)

8.3 Linear Array of Coaxially-fed Monopole Elements in an Infinite Parallel Plate Waveguide

Numerical results for active admittance, probe current distribution and coupling (scattering) coefficients are presented for two typical array element spacings (a) $d = 0.4 \lambda$ and (b) $d = 0.6 \lambda$. Unless otherwise explicitly stated all of the numerical results refer to monopole elements with $a = 0.0106 \lambda$, $b = 0.034 \lambda$ and parallel plate height $h = 0.360 \lambda$. The coaxial feed-lines have $\epsilon_r = 2$ and characteristic impedance $Z_c = 50 \text{ ohms}$. Forty waveguide modes ($n_{\max} = 40$) and 10 probe current terms ($I = 10$) were used in Galerkin's method.

8.3.1 ACTIVE ADMITTANCE, $Y_a(\delta_x)$.

Active admittance is computed from Eq. (4-44) using Eq. (4-47c) for $S_n(\delta_x)$. Figures 8-29 and 8-30 display a contour plot of the magnitude of the active reflection coefficient vs probe length (l/λ) and vs parallel plate waveguide height (h/λ), both at broadside scan. It is seen (from Figure 8-29) that for $h_c/\lambda = 0.360$ and $l_c/\lambda = 0.280$ the broadside scan active reflection coefficient is zero. For $d/\lambda = 0.6$ (see Figure 8-30) there is no such point and consequently one has to introduce a matching network to match the element to the 50 ohm feed transmission line. In this section, unless otherwise stated, we assume that in both cases $l/\lambda = 0.28$ and $h/\lambda = 0.360$. Thus, numerical results will be presented for the arrays with the following dimensions:

(a) $d = 0.4 \lambda$	(b) $d = 0.6 \lambda$	(8-3)
$h_c = 0.360 \lambda$	$h = 0.360 \lambda$	
$l_c = 0.280 \lambda$	$l = 0.280 \lambda$	
$a = 0.0106 \lambda$	$a = 0.0106 \lambda$	
$b = 0.034 \lambda$	$b = 0.034 \lambda$	
$Z_c = 50 \Omega (\epsilon_r = 2)$	$Z_c = 50 \Omega (\epsilon_r = 2)$	

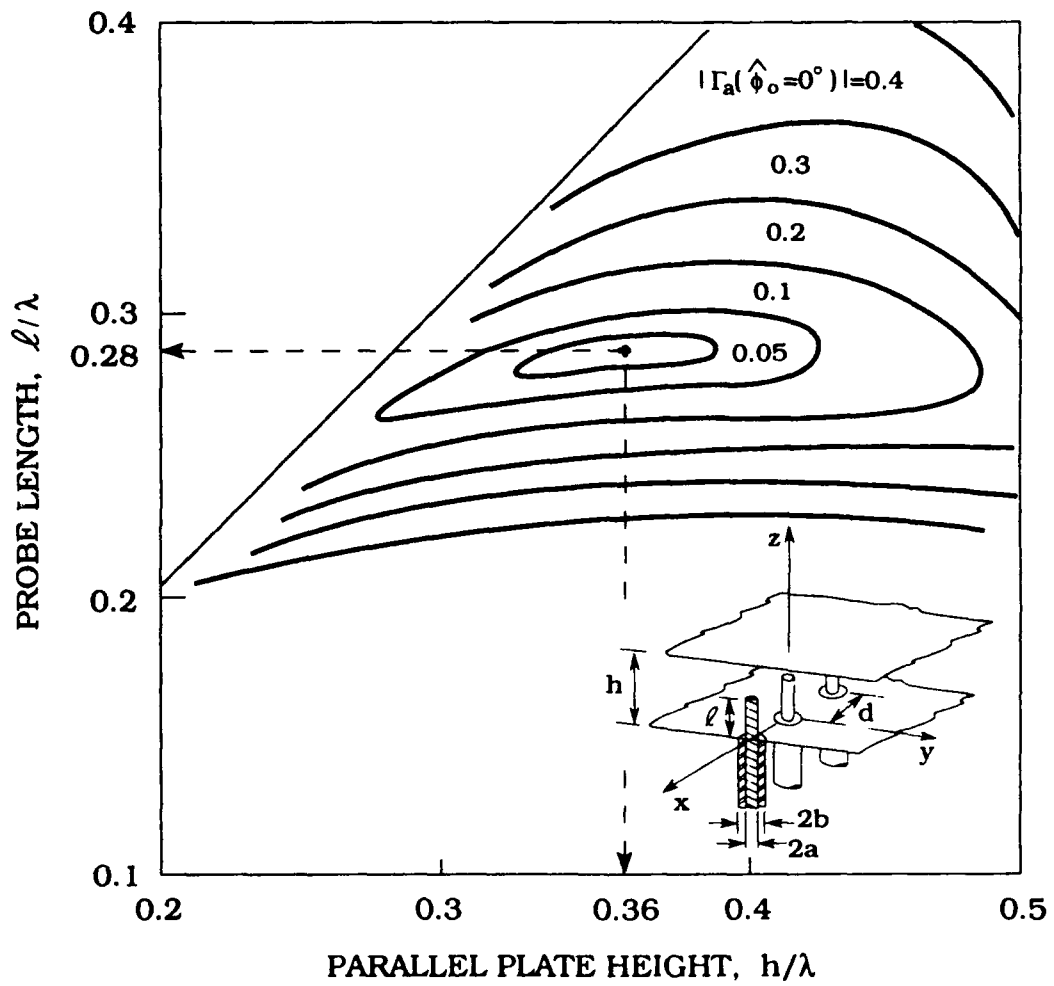


Figure 8-29. Active Reflection Coefficient (Contour Plot of Magnitude) vs Parallel Plate Height and vs Probe Length
 $(d/\lambda = 0.4, a/\lambda = 0.0106, b/\lambda = 0.0343, Z_c = 50 \Omega, \hat{\phi}_o = 0^\circ)$

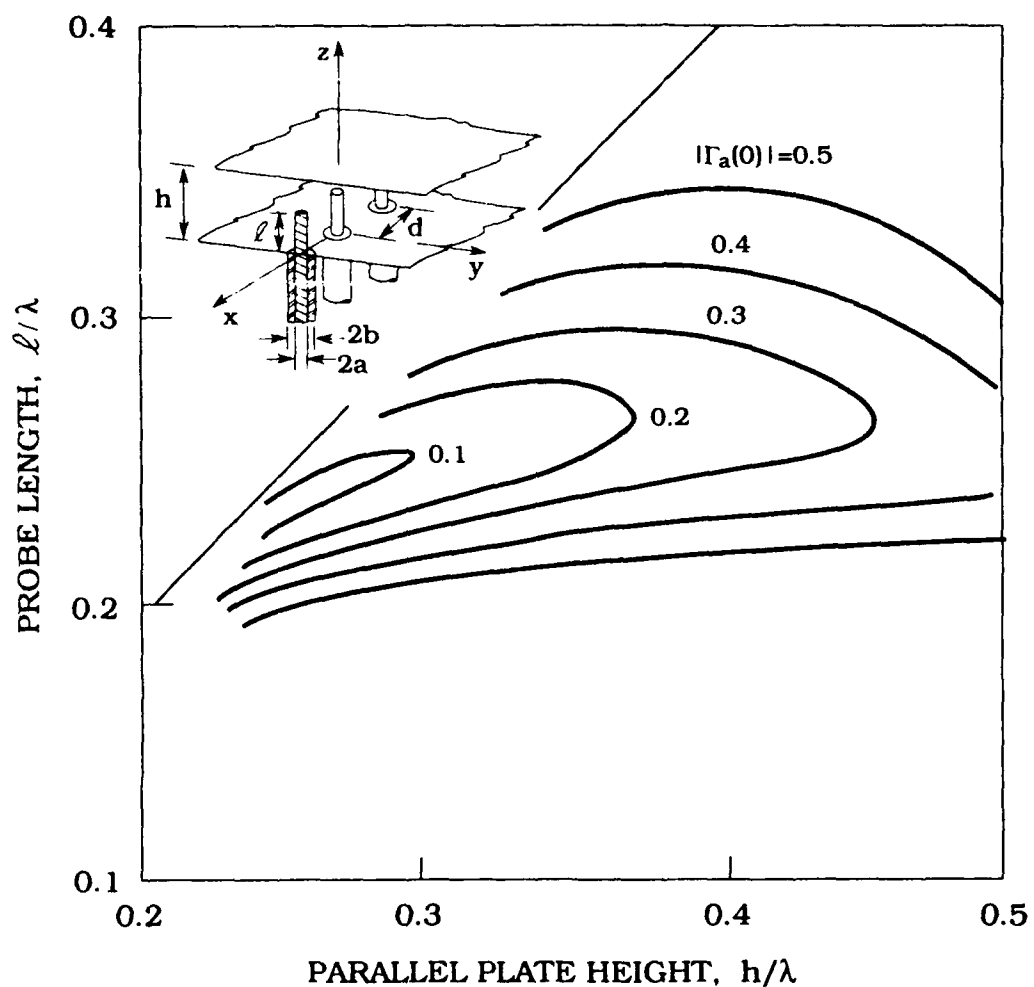


Figure 8-30. Active Reflection Coefficient (Contour Plot of Magnitude) vs Parallel Plate Height and vs Probe Length
 $(d/\lambda = 0.6, a/\lambda = 0.0106, b/\lambda = 0.0343, Z_c = 50 \Omega, \phi_0 = 0^\circ)$

For these two geometries Figures 8-31 and 8-32, respectively present the active impedance vs probe length l/λ and vs parallel plate distance h/λ . Notice that the active impedance appears to be sensitive to probe length and relatively less sensitive to the distance between the two parallel plates. Also it is interesting to note that for $l/\lambda < 0.280$ the impedance is capacitive (primarily due to the aperture) and for probe lengths $l/\lambda > 0.28$ inductive.

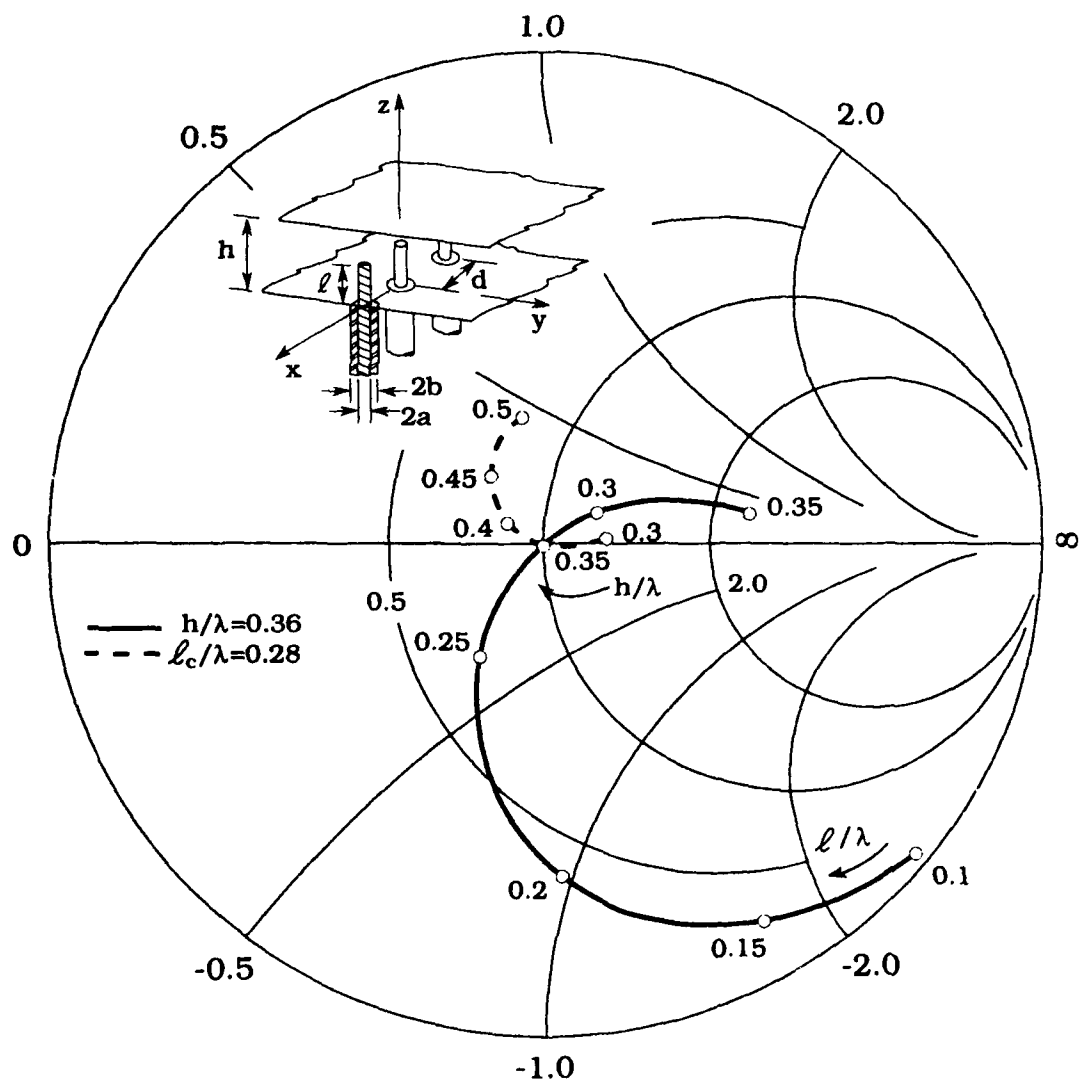


Figure 8-31. Active Impedance vs Parallel Plate Distance and vs Probe Length - Matched Case ($d/\lambda = 0.4$, $h_c/\lambda = 0.36$, $l_c/\lambda = 0.28$, $a/\lambda = 0.0106$, $b/\lambda = 0.0343$, $Z_c = 50 \Omega$, $\phi_0 = 0^\circ$)

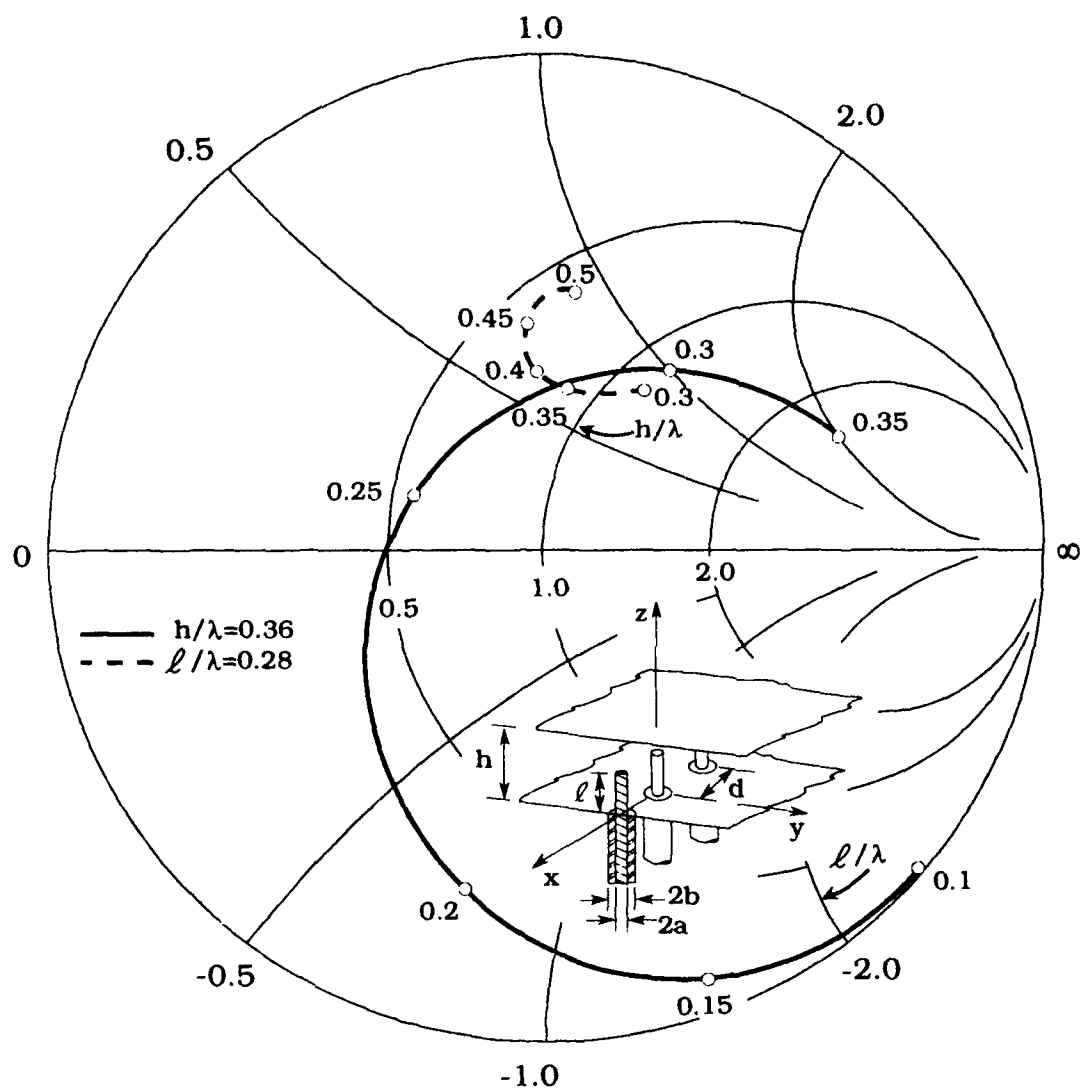


Figure 8-32. Active Impedance vs Parallel Plate Distance and vs Probe Length ($d/\lambda = 0.6$, $h/\lambda = 0.36$, $l/\lambda = 0.28$, $a/\lambda = 0.0106$, $b/\lambda = 0.0343$, $Z_c = 50 \Omega$, $\phi_0 = 0^\circ$)

Dependence of the active impedance on the probe radius a is shown in Figure 8-33. The radius of the coaxial conductor $b = 3.249 a$, so that the characteristic impedance of the coaxial lines is 50 ohms. It is seen that influence of these parameters on active impedance is not very significant.

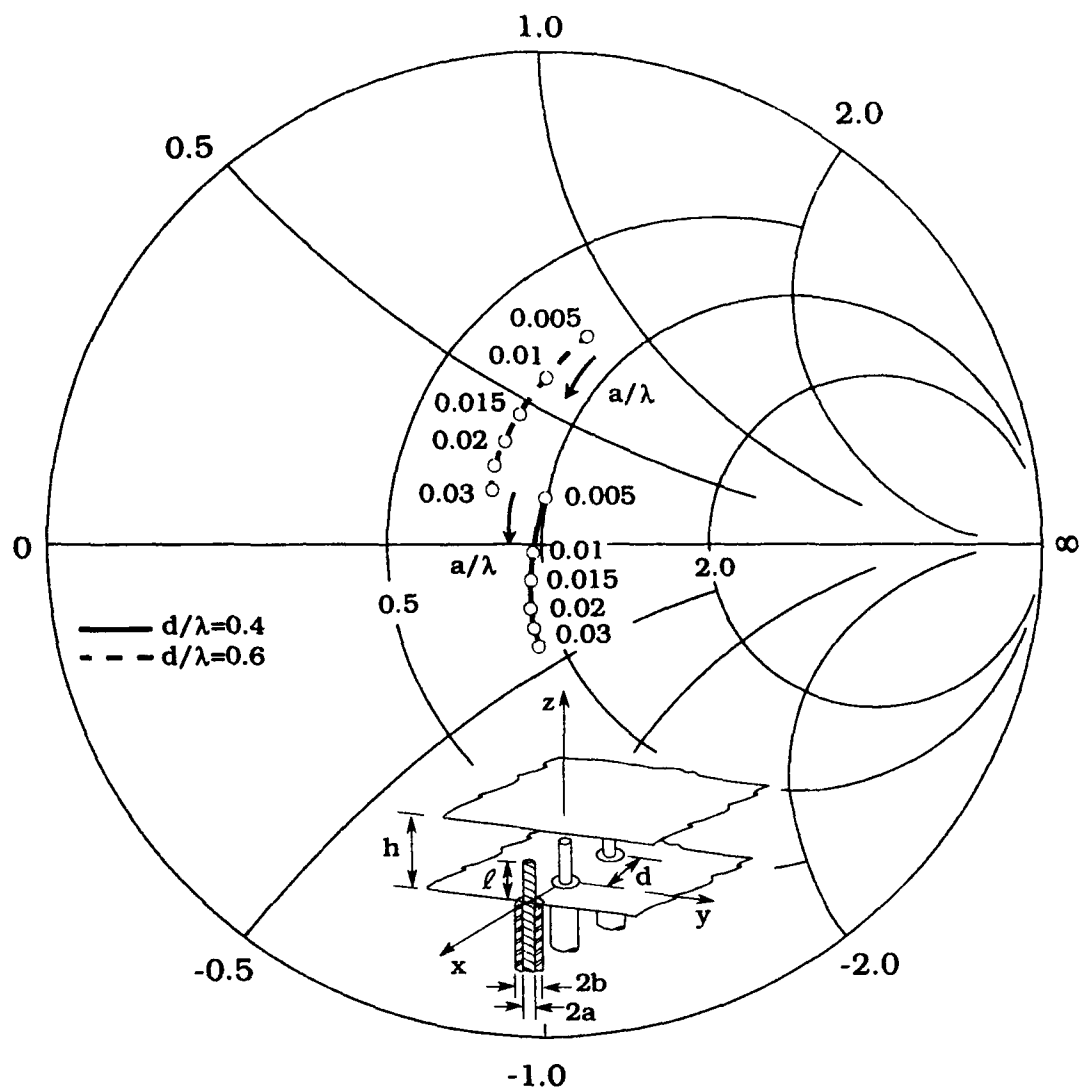


Figure 8-33. Active Impedance vs Probe Radius (Array (a):
 $d/\lambda = 0.4, h_c/\lambda = 0.36, l_c/\lambda = 0.28, b = 3.249 a, Z_c = 50 \Omega, \phi_0 = 0^\circ$
 Array (b): $d/\lambda = 0.6, h/\lambda = 0.36, l/\lambda = 0.28, b = 3.249 a, Z_c = 50 \Omega, \hat{\phi}_0 = 0^\circ$)

For both arrays, (a) and (b), Figure 8-34 exhibits the active impedance at broadside vs frequency. In the matched case [array (a)], the frequency bandwidth corresponding to a VSWR of 2:1 is approximately 30 percent.

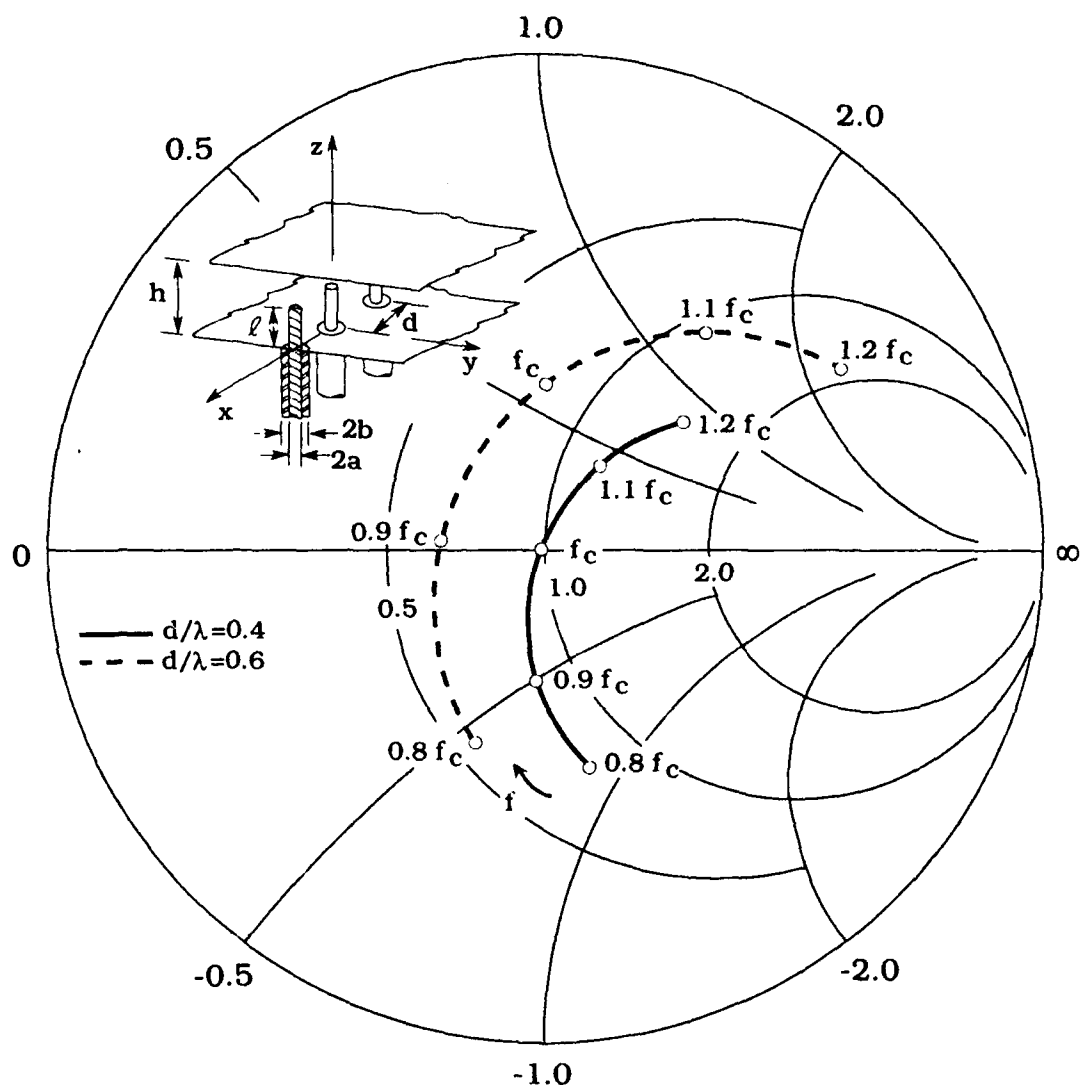


Figure 8-34. Active Impedance vs Frequency (Array (a)):
 $d/\lambda_c = 0.4$, $h_c/\lambda_c = 0.36$, $l_c/\lambda_c = 0.28$, $b/\lambda_c = 3.249$ a/ λ_c , $Z_c = 50 \Omega$,
 $\hat{\phi}_0 = 0^\circ$; Array (b): $d/\lambda_c = 0.6$, $h/\lambda_c = 0.36$, $l/\lambda_c = 0.28$, $b/\lambda_c = 3.249$ a/ λ_c ,
 $Z_c = 50 \Omega$, $\hat{\phi}_0 = 0^\circ$)

Figures 8-35 and 8-36 show the active impedance variation vs scan for three frequencies: $f \approx 0.9f_c$, f_c , and $1.1f_c$ where f_c is center frequency. Notice that the array (a) is matched to a 50 ohm coaxial line at f_c and broadside scan ($\hat{\phi}_0 = 0^\circ$).

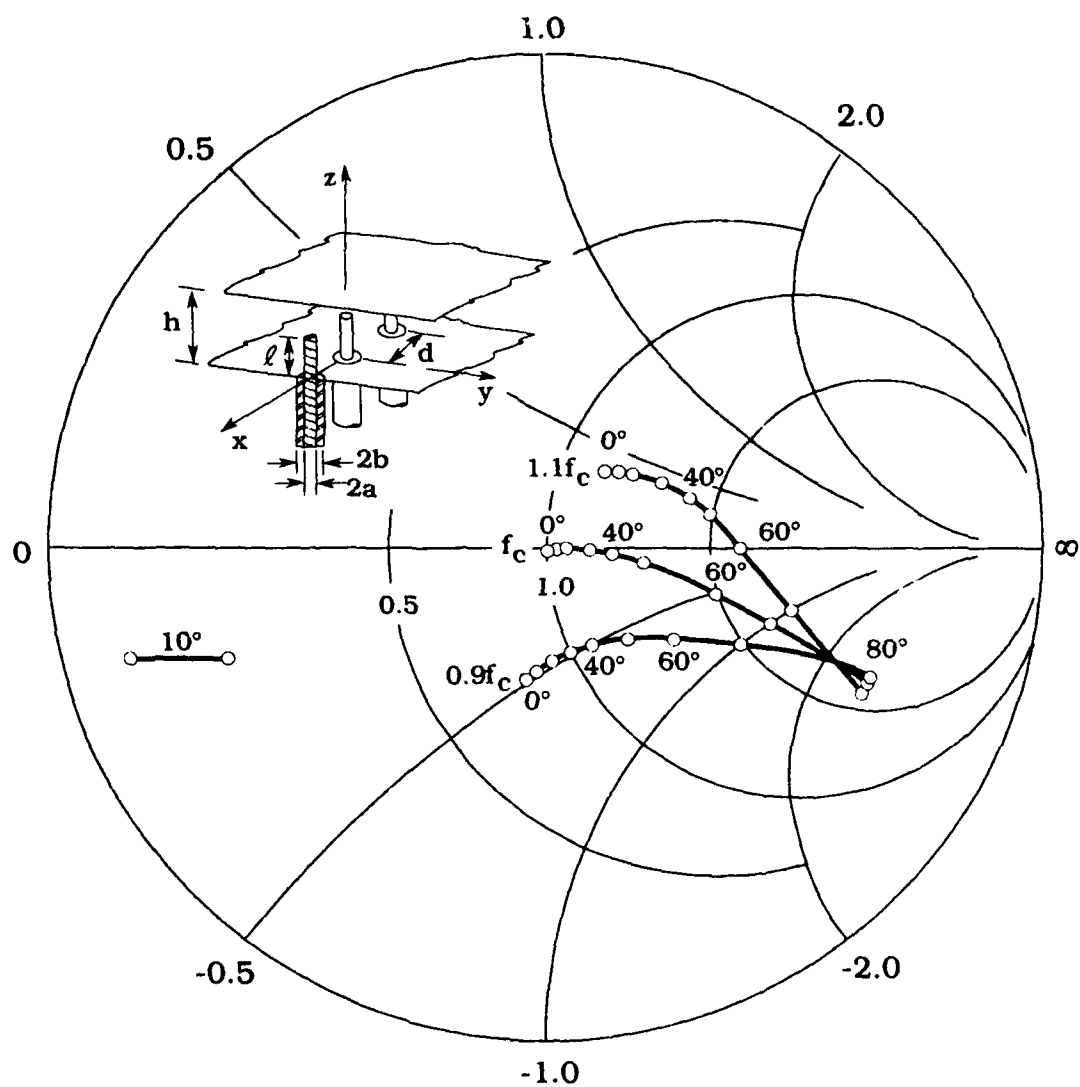


Figure 8-35. Active Impedance vs Scan; Parameter: Frequency $f = 0.9 f_c, f_c$, and $1.1 f_c$ ($d/\lambda_c = 0.4, h_c/\lambda_c = 0.36, L_c/\lambda_c = 0.28, a/\lambda_c = 0.0106, b/\lambda_c = 0.0343, Z_c = 50 \Omega$)

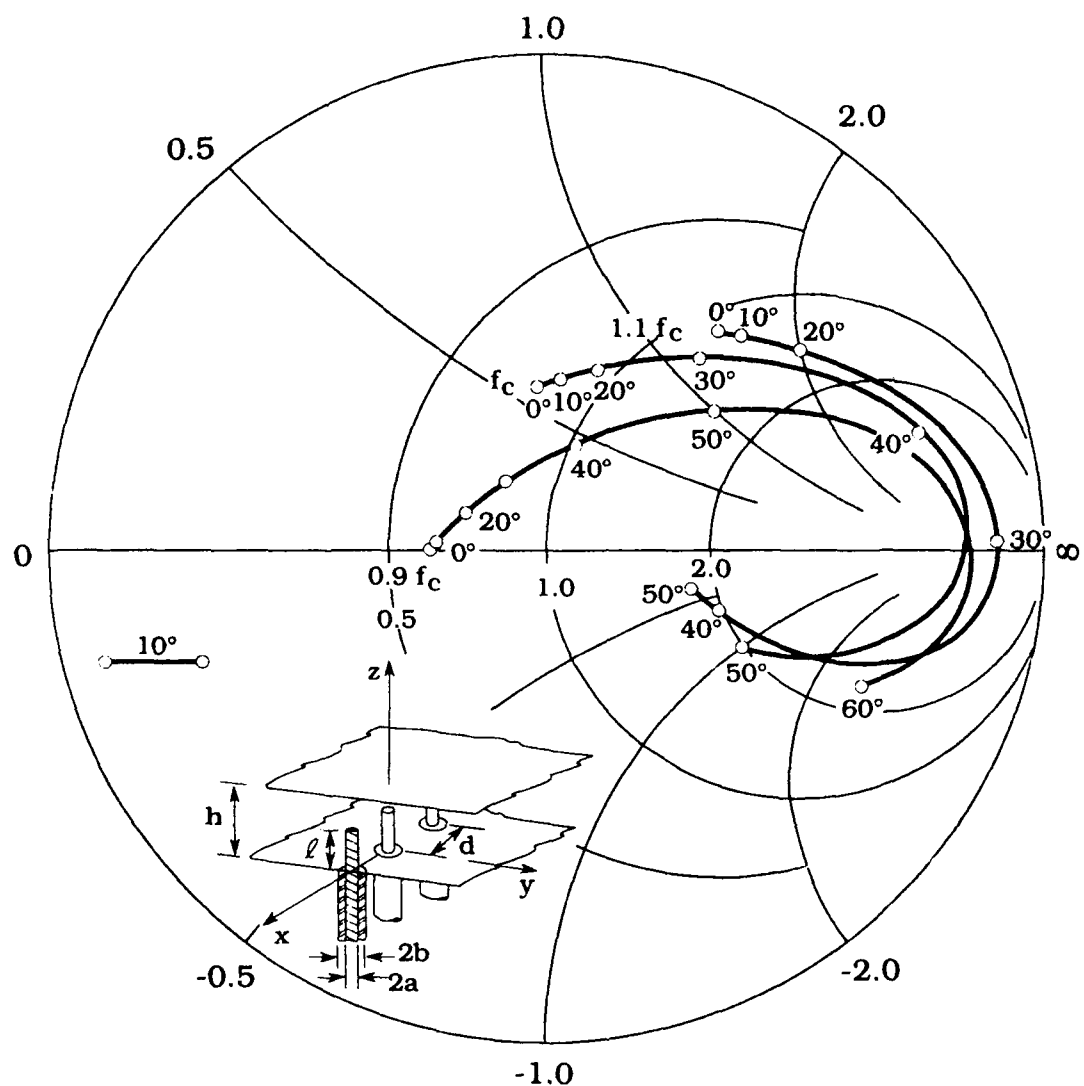


Figure 8-36. Active Impedance vs Scan; Parameter: Frequency $f = 0.9 f_c$, f_c , and $1.1 f_c$ ($d/\lambda_c = 0.6$, $h/\lambda_c = 0.36$, $l/\lambda_c = 0.28$, $a/\lambda_c = 0.0106$, $b/\lambda_c = 0.0343$, $Z_c = 50 \Omega$)

8.3.2 PROBE CURRENT, $I_z(z)$

The active array probe current distribution $I_z(z)$ has been calculated from Eq. (7-3a).

Figures 8-37 to 8-40 show the magnitude and phase of the probe current vs z/λ for both arrays, and for the three probe lengths $l/\lambda = 0.15$, 0.28 , and 0.3 . Notice that the magnitude of current along the probe has a basic $\sin k(z-l)$ variation.

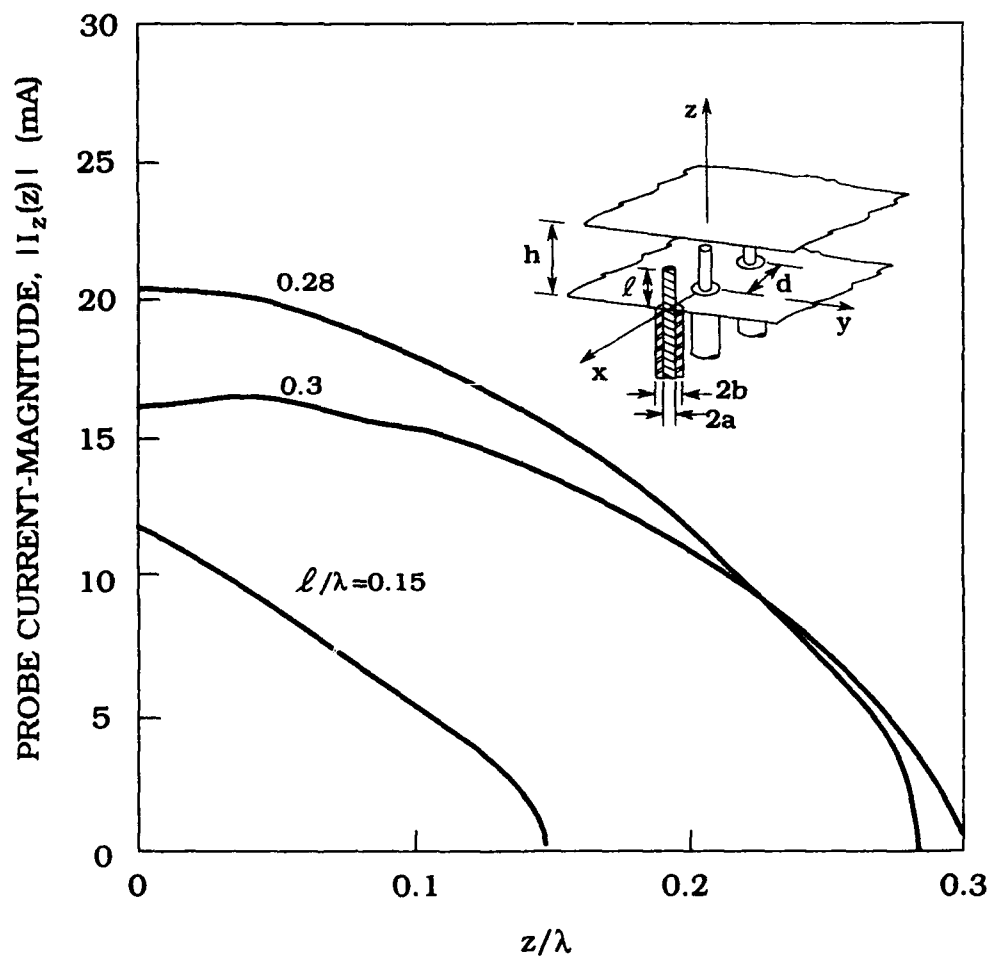


Figure 8-37. Probe Current - Magnitude; Parameter: $l/\lambda = 0.15, 0.28$, and 0.3 ($d/\lambda = 0.4$, $h/\lambda = 0.36$, $a/\lambda = 0.0106$, $b/\lambda = 0.0343$, $Z_c = 50 \Omega$, $\phi_0 = 0^\circ$)

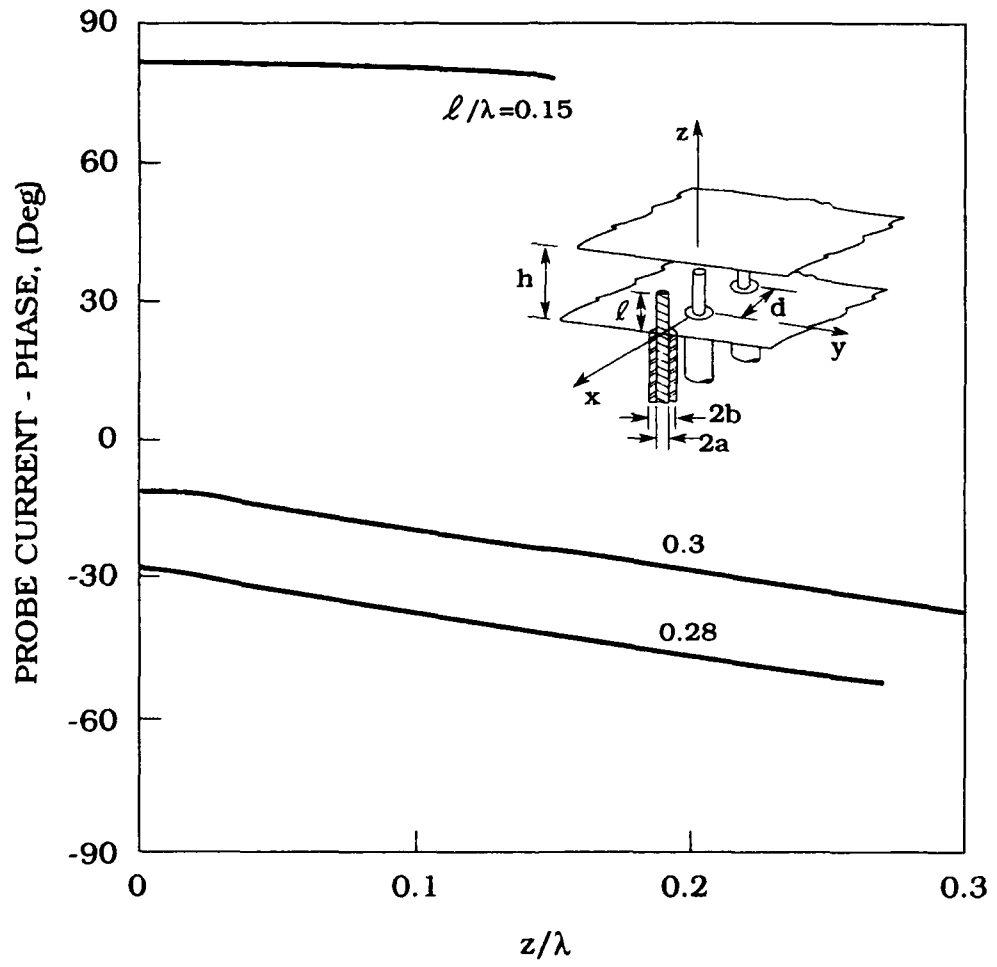


Figure 8-38. Probe Current - Phase; Parameter: $l/\lambda = 0.15, 0.28$, and 0.3 ($d/\lambda = 0.4$, $h/\lambda = 0.36$, $a/\lambda = 0.0106$, $b/\lambda = 0.0343$, $Z_c = 50 \Omega$, $\hat{\phi}_0 = 0^\circ$)

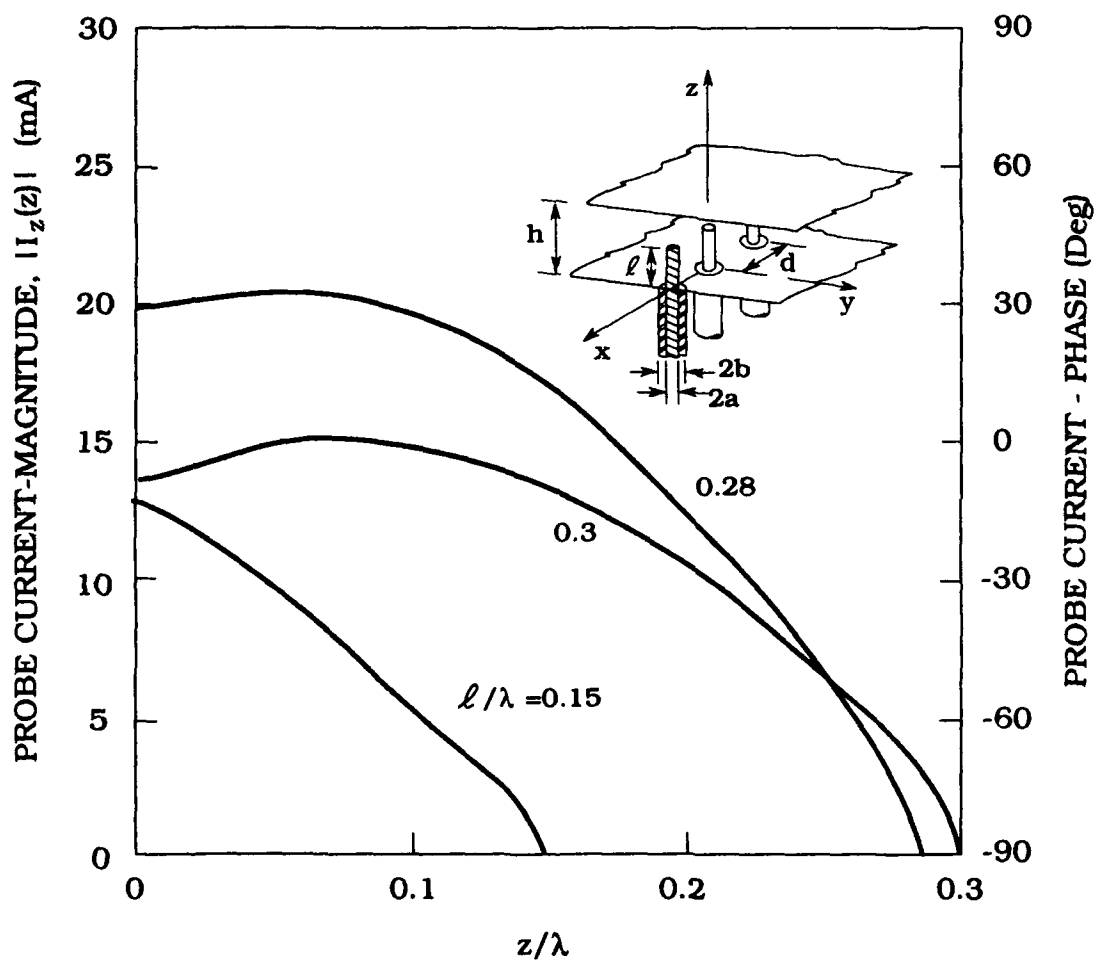


Figure 8-39. Probe Current - Magnitude; Parameter: $l/\lambda = 0.15$, 0.28 , and 0.3 ($d/\lambda = 0.6$, $h/\lambda = 0.36$, $a/\lambda = 0.0106$, $b/\lambda = 0.0343$, $Z_c = 50 \Omega$, $\hat{\phi}_0 = 0^\circ$)

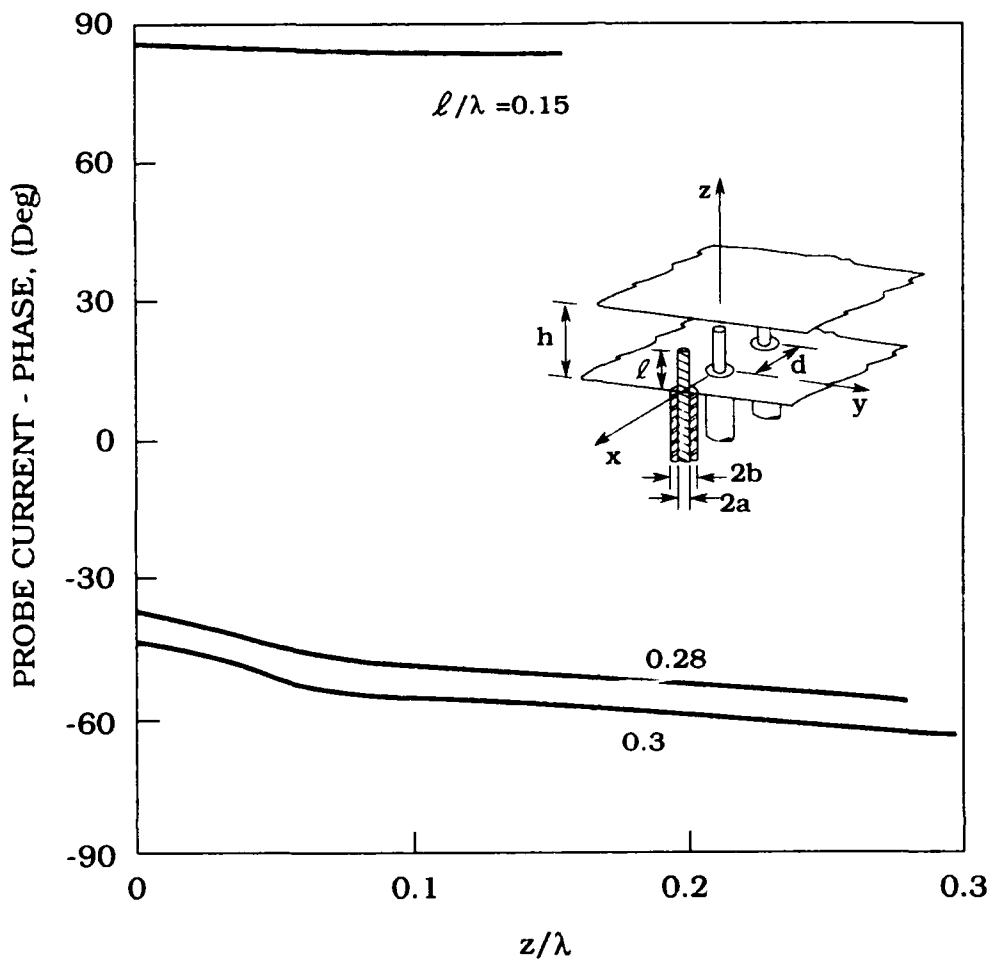


Figure 8-40. Probe Current - Phase; Parameter: $l/\lambda = 0.15, 0.28$, and 0.3 ($d/\lambda = 0.6$, $h/\lambda = 0.36$, $a/\lambda = 0.0106$, $b/\lambda = 0.0343$, $Z_c = 50 \Omega$, $\phi_0 = 0^\circ$)

As already mentioned in our numerical computations we set $I = 10$ and aperture voltage $V_0 = 1V$ which in array (a) gives $|I_z(z=0)| \approx 20$ mA as expected since this element is matched to a 50 ohm coaxial feed line.

For both arrays [(a) and (b)], each with the specified three probe lengths the probe current expansion coefficients c_i as given by Eq. (7-3b) are tabulated in Tables 8-13 to 8-18. In each case the coefficients are given for a single ($I=1$) and for ten ($I=10$) current terms in Eq. (7-3a).

Table 8-13. Probe Current Expansion Coefficients; Parameter:
 Total Number of Current Terms $I = 1, 10$ ($d/\lambda = 0.4, l/\lambda = 0.15,$
 $h/\lambda = 0.36, a/\lambda = 0.0106, b/\lambda = 0.0343, Z_c = 50 \Omega, \phi_0 = 0^\circ$)

I	I=1		I=10	
	$ c'_1 $ mA	ϕ'_1'' Deg.	$ c'_1 $ mA	ϕ'_1'' Deg.
1	10.108	-97.37	10.431	-98.26
2			0.326	117.75
3			0.660	-95.91
4			0.043	163.83
5			0.261	-96.36
6			0.026	-145.45
7			0.144	-96.82
8			0.023	-126.97
9			0.094	-97.20
10			0.021	-119.26

Table 8-14. Probe Current Expansion Coefficients; Parameter:
 Total Number of Current Terms $I = 1, 10$ ($d/\lambda = 0.4, l_c/\lambda = 0.28,$
 $h_c/\lambda = 0.36, a/\lambda = 0.0106, b/\lambda = 0.0343, Z_c = 50 \Omega, \phi_0 = 0^\circ$)

I	I=1		I=10	
	$ c'_1 $ mA	ϕ'_1'' Deg.	$ c'_1 $ mA	ϕ'_1'' Deg.
1	23.813	174.62	24.452	171.94
2			2.533	115.37
3			0.598	-154.33
4			0.599	124.40
5			0.255	-159.36
6			0.293	128.15
7			0.149	-163.86
8			0.180	130.78
9			0.101	-167.66
10			0.124	132.84

Table 8-15. Probe Current Expansion Coefficients; Parameter:
 Total Number of Current Terms $I = 1, 10$ ($d/\lambda = 0.4$, $l/\lambda = 0.30$,
 $h/\lambda = 0.36$, $a/\lambda = 0.0106$, $b/\lambda = 0.0343$, $Z_c = 50 \Omega$, $\hat{\phi}_0 = 0^\circ$)

i	I=1		I=10	
	$ c'_i $ mA	ϕ'_i Deg.	$ c'_i $ mA	ϕ'_i Deg.
1	19.667	160.55	17.598	160.05
2			2.654	105.96
3			0.440	-151.30
4			0.611	113.69
5			0.187	-158.92
6			0.295	116.62
7			0.109	-165.23
8			0.180	118.63
9			0.073	-170.60
10			0.123	120.23

Table 8-16. Probe Current Expansion Coefficients; Parameter:
 Total Number of Current Terms $I = 1, 10$ ($d/\lambda = 0.6$, $l/\lambda = 0.15$,
 $h/\lambda = 0.36$, $a/\lambda = 0.0106$, $b/\lambda = 0.0343$, $Z_c = 50 \Omega$, $\hat{\phi}_0 = 0^\circ$)

i	I=1		I=10	
	$ c'_i $ mA	ϕ'_i Deg.	$ c'_i $ mA	ϕ'_i Deg.
1	10.999	-95.27	11.479	-96.01
2			0.220	123.46
3			0.707	-94.41
4			0.037	-152.64
5			0.280	-94.73
6			0.035	-119.84
7			0.156	-95.04
8			0.031	-111.45
9			0.102	-95.31
10			0.026	-107.80

Table 8-17. Probe Current Expansion Coefficients: Parameter:
 Total Number of Current Terms I = 1, 10 ($d/\lambda = 0.6$, $l/\lambda = 0.28$,
 $h/\lambda = 0.36$, $a/\lambda = 0.0106$, $b/\lambda = 0.0343$, $Z_c = 50 \Omega$, $\phi_0 = 0^\circ$)

i	I=1		I=10	
	$ c_i'' $ mA	ϕ_i'' Deg.	$ c_i'' $ mA	ϕ_i'' Deg.
1	26.626	137.01	22.679	135.00
2			3.006	104.73
3			0.396	171.61
4			0.738	109.63
5			0.183	163.40
6			0.364	111.50
7			0.115	157.29
8			0.224	112.78
9			0.082	152.76
10			0.155	113.77

Table 8-18. Probe Current Expansion Coefficients: Parameter:
 Total Number of Current Terms I = 1, 10 ($d/\lambda = 0.6$, $l/\lambda = 0.30$,
 $h/\lambda = 0.36$, $a/\lambda = 0.0106$, $b/\lambda = 0.0343$, $Z_c = 50 \Omega$, $\phi_0 = 0^\circ$)

i	I=1		I=10	
	$ c_i'' $ mA	ϕ_i'' Deg.	$ c_i'' $ mA	ϕ_i'' Deg.
1	19.249	127.31	16.695	127.31
2			2.858	98.14
3			0.231	-166.54
4			0.677	102.34
5			0.103	176.80
6			0.329	103.81
7			0.065	165.14
8			0.201	104.80
9			0.047	156.66
10			0.137	105.57

As for a single element, the active admittance can be also computed using Eq. (8-1) where now the probe current is a function of the inter-element phasing δ_x . For the same geometries, Table 8-19 compares the results for input admittance at broadside scan obtained from Eqs. (4-44) and (8-2). In all cases $I = 10$. One may notice the small difference (less than 1 percent) between the two results.

Table 8-19. Comparison Between Results for Active Admittance $Y_a = G_a + jB_a$:
 Parameter: $d/\lambda = 0.4, 0.6$ [Array (a): $d/\lambda = 0.4, l/\lambda = 0.15, 0.28, 0.30, h/\lambda = 0.36, a/\lambda = 0.0106, b/\lambda = 0.0343, Z_c = 50 \Omega, \hat{\phi}_0 = 0^\circ$; Array (b): $d/\lambda = 0.6, l/\lambda = 0.15, 0.28, 0.3, h/\lambda = 0.36, a/\lambda = 0.0106, b/\lambda = 0.0343, Z_c = 50 \Omega, \hat{\phi}_0 = 0^\circ$]

l/λ	Y_a from Eq. (4-44)				Y_a from Eq. (8-2)			
	$d/\lambda = 0.4$		$d/\lambda = 0.6$		$d/\lambda = 0.4$		$d/\lambda = 0.6$	
	G_a mS	B_a mS	G_a mS	B_a mS	G_a mS	B_a mS	G_a mS	B_a mS
0.15	1.392	11.662	1.118	12.683	1.385	11.724	1.111	12.739
0.28	20.453	0.713	15.489	-11.872	20.454	0.647	15.489	-11.939
0.30	16.017	-1.958	9.833	-9.037	16.023	-2.049	9.836	-9.130

8.3.3 COUPLING COEFFICIENTS, S^p

Coupling coefficients were computed using Eq. (4-52).

Figure 8-41 shows the amplitude of the coupling coefficients for both arrays with (a) $d/\lambda = 0.4$ and (b) $d/\lambda = 0.6$. The coupling coefficients decay monotonically vs element number. As can be seen from Figure 8-42, for elements distant from the excited monopole the coupling is primarily due to the parallel plate waveguide TEM mode whose amplitude decays as $(pd)^{-3/2}$. For this reason one would expect that coupling coefficients vs element number p decay faster for $d/\lambda = 0.6$ than for $d/\lambda = 0.4$. In Figure 8-41 however, when p is large, the coupling coefficients for $d/\lambda = 0.4$ decay faster than for $d/\lambda = 0.6$. This is because the elements of array (a) ($d/\lambda = 0.4$) are better matched to a 50 ohm coaxial line than elements of array (b) (with $d/\lambda = 0.6$) and consequently they "absorb" more power from the TEM mode propagating along the array from the excited ($p=0$) element. Also one sees that for the elements close to the excited one (p is small) the distance factor $(pd)^{-3/2}$ is more pronounced than the effect due to the matching of the elements, and consequently in this region the coupling coefficients of array (b) decay faster than those of array (a). The two curves cross at $p=5$ (See figure 8-41) which means that at this particular element the two effects (element spacing and matching) are about the same.

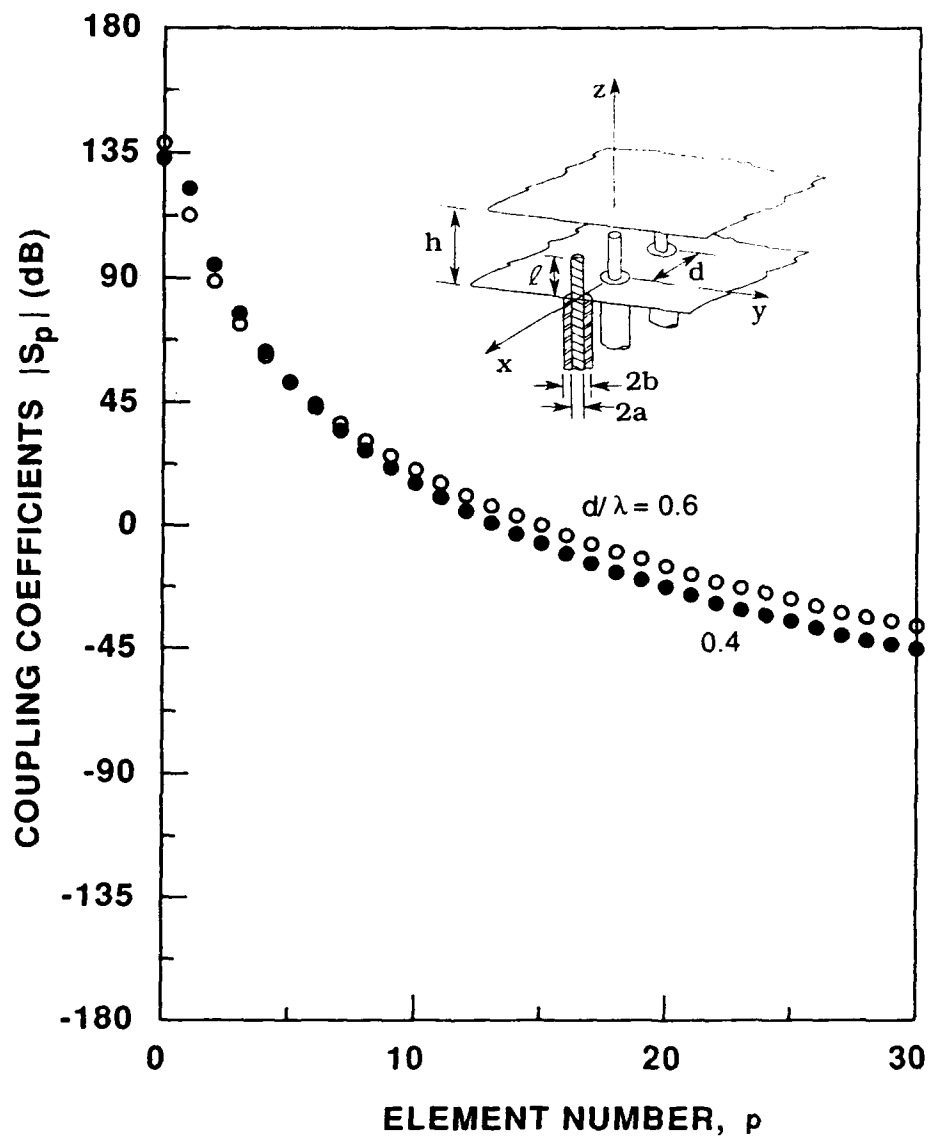


Figure 8-41. Amplitude of Coupling Coefficients vs Element Serial Number:
**Parameter: $d/\lambda = 0.4, 0.6$ [Array (a): $d/\lambda = 0.4$, $h_c/\lambda = 0.36$, $l_c/\lambda = 0.28$,
 $a/\lambda = 0.0106$, $b/\lambda = 0.0343$, $Z_c = 50 \Omega$; Array (b): $d/\lambda = 0.6$, $h/\lambda = 0.36$, $l/\lambda = 0.28$,
 $a/\lambda = 0.0106$, $b/\lambda = 0.0343$, $Z_c = 50 \Omega$]**

Figure 8-42 exhibits the coupling coefficient's differential phase $\Delta\phi_p$ where with

$$S^p = |S^p| e^{-j\phi_p} \quad (8-4a)$$

we define

$$\Delta\phi_p = \phi_p - kdp, \quad k = \frac{2\pi}{\lambda}. \quad (8-4b)$$

In Eq. (8-4b) (kdp) represents the phase delay of the TEM mode from the reference element ($p = 0$) to element p . Thus, for elements close to the excited one the coupling is due to the TEM mode, plus contributions of higher non-propogating parallel plate radial waveguide modes. For elements further removed, the coupling is primarily due to the TEM mode.

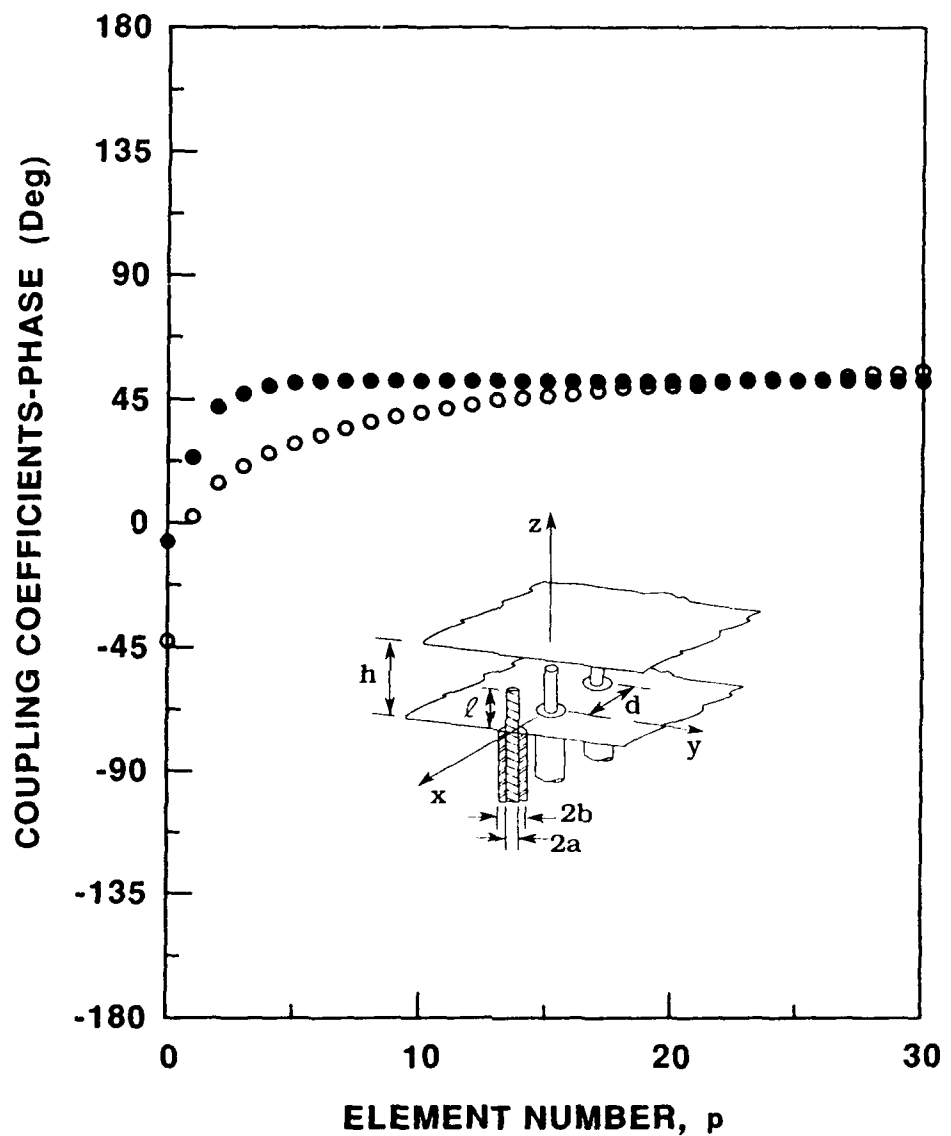


Figure 8-42. Phase of Coupling Coefficients vs Element Serial Number:
 Parameter: $d/\lambda = 0.4, 0.6$ [Array (a): $d/\lambda = 0.4$, $h_c/\lambda = 0.36$, $l_c/\lambda = 0.28$, $a/\lambda = 0.0106$, $b/\lambda = 0.0343$, $Z_c = 50 \Omega$; Array (b): $d/\lambda = 0.6$, $h/\lambda = 0.36$, $l/\lambda = 0.28$, $a/\lambda = 0.0106$, $b/\lambda = 0.0343$, $Z_c = 50 \Omega$]

8.4 Linear Array of Coaxially-fed Monopole Elements in a Semi-Infinite Parallel Plate Waveguide

The active admittance, probe current distribution, coupling coefficients and element patterns were computed for representative values of array and element parameters to exhibit the significant trends. Numerical results presented here are solely for arrays backed by a conducting ground with two typical element spacings (a) $d = 0.4 \lambda$ and (b) $d = 0.6 \lambda$ where λ is the free space wavelength. Unless otherwise explicitly stated, all of the numerical results refer to monopole elements with $a = 0.0106 \lambda$, $b = 0.0343 \lambda$ and parallel plate height $h = 0.369 \lambda$. The coaxial feed-lines with $Z_c = 50 \Omega$ are fully loaded with teflon ($\epsilon_r = 2$). As already mentioned $n_{\max} = 40$ and $I = 10$ in Galerkin's procedure throughout this section.

8.4.1 ACTIVE ADMITTANCE, $Y_a(\delta_x)$

Active admittance $Y_a(\delta_x)$ has been computed from Eq. (4-44) with $S_n(\delta_x)$ as given by Eq. (4-47d). Figures 8-43 and 8-44 show the active impedance $Z_a = 1/Y_a$ at broadside scan vs probe length (solid curve) for $s/\lambda = 0.15, 0.2, 0.25$, and 0.3 , and vs probe to ground distance (dashed curve) for $l/\lambda = 0.15, 0.2, 0.25$, and 0.3 . The inter-element spacings are: (a) $d = 0.4 \lambda$ and (b) $d = 0.6 \lambda$, while the distance between the parallel plates is $h = 0.369 \lambda$. The Smith chart is normalized to 50 ohms. In case (a), the resonant dimensions are approximately $l/\lambda = 0.233$ and $s/\lambda = 0.163$. For $l/\lambda < 0.233$, Z_a is capacitive and for $l/\lambda > 0.233$, inductive. In case (b), the resonance occurs approximately at $l/\lambda = 0.25$ and $s/\lambda = 0.245$. In both cases, Z_a is more sensitive to changes of l/λ than of s/λ , and the curves $l/\lambda = \text{const}$ and $s/\lambda = \text{const}$ are nearly orthogonal. This property is useful in determining the pair of values $l_c/\lambda, s_c/\lambda$ that produce an impedance match.

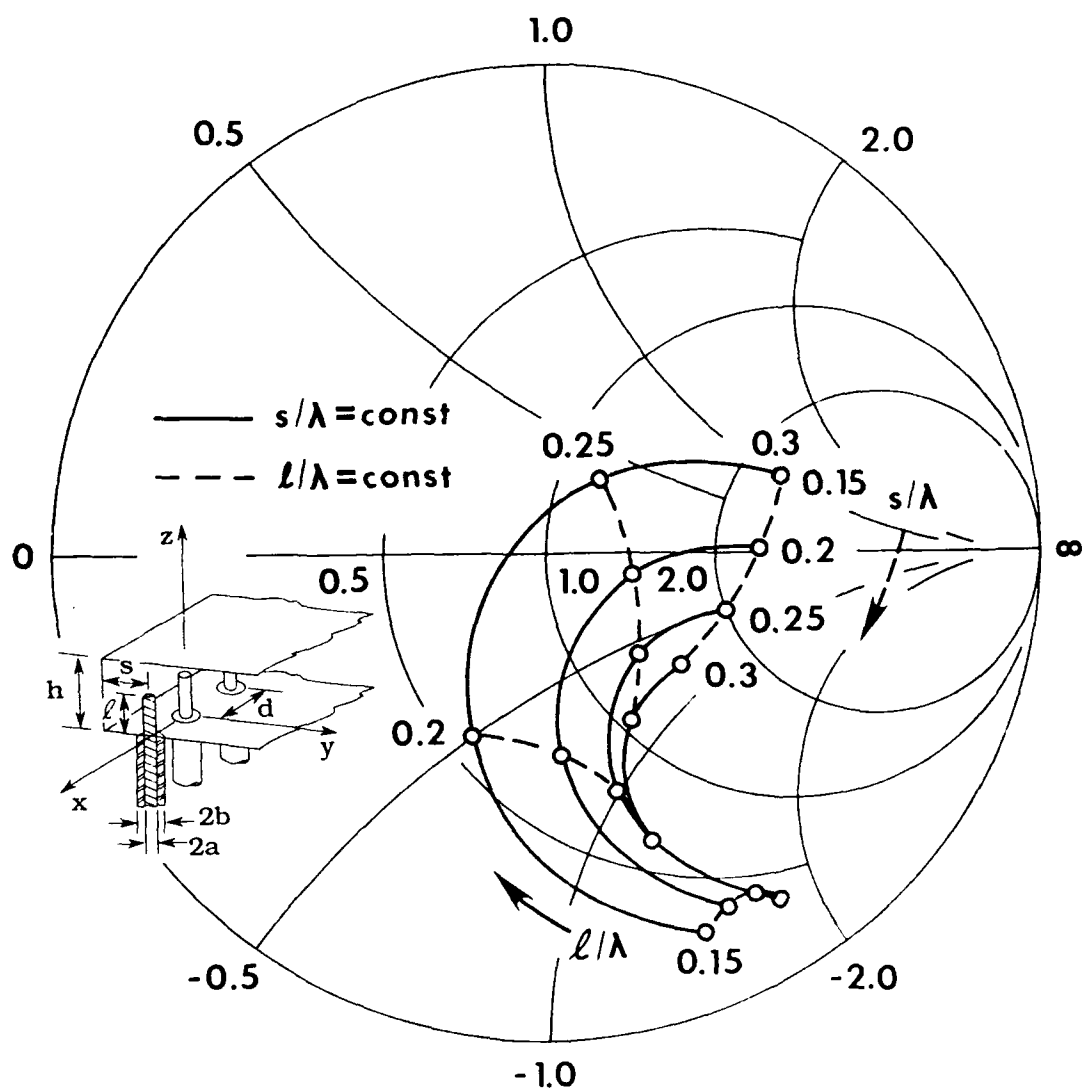


Figure 8-43. Active Impedance vs Probe-Ground Distance s/λ and vs Probe Length l/λ ($d/\lambda = 0.4$, $\hat{\phi}_0 = 0^\circ$)

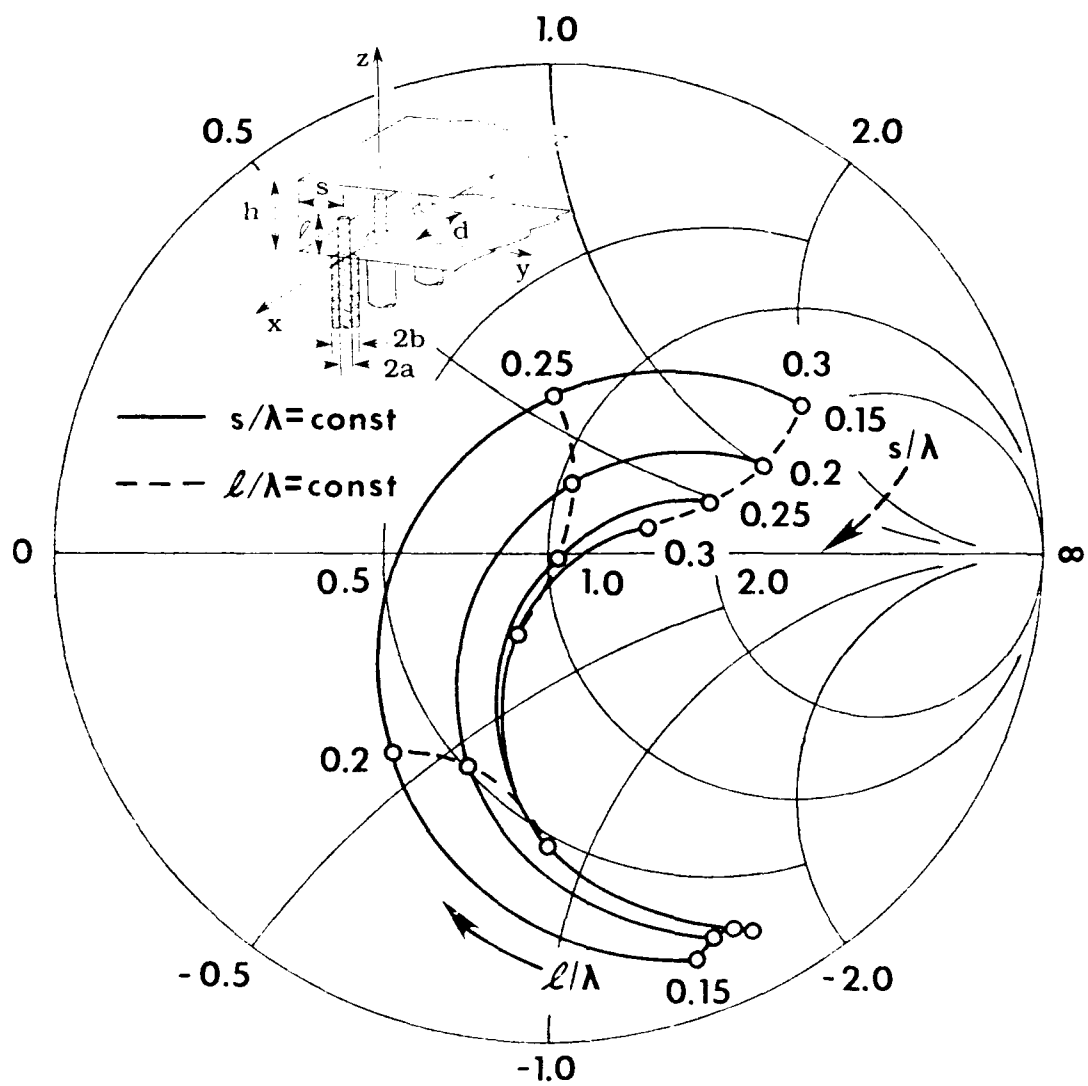


Figure 8-44. Active Impedance vs Probe-Ground Distance s/λ and vs Probe Length l/λ ($d/\lambda = 0.6$, $\phi_0 = 0^\circ$)

For design purposes, Figures 8-45 and 8-46 display contour plots of $|\Gamma_a| = \text{constant}$ vs l/λ and vs s/λ , for both arrays. It is seen that the match is achieved in case (a) for $l_c/\lambda = 0.233$, $s_c/\lambda = 0.163$ and in the case (b) for $l_c/\lambda = 0.250$, $s_c/\lambda = 0.245$. Thus, the two geometries that yield broadside match are:

(a) $d = 0.4 \lambda$
 $h = 0.369 \lambda$
 $l_c = 0.233 \lambda$
 $s_c = 0.163 \lambda$
 $a = 0.0106 \lambda$
 $b = 0.034 \lambda$
 $Z_c = 50 \Omega (\epsilon_r = 2)$

(b) $d = 0.6 \lambda$
 $h = 0.369 \lambda$
 $l_c = 0.25 \lambda$
 $s_c = 0.245 \lambda$
 $a = 0.0106 \lambda$
 $b = 0.034 \lambda$
 $Z_c = 50 \Omega (\epsilon_r = 2)$. (8-5)

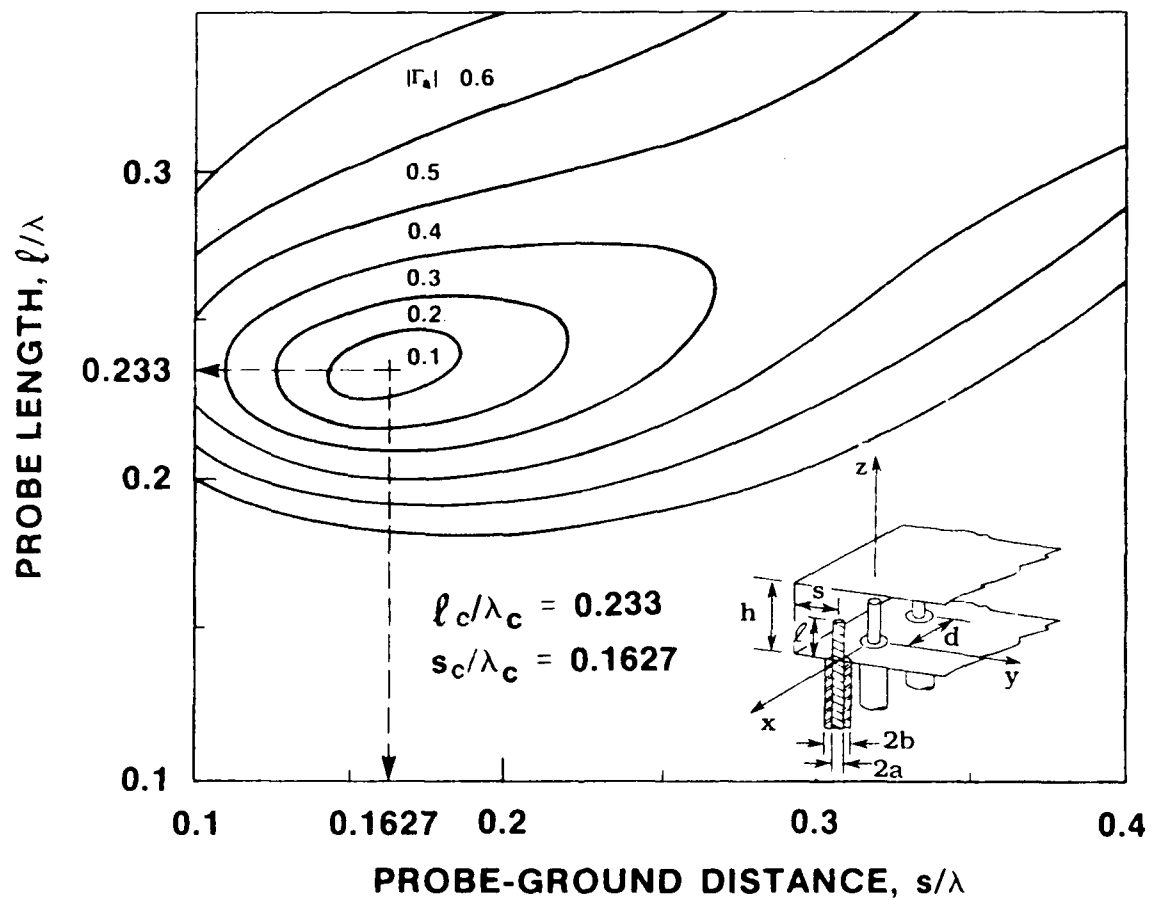


Figure 8-45. Active Reflection Coefficient - Magnitude vs Probe-Ground Distance s/λ and vs Probe Length l/λ ($d/\lambda = 0.4$, $\hat{\phi}_0 = 0^\circ$)

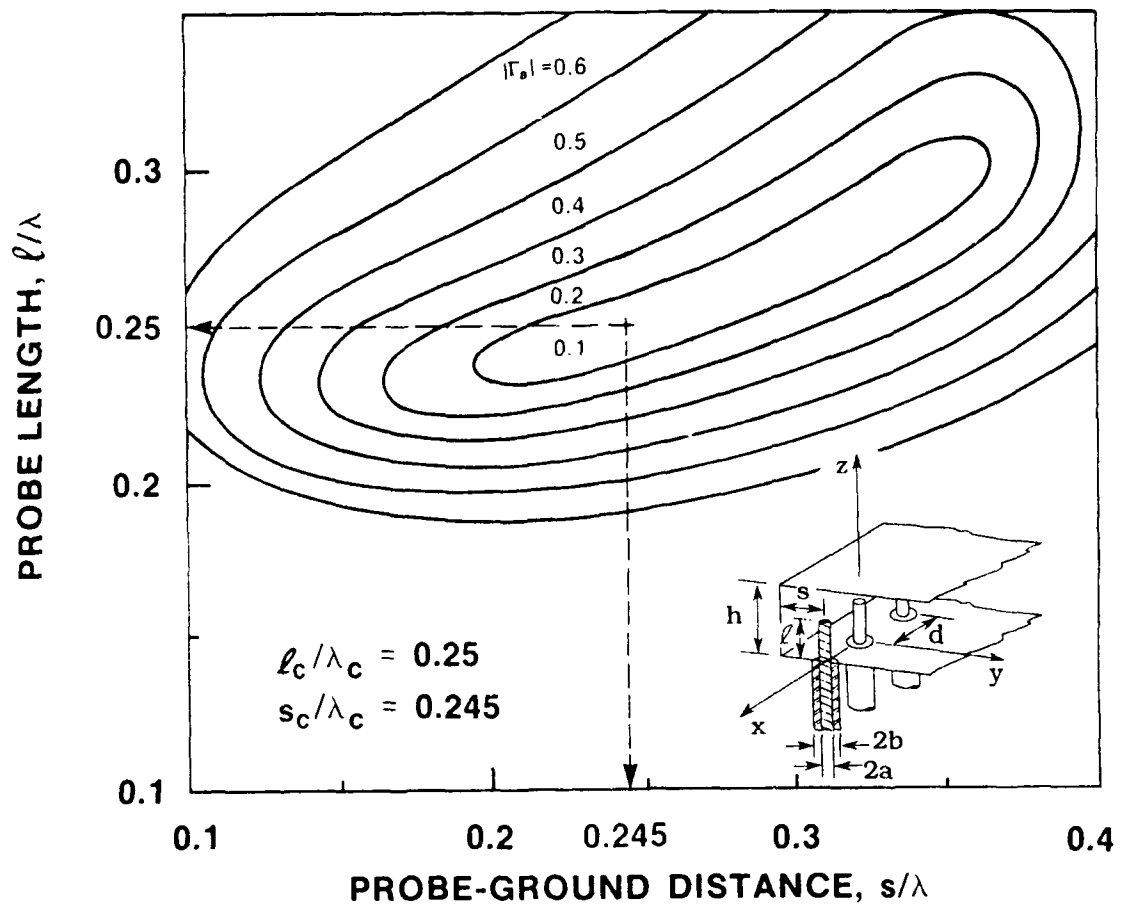


Figure 8-46. Active Reflection Coefficient - Magnitude vs Probe-Ground Distance s/λ and vs Probe Length ℓ/λ ($d/\lambda = 0.6$, $\hat{\phi}_0 = 0^\circ$)

We shall now vary one dimension at a time and observe the variation of active impedance. Figures 8-47 and 8-48 exhibit the dependence of the active impedance on the probe-to-ground distance and on probe length.

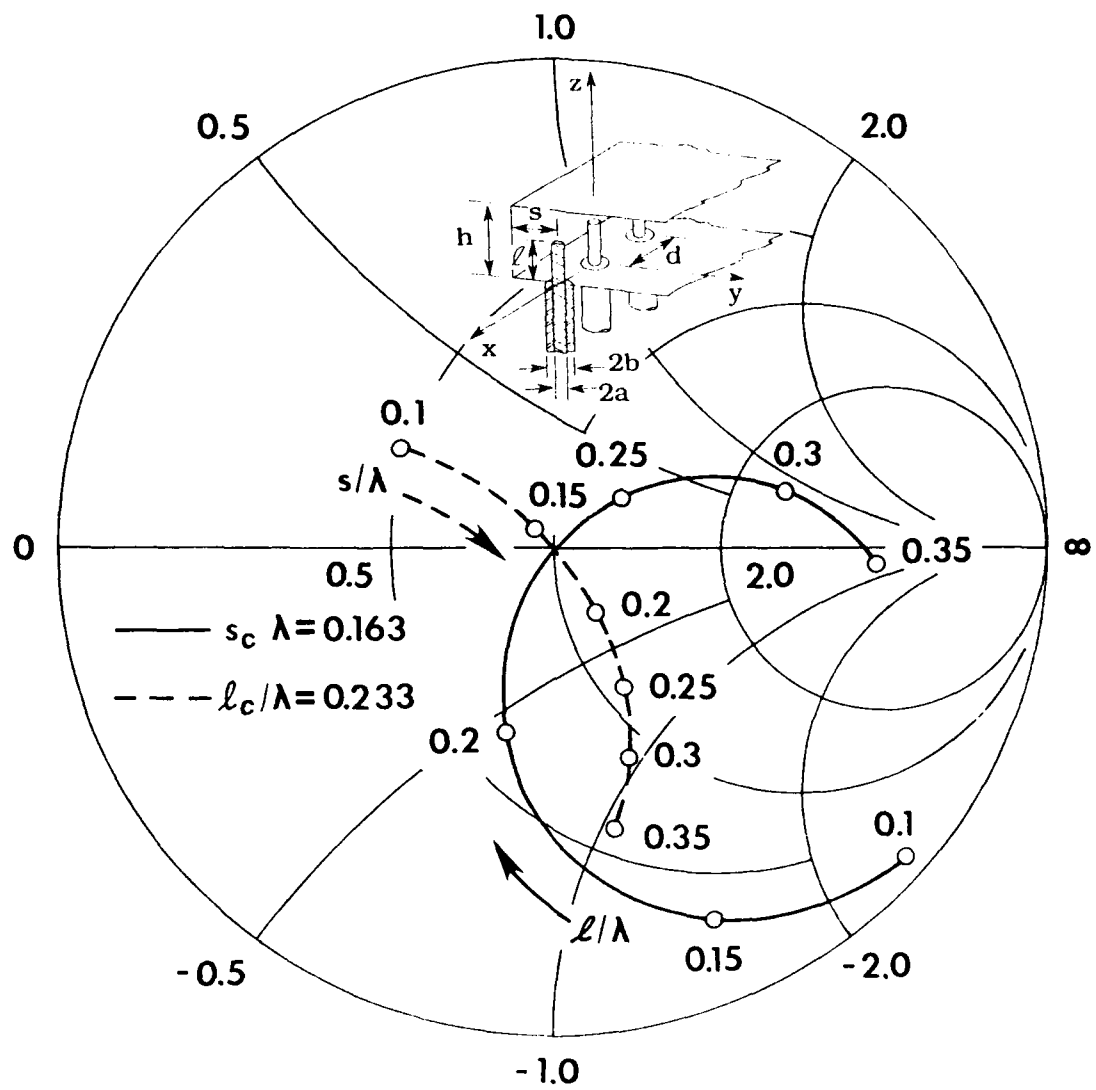


Figure 8-47. Active Impedance vs Probe-Ground Distance s/λ and vs Probe Length l/λ for Array (a) - see Eq. (8-5) for Specifications. ($\hat{\phi}_0 = 0^\circ$)

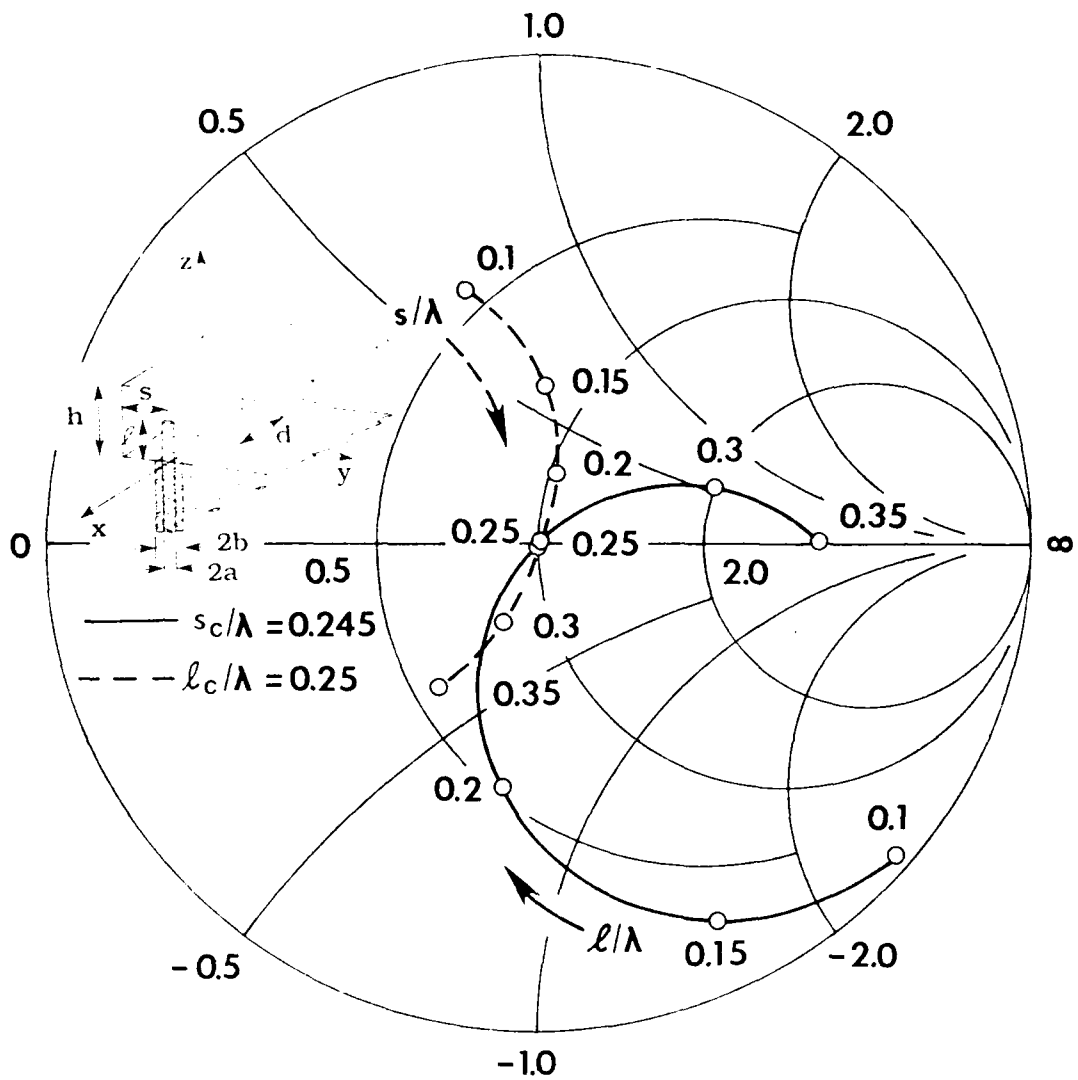


Figure 8-48. Active Impedance vs Probe-Ground Distance s/λ and vs Probe Length l/λ for Array (b) - see Eq. (8-5) for Specifications. ($\hat{\phi}_0 = 0^\circ$)

Figure 8-49 shows the active impedance variation at broadside scan vs parallel plate height h/λ . It is seen from the expanded Smith chart that for h/λ variation from 0.3 to 0.45, $|\Gamma_a(\hat{\phi}_0 = 0^\circ)| < 0.12$ for both arrays, indicating that the active impedance is relatively insensitive to the waveguide height.

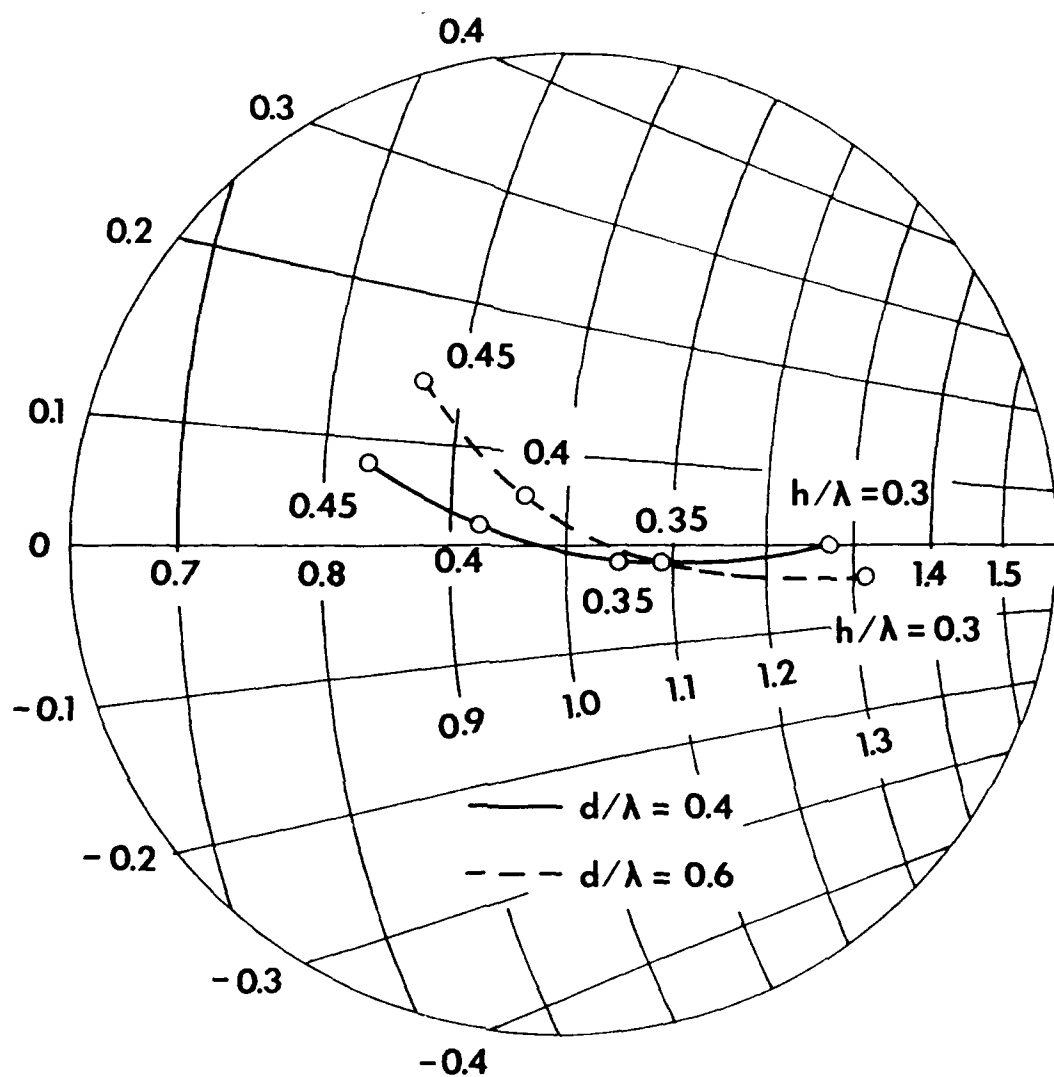


Figure 8-49. Active Impedance vs Parallel Plate Height h/λ for Arrays (a) and (b). ($\hat{\phi}_0 = 0^\circ$)

The dependence of the active impedance on the probe radius a is shown in Figure 8-50. The radius of the outer coaxial conductor is $b = 3.249 a$, so that the characteristic impedance of the coaxial feed lines always remains 50 ohms.

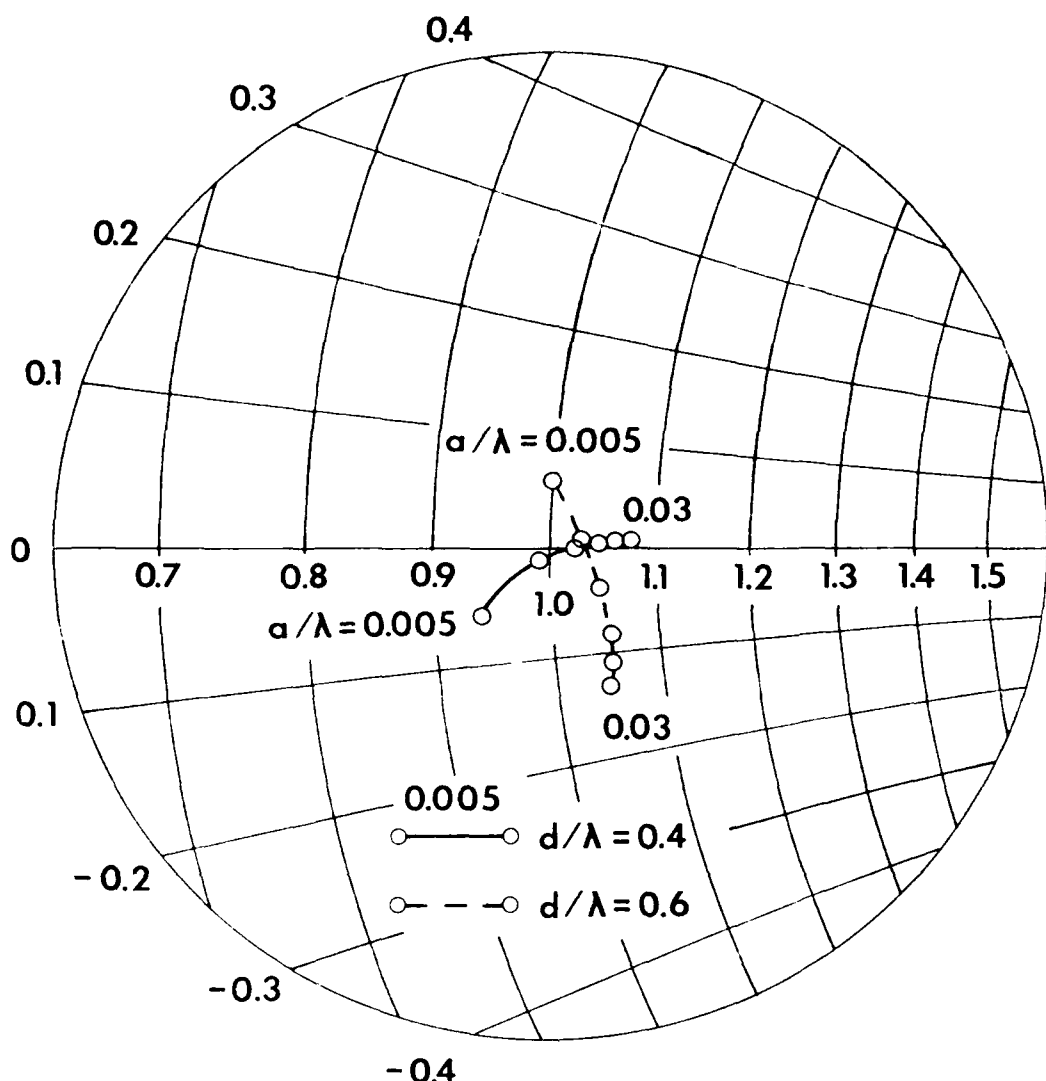


Figure 8-50. Active Impedance vs Probe Radius
for Arrays (a) and (b). ($b = 3.249$ a, $\hat{\phi}_0 = 0^\circ$)

It is seen that the influence of these parameters on active impedance is practically insignificant. We conclude that the active impedance is quite sensitive to the probe length and to the probe-to-ground distance and almost independent of the distance between the two parallel plates and probe radius (at least with coaxial feed lines having $Z_c = 50$ ohms).

Figure 8-51 shows the active impedance at broadside vs frequency for the array geometries of Eq. (8-5). It is seen that the broadside bandwidth for VSWR of 2:1 is approximately 30 percent.

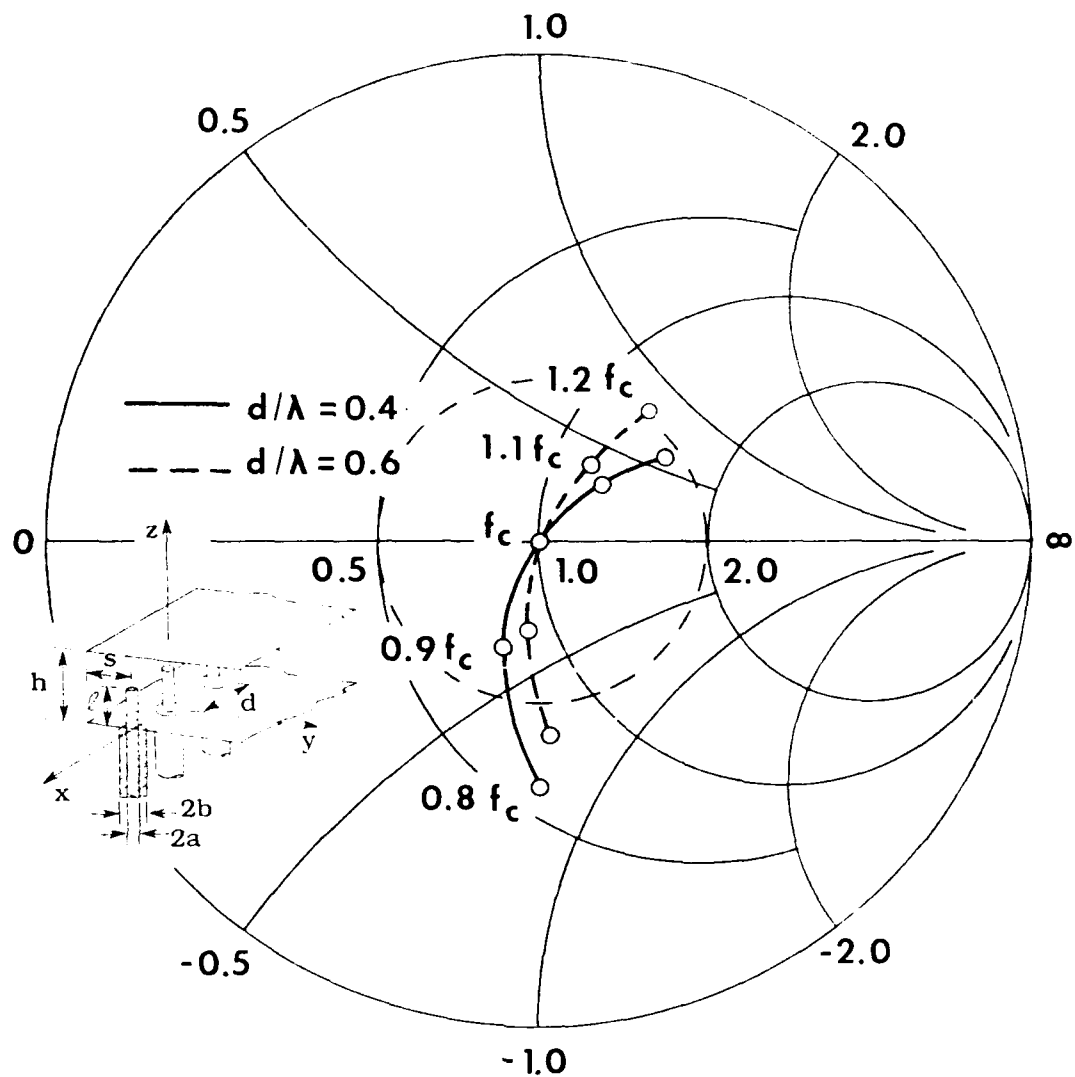


Figure 8-51. Active Impedance vs Frequency for Arrays (a) and (b), ($\hat{\phi}_0 = 0^\circ$)

Figures 8-52 and 8-53 exhibit the scan dependence of active impedance for the same geometry and for the three frequencies: $f = 0.9f_c$, f_c , and $1.1f_c$ where f_c is the center frequency. One observes that the arrays are matched to a 50 ohm coaxial feed line at f_c and broadside scan ($\hat{\phi}_0 = 0^\circ$) and that the bandwidth corresponding to a VSWR of 2:1 is approximately 20 percent in a 35° off-broadside scan range.

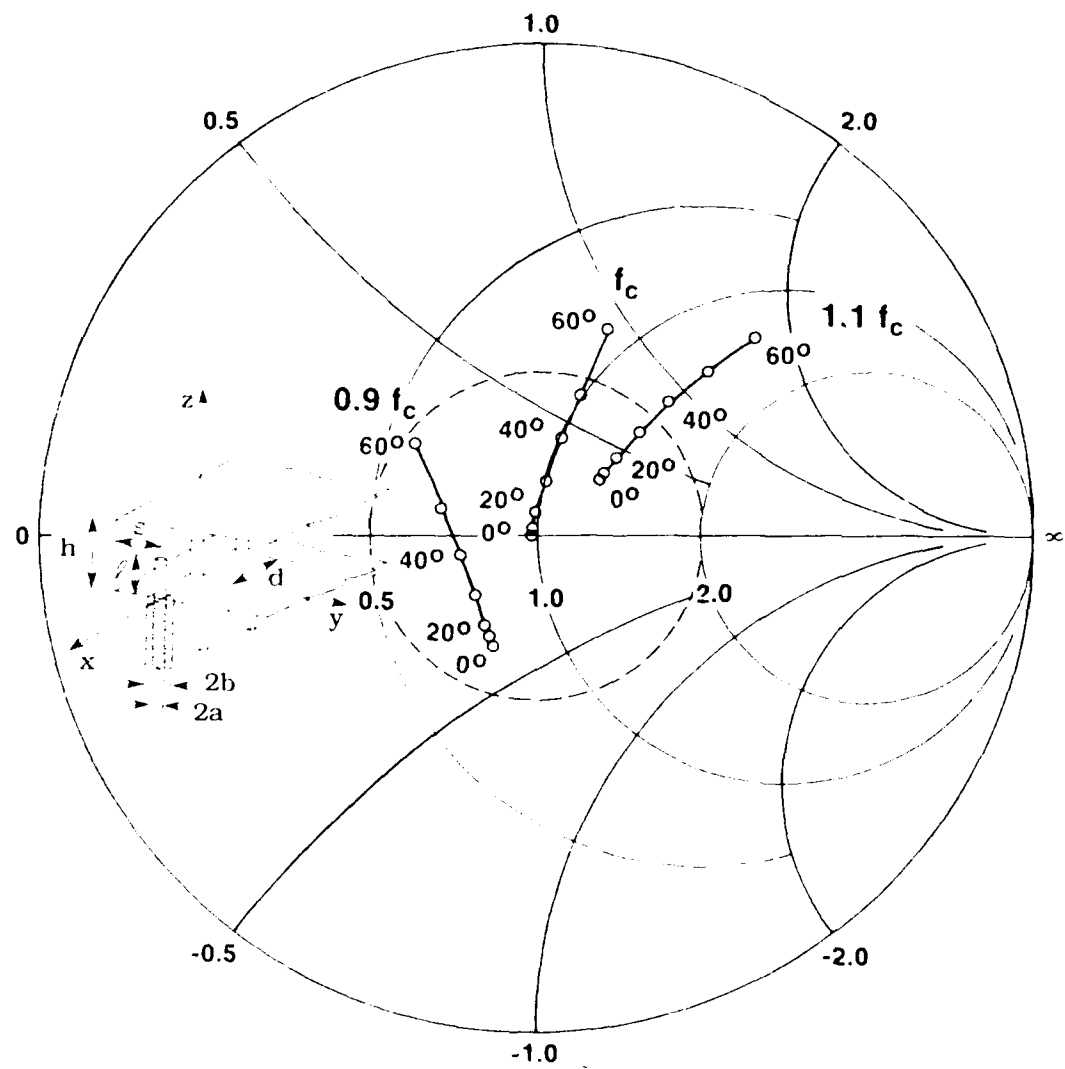


Figure 8-52. Active Impedance vs Scan for Array (a); Parameter: $f = 0.9f_c$, f_c , and $1.1f_c$

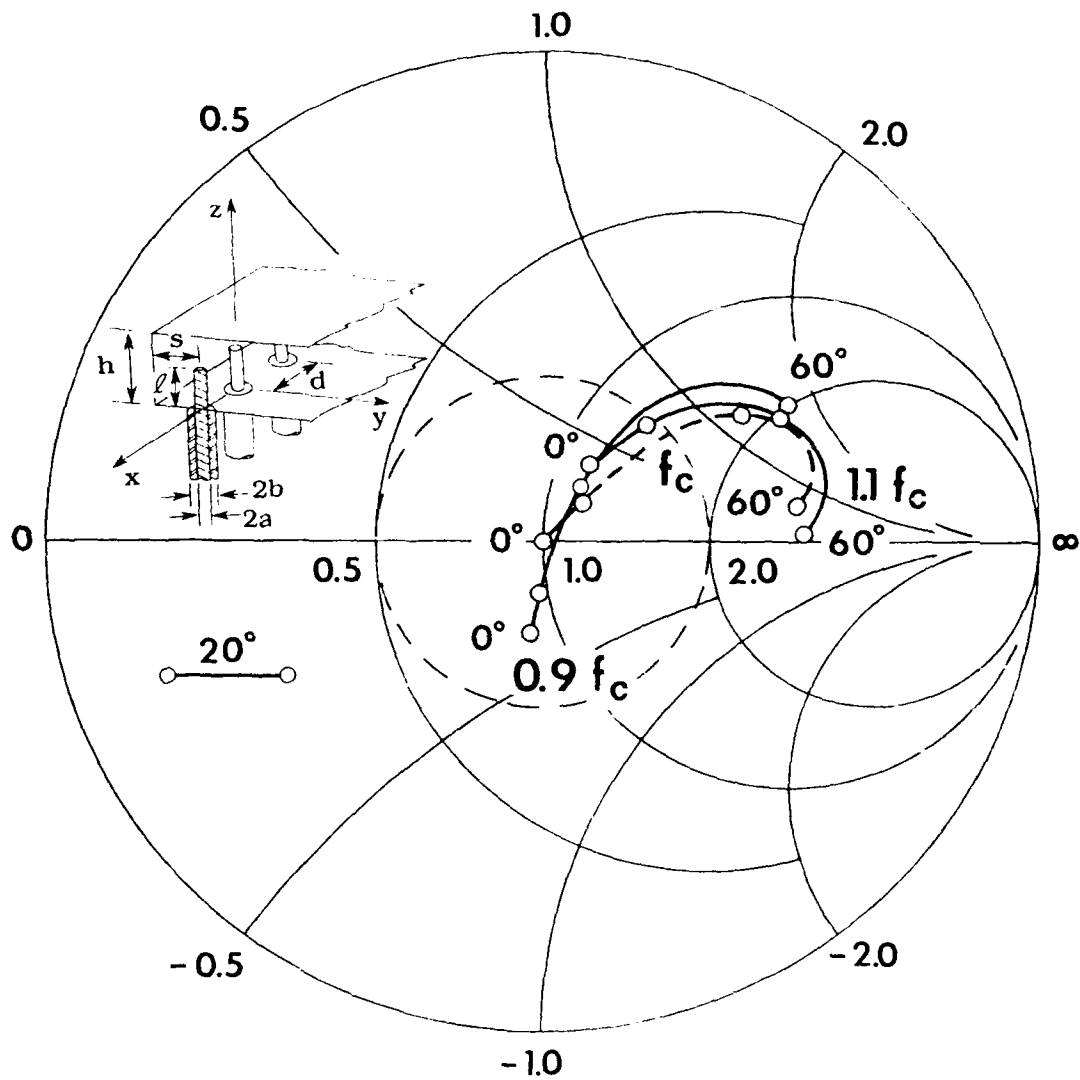


Figure 8-53. Active Impedance vs Scan for Array (b); Parameter: $f = 0.9f_c$, f_c , and $1.1f_c$

8.4.2 PROBE CURRENT, $I_z(z)$

The active array probe current $I_z(z)$ has been computed using Eqs. (7-3) with $V_0 = 1$.

Figures 8-54 and 8-55 show the magnitude and phase of I_z vs z/λ for the array (a) for three probe lengths 0.15λ , 0.233λ (matched case) and 0.3λ . It is seen that the magnitude of current along the probe has a basic $\sin k(z - l)$ variation. For short probes ($l < 0.15\lambda$), the probe current is almost a linear function of z , which is expected since $\sin k(z - l) \approx k(z - l)$ when $l/\lambda \leq 0.15$.

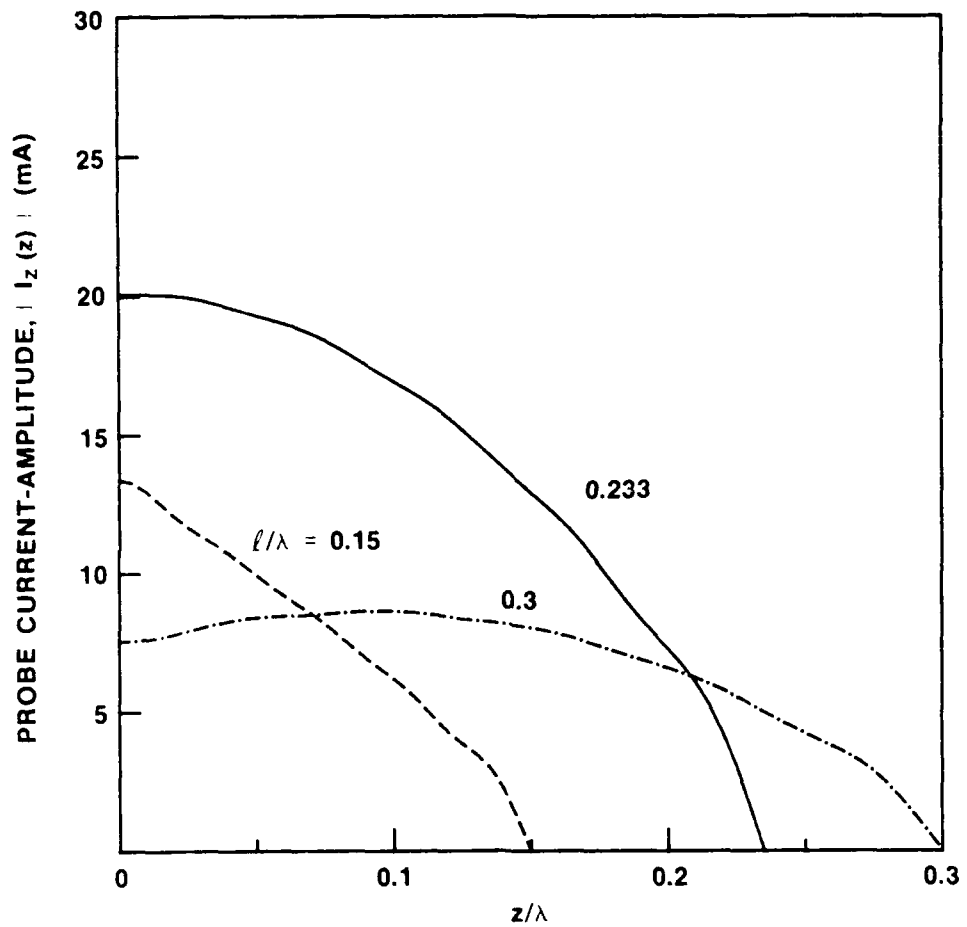


Figure 8-54. Probe Current - Magnitude for Array
 (a). ($\widehat{\phi}_0 = 0^\circ$); Parameter: $l/\lambda = 0.15, 0.233$, and 0.3

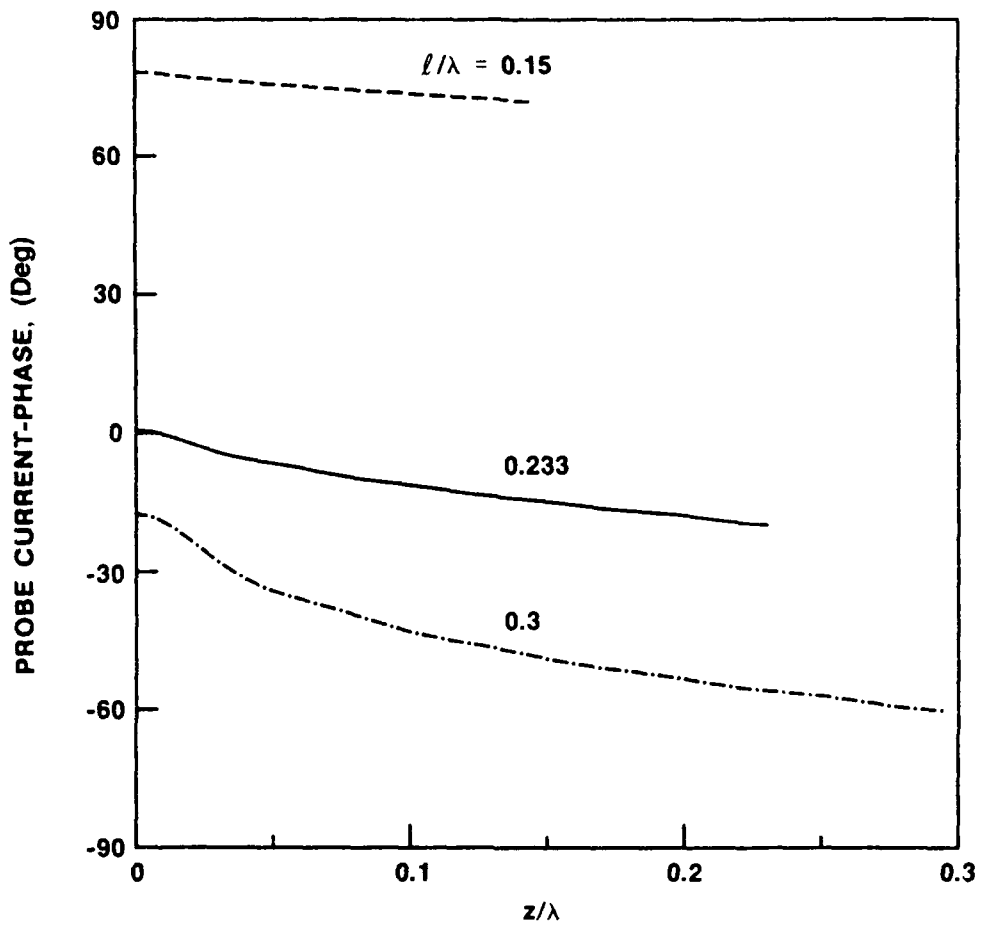


Figure 8-55. Probe Current - Phase for Array (a),
 $(\hat{\phi}_0 = 0^\circ)$; Parameter: $l/\lambda = 0.15, 0.233$, and 0.3

Figures 8-56 and 8-57 exhibit the magnitude and phase, respectively, of the probe current distribution for array (b) for three probe lengths 0.15λ , 0.25λ (matched case) and 0.3λ . A probe current distribution similar to that in array (a) is found.

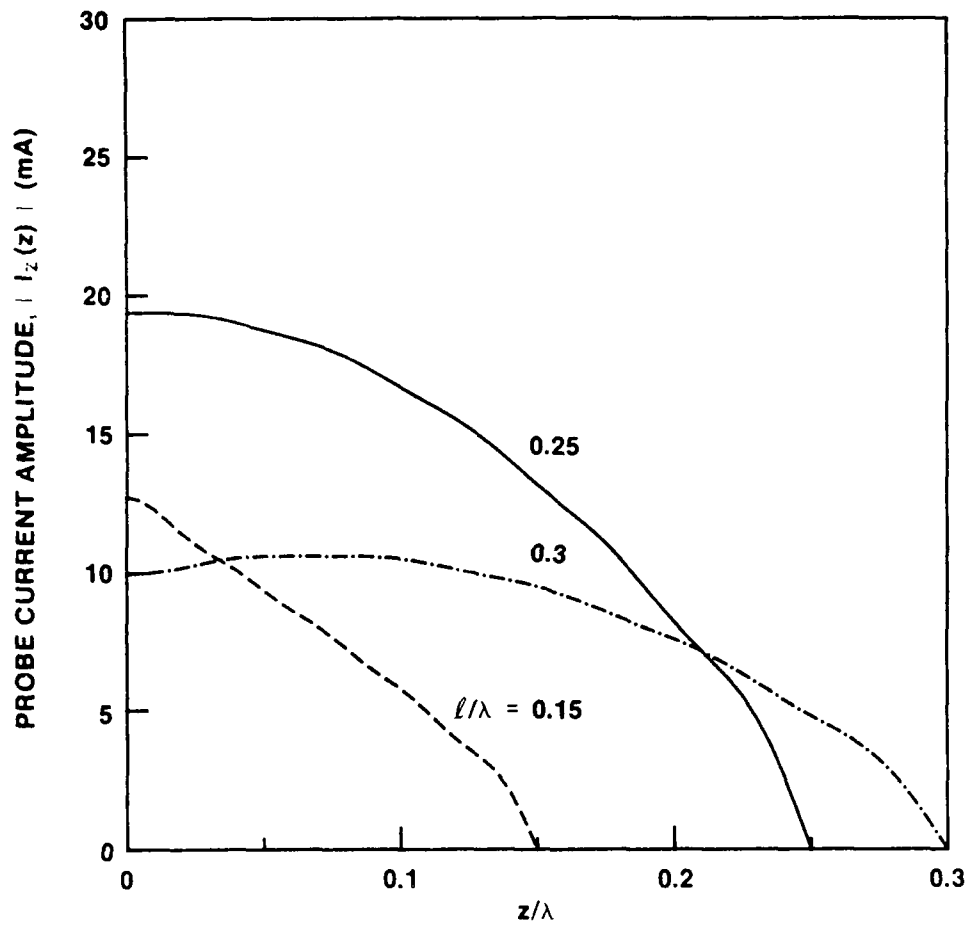


Figure 8-56. Probe Current - Magnitude for Array (b), ($\hat{\phi}_0 = 0^\circ$); Parameter: $l/\lambda = 0.15, 0.25$, and 0.3

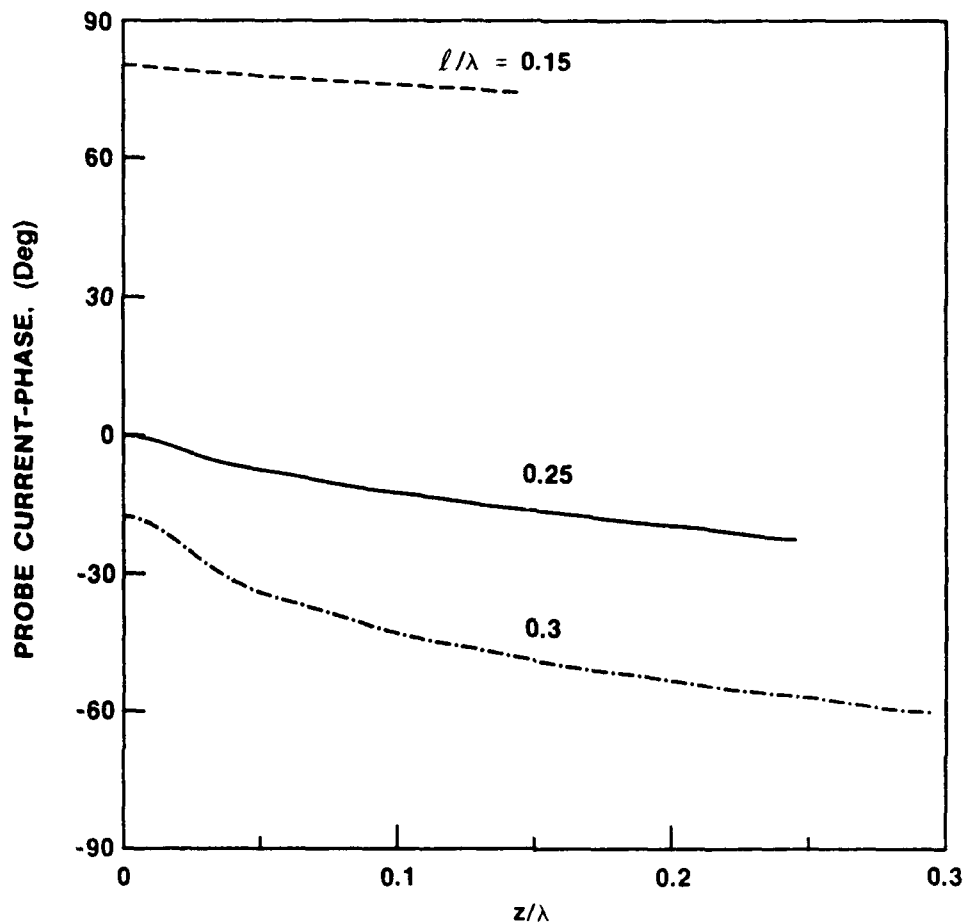


Figure 8-57. Probe Current - Phase for Array
 (b), ($\hat{\phi}_0 = 0^\circ$); Parameter: $l/\lambda = 0.15, 0.25$, and 0.3

For both arrays (a) and (b), each with the three probe lengths specified above, the probe current expansion coefficients c''_i of Eq. (7-3b) are listed in Tables 8-20 to 8-25, for a single ($I = 1$) and ten ($I = 10$) current terms in Eq. (7-3a).

Table 8-20. Probe Current Expansion Coefficients; Parameter:
 Total Number of Current Terms I = 1, 10 ($d/\lambda = 0.4$, $h/\lambda = 0.369$,
 $l/\lambda = 0.15$, $s/\lambda = 0.163$, $a/\lambda = 0.0106$, $b/\lambda = 0.0343$, $Z_c = 50 \Omega$, $\hat{\phi}_0 = 0^\circ$)

I	I=1		I=10	
	$ c_1'' $ mA	ϕ_1'' Deg.	$ c_1'' $ mA	ϕ_1'' Deg.
1	11.606	-101.98	12.147	-103.79
2			0.327	152.94
3			0.733	-100.281
4			0.084	-161.08
5			0.292	-100.98
6			0.055	-139.39
7			0.163	-101.68
8			0.042	-129.90
9			0.107	-102.26
10			0.034	-124.77

Table 8-21. Probe Current Expansion Coefficients; Parameter:
 Total Number of Current Terms I = 1, 10 ($d/\lambda = 0.4$, $h/\lambda = 0.369$,
 $l_c/\lambda = 0.233$, $s_c/\lambda = 0.163$, $a/\lambda = 0.0106$, $b/\lambda = 0.0343$, $Z_c = 50 \Omega$, $\hat{\phi}_0 = 0^\circ$)

I	I=1		I=10	
	$ c_1'' $ mA	ϕ_1'' Deg.	$ c_1'' $ mA	ϕ_1'' Deg.
1	24.221	177.78	21.295	171.90
2			2.452	124.19
3			0.673	-162.97
4			0.602	131.37
5			0.286	-167.02
6			0.298	135.01
7			0.169	-170.96
8			0.185	137.62
9			0.115	-174.17
10			0.128	139.64

Table 8-22. Probe Current Expansion Coefficients: Parameter:
 Total Number of Current Terms I = 1, 10 ($d/\lambda = 0.4$, $h/\lambda = 0.369$,
 $l/\lambda = 0.3$, $s/\lambda = 0.163$, $a/\lambda = 0.0106$, $b/\lambda = 0.0343$, $Z_c = 50 \Omega$, $\hat{\phi}_0 = 0^\circ$)

I	I=1		I=10	
	$ c'_1 $ mA	ϕ''_1 Deg.	$ c''_1 $ mA	ϕ''_1 Deg.
1	10.965	137.52	9.630	139.85
2			2.535	95.91
3			0.268	-124.75
4			0.565	100.18
5			0.100	-135.84
6			0.268	101.77
7			0.052	-146.59
8			0.161	102.86
9			0.033	-157.35
10			0.109	103.75

Table 8-23. Probe Current Expansion Coefficients: Parameter:
 Total Number of Current Terms I = 1, 10 ($d/\lambda = 0.6$, $h/\lambda = 0.369$,
 $l/\lambda = 0.15$, $s/\lambda = 0.245$, $a/\lambda = 0.0106$, $b/\lambda = 0.0343$, $Z_c = 50 \Omega$, $\hat{\phi}_0 = 0^\circ$)

I	I=1		I=10	
	$ c'_1 $ mA	ϕ''_1 Deg.	$ c''_1 $ mA	ϕ''_1 Deg.
1	11.008	-100.31	11.454	-101.74
2			0.312	138.78
3			0.703	-98.62
4			0.065	-169.77
5			0.279	-99.23
6			0.044	-140.68
7			0.156	-99.85
8			0.035	-128.91
9			0.102	-100.37
10			0.029	-122.95

Table 8-24. Probe Current Expansion Coefficients; Parameter:
 Total Number of Current Terms I = 1, 10 (d/λ = 0.6, h/λ = 0.369,
 $I_c/\lambda = 0.25$, s_c/λ = 0.245, a/λ = 0.0106, b/λ = 0.0343, Z_c = 50 Ω, $\phi_0 = 0^\circ$)

I	I=1		I=10	
	c ₁ '' mA	ϕ ₁ '' Deg.	c ₁ '' mA	ϕ ₁ '' Deg.
1	23.138	174.41	20.516	170.44
2			2.442	118.88
3			0.604	-159.56
4			0.590	126.69
5			0.258	-164.31
6			0.290	130.35
7			0.152	-168.77
8			0.179	132.95
9			0.103	-172.45
10			0.124	134.99

Table 8-25. Probe Current Expansion Coefficients; Parameter:
 Total Number of Current Terms I = 1, 10 (d/λ = 0.6, h/λ = 0.369,
 $I/\lambda = 0.3$, s/λ = 0.245, a/λ = 0.0106, b/λ = 0.0343, Z_c = 50 Ω, $\phi_0 = 0^\circ$)

I	I=1		I=10	
	c ₁ '' mA	ϕ ₁ '' Deg.	c ₁ '' mA	ϕ ₁ '' Deg.
1	13.321	144.73	11.848	146.37
2			2.561	98.03
3			0.296	-134.35
4			0.577	103.52
5			0.117	-145.75
6			0.275	105.54
7			0.064	-155.72
8			0.166	106.93
9			0.042	-164.79
10			0.112	108.04

It is interesting to note that, since the probe current across the aperture should be continuous, one could approximately determine the input admittance simply from Eq. (8-1) that is,

$$Y_a(\delta_x) = \frac{I_z(z=0^+)}{V_0}$$

For V_0 set equal to 1, Table 8-26 compares results for the active admittance obtained from Eqs. (4-44) and (8-6) for the geometries of Tables 8-20 to 8-25. In both cases $I = 10$. As one may see, the difference between these two results is less than 1 percent which substantiates the single mode approximation for the field in the aperture.

Table 8-26. Comparison Between Results for Active Admittance
 $Y_a = G_a + jB_a$; Parameter: $d/\lambda = 0.4, 0.6$ [Array (a) : $d/\lambda = 0.4$,
 $l/\lambda = 0.15, 0.233$, and 0.3 , $s/\lambda = 0.163$, $h/\lambda = 0.369$, $a/\lambda = 0.0106$,
 $b/\lambda = 0.0343$, $Z_c = 50 \Omega$, $\hat{\phi}_0 = 0^\circ$; Array (b): $d/\lambda = 0.6$, $l/\lambda = 0.15$,
 0.25 , and 0.3 , $s/\lambda = 0.245$, $h/\lambda = 0.369$, $a/\lambda = 0.0106$,
 $b/\lambda = 0.0343$, $Z_c = 50 \Omega$, $\hat{\phi}_0 = 0^\circ$]]

l/λ	Y_a from Eq. (4-44)				Y_a from Eq. (8-6)			
	$d/\lambda = 0.4$		$d/\lambda = 0.6$		$d/\lambda = 0.4$		$d/\lambda = 0.6$	
	G_a mS	B_a mS	G_a mS	B_a mS	G_a mS	B_a mS	G_a mS	B_a mS
0.15	2.694	13.038	2.168	12.495	2.679	13.093	2.156	12.554
0.233	20.090	0.199			20.066	0.197		
0.25			19.380	-0.006			19.367	-0.031
0.30	7.179	-2.189	9.616	-2.530	7.181	-2.277	9.619	-2.618

8.4.3 COUPLING COEFFICIENTS, S^P

Figure 8-58 shows the amplitude of the coupling coefficients for both arrays (a) and (b). The coupling coefficients decay monotonically vs element number. As will be seen in Figure 8-59, for elements distant from the excited monopole the coupling is primarily due to the parallel plate guide TEM mode (launched by the excited element and its image), the amplitude of which decays as $(pd)^{-3/2}$. For this reason the coupling coefficients vs element number p decay faster for $d/\lambda = 0.6$ than for $d/\lambda = 0.4$ as can be seen from Figure 8-58. On the other hand $|S^P|$ decays faster per wavelength for array (a) than array (b). Also it is interesting to note that $S^0 = -9.2$ dB for $d/\lambda = 0.4$ and $S^0 = -13.2$ dB for $d/\lambda = 0.6$, which since both arrays are matched at broadside, confirms the fact that coupling from neighboring elements to the reference $p = 0$ element is stronger for smaller element spacings.

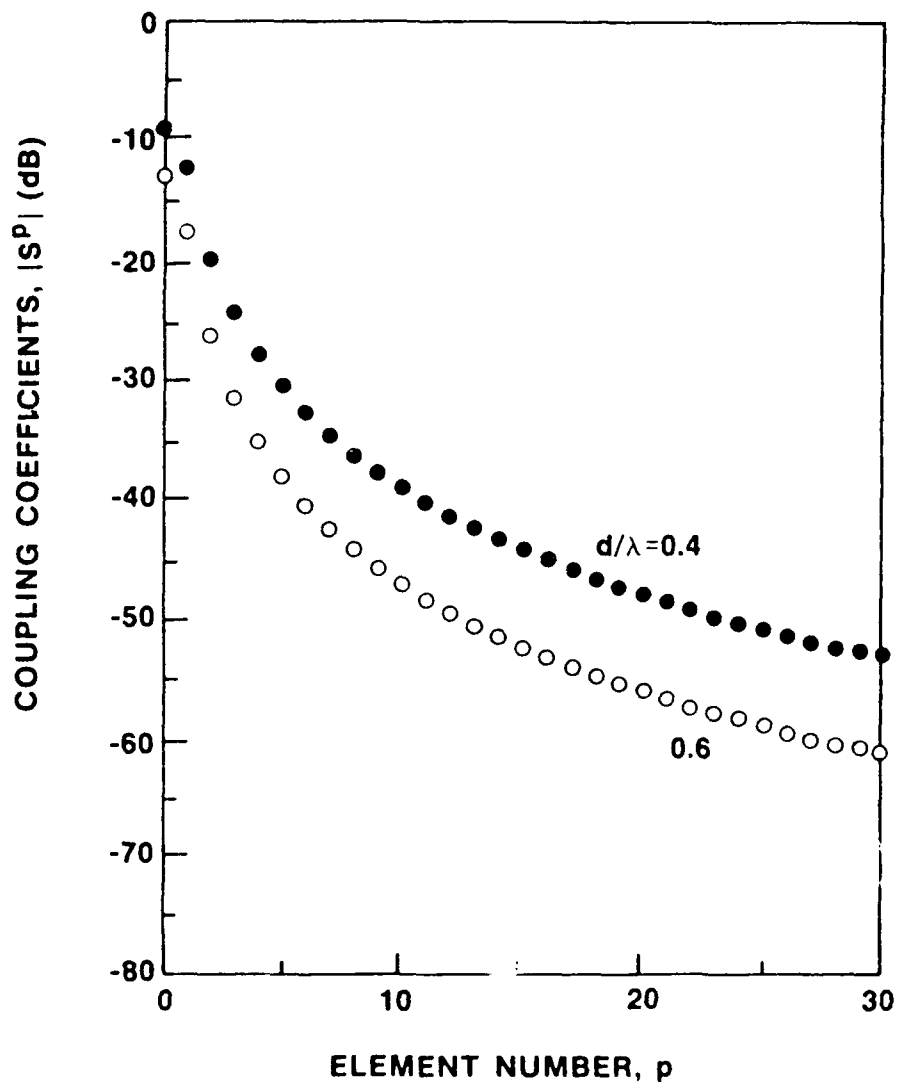


Figure 8-58. Coupling Coefficients - Magnitude for Arrays (a) and (b)

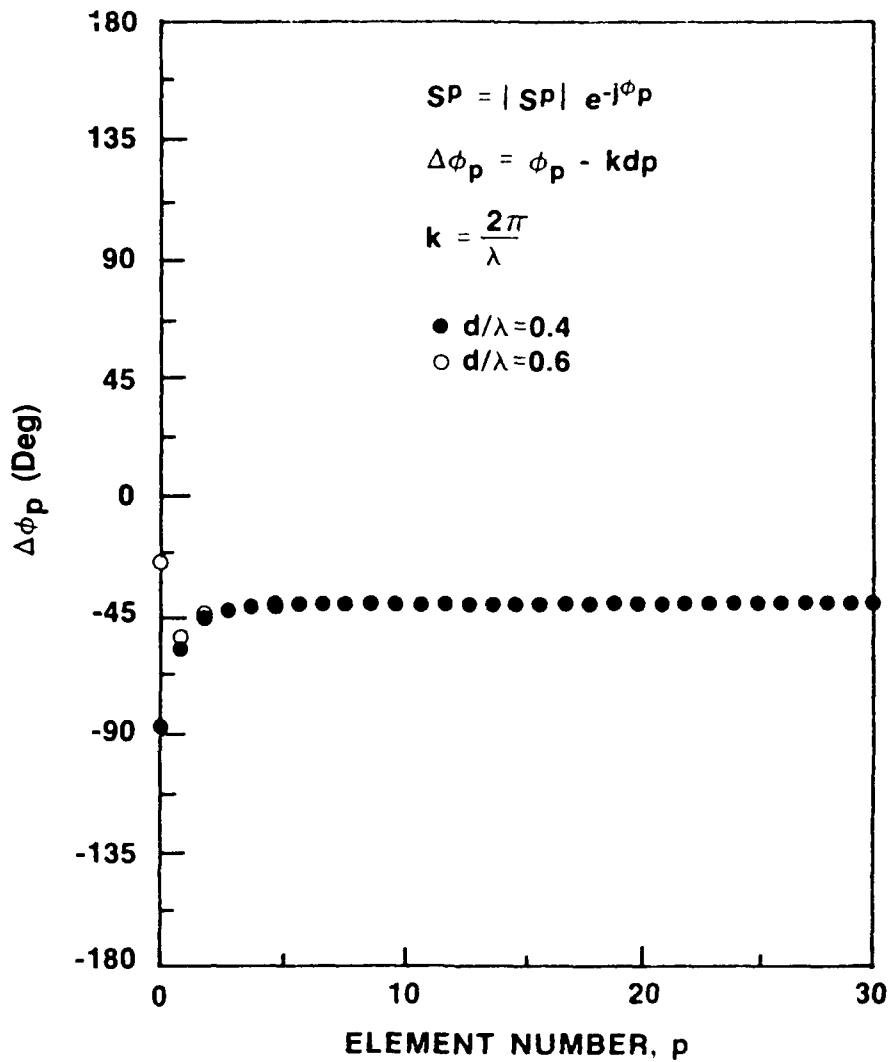


Figure 8-59. Coupling Coefficients - Phase for Arrays (a) and (b)

Figure 8-59 exhibits the coupling coefficient's differential phase $\Delta\phi_p$ as defined in Eq. (8-4) for two element spacings. For monopoles close to the excited element the coupling is due, in addition to the TEM mode, to contributions of higher, non-propagating parallel plate waveguide modes. For elements further removed, the coupling is primarily due to the TEM mode.

8.4.4 ELEMENT PATTERN, $g_z^{(e)}(\hat{\phi})$

An expression for the field element pattern $g_z^{(e)}(\hat{\phi})$ is given in Eq. (6-31).

Figures 8-60 and 8-62 show the dependence of the element pattern amplitude on the interelement spacing and frequency. In each case, the array and element geometry are appropriate to a broadside match at center frequency f_c . There are two basic differences between the two patterns. First, broadside gain is higher for $d/\lambda_c = 0.6$ than for $d/\lambda_c = 0.4$, which is expected since broadside gain is equal to the unit cell gain $(2\pi d/\lambda_c)^{1/2}$. Second, it is observed that while the pattern is smooth for $d/\lambda_c = 0.4$, for $d/\lambda_c = 0.6$ the element pattern exhibits a substantial drop-off near $\hat{\phi} = 42^\circ$. This drop-off is caused by an end-fire grating lobe condition (EGL) which occurs at

$$\hat{\phi}_{EGL} = \sin^{-1}\left(\frac{\lambda_c}{d} - 1\right). \quad (8-7)$$

It is observed, however, that no element pattern null is found. This is expected, because the image array reduces the asymptotic decay of coupling coefficients.

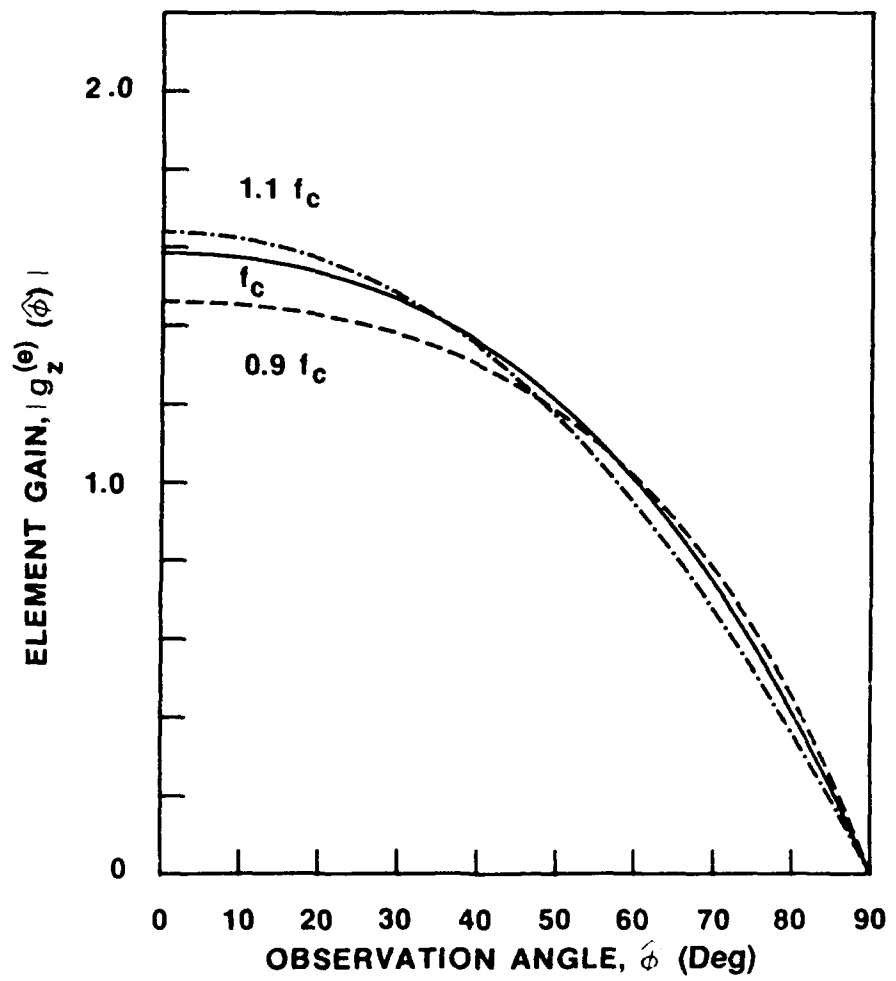


Figure 8-60. Element Pattern - Magnitude for Array (a); Parameter $f = 0.9f_c, f_c$, and $1.1f_c$

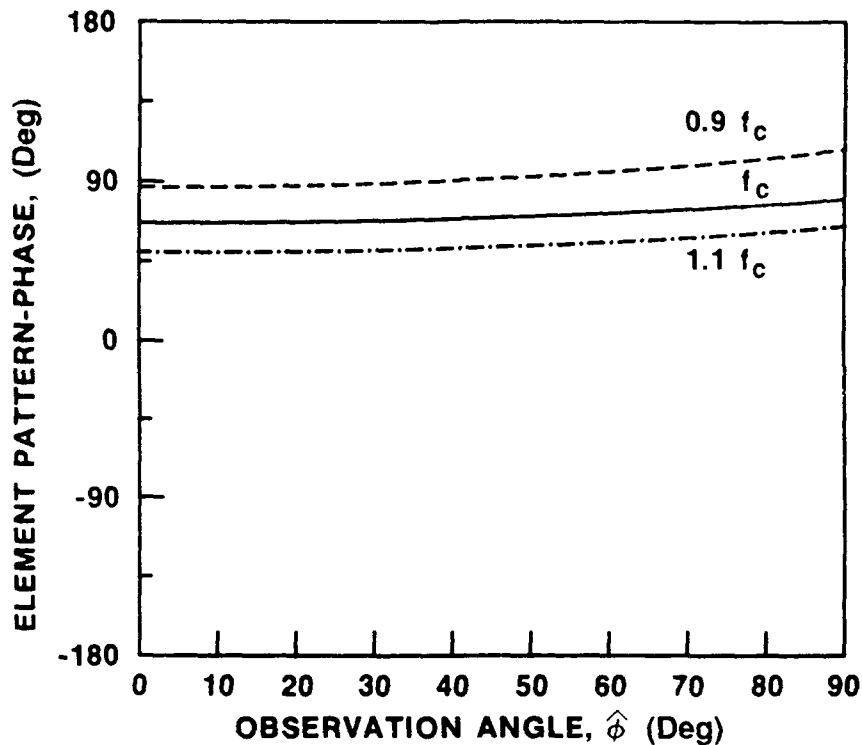


Figure 8-61. Element Pattern - Phase for Array (a); Parameter $f = 0.9f_c, f_c$, and $1.1f_c$

It can be seen from Figures 8-60 and 8-62 that the voltage element gain pattern does not change significantly in a 20 percent frequency band. The pattern shape depends primarily on d/λ as already discussed while the broadside gain is governed by a factor $[(2\pi d/\lambda) (1 - |\Gamma_a(0)|^2)]^{1/2}$. As seen from Figure 8-62 even though the gain in the broadside direction is high within a 20 percent frequency band, the element has a very limited angular range for practical applications (up to $\pm 30^\circ$ off-broadside at $f = 1.1f_c$).

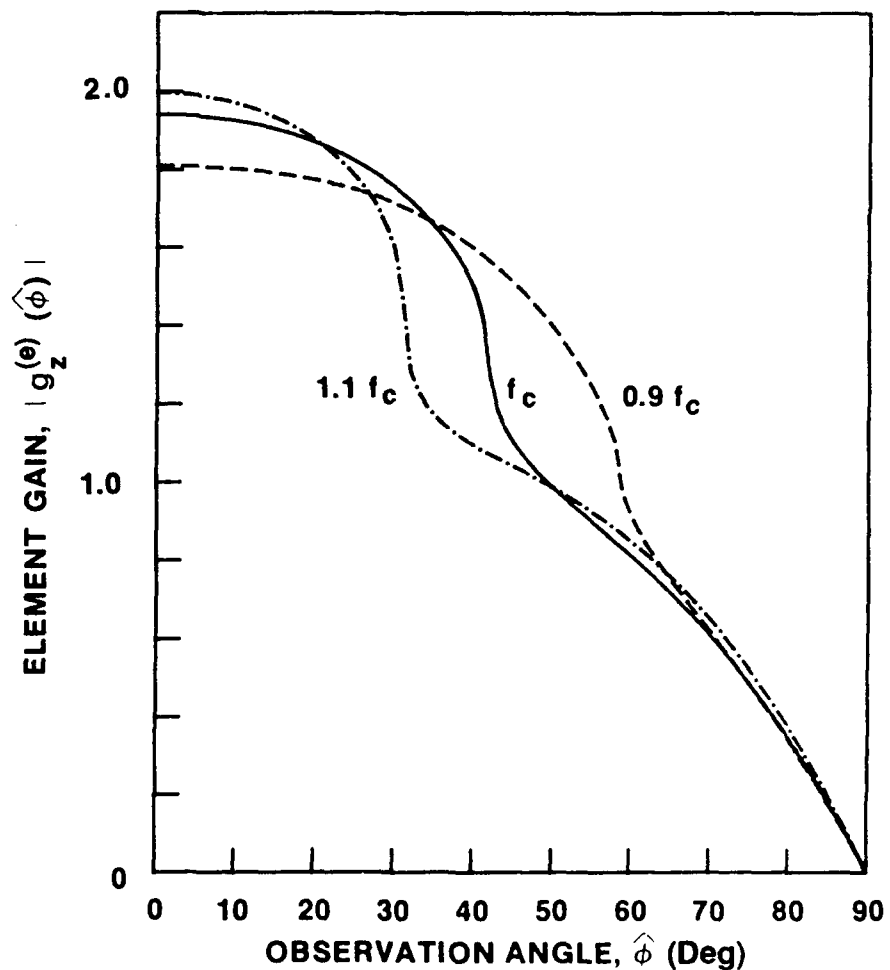


Figure 8-62. Element Pattern - Magnitude for Array (b); Parameter: $f = 0.9f_c$, f_c , and $1.1f_c$

For the same geometry and frequencies, Figures 8-61 and 8-63 exhibit the element pattern phase. One observes that the phase varies only by a few degrees up to the EGL drop-off. Thus, the EGL position essentially determines the limit of usefulness of the element, both in amplitude and phase. Since the phase reference point is at the probe location we conclude that the phase center location is near the probe element. This feature becomes important in the design of beamforming arrays on curved surfaces.

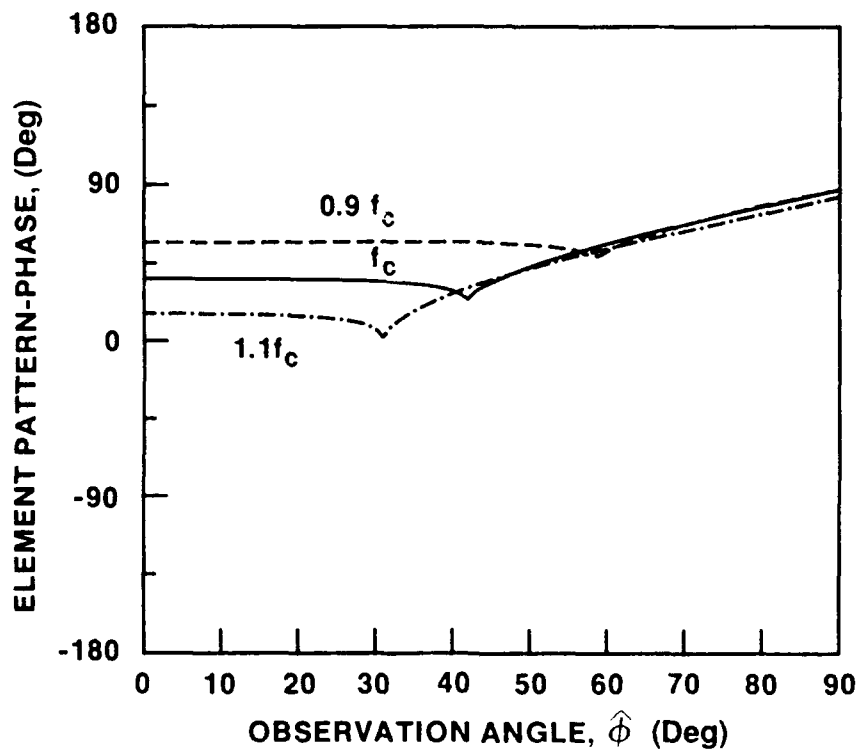


Figure 8-63. Element Pattern - Phase for Array (b); Parameter: $f = 0.9f_c, f_c$, and $1.1f_c$

9. EXPERIMENTS

This chapter describes the experimental effort and presents measured data that strongly support the validity of the analysis and accuracy of the computer program.

To validate the theory, a 30-element linear array of coaxially-fed monopoles in a parallel plate waveguide, and a one and two-half element waveguide simulator were constructed. The array and element construction are described. An illustrative method of selection of optimal geometry for element match in an array environment, as well as the dependence of important design parameters on the array and element geometry is discussed. The measured data are presented for active impedance, coupling coefficients, and element patterns. The measurements show an excellent agreement with theoretically predicted results.

9.1 Array Description

The experimental array is shown in Figures 9-1 and 9-2. The array contains 30 probe elements in a (4 x 6 feet) parallel plate guide set-up. To simulate an infinite parallel plate region, a 5-inch pyramid of absorbing material was placed along the edges of the parallel plates. In Figure 9-2 the top plate was removed to display a section of the array. Figure 9-3 shows schematically the top and the side view of the array with relevant dimensions.

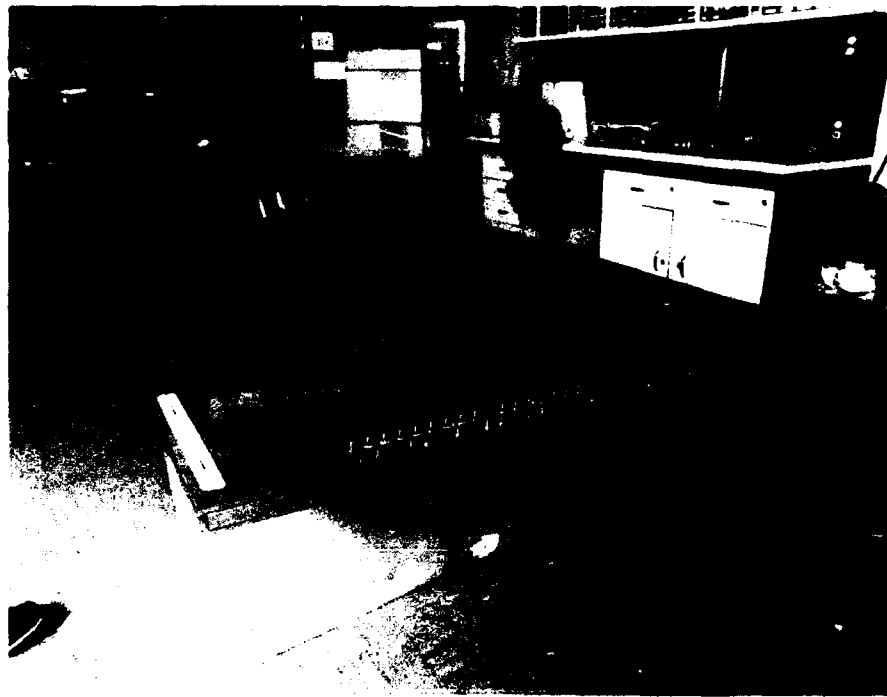


Figure 9-1. A 30-element Linear Array of Coaxially-Fed Monopoles in a Parallel Plate Region. See Eq. (8-5) for specifications

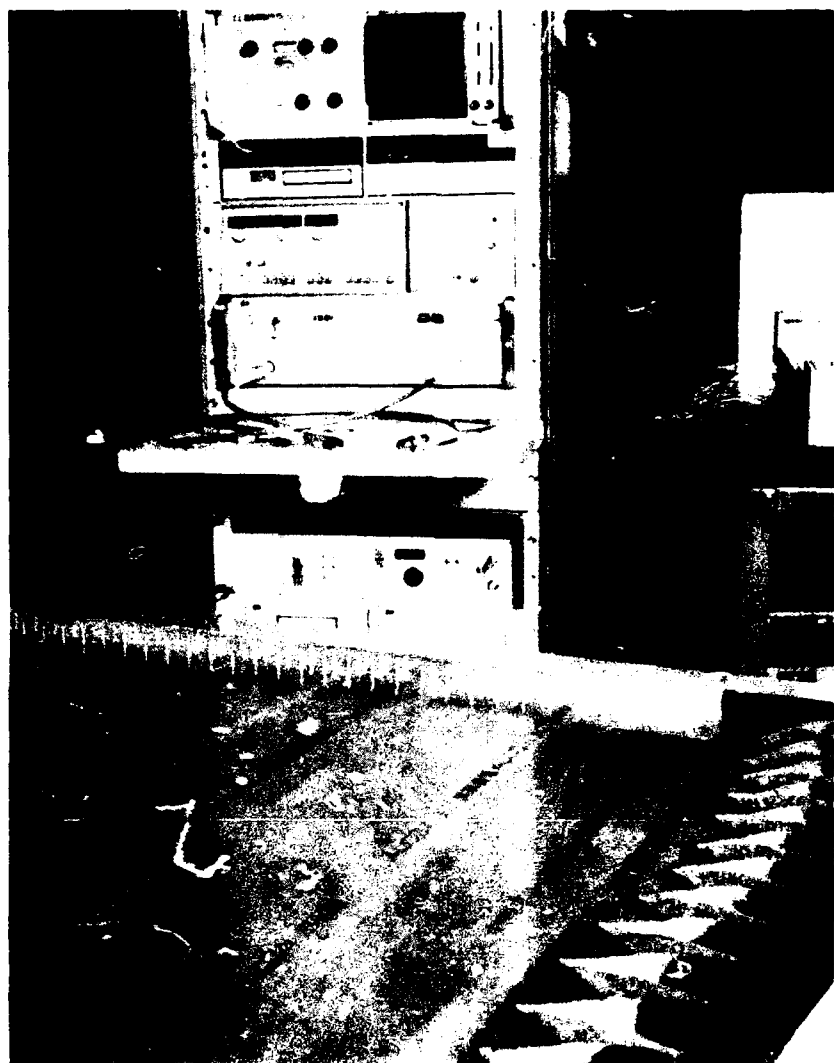


Figure 9-2. A 30-element Linear Array of Coaxially-Fed Monopoles in a Parallel Plate Region (Top Plate Removed to Display the Array Elements)

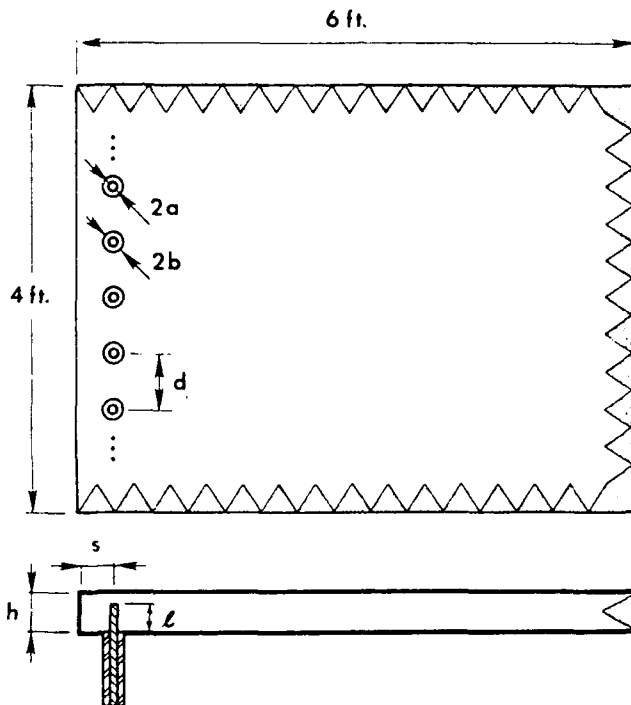


Figure 9-3. Top and Side View of Linear Array

The linear array parameters are: l , the length of coaxially-fed monopoles; $h < \lambda/2$, the parallel plate waveguide height; d , the element spacing; s , the distance between the probe elements and the back-plane; $a \ll \lambda$, the probe radius, while a and b are, respectively, the inner and outer radii of the coaxial feed lines. The coaxial feed lines are filled with teflon ($\epsilon_r = 2$) and have a characteristic impedance $Z_c = 50$ ohms. The geometry of the array is identical to that of array (a) in Eq. (8-5). Specific dimensions at center frequency $f_c = 5.0$ GHz ($\lambda_c = 2.360"$) are:

$$d = 0.4 \lambda_c (0.945")$$

$$h = 0.369 \lambda_c (0.872")$$

$$l = 0.233 \lambda_c (0.550")$$

$$s = 0.163 \lambda_c (0.385")$$

$$a = 0.0106 \lambda_c (0.025")$$

$$b = 0.0343 \lambda_c (0.081")$$

$$Z_c = 50 \Omega (\epsilon_r = 2).$$

The l and s were chosen to yield a broadside match at f_c . (See Section 8.4.1). Parallel plate height $h = 0.872"$ corresponds to C-band rectangular waveguide and was chosen for easy simulator construction.

9.2 Monopole Element Design

The array elements shown in Figure 9-4 are Omni Spectra's Flange Mount Jack Receptacles (model No. 204 CC, part No. 2052-1201-00) with $a = 0.025"$ and $b = 0.081"$. As mentioned, the element dimensions (l , and s) were determined by the requirement that the array be matched for broadside scan ($\phi_0 = 0^\circ$) at center frequency f_c . Figure 8-45 displays a contour plot of magnitude of the active reflection coefficient Γ_a vs probe length l/λ_c and probe to ground distance s/λ_c . It is seen that the active reflection coefficient $\Gamma_a(\phi_0 = 0^\circ)$ vanishes when $l/\lambda_c = 0.233$, $s/\lambda_c = 0.163$.

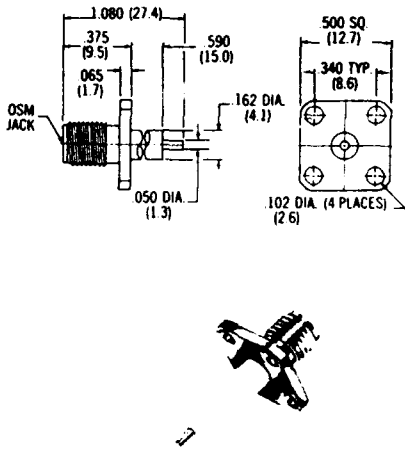


Figure 9-4. Coaxial Monopole Element

For the above geometry, Figure 8-51 exhibits the frequency dependence of active impedance at broadside scan, while Figure 8-52 exhibits active impedance dependence on scan angle ϕ_0 at f_c . It is seen that the frequency bandwidth corresponding to a VSWR of 2:1 is approximately 20 percent for a scan range of 35° .

9.3 Waveguide Simulator

To validate the theoretical predictions for active impedance a one and two-half element waveguide simulator was constructed. The (single mode) simulator is shown in Figures 9-5 and 9-6. The simulator waveguide dimensions, shown in Figure 9-7, are $2d \times h$, that is, $1.872"$

$\times 0.872"$, which corresponds to a standard C-band rectangular waveguide. The waveguide was terminated in a matched load with a VSWR < 1.02 over the frequency band 4 to 6 GHz. In view of Figure 9-8 and the relation

$$\sin \hat{\phi}_0 = \frac{\lambda}{4d} . \quad (9-1)$$

it is seen that the device simulates scan conditions from $\hat{\phi}_0 = 52^\circ$ off-broadside at 4.0 GHz through $\hat{\phi}_0 = 40^\circ$ at 5.0 GHz to $\hat{\phi}_0 = 32^\circ$ at 6.0 GHz.

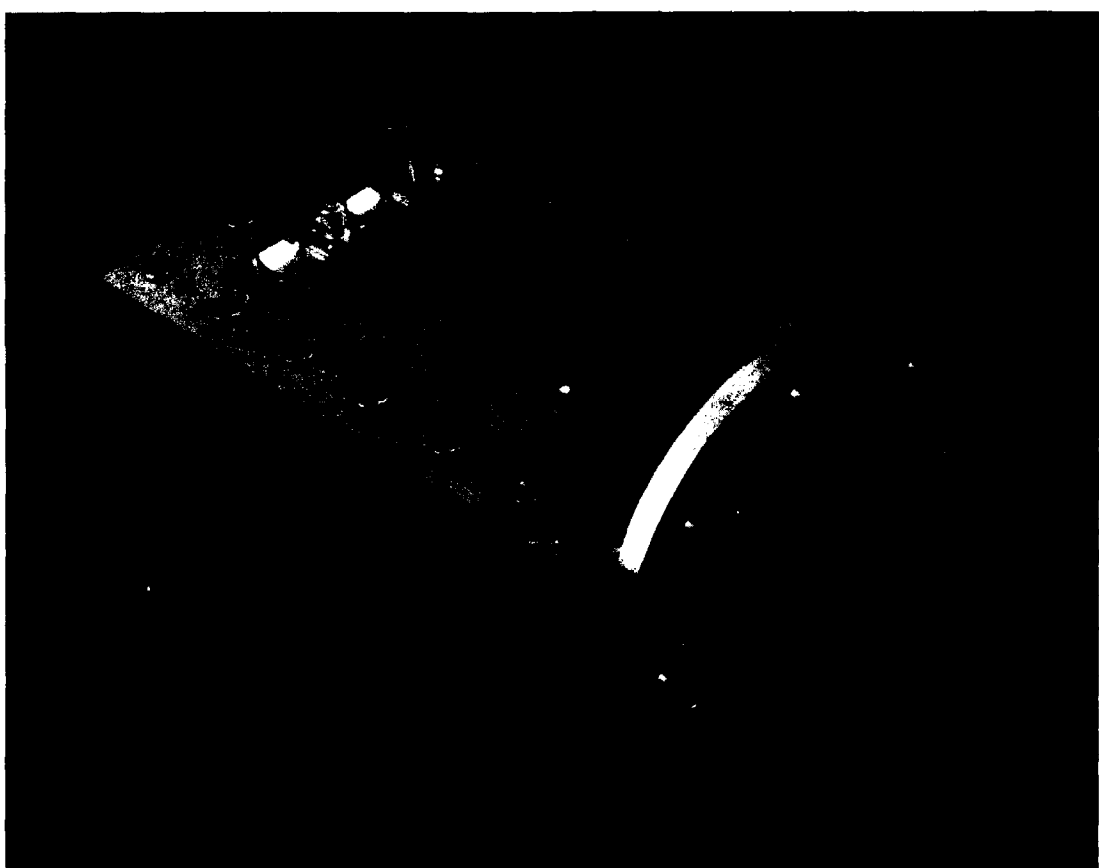
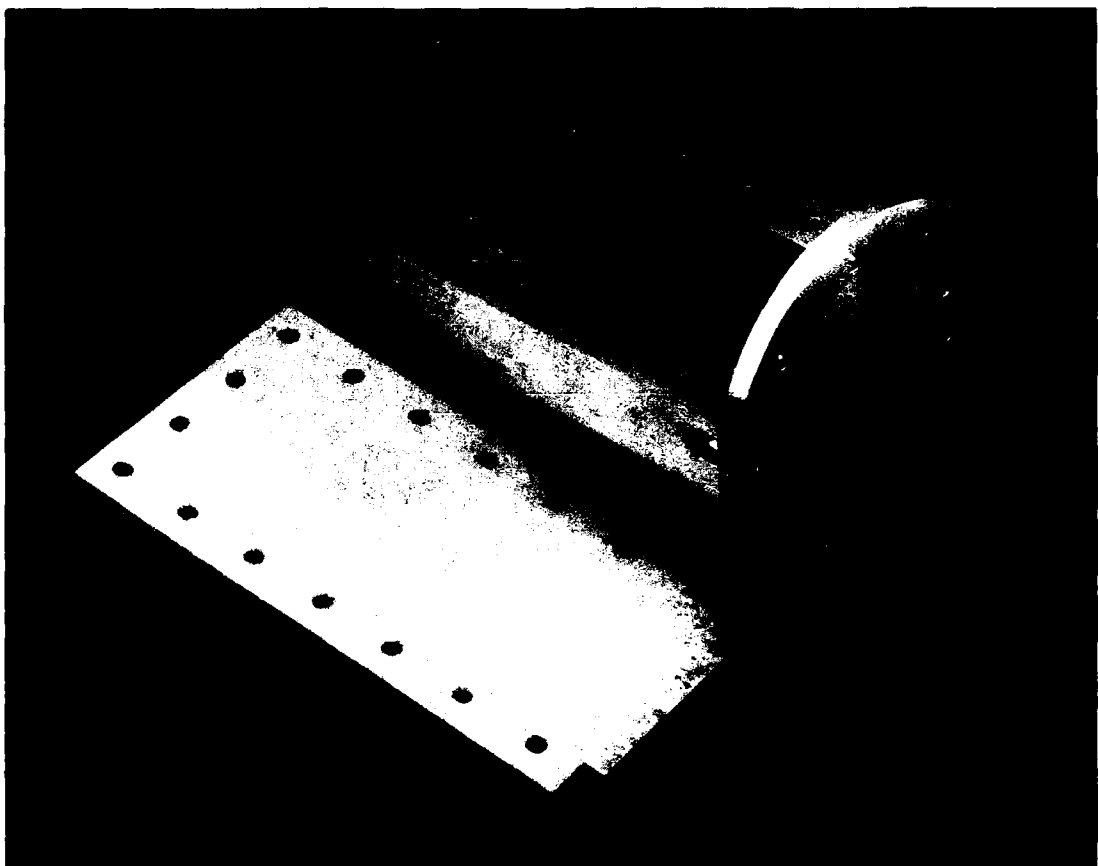


Figure 9-5. A One and Two-Half Element Waveguide Simulator



**Figure 9-6. A One and Two-Half Element Waveguide Simulator
(Top Plate Removed to Display the Monopole Elements)**

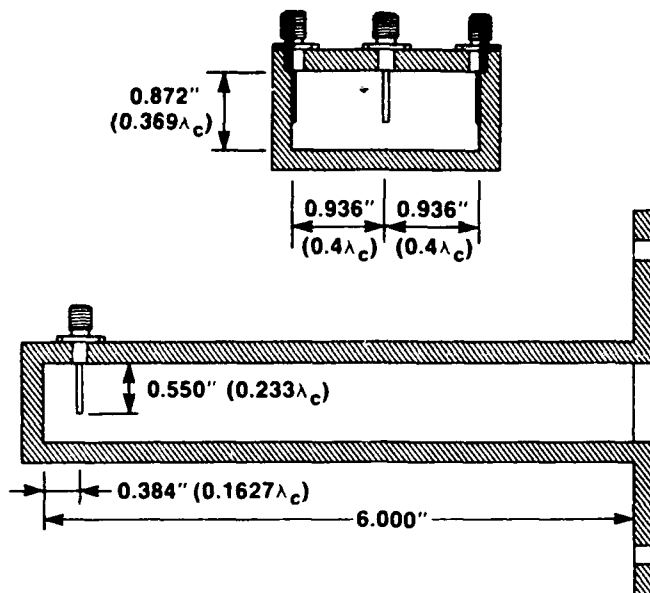
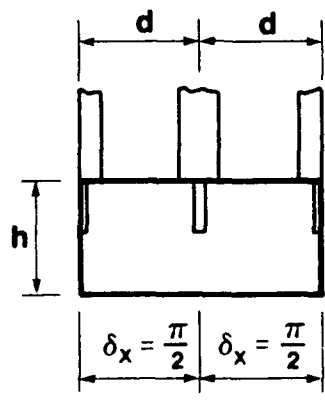


Figure 9-7. A One and Two-Half Element Waveguide Simulator with Dimensions



$$\sin \hat{\phi}_o = \frac{\pi}{2kd}$$

Figure 9-8. Cross Section of Waveguide Simulator
Pertaining to Relation Between Frequency and Scan Angle

The active reflection coefficient measurements were performed with a HP-8410 Network Analyzer. The measurement test setup is shown in Figure 9-9.

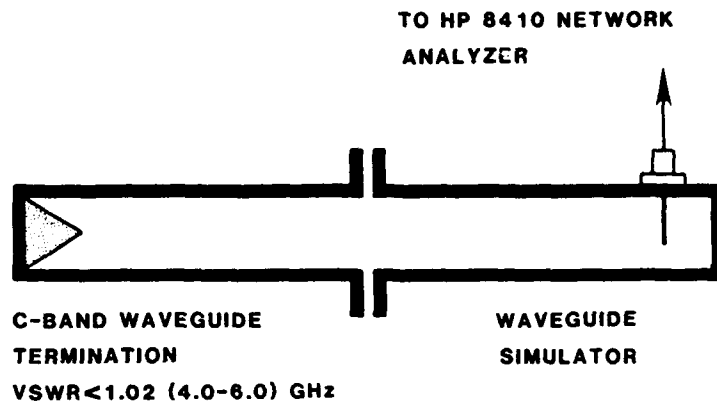


Figure 9-9. Active Reflection Coefficient Measurements Test Set-Up

Figure 9-10 presents a comparison of the theoretical and the measured active impedance vs frequency. The Smith chart is normalized to 50 ohms. An excellent agreement between theory and measurement is observed across the entire band; the two results for the active reflection coefficient differ less than 1 percent in magnitude and less than 3 degrees in phase.

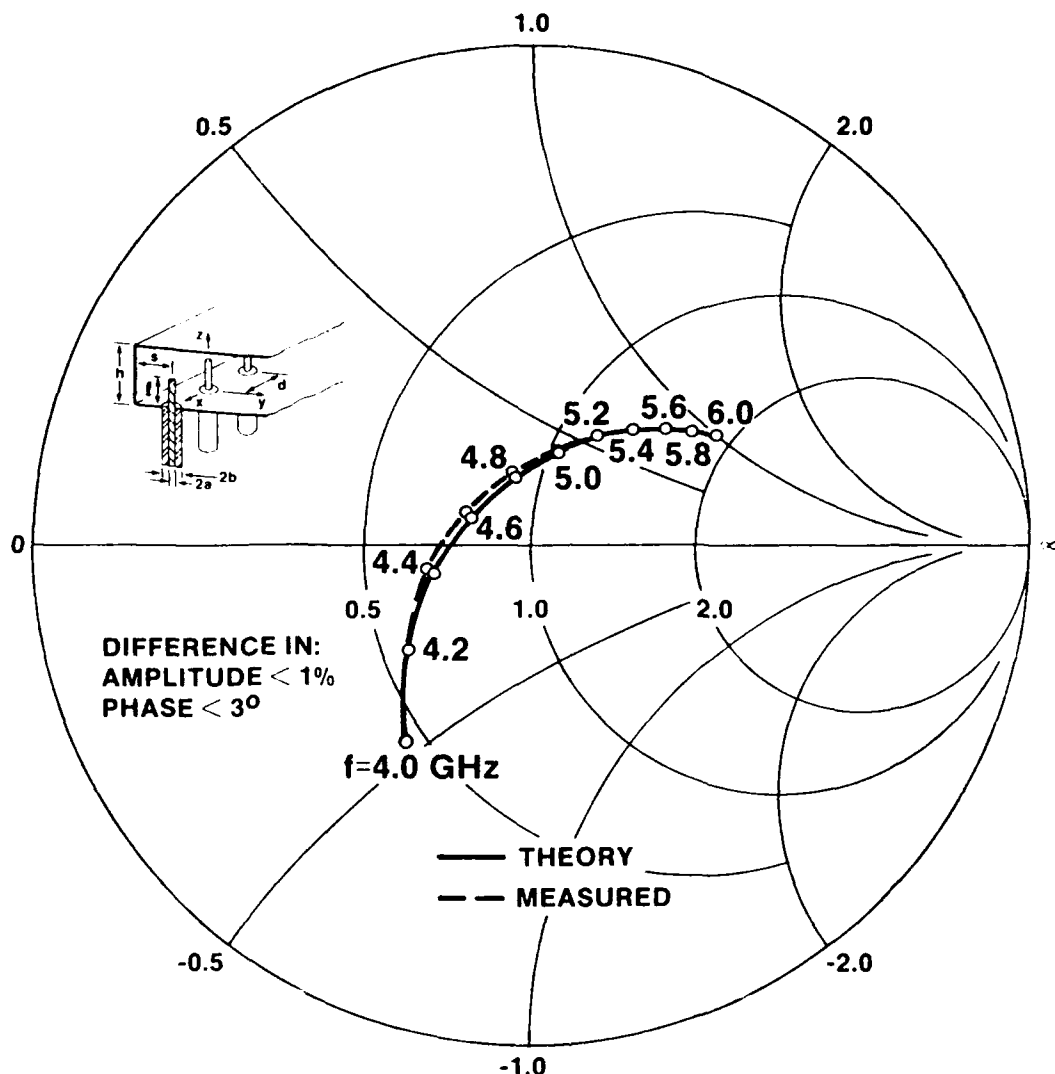


Figure 9-10. Active Impedance vs Frequency - Theory and Simulator Measurements

9.4 Coupling Coefficients

Coupling coefficients were measured in an array of 30 elements down to -35 dB in amplitude, which corresponds approximately to the seventh element from the excited (reference) $p = 0$ element. Below this level, the reflections from the absorber around the edges influenced the measured results.

Figures 9-11 and 9-12 present a comparison between the measured and computed values of coupling coefficients in amplitude and phase, respectively. The difference between the two results is less than 0.3 dB in amplitude and less than 3 degrees in phase.

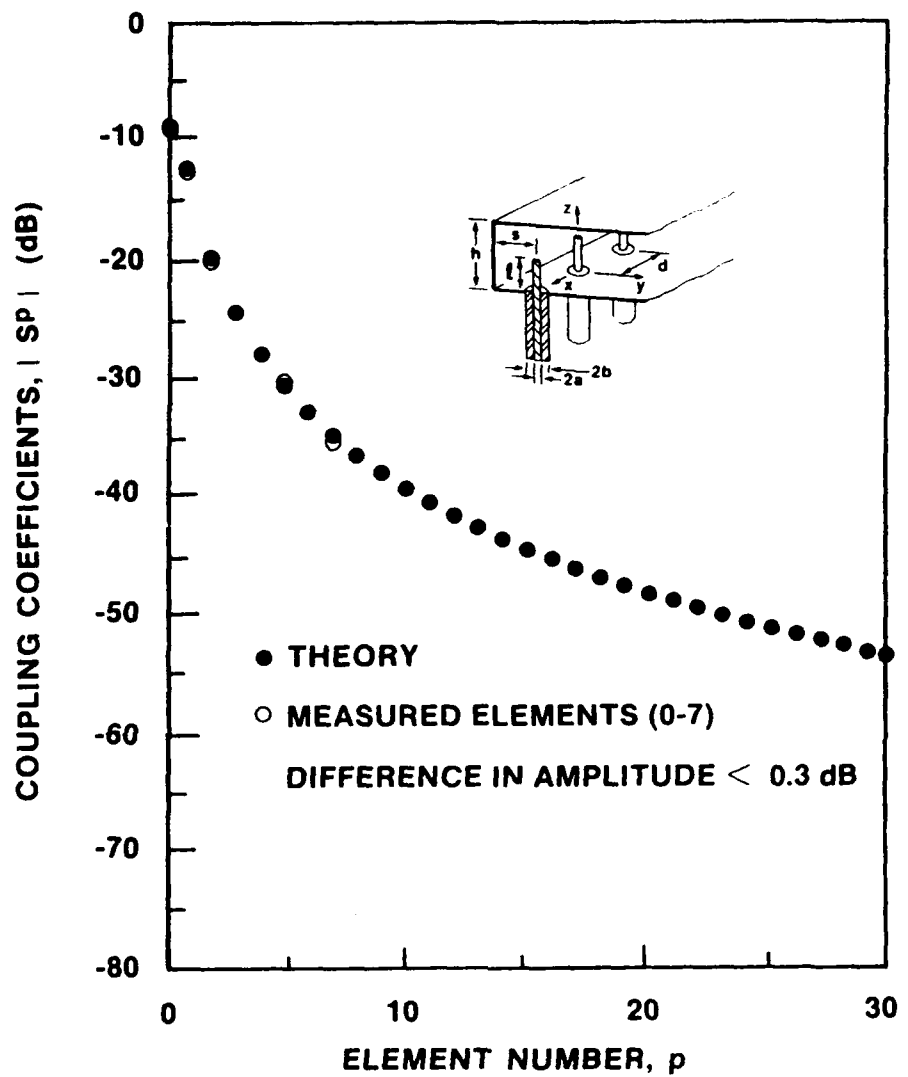


Figure 9-11. Theoretical and Experimental Amplitude of Coupling Coefficients

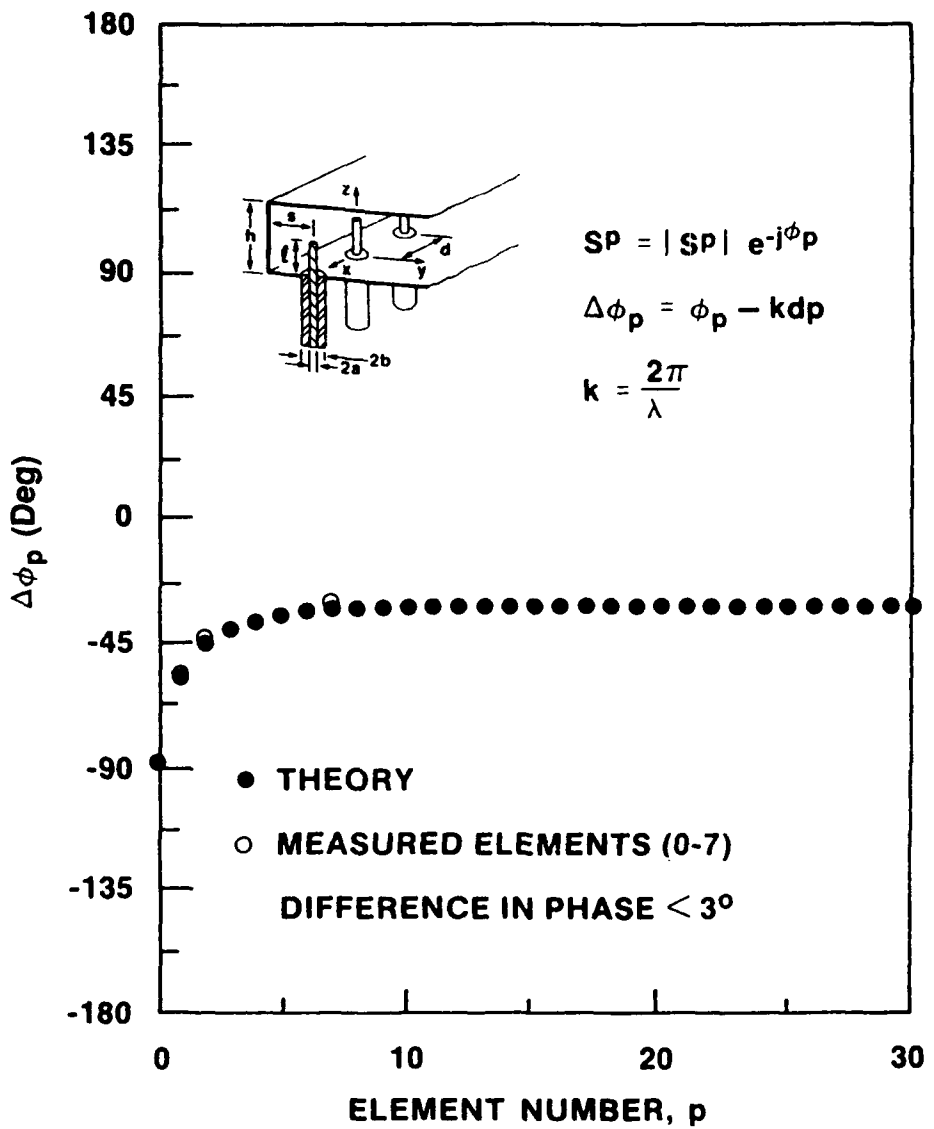


Figure 9-12. Theoretical and Experimental Phase of Coupling Coefficients

9.5 Element Pattern

A linear array of 11 monopoles in a parallel plate region was used to measure the element patterns on a 2000-foot antenna range. A photo of the antenna on the test positioner is shown in Figure 9-13. The test fixture has a semi-circular E-plane flare as shown in Figure 9-14, to impedance match the waveguide to free space. The axis of rotation was at the center element probe location. This element was connected to a 20/20 Scientific Atlanta Antenna Analyzer; other array elements were match-terminated with 50 ohm coaxial loads.



Figure 9-13. Eleven-Element Linear Array on Far-Field Range

11 ELEMENT ARRAY

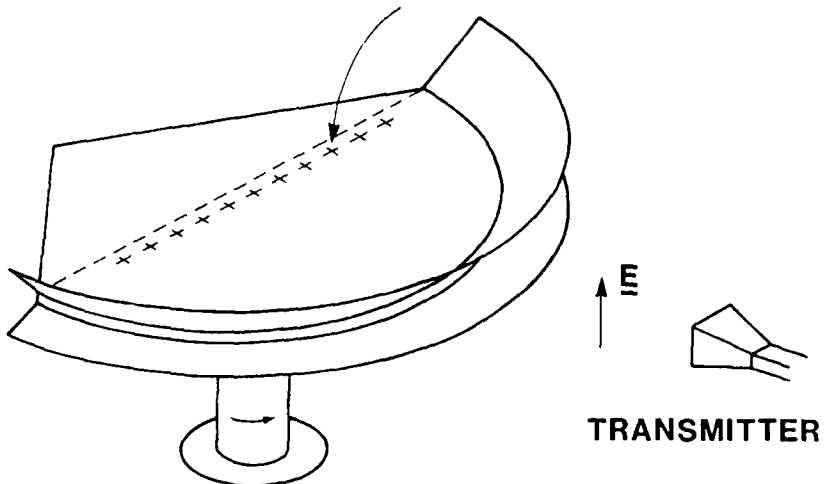


Figure 9-14. Test Fixture for Element Pattern Measurements

Figures 9-15 and 9-16 show the amplitude and phase of the element pattern vs observation angle $\hat{\phi}$ for the following geometry: $h/\lambda = 0.3$, $d/\lambda = 0.72$, $l/\lambda = 0.22$, $a/\lambda = 0.019$, $b/\lambda = 0.062$ at $f = 3.0$ GHz. The amplitude pattern is normalized to the unit cell voltage gain $(2\pi d/\lambda)^{1/2}$. It is seen that the amplitude and phase curves are approximately constant up to $\hat{\phi} = 25^\circ$ off-broadside. The amplitude pattern exhibits a substantial drop-off near $\hat{\phi} = 25^\circ$ while the phase pattern begins to vary rapidly with the observation angle. The sudden change of amplitude and phase patterns is caused by an end-fire grating lobe effect as explained in Section 8.4.4 which for inter-element spacing $d/\lambda = 0.72$ appears at 25° array scan off-broadside.

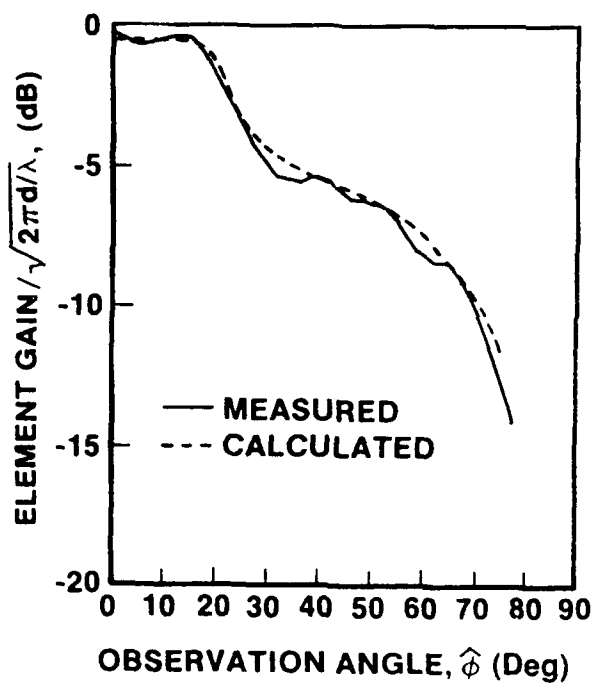


Figure 9-15. Theoretical and Experimental Element Pattern Amplitude

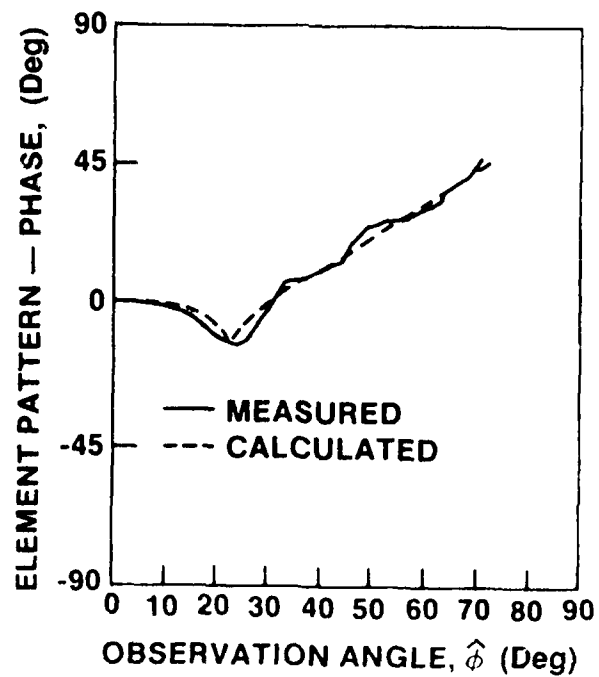


Figure 9-16. Theoretical and Experimental Element Pattern Phase

Since the phase is referenced to the center element, Figure 9-16 also indicates that in the region $0^\circ < \hat{\phi} < 25^\circ$ the "phase center" coincides with the probe location. The ripple in both curves is caused by array edge effects.

The dashed curves in Figures 9-15 and 9-16 represent the theoretical element patterns of the monopole element in an infinite array environment. Good agreement between measured and theoretical results is observed.

10. CONCLUSIONS

An accurate analysis is presented of scan characteristics of an infinite linear array of coaxially-fed thin monopole elements in front of a perfectly conducting backplane in a parallel plate waveguide. Expressions for the active admittance, element patterns and coupling coefficients are given. The relevant expressions can be also applied to arrays in an infinite waveguide region as well as to a single monopole radiating into an infinite or semi-infinite parallel plate region. The numerical results lead to the following conclusions:

- (1) A design method for a matched array element without inclusion of an extra matching network has been established. It is shown that for a given spacing, scan angle and frequency, the element can be perfectly matched by an appropriate choice of a pair of values for l_c/λ and s_c/λ ; at least when $Z_c = 50 \Omega$. It is found that the active admittance is relatively insensitive to the parallel plate separation and to the probe radius (as long as characteristic impedance of the coaxial feed line is 50 ohms). The active impedance exhibits a significant dependence on monopole length (l/λ) and on its distance (s/λ) to a conducting ground.
- (2) With such element design, the frequency bandwidth corresponding to a VSWR of 2:1 is approximately 20 percent for a 35° off-broadside scan range.
- (3) The element gain and phase patterns are predictable. The amplitude and phase curves are approximately constant up to the angle $\hat{\phi}_{EGL}$ off-broadside (the end-fire grating lobe condition). The amplitude pattern exhibits a substantial drop-off near $\hat{\phi}_{EGL}$ while the phase pattern begins to vary rapidly. Thus the EGL position essentially determines the useful range of the element.
- (4) The dipole phase center is located near the element. This information is important in design of microwave feed-through lenses and conformal arrays because it defines the effective radius of curvature of the array surface.
- (5) Close to the excited element the coupling is due to the TEM parallel plate guide mode, as well as to contributions of non-propagating parallel plate waveguide modes. For elements further removed, the coupling is primarily due to the TEM mode, the amplitude of which decays as $(pd)^{-2/3}$ for an array backed by a conducting ground.
- (6) Simplicity, low cost, polarization purity, reasonably wide bandwidth, and relatively high power handling capability make the coaxial monopole a practical element for arrays parallel plate regions.

(7) The close agreement of the experimental and theoretical results for active impedance, coupling coefficients, and element patterns strongly supports the validity of the analysis, and furnishes a firm basis for the matched element design method that was developed.

References

1. Tomasic, B. and Hessel, A. (1982) Linear phased array of coaxially-fed monopole elements in a parallel plate guide, *IEEE/AP-S Symposium Digest*, 144, Albuquerque, New Mexico.
2. Tomasic, B. and Hessel, A. (1985) Linear phased array of coaxially-fed monopole elements in a parallel plate waveguide - experiment, *IEEE/AP-S Symposium Digest*, 23, Vancouver, Canada.
3. Tomasic, B. and Hessel, A. (1985) Arrays of coaxially-fed monopole elements in a parallel plate waveguide, *Phased Arrays 1985 Symposium - Proceedings*, RADC-TR-85-171, 223-250, ADA16931.
4. Williamson, A.G. and Otto, D.V. (1973) Coaxially-fed hollow cylindrical monopole in a rectangular waveguide, *Electron. Lett.*, **9**, (No.10):218-220.
5. Williamson, A.G. (1985) Radial line/coaxial line junctions: Analysis and equivalent circuits, *Int. J. Electronics*, **58**, (No. 1):91-104.
6. Hildebrand, F. (1962) *Advanced Calculus for Applications*, Prentice Hall, Inc., Englewood Cliffs, New Jersey.
7. Williamson, A.G. and Otto, D.V. (1973) Coaxially-fed hollow cylindrical monopole in a rectangular waveguide, *Electron. Lett.*, **9**(No. 10):218.
8. Papoulis, A. (1977) *Signal Analysis*, McGraw-Hill, New York.
9. Infeld, L. et al (1974) On some series of Bessel functions, *J. Math. and Phys.*, **26**:22.
10. Abramowitz, M. and Stegun, I.A. (1964) *Handbook of Mathematical Functions*, United States Department of Commerce, National Bureau of Standards, Applied Mathematics, **55**.
11. Lee, S.W., Jones, W.R. and Campbell, J.J. (1970) Convergence of numerical solution of iris type discontinuity problems, *Antennas and Propagation Symposium Digest*, Columbus, Ohio.

12. Conte, S.D. and de Boor, Carl (1972) *Elementary Numerical Analysis*, McGraw-Hill, New York.
13. Felsen, L.B. and Marcuvitz, N. (1973) *Radiation and Scattering of Waves*, Prentice Hall, Inc., Englewood Cliffs, New Jersey.
14. Gradshteyn, I.S. and I.M. Ryzhik, I.M. (1965) *Table of Integrals, Series, and Products*, Academic Press Inc., New York.

Appendix A

Field Representation in Regions with Piecewise Constant Properties

A1 DERIVATION OF THE TIME-HARMONIC FIELD FROM SCALAR POTENTIALS

As described in Reference 13, the electromagnetic fields excited by time-harmonic electric point currents $\mathbf{J}(\mathbf{r}, t) = \mathbf{J}^0 \delta(\mathbf{r}-\mathbf{r}') e^{j\omega t}$ and magnetic point currents $\mathbf{M}(\mathbf{r}, t) = \mathbf{M}^0 \delta(\mathbf{r}-\mathbf{r}') e^{j\omega t}$ may be represented at $\mathbf{r} \neq \mathbf{r}'$ as:

$$\mathbf{E}(\mathbf{r}, \mathbf{r}') = \nabla \times \nabla \times \mathbf{z}_0 \Pi'(\mathbf{r}, \mathbf{r}') - j\omega\mu \nabla \times \mathbf{z}_0 \Pi''(\mathbf{r}, \mathbf{r}') \quad (A-1a)$$

$$\mathbf{H}(\mathbf{r}, \mathbf{r}') = j\omega\epsilon \nabla \times \mathbf{z}_0 \Pi'(\mathbf{r}, \mathbf{r}') + \nabla \times \nabla \times \mathbf{z}_0 \Pi''(\mathbf{r}, \mathbf{r}') \quad (A-1b)$$

¹³ Felsen, L. B. and Marcuvitz, N. (1973) *Radiation and Scattering of Waves*, Prentice Hall, Inc., Englewood Cliffs, New Jersey.

where the E (prime) and H (double prime) mode Hertz potentials Π' and Π'' , respectively, are related to the scalar potential functions S' and S'' via

$$\Pi'(\mathbf{r}, \mathbf{r}') = \frac{1}{j\omega\epsilon} \mathbf{J}^0 \cdot \nabla' \times \nabla' \times \mathbf{z}_0 S'(\mathbf{r}, \mathbf{r}') - \mathbf{M}^0 \cdot \nabla' \times \mathbf{z}_0 S'(\mathbf{r}, \mathbf{r}') \quad (\text{A-1c})$$

$$\Pi''(\mathbf{r}, \mathbf{r}') = \mathbf{J}^0 \cdot \nabla \times \mathbf{z}_0 S''(\mathbf{r}, \mathbf{r}') + \frac{1}{j\omega\mu} \mathbf{M}^0 \nabla' \times \nabla' \times \mathbf{z}_0 S''(\mathbf{r}, \mathbf{r}'). \quad (\text{A-1d})$$

The longitudinal electric current element $\mathbf{J}^0 = \mathbf{z}_0 J_z^0$, $\mathbf{M}^0 = 0$, contributes only to $\Pi'(\mathbf{r}, \mathbf{r}')$, thereby exciting E-modes only, and a longitudinal magnetic current $\mathbf{M}^0 = \mathbf{z}_0 M_z^0$, $\mathbf{J}^0 = 0$, generates only H-modes, whereas both mode types are excited by a transversely directed source of either electric or magnetic current. If $\mathbf{E}(\mathbf{r}, \mathbf{r}')$ and $\mathbf{H}(\mathbf{r}, \mathbf{r}')$ satisfy the Maxwell field equations for point current excitation, then $S'(\mathbf{r}, \mathbf{r}')$ and $S''(\mathbf{r}, \mathbf{r}')$ satisfy the differential equation

$$(\nabla^2 + k^2) \nabla_t^2 S'(\mathbf{r}, \mathbf{r}') = \delta(\mathbf{r} - \mathbf{r}') \quad (\text{A-2a})$$

$$(\nabla^2 + k^2) \nabla_t^2 S''(\mathbf{r}, \mathbf{r}') = \delta(\mathbf{r} - \mathbf{r}'), \quad k^2 = \omega^2 \mu \epsilon \quad (\text{A-2b})$$

subject to appropriate boundary conditions. By defining

$$-\nabla_t^2 S'(\mathbf{r}, \mathbf{r}') = G'(\mathbf{r}, \mathbf{r}') \quad (\text{A-3a})$$

$$-\nabla_t^2 S''(\mathbf{r}, \mathbf{r}') = G''(\mathbf{r}, \mathbf{r}') \quad (\text{A-3b})$$

one may relate S' and S'' to the corresponding Green's functions G' and G'' of the scalar wave equations by

$$(\nabla^2 + k^2) G'(\mathbf{r}, \mathbf{r}') = -\delta(\mathbf{r} - \mathbf{r}') \quad (\text{A-3c})$$

$$(\nabla^2 + k^2) G''(\mathbf{r}, \mathbf{r}') = -\delta(\mathbf{r} - \mathbf{r}'). \quad (A-3d)$$

Since an arbitrarily oriented source may be decomposed into a transverse and longitudinal part, it is useful to list the corresponding reduction of (A-1c) and (A-1d) for these separate cases. When the source is transverse ($\mathbf{J}_z^0 = \mathbf{M}_z^0 = 0$),

$$\Pi'(\mathbf{r}, \mathbf{r}') = \left(\frac{1}{j\omega\epsilon} \mathbf{J}_t^0 \frac{\partial}{\partial z'} + \mathbf{M}_t^0 \times \mathbf{z}_0 \right) \cdot \nabla_t' S'(\mathbf{r}, \mathbf{r}') \quad (A-4a)$$

$$\Pi''(\mathbf{r}, \mathbf{r}') = \left(\mathbf{z}_0 \times \mathbf{J}_t^0 + \frac{1}{j\omega\mu} \mathbf{M}_t^0 \frac{\partial}{\partial z'} \right) \cdot \nabla_t' S''(\mathbf{r}, \mathbf{r}') \quad (A-4b)$$

whereas for a longitudinal source ($\mathbf{J}_t^0 = \mathbf{M}_t^0 = 0$),

$$\Pi'(\mathbf{r}, \mathbf{r}') = \frac{J_z^0}{j\omega\epsilon} G'(\mathbf{r}, \mathbf{r}') \quad (A-4c)$$

$$\Pi''(\mathbf{r}, \mathbf{r}') = \frac{M_z^0}{j\omega\mu} G''(\mathbf{r}, \mathbf{r}'). \quad (A-4d)$$

From transmission line analysis along the z axis, with eigenfunctions evaluated in the cross section transverse to z , one has the following solutions of Eqs. (A-2) and (A-3) in terms of a modal expansion:

$$S'(\mathbf{r}, \mathbf{r}') = \frac{1}{j\omega\epsilon} \sum_l \frac{\Phi_l(\rho) \Phi_l^*(\rho')}{k_{tl}^2} Y_l(z, z') \quad k_{tl} \neq 0 \quad (A-5a)$$

$$S''(\mathbf{r}, \mathbf{r}') = \frac{1}{j\omega\mu} \sum_i \frac{\Psi_i(\rho) \Psi_i^*(\rho')}{k_{ti}''^2} Z''_i(z, z'), \quad k_{ti}'' \neq 0 \quad (A-5b)$$

or,

$$G'(\mathbf{r}, \mathbf{r}') = \frac{1}{j\omega\epsilon} \sum_i \Phi_i(\rho) \Phi_i^*(\rho') Y'_i(z, z') \quad (A-5c)$$

$$G''(\mathbf{r}, \mathbf{r}') = \frac{1}{j\omega\mu} \sum_i \Psi_i(\rho) \Psi_i^*(\rho') Z''_i(z, z'). \quad (A-5d)$$

It is recalled that $\Phi_i(\rho)$ and $\Psi_i(\rho)$ are scalar eigenfunctions that have been listed in Reference 13 for a variety of cross sections. The $Y'_i(z, z')$ and $Z''_i(z, z')$ are, respectively, the E-mode current excited by a unit voltage generator and the H-mode voltage excited by a unit current generator, and they are related to the one-dimensional E-and H-mode Green's functions by

$$Y'_i(z, z') = j\omega\epsilon g'_{zi}(z, z') \quad (A-6a)$$

$$Z''_i(z, z') = j\omega\mu g''_{zi}(z, z') \quad (A-6b)$$

where $g'_{zi}(z, z')$ and $g''_{zi}(z, z')$ satisfy the equation

$$\left(\frac{d^2}{dz^2} + \kappa_i^2 \right) g_{zi}(z, z') = -\delta(z - z') \quad (A-6c)$$

with

$$\kappa_i^2 = k^2 - k_{ti}^2 \quad (A-6d)$$

subject to appropriate boundary conditions at the endpoints of the z domain.

A2 MODAL REPRESENTATION FOR UNBOUNDED CROSS SECTIONS

Because there are no transverse boundaries, the eigenvalue problems for the E- and H-modes are identical so that $\Phi_i = \Psi_i$, and the distinction between the E- and H-mode Green's function resides solely in their longitudinal dependence. For the circular waveguide description of $G(\mathbf{r}, \mathbf{r}')$ (with ξ denoting k_z),

$$G(\mathbf{r}, \mathbf{r}') = \frac{1}{2\pi} \sum_{m=-\infty}^{\infty} e^{-jm(\phi-\phi')} \int_0^{\infty} \xi J_m(\xi\rho) J_m(\xi\rho') g_{z_i}(z, z'; \kappa_i) d\xi. \quad (A-7)$$

It will be useful to employ a representation involving a range of integration in ξ from $-\infty$ to ∞ instead of Eq. (A-7). Provided that $g_{z_i}(z, z')$ is an even function of ξ , a requirement satisfied by the longitudinal Green's functions to be encountered subsequently, the desired representation may be derived as follows. Upon introducing

$$J_m(\xi\rho) = \frac{1}{2} [H_m^{(1)}(\xi\rho) + H_m^{(2)}(\xi\rho)] \quad (A-8)$$

where $H_m^{(1)}(\xi\rho)$ and $H_m^{(2)}(\xi\rho)$ are the Hankel function of the first and second kind of order m and argument $\xi\rho$. One may write Eq. (A-7) as

$$G(\mathbf{r}, \mathbf{r}') = \frac{1}{2\pi} \sum_{m=-\infty}^{\infty} e^{-jm(\phi-\phi')} (I_1 + I_2) \quad (A-9a)$$

where

$$I_1 = \frac{1}{2} \int_0^{\infty} \xi H_m^{(1)}(\xi\rho) J_m(\xi\rho') d\xi \quad (A-9b)$$

$$I_2 = \frac{1}{2} \int_0^{\infty} \xi H_m^{(2)}(\xi\rho) J_m(\xi\rho') d\xi. \quad (A-9c)$$

If the range of ξ is to be extended to $\xi = -\infty$, the $\xi = 0$ branch-point singularity arising from the presence of the Hankel function [and also of the Bessel function in (A-7)], must be accounted for in the integrands of I_1 and I_2 , since m is not an integer. To assure single-valuedness of the integrands when continued into the complex ξ plane, we introduce a branch cut along the negative real ξ axis (see Figure A-1). The following parametric relations then provide the means for mapping ξ into $-\xi$ ($0 < \xi < \infty$):

$$J_m(xe^{j\pi}) = e^{jmx} J_m(x) \quad (A-10a)$$

$$H_m^{(1)}(xe^{j\pi}) = -e^{-jmx} H_m^{(2)}(x). \quad (A-10b)$$

Suppose we introduce the change of variable $\bar{\xi} = \xi e^{-j\pi}$ in the integrand of I_1 in Eq. (A-9b). Then,

$$\xi = \bar{\xi} e^{j\pi} \quad (A-11a)$$

$$d\xi = e^{j\pi} d\bar{\xi} \quad (A-11b)$$

and

$$I_1 = \frac{1}{2} e^{j\pi} \int_0^{\infty e^{-j\pi}} \bar{\xi} H_m^{(1)}(\bar{\xi}\rho e^{j\pi}) J_m(\bar{\xi}\rho' e^{j\pi}) d\bar{\xi} \quad (A-11c)$$

or,

$$I_1 = \frac{1}{2} \int_{-\infty e^{-j\pi}}^0 \bar{\xi} H_m^{(2)}(\bar{\xi}\rho) J_m(\bar{\xi}\rho') d\bar{\xi} \quad (A-11d)$$

where Eq. (A-11d) follows from Eq. (A-11c) and the use of Eq. (A-10). Thus, $I_1 + I_2$ may be written as

$$I_1 + I_2 = \frac{1}{2} \int_{-\infty e^{-j\pi}}^{\infty} \xi H_m^{(2)}(\xi\rho) J_m(\xi\rho') d\xi = \frac{1}{2} \int_{-\infty e^{-j\pi}}^{\infty} \xi H_m^{(2)}(\xi\rho') J_m(\xi\rho) d\xi. \quad (A-12)$$

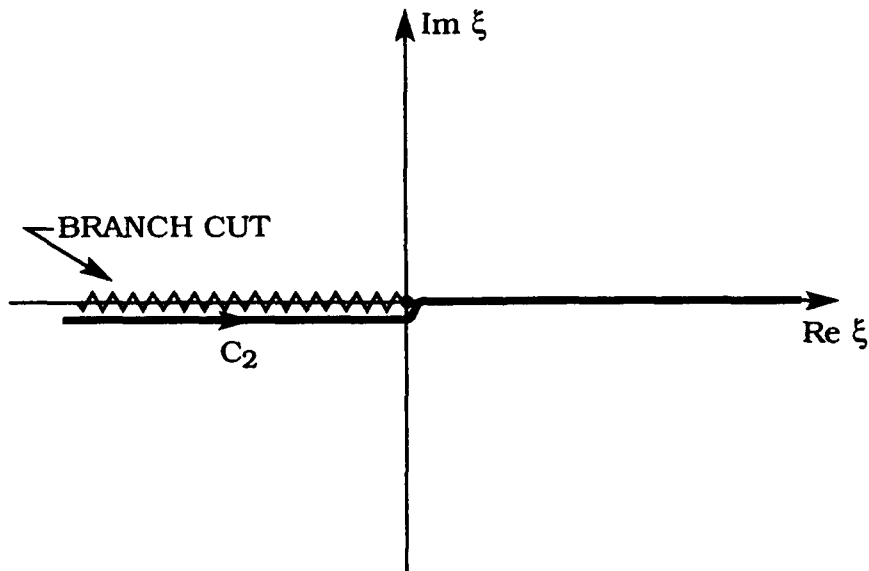


Figure A-1. Integration Path in the Complex ξ -Plane

The contour of integration extends along the bottom edge of the branch cut and the positive real axis as is shown in Figure A-1. The alternative expression with ρ and ρ' interchanged, given by the second integral in Eq. (A-12), is deduced by representing $J_m(\xi\rho')$ in Eq. (A-7) in terms of the Hankel function contribution in Eq. (A-8), and proceeding as above. The integral representations in Eq. (A-12) permit deformation of the contour of integration into the complex ξ -plane. To show this, we examine the asymptotic behavior of the Bessel and Hankel functions for large values of their argument:

$$J_m(z) \sim \sqrt{\frac{2}{\pi z}} \cos\left(z - \frac{m\pi}{2} - \frac{\pi}{4}\right), \quad |z| \rightarrow \infty, -\pi < \arg z < \pi \quad (A-13a)$$

$$H_m^{(1,2)}(z) \sim \sqrt{\frac{2}{\pi z}} e^{\pm j\left(z - \frac{m\pi}{2} - \frac{\pi}{4}\right)}, \quad |z| \rightarrow \infty, -\pi < \arg z < \pi \quad (A-13b)$$

where z is a complex variable whose argument lies between $-\pi$ and $+\pi$. If $\text{Im}(z) < 0$, the magnitude of $H_m^{(2)}(z)$ decays like $\exp[-\text{Im}(z)]$, while that of $\text{Im}(z) > 0$ increases like $\exp[\text{Im}(z)]$, so that

$$|H_m^{(2)}(\xi\rho) J_m(\xi\rho')| \sim \frac{1}{\pi\sqrt{\rho\rho'|\xi|}} e^{+(\text{Im}\{\xi\})(\rho-\rho')} \quad |\xi| \rightarrow \infty, -\pi < \arg \xi < 0. \quad (A-14)$$

For $\rho > \rho'$ the integrand of the first integral in Eq. (A-12) therefore decays exponentially over an infinite semicircle in the bottom half of the complex ξ -plane, while for $\rho < \rho'$, the integrand of the second integral exhibits a similar behavior.

The contour C_2 in Figure A-1 can thus be deformed away from the real axis at $|\xi| \rightarrow \infty$ into path C'_2 in the bottom half of the ξ -plane; in consequence, the Green's function in Eq. (A-9a) can be represented as

$$G(r, r') = \frac{1}{4\pi} \sum_{m=-\infty}^{\infty} e^{-j\text{Im}(\phi-\phi')} \int_{C'_2} \xi J_m(\xi\rho_c) H_m^{(2)}(\xi\rho_s) g_{z1}(z, z'; \kappa_1) d\xi \quad (A-15)$$

where ρ_c and ρ_s denote the lesser and greater, respectively, of the quantities ρ and ρ' . The choice of transformation involving $H_m^{(2)}$ instead $H_m^{(1)}$ is motivated by the fact that, for a time dependence $\exp(j\omega t)$, the former satisfies the radiation condition at $\rho \rightarrow \infty$ in a natural manner and facilitates subsequent asymptotic evaluation of the integral.

Since $\kappa_{t1}^2 = \xi^2$ for a circular waveguide representation, it follows from Eqs (A-5a), (A-5b), (A-6a) and (A-6b), that in cylindrical coordinates,

$$S(r, r') = \frac{1}{4\pi} \sum_{m=-\infty}^{\infty} e^{-jm(\phi-\phi')} \int_{C_2} \frac{1}{\xi} J_m(\xi \rho_-) H_m^{(2)}(\xi \rho_+) g_{zl}(z, z'; \kappa_i) d\xi \quad (A-16a)$$

where $g_{zl}(z, z'; \kappa_i)$ depends on k_{z1} through the longitudinal propagation constant

$$\kappa_i = \sqrt{k^2 - k_{z1}^2}, \quad \text{Im}\{\kappa_i\} \leq 0. \quad (A-16b)$$

Appendix B

Magnetic Ring Source In An Infinite Parallel Plate Waveguide - Radial Mode Representation

B 1 RADIAL TRANSMISSION LINE REPRESENTATION

In this Appendix we derive expressions for the fields in the parallel plate region due to a magnetic ring source of width $(b-a)$ by an approach in which the propagation direction is assumed to be radial. The problem is simplified by first considering magnetic ring source excitation with $\mathbf{M}(\rho', z') = \Phi_0 \delta(\rho - \rho') \delta(z - z')$, $(z'=0)$, and then obtaining the total response by use of the superposition theorem.

Since the magnetic source is transverse (to ρ) with $\partial/\partial\phi' = 0$, only E-modes with respect to ρ are excited. Field components transverse to ρ can be expressed in the form

$$E_z(\rho, \phi, z) = \sum_{n=0}^{\infty} V_n'(\rho) e_{zn}'(\phi, z) \quad (B-1a)$$

$$H_\phi(\rho, \phi, z) = \sum_{n=0}^{\infty} I'_n(\rho) h'_{\phi n}(\rho, \phi, z) \quad (B-1b)$$

where the E-mode transverse vector eigenfunctions e'_{zn} and $h'_{\phi n}$ are

$$e'_{zn}(\phi, z) = \frac{1}{\sqrt{2\pi}} \sqrt{\frac{\epsilon_n}{h}} \cos \frac{n\pi z}{h} \quad (B-1c)$$

$$h'_{\phi n}(\rho, \phi, z) = -\frac{1}{\sqrt{2\pi}} \sqrt{\frac{\epsilon_n}{h}} \frac{1}{\rho} \cos \frac{n\pi z}{h} \quad (B-1d)$$

with

$$\epsilon_n = \begin{cases} 1, & n=0 \\ 2, & n \geq 1 \end{cases} \quad (B-1e)$$

The e'_{zn} and $h'_{\phi n}$ possess the following orthonormality properties over the cross-sectional domain S

$$\iint_S e'_m \times h'^*_n \cdot \rho_0 \, dS = \delta_{mn}, \quad dS = \rho \, d\phi \, dz. \quad (B-2)$$

The asterisk denotes the complex conjugate, and the Kronecker delta is:

$\delta_{mn} = 0, m \neq n; \delta_{mn} = 1$. In Eqs. (B-1a) and (B-1b) the total modal voltage and current are

$$V'_n(\rho) = \int V_n(\rho, \rho') \, d\rho' \quad (B-3a)$$

$$I'_n(\rho) = \int I_n(\rho, \rho') d\rho' \quad (B-3b)$$

where $V_n(\rho, \rho')$ and $I_n(\rho, \rho')$ are voltage and current at ρ due to point sources $v'_n(\rho')$ and $i'_n(\rho')$ at ρ' . Since $M(\rho, z')$ is transverse (to ρ), the magnetic current ring source can be represented by a point voltage generator $v'_n(\rho')$ on an equivalent radial transmission line at ρ' , where

$$\begin{aligned} v'_n(\rho') &= \iint_{\text{source}} \mathbf{M}(\rho, \rho') \cdot \mathbf{h}_n^* (\rho', \phi', z') dS \\ &= \int_{\phi'=0}^{2\pi} \phi_0 M(-\phi_0) \frac{1}{\sqrt{2\pi}} \sqrt{\frac{\epsilon_n}{h}} \frac{1}{\rho'} \cos \frac{n\pi}{h} z' \rho' d\phi' = -M\sqrt{2\pi} \sqrt{\frac{\epsilon_n}{h}}. \end{aligned} \quad (B-4)$$

The radial transmission-line equations that apply to the indicated point-source excitation are

$$-\frac{d}{d\rho} V'_n(\rho, \rho') = j\kappa_n Z'_n \frac{1}{\rho} I'_n(\rho, \rho') + v'_n(\rho') \quad (B-5a)$$

$$-\frac{d}{d\rho} I'_n(\rho, \rho') = j\kappa_n Y'_n \rho V'_n(\rho, \rho') \quad (B-5b)$$

where

$$Z'_n = \frac{1}{Y'_n} = \frac{\kappa_n}{\omega \epsilon_0} \quad (B-5c)$$

$$\kappa_n = \sqrt{k^2 - \left(\frac{n\pi}{h}\right)^2}, \quad \text{Im} \{ \kappa_n \} \leq 0. \quad (B-5d)$$

To determine $V'_n(\rho, \rho')$ and $I'_n(\rho, \rho')$ we first determine the amplitude of the voltage and current at the generator terminals ρ'_- and ρ'_+ . The determination of voltages $V'_n(\rho, \rho')$ and currents

$I'_n(\rho, \rho')$ at any point ρ on a transmission line with constants κ_n and Z_n then follows from Eq. (B-5).

To that end, we consider the network problem shown in Figure B-1, where $\overleftarrow{Z}(\rho')$ and $\overrightarrow{Z}(\rho')$ are the impedances seen looking to the left and to the right, respectively, from the generator terminals.

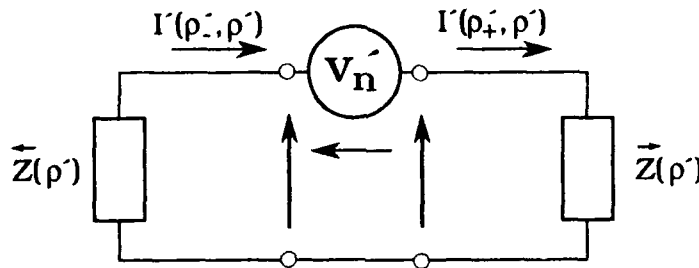


Figure B-1. Network Representation for Voltage Point-Source Excited Radial Transmission Line

The voltage $V'_n(\rho)$ satisfies Bessel's differential equation

$$\left[\frac{1}{\rho} \frac{d}{d\rho} \left(\rho \frac{d}{d\rho} \right) + \kappa_n^2 \right] V'_n(\rho) = 0 \quad (B-6a)$$

and for $\rho < \rho'$ the solution can be written in the form

$$\overleftarrow{V}'_n(\rho) = j\kappa_n Z'_n J_0(\kappa_n \rho), \quad \rho < \rho'. \quad (B-6b)$$

Substituting Eq. (B-6b) into Eq. (B-5a),

$$\overleftarrow{I}'_n(\rho) = \kappa_n \rho J_1(\kappa_n \rho). \quad (B-7)$$

Using Eqs. (B-6b) and (B-7)

$$\bar{Z}(\rho') = -\frac{\bar{V}_n(\rho'_-)}{\bar{I}_n(\rho'_-)} = -j \frac{Z'_n}{\rho'} \frac{J_0(\kappa_n \rho')}{J_1(\kappa_n \rho')} . \quad (B-8)$$

Similarly, for $\rho > \rho'$, the solution of (B-6a) is

$$\bar{V}'_n(\rho) = j \kappa_n Z'_n H_0^{(2)}(\kappa_n \rho), \quad \rho > \rho' \quad (B-9a)$$

and after substitution into Eq. (B-5a),

$$\bar{I}'_n(\rho) = \kappa_n \rho H_1^{(2)}(\kappa_n \rho) \quad (B-9b)$$

from which we get

$$\bar{Z}(\rho') = \frac{\bar{V}_n(\rho'_+)}{\bar{I}_n(\rho'_+)} = j \frac{Z'_n}{\rho'} \frac{H_0^{(2)}(\kappa_n \rho')}{H_1^{(2)}(\kappa_n \rho')} . \quad (B-9c)$$

By conventional network analysis it is seen that

$$V'_n(\rho'_+, \rho') = -V'_n(\rho') \frac{\bar{Z}(\rho')}{\bar{Z}(\rho')} \quad (B-10a)$$

$$V'_n(\rho'_-, \rho') = -V'_n(\rho') \frac{\bar{Z}(\rho')}{\bar{Z}(\rho')} \quad (B-10b)$$

where

$$\tilde{\tilde{Z}}(\rho') = \tilde{Z}(\rho') + \tilde{\Sigma}(\rho'). \quad (\text{B-10c})$$

Substitution of Eqs. (B-8) and B-9c into Eq. (B-10) yields

$$V'_n(\rho'_+, \rho') = -j \frac{\kappa_n \pi \rho'}{2} v'_n(\rho') H_0^{(2)}(\kappa_n \rho') J_1(\kappa_n \rho') \quad (\text{B-11a})$$

$$V'_n(\rho'_-, \rho') = -j \frac{\kappa_n \pi \rho'}{2} v'_n(\rho') J_0(\kappa_n \rho') H_1^{(2)}(\kappa_n \rho') \quad (\text{B-11b})$$

and

$$\tilde{Z}(\rho') = \frac{2 Z_n'}{\pi \kappa_n \rho'^2} \frac{1}{J_1(\kappa_n \rho') H_1^{(2)}(\kappa_n \rho')} \quad (\text{B-11c})$$

where we have used the Wronskian relation

$$W[J_0(\kappa_n \rho'), H_0^{(2)}(\kappa_n \rho')] = J_0(\kappa_n \rho') H_1^{(2)}(\kappa_n \rho') - J_1(\kappa_n \rho') H_0^{(2)}(\kappa_n \rho') = j \frac{2}{\pi \kappa_n \rho'}. \quad (\text{B-11d})$$

In view of (B-6b) and (B-9a) the modal voltage on the radial transmission line at ρ due to the point source at ρ' follows from Eqs. (B-11a) and (B-11b), that is,

$$V'_n(\rho, \rho') = -j \frac{\kappa_n \pi \rho'}{2} v'_n(\rho') \begin{cases} J_1(\kappa_n \rho') H_0^{(2)}(\kappa_n \rho), & \rho > \rho' \\ J_0(\kappa_n \rho) H_1^{(2)}(\kappa_n \rho'), & \rho < \rho' \end{cases} \quad (\text{B-12a})$$

or upon substitution of Eq. (B-4) for $v'_n(\rho')$

$$V'_n(\rho, \rho') = -j \frac{\kappa_n \pi \sqrt{2\pi} V_0}{2 \ln \frac{b}{a}} \sqrt{\frac{\epsilon_n}{h}} \begin{cases} J_1(\kappa_n \rho') H_0^{(2)}(\kappa_n \rho), & \rho > \rho' \\ J_0(\kappa_n \rho) H_1^{(2)}(\kappa_n \rho'), & \rho < \rho' \end{cases} \quad (B-12b)$$

Equation (B-12b) can be briefly checked by noting that the identity

$$V'_n(\rho_+, \rho') + V'_n(\rho') - V'_n(\rho_-, \rho') = 0 \quad (B-13)$$

must be satisfied. Substituting Eqs. (B-11a), (B-11b) and (B-4) into Eq. (B-13) one finds that indeed Eq. (B-13) holds.

The modal voltage due to the magnetic ring source of width $(b-a)$ can now be obtained from Eq. (B-3a) where the integration over ρ' extends over the source region. Thus,

$$V'_n(\rho) = -j \frac{\kappa_n \pi \sqrt{2\pi} V_0}{2 \ln \frac{b}{a}} \sqrt{\frac{\epsilon_n}{h}} \begin{cases} H_0^{(2)}(\kappa_n \rho) \int_a^b J_1(\kappa_n \rho') d\rho' & \rho \geq b \\ H_0^{(2)}(\kappa_n \rho) \int_a^{\rho} J_1(\kappa_n \rho') d\rho' + J_0(\kappa_n \rho) \int_{\rho}^b H_1^{(2)}(\kappa_n \rho') d\rho' & a \leq \rho \leq b \\ J_0(\kappa_n \rho) \int_a^b H_1^{(2)}(\kappa_n \rho') d\rho' & \rho \leq a \end{cases} \quad (B-14a)$$

$$= j \frac{\pi \sqrt{2\pi} V_0}{2 \ln \frac{b}{a}} \sqrt{\frac{\epsilon_n}{h}} \begin{cases} H_0^{(2)}(\kappa_n \rho) J_1 & \rho \geq b \\ J_0(\kappa_n \rho) H_0^{(2)}(\kappa_n b) - H_0^{(2)}(\kappa_n \rho) J_0(\kappa_n a) & a \leq \rho \leq b \\ J_0(\kappa_n \rho) H_1 & \rho \leq a \end{cases} \quad (B-14a)$$

where

$$J_n = J_0(\kappa_n b) - J_0(\kappa_n a) \quad (B-14b)$$

$$H_n = H_0^{(2)}(\kappa_n b) - H_0^{(2)}(\kappa_n a). \quad (B-14c)$$

Substituting Eq. (B-14) into Eq. (B-1a) with e_{zn} defined in Eq. (B-1c), we see that the z -component of the electric field due to the magnetic current ring source at $z = 0$ in an infinite parallel plate waveguide is

$$E_z(r) = \sum_{n=0}^{\infty} V_n'(\rho) e_{zn}(\phi, z)$$

$$= j \frac{\pi V_0}{2h \ln \frac{b}{a}} \sum_{n=0}^{\infty} \epsilon_n \cos \frac{n\pi}{h} z \begin{cases} H_0^{(2)}(\kappa_n \rho) J_n & , \rho \geq b \\ J_0(\kappa_n \rho) H_0^{(2)}(\kappa_n b) - H_0^{(2)}(\kappa_n \rho) J_0(\kappa_n a), & a \leq \rho \leq b. \\ J_0(\kappa_n \rho) H_n & , \rho \leq a \end{cases} \quad (B-15)$$

The magnetic field $H_\phi(r)$ can be obtained from Eq. (B-1b) using Eqs. (B-5a) and (B-12) as demonstrated below. From Eq. (B-5a) at $\rho \neq \rho'$,

$$I_n'(\rho, \rho') = -j \frac{\rho}{\kappa_n Z_n} \frac{d}{d\rho} V_n'(\rho, \rho'). \quad (B-16)$$

Substitution of Eq. (B-12) into Eq. (B-16) yields

$$I_n'(\rho, \rho') = \frac{\kappa_n \rho \pi \sqrt{2\pi} V_0}{Z_n 2 \ln \frac{b}{a}} \sqrt{\frac{\epsilon_n}{h}} \begin{cases} J_1(\kappa_n \rho') H_1^{(2)}(\kappa_n \rho), & \rho > \rho' \\ J_1(\kappa_n \rho) H_1^{(2)}(\kappa_n \rho'), & \rho < \rho' \end{cases} \quad (B-17)$$

Consequently, using Eq. (B-3b) one has

$$I_n'(\rho) = \frac{\kappa_n \rho \pi \sqrt{2\pi} V_0}{Z_n' 2 \ln \frac{b}{a}} \sqrt{\frac{\epsilon_n}{h}}$$

$$\begin{cases} H_1^{(2)}(\kappa_n \rho) \int_a^b J_1(\kappa_n \rho') d\rho' & , \rho \geq b \\ H_1^{(2)}(\kappa_n \rho) \int_a^{\rho} J_1(\kappa_n \rho') d\rho' + J_1(\kappa_n \rho) \int_{\rho}^b H_1^{(2)}(\kappa_n \rho') d\rho' , & a \leq \rho \leq b \\ J_1(\kappa_n \rho) \int_a^b H_1^{(2)}(\kappa_n \rho') d\rho' & , \rho \leq a \end{cases} \quad (B-18a)$$

or

$$I_n'(\rho) = - \frac{\rho \pi \sqrt{2\pi} V_0}{Z_n' 2 \ln \frac{b}{a}} \sqrt{\frac{\epsilon_n}{h}}$$

$$\begin{cases} H_1^{(2)}(\kappa_n \rho) J_n & , \rho \geq b \\ J \frac{2}{\pi \kappa_n \rho} + J_1(\kappa_n \rho) H_0^{(2)}(\kappa_n b) - H_1^{(2)}(\kappa_n \rho) J_0(\kappa_n a) , & a \leq \rho \leq b \\ J_1(\kappa_n \rho) H_n & , \rho \leq a \end{cases} \quad (B-18b)$$

Thus, from Eqs. (B-1b), (B-1d) and (B-18b), the magnetic field due to a magnetic ring source of width (b-a) is

$$H_\phi(\rho, z) = K \eta_0 V_0 \sum_{n=0}^{\infty} \frac{\epsilon_n}{\sqrt{1 - \left(\frac{n\pi}{kh}\right)^2}} \cos \frac{n\pi}{h} z$$

$$\begin{cases} H_1^{(2)}(\kappa_n \rho) J_n & \rho \geq b \\ J \frac{2}{\pi \kappa_n \rho} + J_1(\kappa_n \rho) H_0^{(2)}(\kappa_n b) - H_1^{(2)}(\kappa_n \rho) J_0(\kappa_n a), & a \leq \rho \leq b \\ J_1(\kappa_n \rho) H_n & \rho \leq a \end{cases} \quad (B-19a)$$

where

$$K = \frac{\pi}{2h \ln \frac{b}{a}}. \quad (B-19b)$$

B2 RADIAL MAGNETIC GREEN'S FUNCTION REPRESENTATION

The expressions for the electromagnetic field in an infinite parallel plate region due to an annular aperture driven by a coaxial transmission line are derived in this section by an alternative method using a magnetic Green's function $G^{(m)}$.

An open-ended aperture of a coaxial line of inner and outer radii a and b , respectively, is considered to be located on the bottom plate of the perfectly conducting infinite parallel plate waveguide of height h as shown in Figure B-2. A cylindrical coordinate system (ρ, ϕ, z) is chosen with z along the axis of rotational symmetry of the annular aperture. The aperture electric field is assumed to be that of the TEM transmission line mode

$$E(\rho, z=0) = \rho_0 \frac{V_0}{\rho \ln \frac{b}{a}}; \quad a \leq \rho \leq b \quad (B-20)$$

where V_0 is the modal voltage at the aperture.

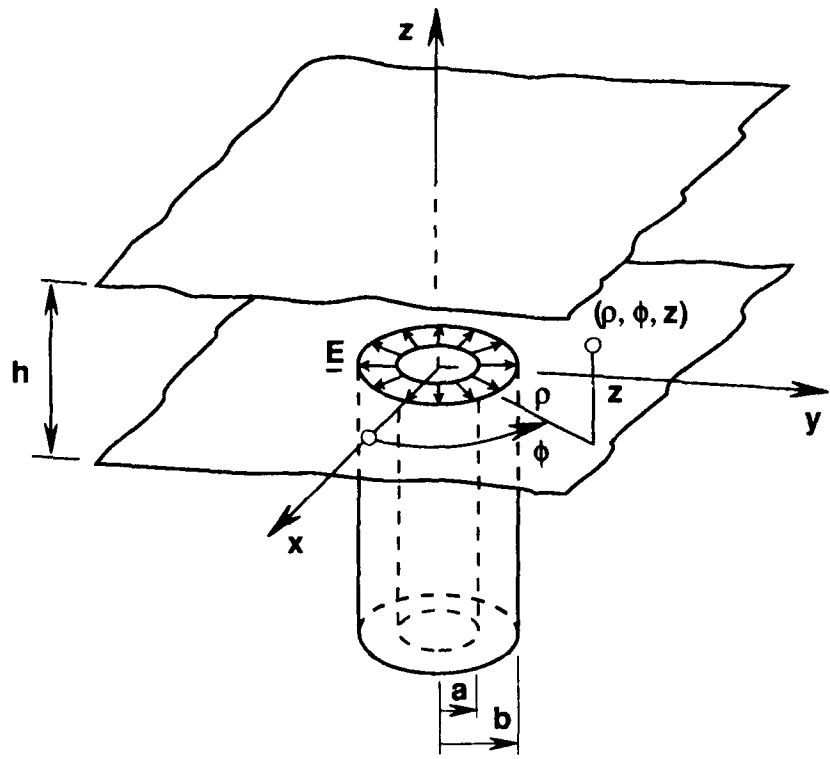


Figure B-2. Coaxially Driven Annular Aperture in an Infinite Parallel Plate Waveguide

Using the equivalence principle, the problem of Figure B-2 becomes that of a magnetic ring source in the infinite parallel plate waveguide as shown in Figure B-3, where the magnetic current density is

$$M(\rho, z; t) = \mu_0 M_\phi(\rho, z) e^{j\omega t} : a \leq \rho \leq b \quad (B-21a)$$

with

$$M_\phi(\rho, z) = - \frac{V_0}{\rho \ln \frac{b}{a}} \delta(z). \quad (B-21b)$$

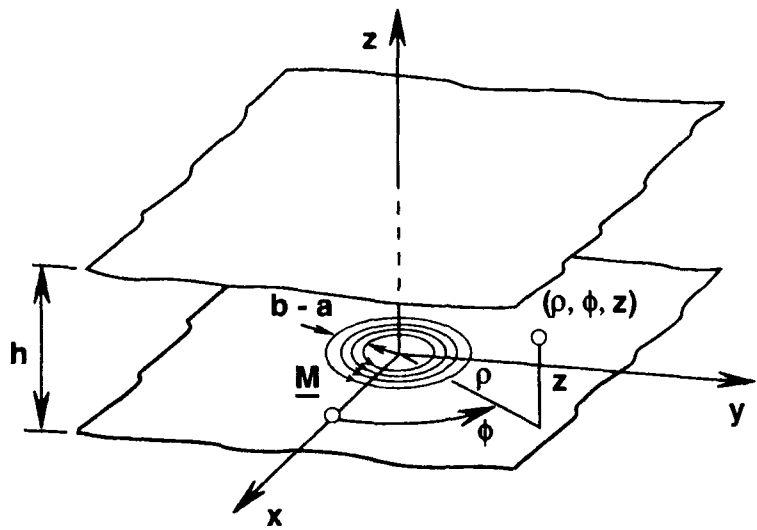


Figure B-3. Annular Magnetic Current Ring Source in an Infinite Parallel Plate Waveguide

To determine the field in the parallel plate region due to the magnetic current density of Eq. (B-21a) it is convenient to formulate the problem in terms of the single component of the magnetic field H_ϕ . We readily find that H_ϕ satisfies the differential equation

$$\frac{\partial}{\partial \rho} \left[\frac{1}{\rho} \frac{\partial}{\partial \rho} (\rho H_\phi) \right] + k^2 H_\phi + \frac{\partial^2 H_\phi}{\partial z^2} = j\omega \epsilon_0 M_\phi \quad (B-22a)$$

which follows from Maxwell's equations

$$\nabla \times \mathbf{E} = -j\omega \mu_0 \mathbf{H} - \mathbf{M} \quad (B-22b)$$

$$\nabla \times \mathbf{H} = j\omega \epsilon_0 \mathbf{E} \quad (B-22c)$$

with $\partial/\partial\phi=0$. The condition $\partial/\partial\phi=0$ is due to absence of angular variation of M_ϕ and the rotational symmetry of the structure.

The associated electric field components are

$$E_\rho = - \frac{1}{j\omega\epsilon_0} \frac{\partial H_\phi}{\partial z} \quad (B-23a)$$

$$E_z = \frac{1}{j\omega\epsilon_0} \frac{1}{\rho} \frac{\partial}{\partial \rho} (\rho H_\phi) \quad (B-23b)$$

with

$$E_\phi = H_\rho = H_z = 0. \quad (B-23c)$$

The solution of Eq. (B-22a) can be written in terms of a magnetic Green's function as

$$H_\phi(\rho, z) = -j\omega\epsilon_0 \int_{\rho'=a}^b M_\phi(\rho', z') G^{(m)}(\rho, z; \rho', z') d\rho'. \quad (B-24)$$

The Green's function $G^{(m)}$ which represents the magnetic field due to a unit magnetic current loop (shown in Figure B-4) satisfies the differential equation

$$\frac{\partial}{\partial \rho} \left[\frac{1}{\rho} \frac{\partial}{\partial \rho} (\rho G^{(m)}) \right] + k^2 G^{(m)} + \frac{\partial^2 G^{(m)}}{\partial z^2} = -\delta(\rho - \rho') \delta(z - z'). \quad (B-25)$$

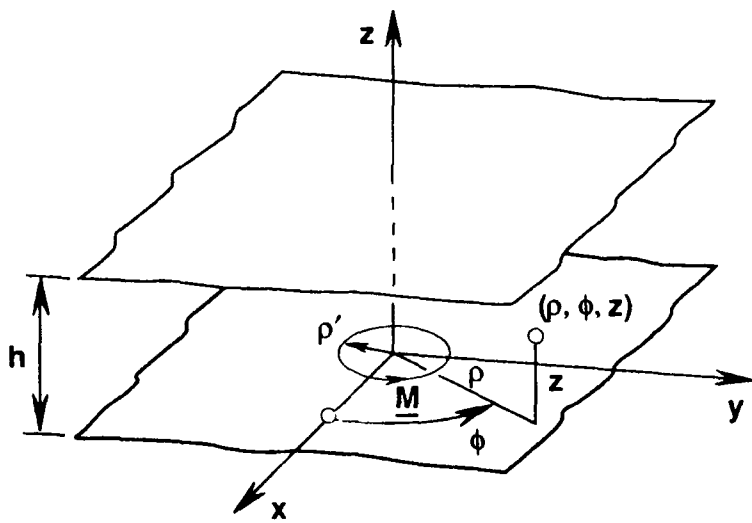


Figure B-4. Unit Annular Magnetic Current Loop in an Infinite Parallel Plate Waveguide

An appropriate solution to Eq. (B-25) can be written in the form

$$G^{(m)}(\rho, z; \rho', z') = \sum_{n=0}^{\infty} g_n(\rho, \rho') \cos \frac{n\pi}{h} z f_n(z'). \quad (B-26)$$

Substituting Eq. (B-26) into Eq. (B-25) and then multiplying both sides of Eq. (B-25) by $\cos(n\pi z/h)$ and integrating from $z=0$ to h , where we use the orthogonality property of the eigenfunctions and the integral property of the delta function, we obtain

$$f_n(z') = \frac{\epsilon_n}{h} \cos \frac{n\pi}{h} z' \quad (B-27a)$$

where

$$\epsilon_n = \begin{cases} 1, & n=0 \\ 2, & n \geq 1 \end{cases} \quad (B-27b)$$

Substitution of Eq. (B-26) into Eq. (B-25), and then Eq. (B-25) into Eq. (B-24) yields the differential equation for the radial Green's function g_n :

$$\left(\frac{1}{\rho} \frac{d}{d\rho} \rho \frac{d}{d\rho} + \kappa_n^2 - \frac{1}{\rho^2} \right) g_n(\rho, \rho') = -\delta(\rho - \rho'). \quad (B-28)$$

The solution for g_n , which satisfies the homogeneous differential equation corresponding to Eq. (B-28) is

$$g_n(\rho, \rho') = \begin{cases} A J_1(\kappa_n \rho) & \rho < \rho' \\ B H_1^{(2)}(\kappa_n \rho), & \rho > \rho' \end{cases} \quad (B-29)$$

which ensures finiteness of g_n at $\rho=0$ and decay of g_n as $\rho \rightarrow \infty$. The $J_1(\kappa_n \rho)$ and $H_1^{(2)}(\kappa_n \rho)$ denote Bessel functions of the first kind and Hankel functions of the second kind, both of first order. To determine the coefficients A and B , we use

$$g_n(\rho' + \Delta, \rho') = g_n(\rho' - \Delta, \rho'), \quad \Delta \rightarrow 0 \quad (B-30a)$$

$$\left. \frac{dg_n(\rho, \rho')}{d\rho} \right|_{\rho' - \Delta}^{\rho' + \Delta} = -1, \quad \Delta \rightarrow 0 \quad (B-30b)$$

which gives a system of two simultaneous algebraic equations

$$\begin{bmatrix} J_1(\kappa_n \rho') - H_1^{(2)}(\kappa_n \rho') \\ J_1(\kappa_n \rho') - H_1^{(2)'}(\kappa_n \rho') \end{bmatrix} = \begin{bmatrix} A \\ B \end{bmatrix} = \begin{bmatrix} 0 \\ \frac{1}{\kappa_n} \end{bmatrix}. \quad (B-30c)$$

Solving Eq. (B-30c) we find

$$A = -\frac{j\pi\rho'}{2} H_1^{(2)}(\kappa_n \rho') \quad (B-31a)$$

$$B = -\frac{j\pi\rho'}{2} J_1(\kappa_n \rho') \quad (B-31b)$$

where we used the relation for the Wronskian

$$W\{J_v(x), H_v^{(2)}(x)\} = -\frac{j2}{\pi x}. \quad (B-31c)$$

Consequently,

$$g_n(\rho, \rho') = -\frac{j\pi\rho'}{2} J_1(\kappa_n \rho_<) H_1^{(2)}(\kappa_n \rho_>). \quad (B-32)$$

Substituting Eqs. (B-26) and (B-32) into Eq. (B-25), the Green's function $G^{(m)}$ is

$$G^{(m)}(\rho, z; \rho', z') = -\frac{j\pi\rho'}{2h} \sum_{n=0}^{\infty} \epsilon_n J_1(\kappa_n \rho_<) H_1^{(2)}(\kappa_n \rho_>) \cos \frac{n\pi}{h} z \cos \frac{n\pi}{h} z'. \quad (B-33)$$

Using this result in Eq. (B-24) we can now determine the H_ϕ due to a magnetic current distribution [Eq. (B-21b)]. After integration we get

$$H_\phi(\rho, z) = -\sqrt{\frac{\epsilon_0}{\mu_0}} \frac{\pi V_0}{2h \ln \frac{b}{a}} \sum_{n=0}^{\infty} \frac{\epsilon_n}{\sqrt{1 - \left(\frac{n\pi}{kh}\right)^2}} \cos \frac{n\pi z}{h}$$

$$\begin{cases} H_1^{(2)}(\kappa_n \rho) [J_0(\kappa_n b) - J_0(\kappa_n a)] & : \rho \geq b \\ J \frac{2}{\pi \kappa_n \rho} + J_1(\kappa_n \rho) H_0^{(2)}(\kappa_n b) - H_1^{(2)}(\kappa_n \rho) J_0(\kappa_n a); & a \leq \rho \leq b \\ J_1(\kappa_n \rho) [H_0^{(2)}(\kappa_n b) - H_0^{(2)}(\kappa_n a)] & : \rho \leq a. \end{cases} \quad (B-34)$$

which upon substitution into Eqs. (B-23a) and (B-23b) gives the field components E_ρ, E_z .

Appendix C

Cylindrical Electric Current Source In An Infinite Parallel Plate Waveguide - Radial Mode Representation

C 1 RADIAL TRANSMISSION LINE REPRESENTATION

In this Appendix we derive expressions for the fields in the parallel plate region due to a (transverse to ρ) circular cylindrical electric current source

$$J_t(r') = z_0 J_z(z') \delta(\rho-a), \quad 0 \leq z' \leq l \quad (C-1)$$

by an approach where the propagation direction is assumed to be radial.

Since the electric current is transverse (to ρ) with $\partial/\partial\phi' = 0$, only E-modes with respect to ρ are excited. Relations for the fields E_z and H_ϕ with corresponding vector eigenfunctions $e'_{zn'}$

h'_n are given by Eq. (B-1). Since $\mathbf{J}(\mathbf{r}') = \mathbf{J}_t(\mathbf{r}')$ is transverse (to ρ), the electric current source can be represented by a point current generator $i'_n(\rho')$ on an equivalent transmission line at $\rho' = a$, where

$$i'_n(\rho') = \iint_{\text{source}} \mathbf{J}_t(\mathbf{r}') \cdot \mathbf{e}'^*(\rho', \phi', z') dS'. \quad (\text{C-2})$$

Substituting Eqs. (C-1) and (B-1c) into Eq. (C-2) gives

$$i'_n(\rho') = \int_{\phi'=0}^{2\pi} \int_{z'=0}^l z_0 J_z(z') \cdot z_0 \frac{1}{\sqrt{2\pi}} \sqrt{\frac{\epsilon_n}{h}} \cos \frac{n\pi}{h} z' \rho' d\phi' dz' = \sqrt{2\pi} a \sqrt{\frac{\epsilon_n}{h}} I_n \delta(\rho - a) \quad (\text{C-3a})$$

where

$$I_n = \int_{z'=0}^l J_z(z') \cos \frac{n\pi}{h} z' dz'. \quad (\text{C-3b})$$

The $V'_n(\rho)$ and $I'_n(\rho)$ in Eq. (B-1) satisfy the radial transmission line equations

$$-\frac{d}{d\rho} V'_n(\rho) = j\kappa_n Z'_n \frac{1}{\rho} I'_n(\rho) \quad (\text{C-4a})$$

$$-\frac{d}{d\rho} I'_n(\rho) = j\kappa_n Y'_n \rho V'_n(\rho) + i'_n(\rho) \quad (\text{C-4b})$$

where Z'_n , Y'_n and κ_n are given by Eqs. (B-5c) and (B-5d).

As in Appendix B, to determine $V'_n(\rho)$ and $I'_n(\rho)$ we first determine the amplitude of the voltage and current at the generator terminals ρ'_- and ρ'_+ . The voltage $V'_n(\rho)$ and current $I'_n(\rho)$ at any point ρ on a transmission line with constants κ_n and Z_n then follow from Eq. (C-4).

To that end, we consider the network problem shown in Figure C-1, where $\overleftarrow{Y}(\rho')$ and $\overrightarrow{Y}(\rho')$ are the admittances seen looking to the left and to the right, respectively, from the generator terminals.

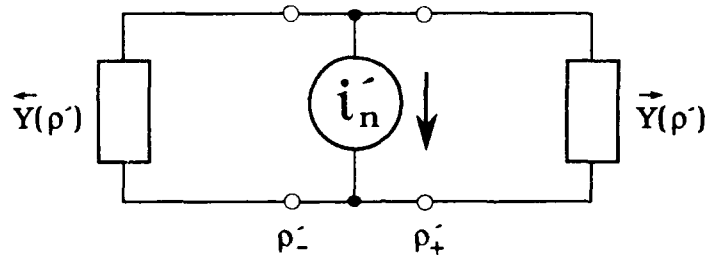


Figure C-1. Network Representation for Current Point-Source Excited Radial Transmission-Line

The $\overleftarrow{Y}(\rho')$ is

$$\overleftarrow{Y}(\rho') = -\frac{\overleftarrow{I}_n(\rho')}{\overleftarrow{V}_n(\rho')} = j Y_n \rho' \frac{J_1(\kappa_n \rho')}{J_0(\kappa_n \rho')} \quad (C-5)$$

where Eqs. (B-6b) and (B-7) for $V'_n(\rho')$ and $I'_n(\rho')$ have been used. Similarly, using Eqs. (B-9a) and (B-9b),

$$\overrightarrow{Y}(\rho') = \frac{\overrightarrow{I}_n(\rho')}{\overrightarrow{V}_n(\rho')} = -Y_n \rho' \frac{H_1^{(2)}(\kappa_n \rho')}{H_0^{(2)}(\kappa_n \rho')} \quad (C-6)$$

We define

$$\overleftrightarrow{Y}(\rho') = \overleftarrow{Y}(\rho') + \overrightarrow{Y}(\rho') = \frac{2Y_n}{\pi \kappa_n} \frac{1}{J_0(\kappa_n \rho') H_0^{(2)}(\kappa_n \rho')} \quad (C-7)$$

where we have again used the Wronskian relation (B-11d). Consequently, the modal voltage at the generator terminals is

$$V'_n(\rho'_+, \rho') = V'_n(\rho'_-, \rho') = -\frac{i'_n(\rho')}{\dot{Y}(\rho')} = -i'_n(\rho') \frac{\pi \kappa_n}{2Y_n} J_0(\kappa_n \rho') H_0^{(2)}(\kappa_n \rho') \quad (C-8)$$

In view of Eqs. (B-6b) and (B-9a) the modal voltage on the radial transmission-line at ρ due to the point current source at $\rho' = a$ follows from Eq. (C-8), that is,

$$V'_n(\rho, \rho') = -i'_n(\rho') \frac{\pi \kappa_n}{2Y_n} \begin{cases} J_0(\kappa_n \rho') H_0^{(2)}(\kappa_n \rho), \rho \geq \rho' \\ J_0(\kappa_n \rho) H_0^{(2)}(\kappa_n \rho'), \rho \leq \rho' \end{cases} \quad (C-9a)$$

or upon substitution of Eq. (C-3a) for $i'_n(\rho' = a)$

$$V'_n(\rho, \rho') = -\frac{\sqrt{2\pi} a \pi \kappa_n}{2Y_n} \sqrt{\frac{\epsilon_n}{h}} I_n \delta(\rho - a) \begin{cases} J_0(\kappa_n \rho') H_0^{(2)}(\kappa_n \rho), \rho \geq \rho' \\ J_0(\kappa_n \rho) H_0^{(2)}(\kappa_n \rho'), \rho \leq \rho' \end{cases} \quad (C-9b)$$

Consequently,

$$V'_n(\rho) = \int_{\text{source}} V'_n(\rho, \rho') d\rho' = -\frac{\sqrt{2\pi} \pi a \kappa_n}{2Y_n} \sqrt{\frac{\epsilon_n}{h}} I_n \begin{cases} J_0(\kappa_n a) H_0^{(2)}(\kappa_n \rho), \rho \geq \rho' \\ J_0(\kappa_n \rho) H_0^{(2)}(\kappa_n a), \rho \leq \rho' \end{cases} \quad (C-10)$$

Substituting Eq. (C-10) into Eq. (B-1a) with e_{zn} defined in Eq. (B-1c), the z-component of the electric field due to the circular cylindrical electrical current distribution of Eq. (C-1) in an infinite parallel plate waveguide is

$$E_z(r) = \sum_{n=0}^{\infty} V'_n(\rho) e_{zn}(\phi, z) = -\frac{\pi a}{2h\omega\epsilon_0} \sum_{n=0}^{\infty} \epsilon_n \kappa_n^2 C_n(z) I_n \begin{cases} J_0(\kappa_n a) H_0^{(2)}(\kappa_n \rho), \rho \geq a \\ J_1(\kappa_n \rho) H_0^{(2)}(\kappa_n a), \rho \leq a \end{cases} \quad (C-11)$$

Notice that Eq. (C-11) is identical to Eq. (3-11b) obtained by an alternate analysis based on an axial transmission line representation.

The magnetic field can be obtained from Eq. (B-1b) where $I'_n(\rho)$ follows from the transmission line equations (C-4a) and (C-10). Hence at $r \neq r'$,

$$I'_n(\rho) = -j \frac{\rho Y_n}{\kappa_n} \frac{d}{d\rho} V'_n(\rho) = -j \frac{\sqrt{2\pi} \pi a \kappa_n \rho}{2} \sqrt{\frac{\epsilon_n}{h}} I_n \begin{cases} J_0(\kappa_n a) H_1^{(2)}(\kappa_n \rho), \rho \geq a \\ J_1(\kappa_n \rho) H_0^{(2)}(\kappa_n a), \rho \leq a \end{cases} \quad (C-12)$$

Substitution of Eqs. (C-12) and (B-1d) into Eq. (B-1b) yields

$$H_\phi(r) = j \frac{\pi a}{2h} \sum_{n=0}^{\infty} \epsilon_n \kappa_n C_n(z) I_n \begin{cases} J_0(\kappa_n a) H_1^{(2)}(\kappa_n \rho), \rho \geq a \\ J_1(\kappa_n \rho) H_0^{(2)}(\kappa_n a), \rho \leq a \end{cases} \quad (C-13)$$

which is the same as Eq. (3-13).

C2 RADIAL ELECTRIC GREEN'S FUNCTION REPRESENTATION

In this section we derive expressions for the electromagnetic field in an infinite parallel plate region due to a circular cylindrical electric current source via an alternative radial electric Green's function representation.

The geometry under consideration is shown in Figure C-2 where a and l are the radius and length of the cylindrical source and h is the height of the infinite parallel plate waveguide. A cylindrical coordinate system (ρ, ϕ, z) with unit vectors (ρ_0, ϕ_0, z_0) is chosen so that the z axis coincides with the axis of the cylindrical source. The source electric current density distribution is assumed to be

$$J(\rho, z; t) = z_0 \delta(\rho - a) J_z(z) e^{j\omega t}, \quad 0 \leq z \leq l. \quad (C-14)$$

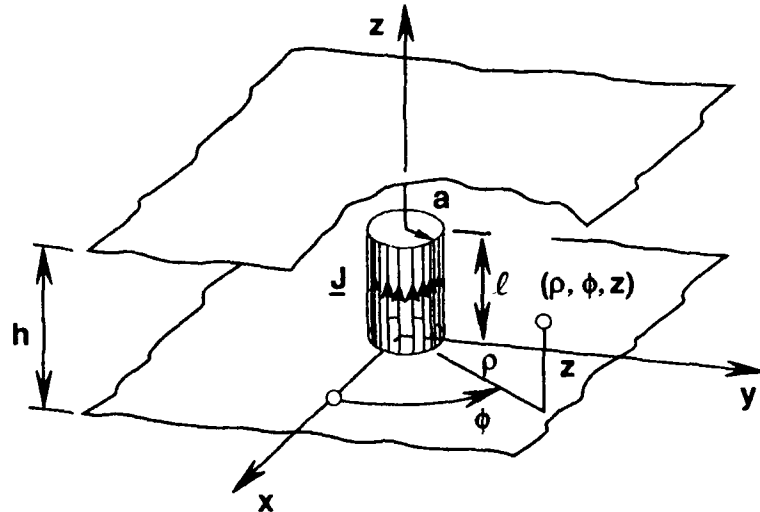


Figure C-2. Circular Cylindrical Axial Electric Current Source in an Infinite Parallel Plate Waveguide

Since the current density is axial, the electromagnetic fields can be derived from a single component of vector potential $A_z(\rho, z)$ satisfying

$$\nabla^2 A_z(\rho, z) + k^2 A_z(\rho, z) = -\mu_0 \delta(\rho - a) J_z(z), \quad k = \frac{2\pi}{\lambda}. \quad (C-15)$$

The field components are then given by

$$E_\rho = \frac{1}{j\omega \mu_0 \epsilon_0} \frac{\partial A_z}{\partial z \partial \rho} \quad (C-16a)$$

$$E_z = -\frac{j\omega}{k^2} \left(\frac{\partial^2 A_z}{\partial z^2} + k^2 A_z \right) \quad (C-16b)$$

$$H_\phi = -\frac{1}{\mu_0} \frac{\partial A_z}{\partial \rho} \quad (C-16c)$$

$$E_\phi = H_\rho = H_z = 0. \quad (C-16d)$$

The solution of Eq. (C-15) can be written in the form

$$A_z(\rho, z) = \mu_0 \int_{z'=0}^l J_z(z') G^{(e)}(\rho, z; a, z') dz' \quad (C-17a)$$

where the electric Green's function $G^{(e)}$ satisfies the scalar Helmholtz equation

$$\nabla^2 G^{(e)} + k^2 G^{(e)} = -\delta(\rho-a) \delta(z-z'). \quad (C-17b)$$

Here $G^{(e)}(\rho, z; a, z')$ represents the vector potential due to a unit axial electric current loop shown in Figure C-3, and is subject to the boundary conditions $\partial G^{(e)} / \partial z = 0$ at $z = 0, h$ and the radiation condition as $\rho \rightarrow \infty$.

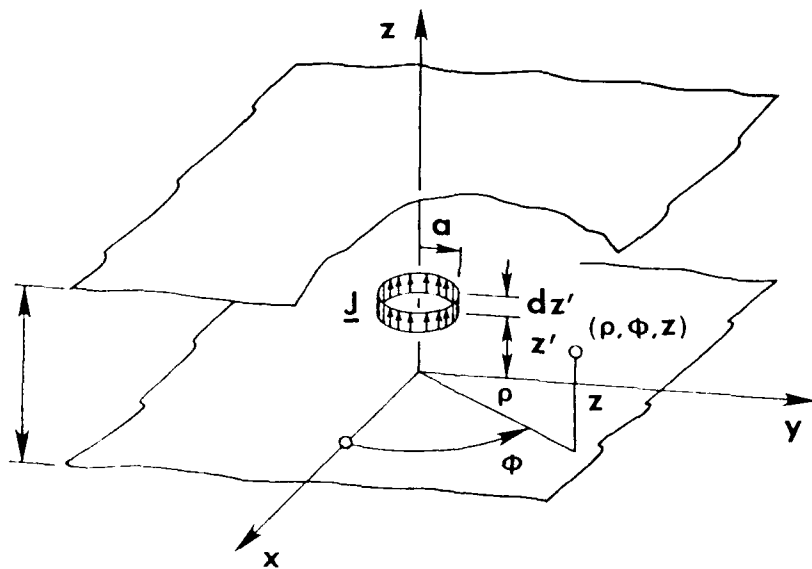


Figure C-3. Unit Axial Electric Current Loop in an Infinite Parallel Plate Waveguide

Since $\partial/\partial\phi = 0$, Eq. (C-17b) becomes

$$\left(\frac{1}{\rho} \frac{\partial}{\partial \rho} \rho \frac{\partial}{\partial \rho} + k^2 + \frac{\partial^2}{\partial z^2} \right) G^{(e)}(\rho, z; a, z') = -\delta(\rho - a) \delta(z - z'). \quad (C-18)$$

An appropriate representation of $G^{(e)}$ is

$$G^{(e)}(\rho, z; a, z') = \sum_{n=0}^{\infty} f_n(z') g_n(\rho, a) \cos \frac{n\pi}{h} z. \quad (C-19)$$

Substituting Eq. (C-19) into Eq. (C-18), then multiplying both sides of Eq. (C-18) by $\cos(n\pi z/h)$ and integrating from $z = 0$ to h , where we use the orthogonality property of the eigenfunctions and the integral property of the delta function, we obtain

$$f_n(z') = \frac{\epsilon_n}{h} \cos \frac{n\pi}{h} z' \quad (C-20a)$$

where

$$\epsilon_n = \begin{cases} 1, & n=0 \\ 2, & n \geq 1 \end{cases} \quad (C-20b)$$

In view of Eq. (C-20), substitution of Eq. (C-19) into Eq. (C-18) yields the ordinary differential equation

$$\left(\frac{1}{\rho} \frac{d}{d\rho} \rho \frac{d}{d\rho} + \kappa_n^2 \right) g_n(\rho, a) = -\delta(\rho - a) \quad (C-21a)$$

where

$$\kappa_n^2 = k^2 - \left(\frac{n\pi}{h}\right)^2, \quad \operatorname{Im}\{\kappa_n\} \leq 0. \quad (C-21b)$$

The solution for the radial Green's function g_n that satisfies the homogeneous differential equation corresponding to Eq. (C-21a) is

$$g_n(\rho, a) = \begin{cases} A J_0(\kappa_n \rho) & \rho < a \\ B H_0^{(2)}(\kappa_n \rho) & \rho > a \end{cases} \quad (C-22)$$

which ensures finiteness of g_n at $\rho = 0$ and decay of g_n as $\rho \rightarrow \infty$. The $J_0(\kappa_n \rho)$ and $H_0^{(2)}(\kappa_n \rho)$ denote Bessel functions of the first kind and Hankel functions of the second kind, both of zero order.

To determine the coefficients A and B, we use the properties of the radial Green's function g_n at $\rho = a$, namely

$$g_n(a + \Delta, a) = g_n(a - \Delta, a); \quad \Delta \rightarrow 0 \quad (C-23a)$$

$$\frac{dg_n(\rho, a)}{d\rho} \Big|_{a-\Delta}^{a+\Delta} = -1; \quad \Delta \rightarrow 0. \quad (C-23b)$$

These give a pair of simultaneous algebraic equations

$$\begin{bmatrix} J_0(\kappa_n a) & -H_0^{(2)}(\kappa_n a) \\ J'_0(\kappa_n a) & -H_0^{(2)'}(\kappa_n a) \end{bmatrix} \begin{bmatrix} A \\ B \end{bmatrix} = \begin{bmatrix} 0 \\ \frac{1}{\kappa_n} \end{bmatrix} \quad (C-24)$$

where the prime denotes the derivative of the Bessel and Hankel functions with respect to the argument. Noting the Wronskian determinant

$$W \left\{ J_0(x), H_0^{(2)}(x) \right\} = - \frac{j2}{\pi x} \quad (C-25a)$$

in Eq. (C-24) we find

$$A = - \frac{j\pi a}{2} H_0^{(2)}(\kappa_n a) \quad (C-25b)$$

$$B = - \frac{j\pi a}{2} J_0(\kappa_n a) \quad (C-25c)$$

and consequently,

$$g_n(\rho, a) = - \frac{j\pi a}{2} J_0(\kappa_n \rho_c) H_0^{(2)}(\kappa_n \rho_s) \quad (C-25d)$$

where for $\rho < a$: $\rho_c = \rho$, $\rho_s = a$ and for $\rho > a$: $\rho_c = a$, $\rho_s = \rho$.

Finally, substituting Eq. (C-25d) into Eq. (C-19), we obtain

$$G^{(e)}(\rho, z; a, z') = - \frac{j\pi a}{2h} \sum_{n=0}^{\infty} \epsilon_n J_0(\kappa_n \rho_c) H_0^{(2)}(\kappa_n \rho_s) \cos \frac{n\pi}{h} z \cos \frac{n\pi}{h} z'. \quad (C-26)$$

The vector potential in a parallel plate region due to the circular cylindrical current distribution of Eq. (C-14) can then be determined from Eq. (C-17a) using Eq. (C-26), that is,

$$A_z(\rho, z) = - \frac{j\pi a \mu_0}{2h} \sum_{n=0}^{\infty} \epsilon_n I_n \cos \frac{n\pi}{h} z \begin{cases} J_0(\kappa_n a) H_0^{(2)}(\kappa_n \rho), \rho \geq a \\ J_0(\kappa_n \rho) H_0^{(2)}(\kappa_n a), \rho \leq a \end{cases} \quad (C-27a)$$

where

$$I_n = \int_{z'=0}^l J_z(z') \cos \frac{n\pi}{h} z' dz'. \quad (C-27b)$$

The field components E_ρ , E_z and H_ϕ can now be found for any prescribed axial electric current distribution $J_z(z')$ from Eq. (C-16).

Appendix D

Addition Theorem for Hankel Functions

Using Reference 14, suppose that $r > 0$, $\rho > 0$, $\phi > 0$, and

$$R = \sqrt{r^2 + \rho^2 - 2r\rho \cos \phi} \quad (D-1)$$

that is, suppose that r , ρ and R are the sides of a triangle, shown in Figure D-1, such that the angle between sides r and ρ is equal to ϕ . Suppose also that $\rho < r$ and that ψ is the angle opposite that side ρ , so that

$$0 < \psi < \frac{\pi}{2} \quad (D-2a)$$

and

¹⁴ Gradshteyn, I.S. and Ryzhik, I.M. (1965) *Table of Integrals, Series, and Products*, Academic Press Inc., New York.

$$e^{j2\psi} = \frac{r - pe^{-j\phi}}{r - pe^{j\phi}}. \quad (D-2b)$$

When these conditions are satisfied, the Addition Theorem for Hankel functions of the second kind, of order zero and of argument kR , is

$$H_0^{(2)}(kR) = J_0(k\rho) H_0^{(2)}(kr) = 2 \sum_{m=1}^{\infty} J_m(k\rho) H_m^{(2)}(kr) \cos m\phi \quad (D-3)$$

where k is an arbitrary complex number.

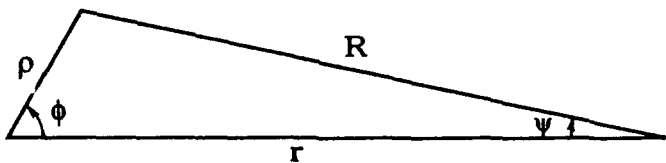


Figure D-1. Triangle Pertaining to Addition
Theorem for Hankel Functions $H_0^{(2)}(kR)$

Appendix E

Convergence Acceleration of Series $S_n(\delta_x)$

E1 INFINITE LINEAR ARRAY OF MONPOLE ELEMENTS IN AN INFINITE PARALLEL PLATE WAVEGUIDE

For the infinite linear array of monopoles in an infinite parallel plate waveguide, the series $S_n(\delta_x)$ is defined by Eq. (4-47c) as

$$S_n(\delta_x) = 2 \sum_{p=1}^{\infty} H_0^{(2)}(\kappa_n p d) \cos p \delta_x. \quad (E-1)$$

The phase increment δ_x between two neighboring elements can be related to the array scan angle $\hat{\phi}_0$ (measured from array broadside) by the standard relation

$$\delta_x = kd \sin \hat{\phi}_0. \quad (E-2)$$

As already mentioned, κ_n is the propagation constant of radial modes in the parallel plate region given by Eq. (4-45e) as

$$\kappa_n = k \sqrt{1 - \left(\frac{n\pi}{kh}\right)^2}, \quad \text{Im}\{\kappa_n\} \leq 0, \quad n=0,1,\dots. \quad (E-3)$$

With respect to κ_n , we distinguish two cases in the convergence acceleration procedure, both considered below.

In the first case, κ_n is real. The rate of convergence \sum_p is predominantly determined by the behavior of Hankel functions $H_0^{(2)}(\kappa_n pd)$ for large p which is

$$H_0^{(2)}(\kappa_n pd) \sim \sqrt{\frac{2}{\pi \kappa_n pd}} e^{-j(\kappa_n pd - \frac{\pi}{4})}, \quad \kappa_n pd \rightarrow \infty. \quad (E-4)$$

Thus, the series \sum_p in Eq. (E-1) converges as $1/\sqrt{p}$, which is too slow for efficient computation. To avoid this difficulty, the slow convergence of this series with respect to the index p is accelerated using the relevant relation given in Reference 9, that is,

$$\begin{aligned} 2 \sum_{p=1}^{\infty} H_0^{(2)}(2\pi y p) \cos(2\pi x p) &= \\ &= -1 + j \frac{2}{\pi} \left(\ln \frac{y}{2} + \gamma \right) + \frac{j}{\pi} \frac{1}{\sqrt{x^2 - y^2}} + \frac{j}{\pi} \sum_{m=1}^{\infty} \left[\frac{1}{\sqrt{(m+x)^2 - y^2}} + \frac{1}{\sqrt{(m-x)^2 - y^2}} - \frac{2}{m} \right] \end{aligned} \quad (E-5)$$

valid for $0 \leq x < 1$. In Eq. (E-5), $\text{Im}\{[(m+x)^2 - y^2]^{1/2}\} \geq 0$, ($m=0,1,\dots$) and Euler's constant $\gamma = 0.577 215 665 \dots$. This relation can be directly applied in Eq. (E-1), with

$$x = \frac{\delta_x}{2\pi} = \frac{d}{\lambda} \sin \hat{\phi}_0 \quad (E-6a)$$

$$y = \frac{d}{\lambda} \sqrt{1 - \left(\frac{n\pi}{kh}\right)^2} \quad (E-6b)$$

It is seen that, basically we have transformed a slowly convergent series \sum_p into a rapidly convergent series \sum_m . The series \sum_m converges as $1/m^3$. To see this, for simplicity let $x = 0$, which corresponds to the broadside array scan condition. In this case, when m is large, that is, $(y/m) \ll 1$, one may write

$$\frac{1}{\sqrt{m^2 - y^2}} = \frac{1}{m \sqrt{1 - \left(\frac{y}{m}\right)^2}} \approx \frac{1}{m} \left[1 + \left(\frac{y}{m}\right)^2 \right] \quad (E-7)$$

Using this relation, we see that \sum_m in Eq. (E-5) is

$$\sum_{m=1}^{\infty} \left[\frac{2}{\sqrt{m^2 - y^2}} - \frac{2}{m} \right] \approx 2y^2 \sum_{m=1}^{\infty} \frac{1}{m^3} \quad (E-8)$$

In the second case, κ_n is imaginary, that is,

$$\kappa_n = -j|\kappa_n| \quad (E-9a)$$

with

$$|\kappa_n| = k \sqrt{\left(\frac{n\pi}{kh}\right)^2 - 1} \geq 0, n > 0. \quad (E-9b)$$

then,

$$H_0^{(2)}(-j|\kappa_n|pd) = j\frac{2}{\pi} K_0(|\kappa_n|pd) \quad (E-9c)$$

where $K_0(|\kappa_n|pd)$ is the Modified Bessel function of order zero and argument $|\kappa_n|pd$. In this case Eq. (E-1) becomes

$$S_n(\delta_x) = j \frac{4}{\pi} \sum_{p=1}^{\infty} K_0(|\kappa_n|pd) \cos p\delta_x, \quad n > 0. \quad (E-10)$$

The convergence rate of this series depends primarily on the asymptotic behavior of Modified Bessel functions $K_0(|\kappa_n|pd)$ for large argument that is, p , which is

$$K_0(|\kappa_n|pd) \sim \sqrt{\frac{\pi}{2|\kappa_n|pd}} e^{-|\kappa_n|pd}, \quad |\kappa_n|pd \rightarrow \infty. \quad (E-11)$$

Equation (E-11) shows that Eq. (E-10) converges rapidly, and therefore there is no need for convergence acceleration.

E2 INFINITE LINEAR ARRAY OF MONPOLE ELEMENTS IN A SEMI-INFINITE PARALLEL PLATE WAVEGUIDE

For the infinite linear array of monopoles in a semi-infinite parallel plate waveguide, the series $S_n(\delta_x)$ is defined by Eq. (4-47d) as

$$S_n(\delta_x) = 2 \sum_{p=1}^{\infty} H_0^{(2)}(\kappa_n pd) \cos p\delta_x - H_0^{(2)}(2\kappa_n s) - 2 \sum_{p=1}^{\infty} H_0^{(2)}\left(\kappa_n d \sqrt{p^2 + \left(\frac{2s}{d}\right)^2}\right) \cos p\delta_x. \quad (E-12)$$

As in the previous section we consider two cases, for real and imaginary values of κ_n .

(1) κ_n is real: The slow convergence of the series in Eq. (E-12) is accelerated with the aid of the following relation ⁹

$$\begin{aligned}
& 2 \sum_{p=1}^{\infty} H_0^{(2)}(2\pi y\sqrt{p^2+z^2}) \cos(2\pi x p) \\
& = \frac{j}{\pi} \frac{e^{-2\pi z\sqrt{x^2-y^2}}}{\sqrt{x^2-y^2}} + \frac{j}{\pi} \sum_{m=1}^{\infty} \left[\frac{e^{-2\pi z\sqrt{(m+x)^2-y^2}}}{\sqrt{(m+x)^2-y^2}} + \frac{e^{-2\pi z\sqrt{(m-x)^2-y^2}}}{\sqrt{(m-x)^2-y^2}} \right] - H_0^{(2)}(2\pi y z), \quad 0 \leq x < 1 \quad (E-13a)
\end{aligned}$$

where for $y^2 > (m+x)^2$

$$\sqrt{(m+x)^2 - y^2} \rightarrow j\sqrt{y^2 - (m+x)^2}. \quad (E-13b)$$

If x and y are those of Eq. (E-6) and

$$z = \frac{2s}{d} \quad (E-14)$$

it is evident that Eq. (E-13) can be used to accelerate the second series in Eq. (E-12). Thus, applying Eq. (E-5) in the first sum and Eq. (E-13) in the second sum, $S_n(\delta_x)$ as given by Eq. (E-12) can be rewritten in the rapidly convergent form

$$\begin{aligned}
S_n(\delta_x) & = -1 + j \frac{2}{\pi} \left(\ln \frac{y}{2} + \gamma \right) + \frac{j}{\pi} \frac{1 - e^{-2\pi z\sqrt{x^2-y^2}}}{\sqrt{x^2-y^2}} \\
& + \frac{j}{\pi} \sum_{m=1}^{\infty} \left[\frac{1 - e^{-2\pi z\sqrt{(m+x)^2-y^2}}}{\sqrt{(m+x)^2-y^2}} + \frac{1 - e^{-2\pi z\sqrt{(m-x)^2-y^2}}}{\sqrt{(m-x)^2-y^2}} - \frac{2}{m} \right] \quad (E-15a)
\end{aligned}$$

where the identity

$$H_0^{(2)}(2\pi y z) = H_0^{(2)}(2\kappa_n s) \quad (E-15b)$$

has been used. As in the previous section, one can show that the series \sum_m in Eq. (E-15a) converges as $1/m^3$.

(2) κ_n is imaginary: When $\kappa_n = -j|\kappa_n|$ with $|\kappa_n|$ that of Eq. (E-9b), $S_n(\delta_x)$ becomes

$$S_n(\delta_x) = j \frac{4}{\pi} \sum_{p=1}^{\infty} K_0(|\kappa_n|pd) \cos p\delta_x - j \frac{2}{\pi} K_0(2|\kappa_n|s) \\ - j \frac{4}{\pi} \sum_{p=1}^{\infty} K_0\left(|\kappa_n|d \sqrt{p^2 + \left(\frac{2s}{d}\right)^2}\right) \cos p\delta_x, \quad n > 0 \quad (E-16)$$

which is a rapidly convergent series.

Appendix F

The Fourier Integral of the Hankel Function

In this Appendix we shall evaluate the Fourier integral

$$I = \int_{-\infty}^{\infty} H_0^{(2)}(k\sqrt{x^2+y^2}) e^{-jk_{xm}x} dx \quad (F-1)$$

where $H_0^{(2)}(k\sqrt{x^2+y^2})$ is the Hankel function of the second kind of order zero and argument $k\sqrt{x^2+y^2}$.

To this end, since the argument of the Hankel function is an even function of X , we may write

$$I = 2 \int_0^{\infty} H_0^{(2)}(k\sqrt{x^2+y^2}) \cos(k_{xm}x) dx. \quad (F-2)$$

Furthermore, Eq. (F-2) can be transformed into

$$I = 2 \int_0^{\infty} J_0(k\sqrt{x^2+y^2}) \cos(k_{xm}x) dx - j2 \int_0^{\infty} Y_0(k\sqrt{x^2+y^2}) \cos(k_{xm}x) dx \quad (F-3)$$

where $J_0(k\sqrt{x^2+y^2})$ and $Y_0(k\sqrt{x^2+y^2})$ are Bessel and Neumann functions of order zero and argument $k\sqrt{x^2+y^2}$.

The integrals in Eq. (F-3) are given in Reference 14 as

$$\int_0^{\infty} J_0(k\sqrt{x^2+y^2}) \cos(k_{xm}x) dx = \begin{cases} \frac{\cos(y\sqrt{k^2-k_{xm}^2})}{\sqrt{k^2-k_{xm}^2}}, & 0 < k_{xm} < k, y > 0 \\ 0, & 0 < k \leq k_{xm}, y > 0 \end{cases} \quad (F-4a)$$

$$\int_0^{\infty} Y_0(k\sqrt{x^2+y^2}) \cos(k_{xm}x) dx = \begin{cases} \frac{\sin(y\sqrt{k^2-k_{xm}^2})}{\sqrt{k^2-k_{xm}^2}}, & 0 < k_{xm} < k, y > 0 \\ -\frac{e^{-y\sqrt{k_{xm}^2-k^2}}}{\sqrt{k_{xm}^2-k^2}}, & 0 < k < k_{xm}, y > 0. \end{cases} \quad (F-4b)$$

Using these results we may write

$$I = \begin{cases} 2 \frac{e^{-jy\sqrt{k^2-k_{xm}^2}}}{\sqrt{k^2-k_{xm}^2}}, & 0 < k_{xm} < k, y > 0 \\ j2 \frac{e^{-y\sqrt{k_{xm}^2-k^2}}}{\sqrt{k_{xm}^2-k^2}}, & 0 < k < k_{xm}, y > 0. \end{cases} \quad (F-5)$$

If we define

$$\kappa_{mo} = \sqrt{k^2 - k_{xm}^2}, \quad k^2 > k_{xm}^2 \quad (F-6a)$$

and

$$\kappa_{mo} = -j\sqrt{k_{xm}^2 - k^2}, \quad k^2 < k_{xm}^2 \quad (F-6b)$$

in Eq. (F-5), then Eq. (F-1) becomes

$$\int_{-\infty}^{\infty} H_0^{(2)}(k\sqrt{x^2 + y^2}) e^{-jk_{xm}x} dx = 2 \frac{e^{-j\kappa_{mo}y}}{\kappa_{mo}}. \quad (F-6c)$$

Appendix G

The Stationary-Phase Method for Evaluation of Integrals

Expressions for the first-order asymptotic evaluation of finite integrals of the type

$$I(\Omega) = \int_{x_a}^{x_b} f(x) e^{-j\Omega q(x)} dx, \quad (G-1)$$

are listed below, where the large parameter Ω is assumed to be positive and $q(x)$ is a real function of the real variable x . If the function $f(x)$ has no singularities near an isolated first-order stationary phase point x_s of $q(x)$, where $q'(x_s)=0$, $q''(x_s) \neq 0$, the asymptotic approximation of $I(\Omega)$ is given by (see Reference 13 for details)

$$I(\Omega) \sim I_s(\Omega) U[(x_s - x_a)(x_b - x_s)] + I_e(\Omega) + O\left(\frac{1}{\Omega^{3/2}}\right), \quad \Omega \rightarrow \infty. \quad (G-2)$$

where $U(\alpha) = 1$ or 0 for $\alpha > 0$ and $\alpha < 0$, respectively. The I_s is the lowest-order contribution from the stationary-phase point, namely

$$I_s(\Omega) = \sqrt{\frac{2\pi}{\Omega|q''(x_s)|}} f(x_s) e^{-j\Omega q(x_s) + j\frac{\pi}{4}}, \quad q''(x_s) \geq 0. \quad (G-3a)$$

and $I_e(\Omega)$ is the lowest-order contribution from the endpoints,

$$I_e(\Omega) = -\frac{1}{j\Omega} \left[\frac{f(x_b)}{q'(x_b)} e^{-j\Omega q(x_b)} - \frac{f(x_a)}{q'(x_a)} e^{-j\Omega q(x_a)} \right]. \quad (G-3b)$$

The stationary point x_s (at which $q'(x_s) = 0$) is assumed to lie on the interval $x_a < x_s < x_b$; if the interval contains several stationary points, sufficiently far apart, $I_s(\Omega)$ is a sum comprising terms representative of each x_s . When the saddle point coincides with either of the end points x_a or x_b , the corresponding endpoint contribution in Eq. (G-3b) is omitted and one takes $1/2$ times the stationary-point contribution in Eq. (G-3a). When the interval $x_a < x < x_b$ does not contain a stationary point, the Heaviside function vanishes and the integral $I(\Omega)$ is approximated by $I_e(\Omega)$ only. When an endpoint moves to infinity, the corresponding contribution is omitted. Relation (G-2) fails when the saddle point x_s approaches one of the endpoints; for example when x_s moves continuously toward and across x_b , the $I_s(\Omega)$ term is discontinuous since the saddle point disappears from the integration interval, and the $I_e(\Omega)$ term diverges, since $q'(x_b) \rightarrow 0$ as $x_b \rightarrow x_s$. In this instance, one requires a more careful asymptotic evaluation that involves the error function or the Fresnel integral.

Appendix H

Test for Power Conservation

In this Appendix we shall demonstrate that the expressions for the active array field due to an infinite array of monopoles radiating into a semi-infinite parallel plate region satisfy the conservation of power condition.

All elements are fed with the same amplitude and progressive phase, $\exp(-j k_{x0} pd)$. This permits one to apply the periodic-structure approach, in which the analysis reduces to a single unit cell shown in Figure H-1. The unit cell consists of a single monopole radiating into a rectangular waveguide with conducting top and bottom walls and phase-shift side walls characterized by Floquet's boundary conditions. The unit cell size is $d \times h$ where as already mentioned $h < \lambda/2$ so that in the semi-infinite parallel plate waveguide, only the TEM ($n = 0$) radial mode propagates. Also in this Appendix, for simplicity of presentation but with no loss of generality, we assume that the inter-element spacing $d < \lambda/2$. In this case only the dominant ($m = 0, n = 0$) Floquet mode propagates in the unit cell. Moreover, to obtain the final conservation of power relation analytically in a closed form, it is assumed that the probe current has only a single term (see Section 4.3).

The conservation of power relation may be stated as

$$P_{\text{inc}} \left(1 - |\Gamma_a(\delta_x)|^2 \right) = P_t. \quad (\text{H-1})$$

Here

$$P_{\text{inc}} = |V_{\text{inc}}|^2 Y_c \quad (\text{H-2})$$

is the TEM mode incident power in the feed-coaxial transmission line with characteristic admittance Y_c . As indicated in previous sections, Γ_a represents the active reflection coefficient defined by Eq. (4-48a). In Eq. (H-1), P_t represents the far-field radiated power within a unit cell of cross section area $d \times h$. It is given by

$$P_t = \text{Re} \int_{-d/2}^{d/2} \int_0^h \hat{\mathbf{E}} \times \hat{\mathbf{H}}^* \cdot \mathbf{y}_0 \, dx \, dz. \quad (\text{H-3})$$

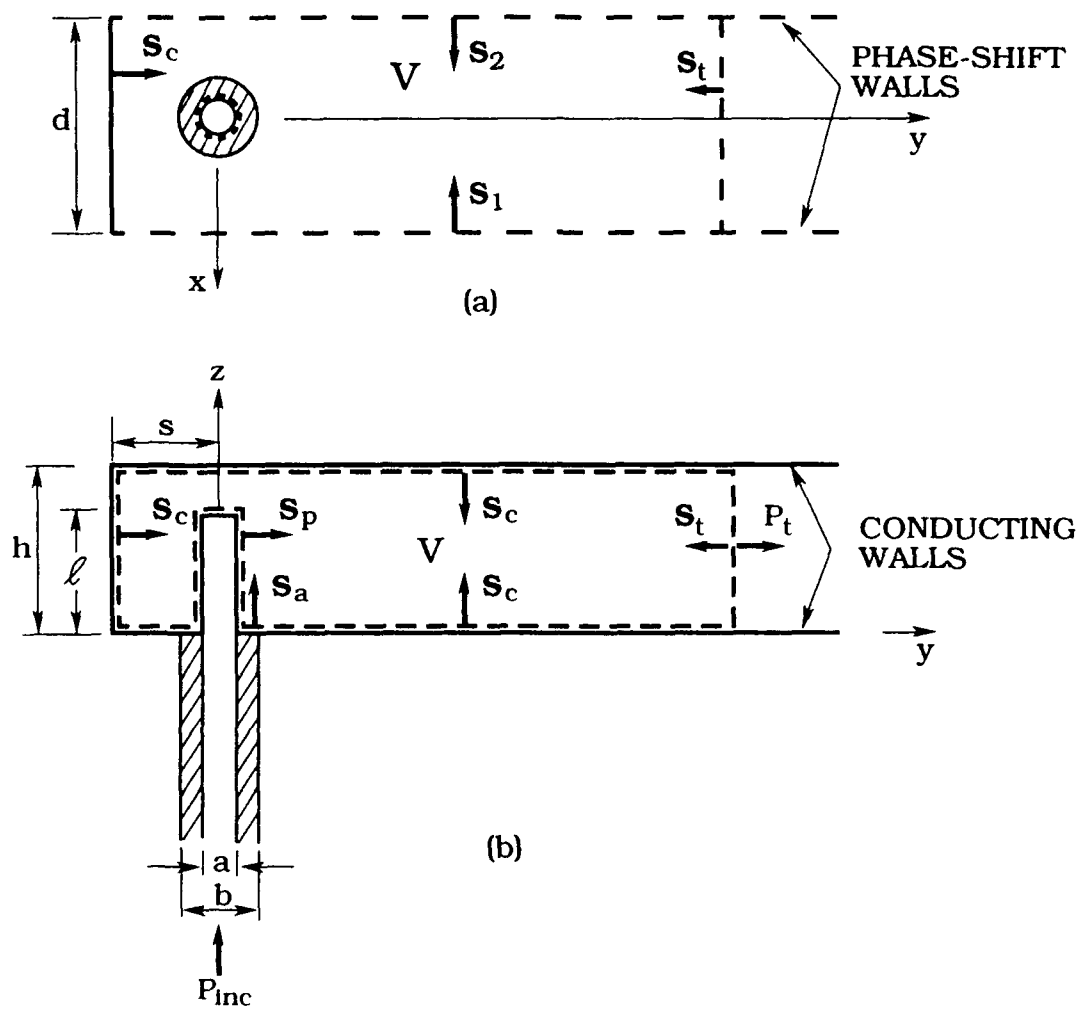


Figure H-1. Top (a) and Side (b) View of the Unit Cell Pertaining to Evaluation of the Complex Poynting Vector

To demonstrate Eq. (H-1) we may refer to a typical unit cell in Figure H-1, in which we consider a volume V bounded by a surface S and containing TE_{mn}^{v} -mode (double prime) fields. From the complex Poynting Vector Theorem, the time-average power transmitted across a closed surface S is given by the integral of the real part of the normal component of the complex Poynting vector $\hat{\mathbf{E}} \times \hat{\mathbf{H}}^*$; that is,

$$\operatorname{Re} \oint_S \hat{\mathbf{E}} \times \hat{\mathbf{H}}^* \cdot d\mathbf{S} = 0 \quad (H-4)$$

since there are no sources inside S . In Eq. (H-4) $d\mathbf{S} = \mathbf{n} dS$ is a vector element surface area directed into the volume V . The surface S consists of the surface S_c around the unit cell conducting walls, the unit cell side walls S_1, S_2 , the terminal plane S_t , and the surface over the aperture and probe area S_a and S_p , respectively. It is assumed that the reference plane S_t is sufficiently far from the radiating element so that only the dominant mode field exists there.

The contribution to the surface integral over the conducting walls is zero since $\hat{\mathbf{E}} \times d\mathbf{S}_c = 0$. The contribution to the surface integral over unit cell side walls, as will be shown, is also zero. This is due to the periodic property of the field, namely,

$$\hat{\mathbf{E}}(x+d, y, z) = \hat{\mathbf{E}}(x, y, z) e^{-jk_{xm}d} \quad (H-5)$$

and the fact that the normals on the opposite unit cell side-walls point in opposite directions (into the volume V). Relation (H-5) is statement of Floquet's Theorem where the transverse wave numbers of the Floquet modes are

$$k_{xm} = k_{x0} + \frac{2\pi}{d} m, \quad m = 0, \pm 1, \dots \quad (H-6)$$

With the help of Eq. (H-5), we write

$$\hat{\mathbf{E}}(d/2, y, z) e^{jk_{xm}d/2} = \hat{\mathbf{E}}(-d/2, y, z) e^{-jk_{xm}d/2} \quad (H-7a)$$

and

$$\hat{\mathbf{H}}(d/2, y, z) e^{jk_{xm}d/2} = \hat{\mathbf{H}}(-d/2, y, z) e^{-jk_{xm}d/2}. \quad (H-7b)$$

Consequently

$$\int_{S_1} \widehat{\mathbf{E}} \times \widehat{\mathbf{H}} \cdot d\mathbf{S}_1 = \int_{S_1} \widehat{\mathbf{E}}(d/2, y, z) \times \widehat{\mathbf{H}}^*(d/2, y, z) \cdot d\mathbf{S}_1 = \int_{S_1} \widehat{\mathbf{E}}(-d/2, y, z) \times \widehat{\mathbf{H}}^*(-d/2, y, z) \cdot d\mathbf{S}_1. \quad (H-8)$$

Since $d\mathbf{S}_1 = -x_0 dy dz = -d\mathbf{S}_2$ in Eq. (H-7), one may write

$$\begin{aligned} & \int_{S_1} \widehat{\mathbf{E}}(-d/2, y, z) \times \widehat{\mathbf{H}}^*(-d/2, y, z) \cdot d\mathbf{S}_1 \\ &= - \int_{S_2} \widehat{\mathbf{E}}(-d/2, y, z) \times \widehat{\mathbf{H}}^*(-d/2, y, z) \cdot d\mathbf{S}_2 = - \int_{S_2} \widehat{\mathbf{E}} \times \widehat{\mathbf{H}} \cdot d\mathbf{S}_2. \end{aligned} \quad (H-9)$$

From Eqs. (H-8) and (H-9) it follows that

$$\int_{S_1} \widehat{\mathbf{E}} \times \widehat{\mathbf{H}} \cdot d\mathbf{S}_1 + \int_{S_2} \widehat{\mathbf{E}} \times \widehat{\mathbf{H}} \cdot d\mathbf{S}_2 = 0 \quad (H-10)$$

and therefore there is no contribution in Eq. (H-4) due to the surface integral over the unit cell side walls S_1 and S_2 .

Consequently Eq. (H-4) reduces to

$$\operatorname{Re} \int_{S_a} \mathbf{E} \times \mathbf{H}^* \cdot \mathbf{n} dS_a + \operatorname{Re} \int_{S_p} \mathbf{E} \times \mathbf{H}^* \cdot \mathbf{n} dS_p + \operatorname{Re} \int_{S_t} \widehat{\mathbf{E}} \times \widehat{\mathbf{H}}^* \cdot \mathbf{n} dS_t = 0. \quad (H-11)$$

As noted earlier \mathbf{E} and $\widehat{\mathbf{E}}$ denote the same active array field in the parallel plate region. The \mathbf{E} represents the active array field in terms of cylindrical radial modes (see chapter 4) while $\widehat{\mathbf{E}}$ represents the active array field in terms of Floquet modes in the unit cell (see Chapter 5). In this Appendix both representations will be used, depending which is most convenient. Equation (H-11) can be further simplified by noting that

$$\int_{S_a} \mathbf{E} \times \mathbf{H}^* \cdot \mathbf{n} dS_a = \int_{S_a} (\mathbf{n} \times \mathbf{M}) \times \mathbf{H}^* \cdot \mathbf{n} dS_a = \int_{S_a} [\mathbf{M}(\mathbf{H}^* \cdot \mathbf{n}) - \mathbf{n}(\mathbf{H}^* \cdot \mathbf{M})] \cdot \mathbf{n} dS_a \quad (H-12)$$

where the relation for the aperture field $\mathbf{E} = \mathbf{n} \times \mathbf{M}$ has been used. Since $\mathbf{H}^* \cdot \mathbf{n} = 0$, Eq. (H-12) becomes

$$\int_{S_a} \mathbf{E} \times \mathbf{H}^* \cdot \mathbf{n} dS_a = - \int_{S_a} \mathbf{H}^* \cdot \mathbf{M} dS_a. \quad (H-13)$$

Here \mathbf{M} is the magnetic ring current given by

$$\mathbf{M} = -\phi_0 \frac{V_0(z=0^-)}{\rho \ln \frac{b}{a}} = \phi_0 M_\phi, \quad a \leq \rho \leq b. \quad (H-14)$$

Similarly, on the probe surface $\mathbf{J} = z_0 \mathbf{J}_z(z) = \mathbf{n} \times \mathbf{H}$ and therefore

$$\int_{S_p} \mathbf{E} \times \mathbf{H}^* \cdot \mathbf{n} dS_p = \int_{S_p} \mathbf{E} \times (\mathbf{J}^* \times \mathbf{n}) \cdot \mathbf{n} dS_p = \int_{S_p} [\mathbf{J}^* (\mathbf{E} \cdot \mathbf{n}) - \mathbf{n} (\mathbf{E} \cdot \mathbf{J}^*)] \cdot \mathbf{n} dS_p \quad (H-15a)$$

or

$$\int_{S_p} \mathbf{E} \times \mathbf{H}^* \cdot \mathbf{n} dS_p = - \int_{S_p} \mathbf{E} \cdot \mathbf{J}^* dS_p \quad (H-15b)$$

since $\mathbf{J}^* (\mathbf{E} \cdot \mathbf{n}) = 0$. Thus, Eq. (H-11) may be written as

$$Re \int_{S_a} \mathbf{H}^* \cdot \mathbf{M} dS_a + Re \int_{S_p} \mathbf{E} \cdot \mathbf{J}^* dS_p = Re \int_{S_t} \hat{\mathbf{E}} \times \hat{\mathbf{H}}^* \cdot \mathbf{y}_0 dS_t. \quad (H-16)$$

In the following three sections we will evaluate the integrals in Eq. (H-16) and show that Eq. (H-16) holds. This verifies the expressions and the relation between the two representations mentioned above for the active array fields introduced in Chapters 4 and 5.

H1 EVALUATION OF THE COMPLEX POYNING VECTOR OVER THE COAXIAL APERTURE AREA

We start from the first integral in Eq. (H-16) which can be written as

$$I_a = \operatorname{Re} \int_{S_a} \mathbf{H}^* \cdot \mathbf{M} dS_a = \operatorname{Re} \int_{\phi=0}^{2\pi} \int_{\rho=a}^b H_\phi^* (\rho, z=0^+) M_\phi \rho d\rho d\phi. \quad (H-17)$$

When Eq. (H-14) is used for M_ϕ , Eq. (H-17) becomes

$$I_a = -\frac{2\pi V_0(z=0^-)}{\ln \frac{b}{a}} \operatorname{Re} \int_{\rho=a}^b H_\phi^* (\rho, z=0^+) d\rho. \quad (H-18)$$

The integral in Eq. (H-18) is given by Eq. (4-43) as

$$\int_a^b H_\phi^* (\rho, z=0^+) d\rho = -\frac{K V_0^*(z=0^-)}{k \zeta_0} \left\{ \sum_{n=0}^{\infty} \frac{\epsilon_n}{\left[1 - \left(\frac{n\pi}{kh} \right)^2 \right]} \left[-j \frac{2}{\pi} \ln \frac{b}{a} + J_n H_0^{(2)}(\kappa_n b) \right. \right. \\ \left. \left. - H_n J_0(\kappa_n a) + J_n^2 S_n^2(\delta_x) \right] - \sum_{n=0}^{\infty} \epsilon_n J_n' J_0(\kappa_n a) [H_n + J_n S_n(\delta_x)] \right\}^* \quad (H-19)$$

where I'_n and $S_n(\delta_x)$ are defined in Eqs. (4-45h) and (4-47d), respectively.

For simplicity we shall assume that the probe current has a single term. In this case Eqs. (4-46) apply, that is,

$$I'_n = c'_1 I_{1n} \quad (H-20a)$$

where

$$I_{1n} = \begin{cases} -2 \frac{\frac{\lambda}{2l}}{\left(\frac{\lambda}{2l}\right)^2 - \left(\frac{n\lambda}{h}\right)^2} \cdot \frac{\lambda}{2l} \neq \frac{n\lambda}{h} \\ -\pi \frac{l}{\lambda} \quad \cdot \frac{\lambda}{2l} = \frac{n\lambda}{h} \end{cases} \quad (H-20b)$$

and

$$c'_1 = c'_{1r} + j c'_{1i} = \frac{B_1}{A_{11}}. \quad (H-20c)$$

Here c'_{1r} and c'_{1i} are real and

$$A_{11} = \sum_{n=0}^{\infty} \epsilon_n \left[1 - \left(\frac{n\pi}{kh} \right)^2 \right] J_0(\kappa_n a) \left[H_0^{(2)}(\kappa_n a) + J_0(\kappa_n a) S_n(\delta_x) \right] I_{1n}^2 \quad (H-21a)$$

$$B_1 = \sum_{n=0}^{\infty} \epsilon_n J_0(\kappa_n a) \left[H_n + I_n S_n(\delta_x) \right] I_{1n}. \quad (H-21b)$$

In view of Eqs. (H-20a) and (H-21b) when substituting Eq. (H-19) into Eq. (H-18) yields

$$I_a = \frac{\kappa |V_0(z=0^-)|^2}{kZ_0} \operatorname{Re} \left\{ \sum_{n=0}^{\infty} \frac{\epsilon_n}{\left[1 - \left(\frac{n\pi}{kh} \right)^2 \right]} \left[-j \frac{2}{\pi} \ln \frac{b}{a} + j_n H_0^{(2)}(\kappa_n b) \right. \right. \\ \left. \left. - H_n J_0(\kappa_n a) + j_n^2 S_n(\delta_x) \right]^* - (c'_1 B_1)^* \right\}. \quad (H-22)$$

To determine the real part of the sum in this relation we first examine $S_n(\delta_x)$. For this reason it is convenient to write

$$S_n(\delta_x) = S_{nr} + j S_{ni} \quad (H-23)$$

where S_{nr} and S_{ni} are real and can be found simply from Appendix E. Since $h < \lambda/2$, only $S_0(\delta_x)$ ($n = 0$) has a real part. In fact, since $d < \lambda/2$ only the $m = 0$ term in Eq. (E-15a) has a real part. It is easy to see that

$$S_{nr}(\delta_x) = -1 + \frac{4}{kd \cos \phi} \sin^2(kd \cos \phi). \quad (H-24)$$

Thus

$$S_n(\delta_x) = \begin{cases} S_{nr} + j S_{ni}, & n = 0 \\ j S_{ni}, & n \geq 1 \end{cases} \quad (H-25)$$

Based on the above discussion we conclude that only the $n = 0$ term in the sum of Eq. (H-22) has a real part.

To obtain an expression for $\operatorname{Re} (c'_1 B_1)^*$ in Eq. (H-18), we write

$$B_1 = B_{1r} + j B_{1i} \quad (H-26)$$

where B_{1r} and B_{1i} are real. Since $h < \lambda/2$ from Eq. (H-21b) we see that

$$B_{1r} = J_0(ka) I_{10} J_0 [1 + S_{or}(\delta_x)] = J_0(ka) I_{10} J_0 \frac{4}{kd \cos \phi} \sin^2(k \cos \phi). \quad (H-27)$$

Therefore

$$\operatorname{Re} \{c'_{1r} B_{1r}\}^* = \operatorname{Re} \{(c'_{1r} - j c'_{1i})(B_{1r} - j B_{1i})\} = c'_{1r} B_{1r} - c'_{1i} B_{1i}. \quad (H-28)$$

Inserting Eq. (H-28) into Eq. (H-22) we finally obtain

$$I_a = \frac{K |V_0(z=0^-)|^2}{k Z_0} \left\{ J_0^2 [1 + S_{or}(\delta_x)] - c'_{1r} B_{1r} + c'_{1i} B_{1i} \right\}. \quad (H-29)$$

H2 EVALUATION OF THE COMPLEX POYNTING VECTOR OVER THE PROBE SURFACE

We next consider the second integral in Eq. (H-16):

$$I_p = \operatorname{Re} \int_{S_p} \mathbf{E} \cdot \mathbf{J}^* dS_p \quad (H-30)$$

Since evaluation of I_p is similar to that of I_a above, our derivation will be brief. Since $\mathbf{E}(a, z)$ and $\mathbf{J}(z)$ have no angular dependence one has

$$I_p = 2\pi a \operatorname{Re} \int_{z=0}^l E_z(a, z) J_z^*(z) dz. \quad (H-31)$$

From Eqs. (4-20a) and (4-20b) for the single probe current term

$$J_z(z) = c_1 \sin \frac{\pi}{2l} (z - l). \quad (H-32)$$

The total tangential field on the probe surface is given by Eq. (4-22a) as

$$E_z(a, z) = jK V_0(z = 0^-) \sum_{n=0}^{\infty} (R_n - P_n I'_n) C_n(z) \quad (H-33)$$

where the functions R_n and P_n are defined in Eqs. (4-22b) and (4-22c), respectively. The I'_n is given by Eq. (4-24a) as

$$I'_n = c'_1 I_{1n} \quad (H-34a)$$

where, from Eqs. (4-24b) and (4-24c)

$$I_{1n} = k \int_0^l C_n(z) \sin \frac{\pi}{2l} (z - l) dz \quad (H-34b)$$

and

$$c'_1 = -j \frac{2\pi a Z_0}{V_0(z = 0^-)} c_1. \quad (H-34c)$$

Substituting Eq. (H-34a) into Eq. (H-33) and subsequently Eqs. (H-32) and (H-33) into Eq. (H-31) we have

$$I_p = \operatorname{Re} \left\{ j \frac{K V_0(z = 0^-) 2\pi a}{k} \sum_{n=0}^{\infty} (R_n - P_n c'_1 I_{1n}) c_1^* I_{1n} \right\}. \quad (H-35)$$

Using Eq. (H-28) we may write

$$I_p = \frac{K|V_0(z=0^-)|^2}{kZ_0} \operatorname{Re} \left\{ \sum_{n=0}^{\infty} \left(c_1'^* I_{1n} R_n - P_n |c_1'|^2 I_{1n}^2 \right) \right\} \quad (H-36a)$$

or in terms of A_{11} and B_1 defined by Eqs. (4-27b) and (4-27c) as

$$A_{11} = \sum_{n=0}^{\infty} P_n I_{1n}^2 \quad (H-36b)$$

$$B_1 = \sum_{n=0}^{\infty} R_n I_{1n} \quad (H-36c)$$

I_p becomes

$$I_p = \frac{K|V_0(z=0^-)|^2}{kZ_0} \operatorname{Re} \left\{ c_1'^* B_1 - |c_1'|^2 A_{11} \right\}. \quad (H-36d)$$

Since [see Eq. (4-27a)]

$$c_1' = \frac{B_1}{A_{11}} \quad (H-37a)$$

we see that

$$I_p = \frac{K|V_0(z=0^-)|^2}{kZ_0} \operatorname{Re} \left\{ \frac{B_1 B_1^*}{A_{11}^*} - \frac{B_1 B_1^*}{A_{11}^*} \right\} = 0. \quad (H-37b)$$

Thus the integral of the complex Poynting vector over the probe surface is zero, as it should be. The boundary conditions for the field on the probe are therefore satisfied.

Although $I_p = 0$, we rewrite Eq. (H-37b) into the form useful in the following analysis. We start from Eq. (H-36d) which can be rewritten in the form

$$I_p = \frac{K|V_0(z=0^-)|^2}{kZ_0} (c'_{1r} B_{1r} + c'_{11} B_{11} - |c'_1|^2 A_{11r}) \quad (H-38a)$$

where Eqs. (H-20c) for c'_1 , (H-26) for B_1 and

$$A_{11} = A_{11r} + j A_{11i} \quad (H-38b)$$

have been used. Since $h < \lambda/2$ and $d < \lambda/2$ it is easy to see that

$$A_{11r} = I_{10}^2 J_0^2(ka) [1 + S_{or}(\delta_x)] = I_{10}^2 J_0^2(ka) \frac{4}{kd \cos \hat{\phi}} \sin^2(kd \cos \hat{\phi}). \quad (H-39)$$

Inserting Eq. (H-39) into Eq. (H-38a) we obtain

$$I_p = \frac{K|V_0(z=0^-)|^2}{kZ_0} \left\{ c'_{1r} B_{1r} + c'_{11} B_{11} - |c'_1|^2 I_{10}^2 J_0^2(ka) [1 + S_{or}(\delta_x)] \right\} = 0. \quad (H-40)$$

We shall now sum Eqs. (H-29) and (H-40), that is

$$I_a + I_p = \frac{K|V_0(z=0^-)|^2}{kZ_0} [J_0^2 - 2c'_{1r} B_{1r} + |c'_1|^2 I_{10}^2 J_0^2(ka)] [1 + S_{or}(\delta_x)]. \quad (H-41)$$

Substitution of Eq. (H-24) for $S_{or}(\delta_x)$ and Eq. (H-27) for B_{1r} , and the relation

$$|I'_0|^2 = |c'_1|^2 \mathfrak{I}_{10}^2 \quad (H-42a)$$

into Eq. (H-41) yields the final result

$$\begin{aligned} I_a + I_p &= \operatorname{Re} \int_{S_a} \mathbf{H}^* \cdot \mathbf{M} dS_a + \operatorname{Re} \int_{S_p} \mathbf{E} \cdot \mathbf{J}^* dS_p = \operatorname{Re} \int_{S_a} \mathbf{H}^* \cdot \mathbf{M} dS_a \\ &= \frac{K|V_0(z=0^-)|^2}{kZ_0} \left[J_0^2 - 2c'_{1r} J_0(ka) \mathfrak{I}_{10} J_0 + |I'_0|^2 J_0^2(ka) \right] \frac{4}{kd \cos \hat{\phi}_0} \sin^2(kd \cos \hat{\phi}_0). \quad (H-42b) \end{aligned}$$

H3 EVALUATION OF THE COMPLEX POYNTING VECTOR OVER THE UNIT CELL CROSS-SECTION AREA

In this section we evaluate the power through the terminal plane S_t , which is given by the integral

$$P_t = \operatorname{Re} \int_{S_t} \hat{\mathbf{E}} \times \hat{\mathbf{H}}^* \cdot \mathbf{y}_0 dS_t. \quad (H-43)$$

We first list expressions relevant to the modal representation for the electromagnetic field in the unit cell. As already mentioned, the latter consists of a single monopole radiating into a rectangular waveguide with conducting top and bottom walls and phase-shift side walls defined by Floquet type boundary conditions. Denoting the transmission direction by y in a Cartesian coordinate system, the transverse field components due to a probe current and magnetic ring source in a unit cell with dimensions $h \times d$ may be expressed in terms of a complete set of TE_{mn}^y modes (double prime) as

$$\hat{\mathbf{E}}_t(\mathbf{r}) = \sum_{m=-\infty}^{\infty} \sum_{n=0}^{\infty} \hat{V}_{mn}''(y) \hat{\mathbf{e}}_{mn}''(x, z). \quad (H-44a)$$

$$\hat{\mathbf{H}}_t(\mathbf{r}) = \sum_{m=-\infty}^{\infty} \sum_{n=0}^{\infty} \hat{I}_{mn}''(y) \hat{\mathbf{h}}_{mn}''(x, z). \quad (H-44b)$$

The normalized vector mode functions are

$$\hat{\mathbf{e}}_{mn}''(x, z) = -\mathbf{z}_0 \frac{k_{xm}}{|k_{xm}|} \frac{e^{-jk_{xm}x}}{\sqrt{d}} \sqrt{\frac{\epsilon_n}{h}} \cos \frac{n\pi}{h} z \quad (H-45a)$$

and

$$\hat{\mathbf{h}}''(x, z) = \mathbf{y}_0 \times \hat{\mathbf{e}}_{mn}''(x, z) \quad (H-45b)$$

where

$$\epsilon_n = \begin{cases} 1, & n = 0 \\ 2, & n \geq 1 \end{cases} \quad (H-45c)$$

Relations (H-45) represent a complete, orthonormal set such that

$$(\hat{\mathbf{e}}_{mn}'' \cdot \hat{\mathbf{e}}_{m'n'}^{''*}) = \int_{-d/2}^{d/2} \int_0^h \hat{\mathbf{e}}_{mn}'' \cdot \hat{\mathbf{e}}_{m'n'}^{''*} dx dz = \delta_{mn, m'n'} \quad (H-46)$$

and similarly for the $\hat{\mathbf{h}}_{mn}''$ functions. The asterisk denotes the complex conjugate and $\delta_{mn, m'n'}$ stands for the standard Kronecker delta function. Modal voltage and current amplitudes

\hat{V}_{mn}'' and \hat{I}_{mn}'' satisfy the transmission-line equations

$$\frac{d\hat{V}_{mn}''(y)}{dy} = -j \kappa_{mn} \hat{Z}_{mn} \hat{I}_{mn}''(y) \quad (H-47a)$$

$$\frac{d\hat{I}_{mn}''(y)}{dy} = -j \kappa_{mn} \hat{Y}_{mn} \hat{V}_{mn}''(y) \quad (H-47b)$$

where the modal characteristic impedances \hat{Z}_{mn}'' and admittances \hat{Y}_{mn}'' and the modal propagation constants κ_{mn} are defined by

$$\hat{Z}_{mn}'' = \frac{1}{\hat{Y}_{mn}''} = \frac{\omega \mu_0}{\kappa_{mn}} \quad (H-47c)$$

$$\kappa_{mn} = \sqrt{k^2 - k_{tmn}^2}, \quad \text{Im} \{ \kappa_{mn} \} \leq 0. \quad (H-47d)$$

The choice of sign on the square root insures the radiation condition for $y \rightarrow \infty$. Here \mathbf{k}_{tmn} is the transverse propagation wave vector

$$\mathbf{k}_{tmn} = \mathbf{x}_0 \mathbf{k}_{xm} + \mathbf{z}_0 \mathbf{k}_{zn} \quad (H-48a)$$

with

$$k_{tmn} = |\mathbf{k}_{tmn}| = \sqrt{k_{xm}^2 + k_{zn}^2} \quad (H-48b)$$

where

$$k_{xm} = k_{x0} + \frac{2\pi}{d} m, \quad m = 0, \pm 1, \dots \quad (H-48c)$$

and

$$k_{zn} = \frac{n\pi}{h}, \quad n = 0, 1, \dots \quad (H-48d)$$

In Eq. (H-48c), $k_{x0}d = \delta_x$ where δ_x is the inter-element steering phase delay.

For the dominant mode field ($m = n = 0$), Eq. (H-44) takes the form

$$\hat{E}_t(r) = \hat{V}_{00}''(y) \hat{e}_{00}''(x) \quad (H-49a)$$

$$\hat{H}_t(r) = \hat{I}_{00}''(y) \hat{h}_{00}''(x) \quad (H-49b)$$

where from Eq. (H-45a)

$$\hat{e}_{00}''(x) = -z_0 \frac{k_{x0}}{|k_{x0}|} \frac{e^{-jk_{x0}x}}{\sqrt{dh}}. \quad (H-49c)$$

Since

$$\hat{I}_{00}'' = \hat{Y}_{00}'' \hat{V}_{00}'' \quad (H-50a)$$

we can see from Eqs. (H-49) and (H-46) that Eq. (H-43) may be written as

$$P_t = |\hat{V}_{00}''|^2 \hat{Y}_{00}'' \quad (H-50b)$$

where the dominant TE_{00}^y -mode characteristic admittance as defined by Eq. (H-47c) is

$$\hat{Y}_{00}'' = \frac{\kappa_{00}}{\omega \mu_0} = \frac{\cos \hat{\phi}_0}{\zeta_0}. \quad (H-50c)$$

In Eq. (H-50c) we used the relations

$$\zeta_0 = \sqrt{\frac{\mu_0}{\epsilon_0}} \quad (H-51a)$$

$$k_{x0} = k \sin \hat{\phi}_0 \quad (H-51b)$$

and [see Eq. (4-47d)]

$$\kappa_{00} = \sqrt{k^2 - k_{x0}^2} = k \cos \hat{\phi}_0 \quad (H-51c)$$

where the scan angle $\hat{\phi}_0$ is measured from array broadside.

The active electric far field in terms of TE_{m0}^y Floquet modes in the unit cell is given by Eq. (6-18) which is valid for $h < \lambda/2$. For convenience we rewrite this relation below:

$$\hat{E}_z(x, y) = -\frac{4K V_0(z=0^-)}{d} \left[J_0 - I'_0 J_0(ka) \right] \sum_{m=-\infty}^{\infty} e^{-jk_{xm}x} e^{-jk_{m0}y} \frac{\sin \kappa_{m0}s}{\kappa_{m0}} e^{-jk_{m0}s} \quad (H-52)$$

where κ_{m0} is given by Eq. (6-12b). Also as already indicated, for simplicity of presentation in this Appendix we assume that the inter-element spacing $d < \lambda/2$ so that at the terminal plane S_t only the propagating $m = n = 0$ Floquet mode exists. In this case Eq. (H-52) reduces to

$$\hat{E}_z(x, y) = -\frac{4K V_0(z=0^-)}{d} \left[J_0 - I'_0 J_0(ka) \right] e^{-jk_{x0}x} e^{-jk_{00}y} \frac{\sin \kappa_{00}s}{\kappa_{00}} e^{-jk_{00}s}. \quad (H-53)$$

We would like to cast Eq. (H-53) into the form of Eq. (H-49a). Comparing these two relations we see that

$$\hat{V}_{00}''(y) = 4K V_0(z=0^-) \sqrt{\frac{h}{d}} \frac{|k_{x0}|}{k_{x0}} \left[J_0 - I'_0 J_0(ka) \right] \frac{\sin \kappa_{00} s}{\kappa_{00}} e^{-j\kappa_{00} s}. \quad (H-54)$$

From here

$$|\hat{V}_{00}''|^2 = 16 K^2 |V_0(z=0^-)|^2 \frac{h}{d} \left[J_0^2 - J_0 I_0^* J_0(ka) - J_0 I'_0 J_0(ka) + |I'_0|^2 J_0^2(ka) \right] \frac{\sin^2 \kappa_{00} s}{\kappa_{00}^2}. \quad (H-55)$$

Since

$$I'_0 = (c'_{1r} + j c'_{1i}) \mathbf{1}_{10} \quad (H-56a)$$

one may write

$$|\hat{V}_{00}''|^2 = \frac{16 K^2 |V_0(z=0^-)|^2}{d} \left[J_0^2 - 2 J_0 J_0(ka) c'_{1r} \mathbf{1}_{10} + |I'_0|^2 J_0^2(ka) \right] \frac{\sin^2 \kappa_{00} s}{\kappa_{00}^2}. \quad (H-56b)$$

The real transmitted power through the terminal plane S_t can be now evaluated from Eq. (H-50b) where the dominant mode characteristic admittance is defined by Eq. (H-50c).

Substitution of Eqs. (H-56b) and (H-50c) into Eq. (H-50b) yields

$$P_t = \frac{4 K^2 |V_0(z=0^-)|^2 h}{k \zeta_0} \left[J_0^2 - 2 J_0 J_0(ka) c'_{1r} \mathbf{1}_{10} + |I'_0|^2 J_0^2(ka) \right] \frac{4}{kd \cos \hat{\phi}_0} \sin^2 (ks \cos \hat{\phi}_0). \quad (H-57)$$

Inserting Eq. (4-5d) for K into Eq. (H-57) we finally obtain

$$P_t = \frac{K |V_0(z=0^-)|^2}{k Z_0} \left[J_0^2 - 2 J_0 J_0(ka) c'_{1r} I_{10} + |I'_0|^2 J_0^2(ka) \right] \frac{4}{kd \cos \hat{\phi}_0} \sin^2(k s \cos \hat{\phi}_0) \quad (H-58a)$$

where

$$Z_0 = \frac{\zeta_0}{2\pi} \ln \frac{b}{a}. \quad (H-58b)$$

We see that Eq. (H-58a) is identical to Eq. (H-42b) and therefore we conclude that Eq. (H-16) is indeed satisfied. The latter relation is directly related to the conservation of power condition [Eq. (H-1)] by the requirement that the complex power across a coaxial aperture must be continuous. Namely,

$$V_0(z=0^-) I_0^*(z=0^-) = \int_{S_a} \mathbf{H}^* \cdot \mathbf{M} dS_a. \quad (H-59)$$

Since, as shown in Section H2

$$\operatorname{Re} \int_{S_p} \mathbf{E} \cdot \mathbf{J}^* dS_p = 0 \quad (H-60a)$$

one sees that

$$V_0(z=0^-) I_0^*(z=0^-) = P_t. \quad (H-60b)$$

The TEM mode voltage and current amplitudes V_0 and I_0 [see Eqs. (4-36) and (4-37)] in the feed coaxial transmission line can be expressed in terms of incident and reflected TEM mode voltages and currents V_{inc} , V_{ref} , and I_{inc} , I_{ref} , and the active reflection coefficient $\Gamma_a(\delta_x)$ as follows:

$$V_0(z=0^-) = V_{\text{inc}}(z=0^-) [1 + \Gamma_a(\delta_x)] \quad (\text{H-61a})$$

$$I_0(z=0^-) = I_{\text{inc}}(z=0^-) - I_{\text{ref}}(z=0^-). \quad (\text{H-61b})$$

Using the identities

$$V_{\text{ref}} = \Gamma_a(\delta_x) V_{\text{inc}} \quad (\text{H-62a})$$

$$I_{\text{inc}} = Y_c V_{\text{inc}} \quad (\text{H-62b})$$

$$I_{\text{ref}} = Y_c V_{\text{ref}} \quad (\text{H-62c})$$

one may write

$$V_0 I_0^* = V_0 \left(I_{\text{inc}}^* - I_{\text{ref}}^* \right) = V_0 Y_c \left(V_{\text{inc}}^* - V_{\text{ref}}^* \right). \quad (\text{H-62d})$$

Inserting Eqs. (H-61a) and (H-62a) into Eq. (H-62d) we obtain

$$V_0 I_0^* = |V_{\text{inc}}|^2 Y_c [1 + \Gamma_a(\delta_x)] [1 - \Gamma_a^*(\delta_x)] = |V_{\text{inc}}|^2 Y_c [1 - |\Gamma_a(\delta_x)|^2] \quad (\text{H-63a})$$

where

$$|V_{\text{inc}}|^2 Y_c = P_{\text{inc}} \quad (\text{H-63b})$$

represents the incident power in the feed transmission line. From Eqs. (H-60b) and (H-63) we see that

$$P_{\text{inc}} [1 - |\Gamma_a(\delta_x)|^2] = P_t \quad (\text{H-64})$$

which is the desired conservation of power relation. Thus, the expressions for the active array field derived in Chapters 4 and 5 indeed satisfy the conservation of power condition.

Appendix I

Numerical Evaluation of the Integral $I(\Omega) = \int_a^b f(x) e^{-j\Omega x} dx$

In this Appendix we consider the problem of evaluating numerically the integral

$$I(\Omega) = \int_a^b f(x) e^{-j\Omega x} dx \quad (I-1)$$

where the function $f(x)$ is specified at a finite number of equally spaced sampling points, and Ω is a large parameter. Since the integrand is a rapidly varying function of x , standard numerical integration techniques cannot be applied because of the large number of integration steps required to achieve a desired computational accuracy.

To develop an efficient integration scheme we assume that $f(x)$ is given by a set of values $\{f(x_i)\}$, $i = 1, 2, \dots, N+1$ on the interval $[a, b]$ where

$$x_i = a + (i-1) \frac{b-a}{N} \quad (I-2)$$

and N is the number of subintervals. We approximate $f(x)$ in each subinterval by a cubic polynomial

$$P_i(x) = C_{0,i} + C_{1,i}(x-x_i) + C_{2,i}(x-x_i)^2 + C_{3,i}(x-x_i)^3 \quad (I-3)$$

with coefficients $C_{n,i}$, $n=0, \dots, 3$, $i=1, \dots, N$ to be determined.

Hence one can write

$$\int_a^b f(x) e^{-j\Omega x} dx \approx \sum_{i=1}^N \int_{x_i}^{x_{i+1}} P_i(x) e^{-j\Omega x} dx. \quad (I-4)$$

It is important to mention that the integrals in Eq. (I-4) can be evaluated in closed form and consequently the integration error is due only to the approximation of $f(x)$ in each subinterval by a cubic polynomial $P_i(x)$. The interpolation error is estimated in Reference 12.

The method of determining $P_i(x)$ is known as cubic spline interpolation and is described in Reference 12. The method is based on the requirement that

$$P_i(x_i) = f(x_i) \quad (I-5a)$$

$$P_i(x_{i+1}) = f(x_{i+1}) \quad (I-5b)$$

$$P_{i-1}(x_i) = P_i(x_i). \quad (I-5c)$$

and

$$P'_i(x_i) = f'(x_i) \quad (I-5d)$$

$$P'_i(x_{i+1}) = f'(x_{i+1}) \quad (I-5e)$$

with $i=1, \dots, N$.

From Reference 12 the coefficients $C_{n,i}$ are

$$C_{0,i} = f(x_i) \quad (I-6a)$$

$$C_{1,i} = \frac{\Delta x_{i-1} f[x_i, x_{i+1}] + \Delta x_i f[x_{i-1}, x_i]}{\Delta x_{i-1} + \Delta x_i} \quad (I-6b)$$

$$C_{2,i} = \frac{f[x_i, x_{i+1}] - C_{1,i}}{\Delta x_i} - C_{3,i} \Delta x_i \quad (I-6c)$$

$$C_{3,i} = \frac{C_{1,i+1} + C_{1,i} - 2 f[x_i, x_{i+1}]}{(\Delta x_i)^2} \quad (I-6d)$$

where

$$\Delta x_i = x_{i+1} - x_i \quad (I-6e)$$

and $i=1, \dots, N+1$.

The standard difference function is

$$f[x_0] = f(x_0) \quad (I-7a)$$

$$f[x_1, x_0] = \frac{f[x_1] - f[x_0]}{x_1 - x_0} \quad (I-7b)$$

$$f[x_2, x_1, x_0] = \frac{f[x_2, x_1] - f[x_1, x_0]}{x_2 - x_0} \quad (I-7c)$$

or in general

$$f[x_n, x_{n-1}, \dots, x_1, x_0] = \frac{f[x_n, x_{n-1}, \dots, x_1] - f[x_{n-1}, x_{n-2}, \dots, x_0]}{x_n - x_0} \quad (I-7d)$$

Rewriting Eq. (I-3) into the form

$$P_1(x) = A_{0,1} + A_{1,1} x + A_{2,1} x^2 + A_{3,1} x^3 \quad (I-8a)$$

where

$$A_{0,1} = C_{0,1} - C_{1,1} x_1 + C_{2,1} x_1^2 - C_{3,1} x_1^3 \quad (I-8b)$$

$$A_{1,1} = C_{1,1} - 2 C_{2,1} x_1 + 3 C_{3,1} x_1^2 \quad (I-8c)$$

$$A_{2,1} = C_{2,1} - 3 C_{3,1} x_1 \quad (I-8d)$$

$$A_{3,1} = C_{3,1} \quad (I-8e)$$

Eq. (I-4) becomes

$$\int_a^b f(x) e^{-j\Omega x} dx = \sum_{l=1}^N \sum_{n=0}^3 A_{n,l} \int_{x_l}^{x_{l+1}} x^n e^{-j\Omega x} dx. \quad (I-9)$$

The integrals in Eq. (I-9) can be evaluated analytically using the general formula from Reference 14

$$\int x^n e^{-j\Omega x} dx = \frac{j}{\Omega} x^n e^{-j\Omega x} + \frac{jn}{\Omega} \int x^{(n+1)} e^{-j\Omega x} dx. \quad (I-10)$$

For the special case of

$$I(\Omega) = \int_{-a}^a f(x) e^{-j\Omega x} dx \quad (I-11a)$$

where $f(x)$ is an even function of x , Eq. (I-11a) reduces to

$$I(\Omega) = 2 \int_0^a f(x) \cos \Omega x dx. \quad (I-11b)$$

In this case

$$\int f(x) \cos \Omega x dx = \sum_{i=1}^N \sum_{n=0}^3 A_{n,i} \int_{x_i}^{x_{i+1}} x^n \cos \Omega x dx \quad (I-12a)$$

where $A_{n,i}$ are given by Eq. (I-8) and

$$\int x^n \cos \Omega x dx = \frac{x^n \sin \Omega x}{\Omega} - \frac{n}{\Omega} \int x^{(n-1)} \sin \Omega x dx. \quad (I-12b)$$

Specifically, the integrals in Eq. (I-12b) are

$$\int_{x_1}^{x_{l+1}} \cos \Omega x \, dx = \frac{\sin \Omega x_{l+1} - \sin \Omega x_1}{\Omega} \quad (I-13a)$$

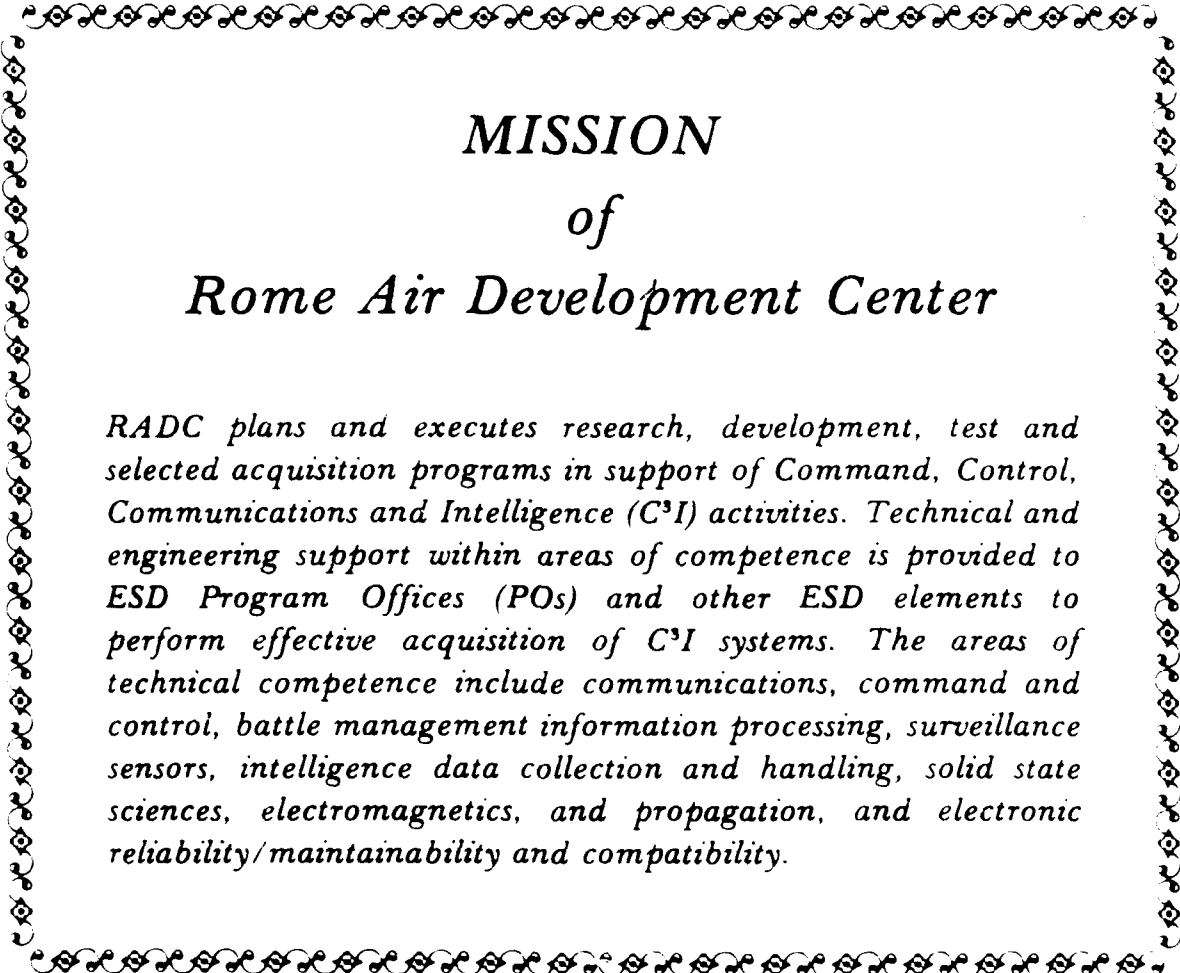
$$\int_{x_1}^{x_{l+1}} x \cos \Omega x \, dx = \frac{\cos \Omega x_{l+1} - \cos \Omega x_1}{\Omega^2} - \frac{x_{l+1} \sin \Omega x_{l+1} + x_1 \sin \Omega x_1}{\Omega} \quad (I-13b)$$

$$\begin{aligned} \int_{x_1}^{x_{l+1}} x^2 \cos \Omega x \, dx &= \frac{2 x_{l+1} \cos \Omega x_{l+1} - 2 x_1 \cos \Omega x_1}{\Omega^2} \\ &+ \left(\frac{x_{l+1}^2}{\Omega} - \frac{2}{\Omega^3} \right) \sin \Omega x_{l+1} - \left(\frac{x_1^2}{\Omega} - \frac{2}{\Omega^3} \right) \sin \Omega x_1 \end{aligned} \quad (I-13c)$$

and

$$\begin{aligned} \int_{x_1}^{x_{l+1}} x^3 \cos \Omega x \, dx &= \left(\frac{3 x_{l+1}^2}{\Omega^2} - \frac{6}{\Omega^4} \right) \cos \Omega x_{l+1} - \left(\frac{3 x_1^2}{\Omega^2} - \frac{6}{\Omega^4} \right) \cos \Omega x_1 \\ &+ \left(\frac{x_{l+1}^3}{\Omega} - \frac{6 x_{l+1}}{\Omega^3} \right) \sin \Omega x_{l+1} - \left(\frac{x_1^3}{\Omega} - \frac{6 x_1}{\Omega^3} \right) \sin \Omega x_1. \end{aligned} \quad (I-13d)$$

Setting $x=k_{x0}$, $\Omega = pd$ and $f(x) = d/\pi \Gamma_a(k_{x0})$, Eqs. (I-12) and (I-13) can be applied to evaluate the coupling coefficients for the infinite linear array of monopoles in the parallel plate waveguide as defined by Eq. (4-52).



MISSION

of

Rome Air Development Center

RADC plans and executes research, development, test and selected acquisition programs in support of Command, Control, Communications and Intelligence (C³I) activities. Technical and engineering support within areas of competence is provided to ESD Program Offices (POs) and other ESD elements to perform effective acquisition of C³I systems. The areas of technical competence include communications, command and control, battle management information processing, surveillance sensors, intelligence data collection and handling, solid state sciences, electromagnetics, and propagation, and electronic reliability/maintainability and compatibility.